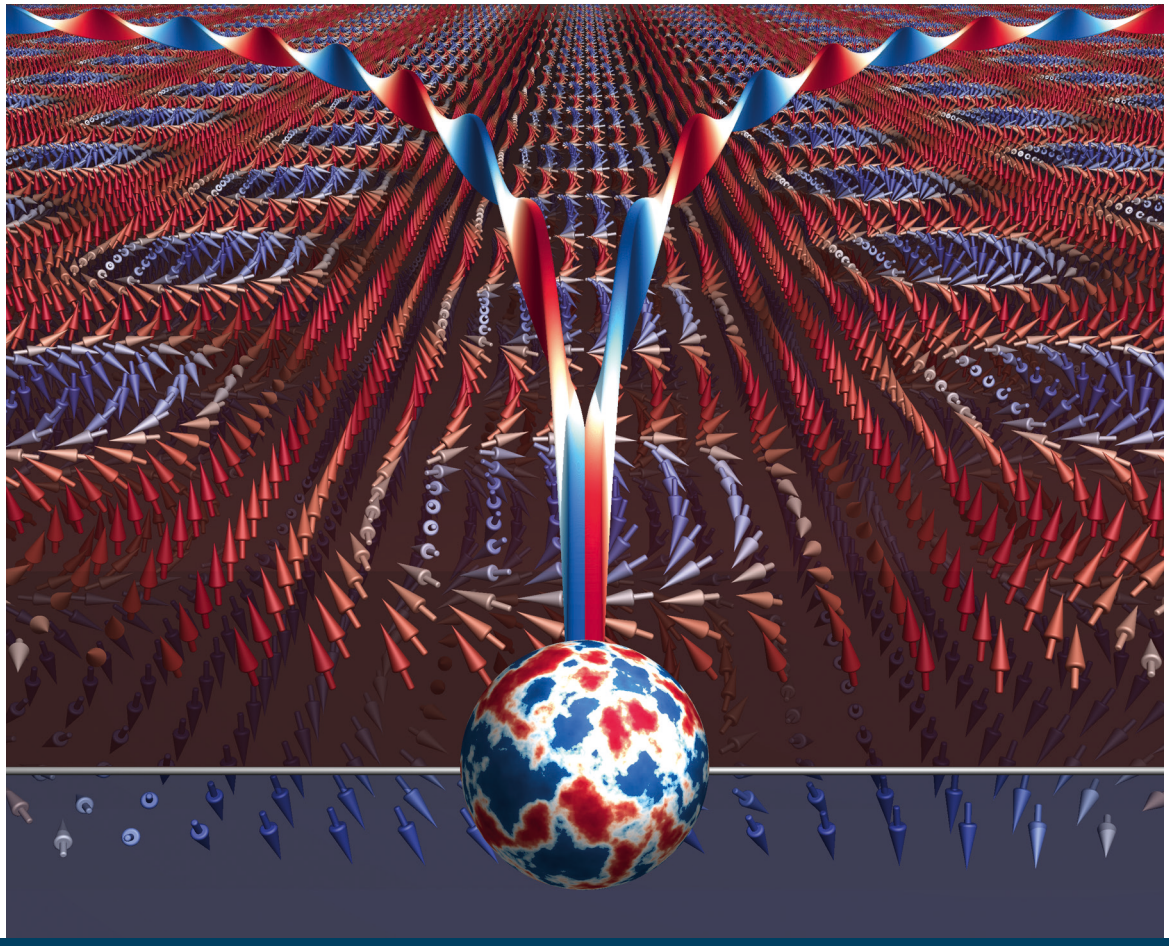

Topological transport in non-Abelian spin textures from first principles

Patrick Markus Buhl

Schlüsseltechnologien / Key Technologies
Band / Volume 197
ISBN 978-3-95806-408-9

Mitglied der Helmholtz-Gemeinschaft

JÜLICH
Forschungszentrum

Schriften des Forschungszentrums Jülich
Reihe Schlüsseltechnologien / Key Technologies Band / Volume 197

Forschungszentrum Jülich GmbH
Peter Grünberg Institut (PGI)
Quanten-Theorie der Materialien (PGI-1/IAS-1)

Topological transport in non-Abelian spin textures from first principles

Patrick Markus Buhl

Schriften des Forschungszentrums Jülich
Reihe Schlüsseltechnologien / Key Technologies Band / Volume 197

ISSN 1866-1807 ISBN 978-3-95806-408-9

Bibliografische Information der Deutschen Nationalbibliothek.
Die Deutsche Nationalbibliothek verzeichnet diese Publikation in der
Deutschen Nationalbibliografie; detaillierte Bibliografische Daten
sind im Internet über http://dnb.d-nb.de abrufbar.

Herausgeber und Vertrieb:	Forschungszentrum Jülich GmbH Zentralbibliothek, Verlag 52425 Jülich Tel.: +49 2461 61-5368 Fax: +49 2461 61-6103 zb-publikation@fz-juelich.de www.fz-juelich.de/zb
Umschlaggestaltung:	Grafische Medien, Forschungszentrum Jülich GmbH
Druck:	Grafische Medien, Forschungszentrum Jülich GmbH
Copyright:	Forschungszentrum Jülich 2019

Schriften des Forschungszentrums Jülich
Reihe Schlüsseltechnologien / Key Technologies, Band / Volume 197

D 82 (Diss., RWTH Aachen University, 2019)

ISSN 1866-1807
ISBN 978-3-95806-408-9

Vollständig frei verfügbar über das Publikationsportal des Forschungszentrums Jülich (JuSER)
unter www.fz-juelich.de/zb/openaccess.

Abstract

Recently, skyrmions attracted huge attention due to their topological character which ensures surprisingly stable, particle-like magnetic excitations on small scales with distinctive dynamical properties. Their characteristic transport signature—the topological Hall effect—has become an established tool for detection of topologically non-trivial ferromagnetic textures. However, this attribute vanishes when considering degenerate antiferromagnetic structures as the associated emergent magnetic field is spin-dependent. This thesis demonstrates the emergence of an alternative transport signature in case of antiferromagnetic skyrmion textures—the topological spin Hall effect.

Firstly, a computational scheme is developed which estimates the topological spin Hall effect based on semiclassical wave-packet dynamics. In the adiabatic limit, their equations of motion allow to treat large-scale magnetic textures on top of locally collinear, small-scale Hamiltonians, here based on density functional theory. Transport expressions are extracted by combination of the equations of motion and the Boltzmann formalism. While the analogous procedure is straightforward for ferromagnetic materials, the wave-packet's $\mathcal{SU}(2)$-nature, caused by degenerate bands, results in additional spin dynamics and non-abelian Berry curvatures which inhibit direct transport evaluation. While the reciprocal-space dynamics are treated on the Boltzmann level, the spin and real-space dynamics are solved iteratively starting from multiple initial positions. Evaluation of the traversed paths results in integrated expressions for the topological spin Hall effect.

Sizable topological spin Hall responses are predicted in simulations for the exemplary Fe/Cu/Fe-trilayers and thin chromium layers when artificially imprinting synthetic and intrinsic antiferromagnetic skyrmions, respectively. The importance of the non-abelian dynamics is demonstrated by large differences relative to comparative calculations of decoupled antiparallel ferromagnets. While the spin evolution results in surprisingly homogeneous transport modifications, the $\boldsymbol{k}$-resolved intra-band overlap has a particularly unpredictable distribution requiring precise density functional theory calculations. Further numerical thoroughness is required because of extreme sensitivity with respect to small reciprocal-space modifications such as slight Fermi energy changes. Furthermore, the evolution of the $\boldsymbol{k}$-dependent transport and overlap properties is shown with respect to thickness variations demonstrating rich tuning potential. Conversely, multiple calculations modifying the skyrmion-radius, -shape, and -density demonstrate the topological invariance of the topological spin Hall effect.

Overall, the topological spin Hall effect is an interesting phenomenon with rich application possibilities. Foremost, it facilitates the discovery of the so far undetected antiferromagnetic skyrmions, but also might provide efficient spin-current generation as required in spintronic applications. Alternatively, it could serve as read-out mechanism of more complex devices like antiferromagnetic, skyrmion-based racetrack memory. Hence, the developed versatile and readily applicable computational scheme is a great addition for future antiferromagnetic skyrmion studies.

Kurzfassung

Seit ihrer Entdeckung haben Skyrmionen viel Aufmerksamkeit aufgrund ihrer topologischen Eigenschaften, wie beispielsweise Stabilität auf kleinen Skalen und teilchenähnlichem dynamischen Verhalten, erhalten. Die charakteristische Transportsignatur – der topologische Hall-Effekt – ist ein etabliertes Werkzeug zur Detektierung topologisch nicht-trivialer ferromagnetischer Strukturen. Allerdings verschwindet dieses Phänomän in antiferromagnetischen Strukturen, da das assoziierte emergente magnetische Feld spinabhängig ist. Diese Arbeit demonstriert das Auftreten einer alternative Transportsignatur im Falle antiferromagnetischer Skyrmionen – den topologischen Spin Hall-Effekt.

Zunächst wird ein Verfahren zur Berechnung des topologischen Spin Hall-Effekts entwickelt, welches auf der Dynamik semiklassischer Wellenpakete basiert. Deren Bewegungsgleichungen erlauben, im adiabatischen Limit, die Verknüpfung von großskalige magnetische Texturen mit kleinskaligen, lokal kollinearen, hier dichtefunktional-basierten Hamiltonians. Anschließend werden Transportausdrücke aus der Kombination dieser Bewegungsgleichungen mit den Boltzmanngleichungen extrahiert. Im ferromagnetischen Fall können die resultierenden Gleichungen direkt ausgewertet werden, allerdings haben die Wellenpakete entarteter Bänder aufgrund ihres $\mathcal{SU}(2)$-Charakters zusätzliche Spindynamik und nichtabelsche Berry-Krümmungen, welche eine direkte Berechnung verhindern. Während die Dynamik im reziproken Raum weiterhin im Boltzmann-Formalismus behandelt werden kann, müssen die Spin- und Realraum-Bewegungsgleichungen von mehreren Anfangszuständen aus iterativ gelöst werden. Die Auswertung dieser Trajektorien erlaubt die Berechnung des topologische Spin Hall-Effekt aus aufintegrierten Größen.

Die anschließende Anwendung ergibt erherbliche topologische Spin Hall Signale in den exemplarischen Fe/Cu/Fe- und Chrom-Dünnschichtsystemen mit aufgeprägten synthetischen beziehungsweise intrinsischen antiferromagnetischen Skyrmionen. Die Berücksichtigung der nichtabelschen Dynamik ist notwendig, wie durch Vergleich mit entkoppelten, antiparallelen Ferromagneten demonstriert wird. Die zusätzliche Spindynamik resultiert in überraschend homogenen Modifikationen, allerdings ist die $\boldsymbol{k}$-abhängige Intraband-Kopplung unvorhersehbar, was genaue Dichtefunktionalberechnungen voraussetzt. Weiterhin sind genaue Modelle notwendig, da selbst kleinen Änderungen im reziproken Raum, wie etwa Fermi-Energie Variationen, zu großen Transportmodifikationen führen. Dies wird auch durch die $\boldsymbol{k}$-anhängigen Transport- und Kopplungseigenschaften demonstriert, deren Schichtdickeabhängigkeit viel Optimierungspotential bietet. Andererseits wird die Invarianz des topologischen Spin Hall-Effekt anhand von Skyrmion Radius-, Form-, und Dichtevariationen verifiziert.

Ingesamt gesehen ist der topologische Spin Hall-Effekt ein interessantes Phänomen mit vielfältigen Anwendungsmöglichkeiten. Zunächst ermöglicht es die experimentelle Verifizierung der bislang unentdeckten antiferromagnetischen Skyrmionen, könnte aber auch zur effizienten Generierung von Spinströmen dienen, welche in spintronischen Anwendungen benötigt werden. Alternativ könnte die Signatur auch als Auslesemechanismus in komplizierteren Bauteilen dienen, wie etwa im Fall von antiferromagnetischem, skyrmion-basiertem Racetrack-Speicher. Dementsprechend ist das hier entwickelte, vielseitige und direkt anwendbare Berechnungsverfahren eine sinnvolle Ergänzung für zukünftige Studien über antiferromagnetische Skyrmionen.

Contents

1

Introduction

Since the beginning of the computer age, magnetic structures have played an important role as information carrier of which the non-volatile version as in hard disk drives and magnetic tape has prevailed to date. With the ensuing miniaturization enforced by increasing demand for computational resources and power efficiency, the utilized structures have shrunken significantly due to tremendous fabrication advancements as well as new ground-breaking concepts enhancing writing and reading procedures [1]. While the magnetic control of a single holmium atom as ultimate goal of this quest has already been achieved [2], reasonable technological implementations are impossible since the required tools and environment conditions are only attainable in laboratories.

An alternative venue to control of increasingly small magnetic domains are skyrmions. These particle-like excitations of the magnetic texture have topological protection which allows surprisingly stable small-scale objects with clear distinction from the trivial background state [3, 4]. While the smallest skyrmions require similar prerequisites as the holmium device, skyrmions were also observed at room temperature demonstrating technological realizability [5]. A further advantage from the electronic point of view is that all necessary procedures can be executed by electric fields only. Creation, destruction [6], and controlled motion [7] of skyrmions has been demonstrated by application of electric fields. Furthermore, the topological Hall effect [8, 9] as transversal transport characteristic of skyrmions enables efficient detection and thus information extraction.

A popular proposal for technological utilization of these exciting properties are race-track memory applications where skyrmions replace domain-walls as basic information carriers [10]. Advantages include the particle-like behavior with repulsion from edges and impurities as well as the tremendously increased energy-efficiency due to the ultra-low current requirements necessary to generate motion [11]. As the hypothetical switching times are compatible to those of conventional random-access memory, skyrmion-based devices provide an opportunity to reintroduce competitive non-volatile random-access or even universal memory. Alternatively, logic gates based on skyrmions have been devised [12] and neuromorphic devices utilizing skyrmion characteristics were proposed [13].

Another promising branch of spintronics are antiferromagnets which have several advantages over their ferromagnetic relatives, mainly the relative indifference to external magnetic fields, absence of stray fields, significantly faster dynamics [14], and general abundance in nature [15].

Recently, significant progress towards electronic control of antiferromagnetic states was achieved both on the theoretical level accurately predicting spin torques and by improved experimental configurations allowing controlled switching between distinct antiferromagnetic states [16]. Furthermore, spin currents can be generated efficiently in antiferromagnetic materials which is a cornerstone of energy-efficient spintronics.

Antiferromagnetic skyrmions were proposed to combine the best of both worlds [17–20]. While the topological properties provide stability, localization, and distinct transport features, the antiferromagnetic character supplies even faster magnetization dynamics, independence of perturbing fields, and vanishing of the skyrmion Hall effect otherwise causing unwanted transversal motion. Unfortunately, no experimental realizations of skyrmions have been reported so far despite their promising features, possibly due to already extraordinary results in ferromagnets, difficulties resolving antiferromagnetic textures, and complications stabilizing skyrmions without support of magnetic fields. Moreover, the topological Hall effect vanishes in compensated antiferromagnetic skyrmions which prevents a frequently used measurement method and, more importantly, inhibits the common electronic read-out mechanism in the proposed technological applications.

Fortunately, the topological spin Hall effect emerges as alternative signature of such antiferromagnetic skyrmions and thus could be analogously used as method for experimental verification or even read-out mechanism in devices. Hence, it is a key feature both in search and application of antiferromagnetic skyrmions, however its theoretical estimation is severely complicated by the degenerate nature of many antiferromagnetic materials and thus relatively unexplored.

This thesis addresses that issue by developing a computational scheme which allows the evaluation of the topological spin Hall effect based on realistic reciprocal-space models with assumed skyrmion texture in the adiabatic limit. More precisely, the approach of this thesis estimates the transport characteristics from semiclassical equations of motion describing the dynamics of degenerate electron wave-packets traversing antiferromagnetic textures. Material parameters are obtained from accurate and versatile *ab-initio* calculations using collinear density functional theory while the texture's real-space dependence is considered as a parameter in the equations of motion only. The cumulative transport properties are obtained through the Boltzmann formalism. Within the constant relaxation time approximation, the reciprocal-space dynamics is directly included into the transport expressions while the wave-packet's real- and spin-dependence are treated iteratively employing the Runge-Kutta formalism. Integration over the Fermi surface, initial real-space positions, and iteration-time of the wave-packet trajectories subsequently allows to evaluate the topological spin Hall effect expressions.

The above procedure is applied to two common synthetic or intrinsic antiferromagnetic thin films with imprinted skyrmionic texture. Sizeable topological spin Hall effects are predicted, the effect of thickness variations is studied, and the dependence with respect to coupling and reciprocal-space features is scrutinized. Furthermore, the topological character is verified through extensive skyrmion texture distortions and type variations. Hence, the functionality of this general method predicting the topological spin Hall effect is demonstrated so that immediate application to suspected antiferromagnetic skyrmion structures is possible.

This thesis is segmented into the following parts. The second chapter starts with an introduction to the general properties characterizing the multifaceted skyrmions. After-

wards, theoretical means are discussed which allow realistic description of magnetic textures. These methods are complemented by experimental techniques verifying skyrmions in different materials and promising propositions for skyrmion utilizations. Then, the concept of antiferromagnetic skyrmions and their established properties are described. The chapter is concluded by definition of the two interpolation possibilities used in this thesis to describe such textures.

The third chapter covers the dynamics of electron wave-packets when traversing magnetic textures with applied fields. First, the ferromagnetic non-degenerate case is reviewed as an introduction to the ensuing dynamics of twofold-degenerate states which are complicated by the non-abelicity of the Berry curvatures. The equations of motion are specified for the cases of collinear and non-collinear antiferromagnets leading to significant simplifications necessary for the transport expressions of the fourth chapter. There, the degenerate and non-degenerate wave-packet dynamics are applied to the Boltzmann formalism after brief overview of the electron and spin Hall effects. The computational details of these transport calculations are covered in the fifth chapter where implementation schemes and convergence with respect to numerical parameters are scrutinized.

In the sixth chapter the previous transport formalism is tested with a simplistic, nearest neighbor tight-binding model of an antiferromagnetic bilayer with imprinted skyrmion texture. Several transport contributions vanish due to the simplistic setup which allows detailed $\boldsymbol{k}$- and energy-resolved investigations of the basic transport effects.

The seventh chapter concisely reviews density function theory from which detailed and accurate material descriptions are obtained. Furthermore, the principles of Wannier functions are outlined which are subsequently used as a basis to an efficient model Hamiltonian. Afterwards, the computational procedures and employed codes implementing the previous methods are summarized and the numerical expressions to extract all necessary reciprocal-space properties for the transport calculations are given.

The eighth chapter covers the FeCuFe-trilayer as an example for synthetic antiferromagnetic skyrmions using a density functional theory based model. First, the topological spin Hall effect of one example thickness is investigated in great detail with variation of the Fermi energy and consideration of spin-orbit coupling on the density functional theory level. Furthermore, the influence of different thicknesses and the evaluations of coupling between the states is studied.

The alternative setup of intrinsic antiferromagnetic skyrmions imprinted on thin chromium layers is considered in the ninth chapter. The topological spin Hall effects are calculated for mono- and triple-layers with focus on the $\boldsymbol{k}$-resolved distributions and dependences on material parameters. Most importantly, the topological character of the skyrmion-associated Hall effect is verified by examination of various different textures that reveals only slight systematical variations.

Finally, the last chapter draws conclusions and summarizes the results.

Parts of this thesis have already been published in Refs. [21, 22]. This includes a brief description of the developed computational procedure, covered in Secs. 4 and 5, as well as the study of the FeCuFe-trilayer (Sec. 8).

2

Skyrmion overview

While many transport mechanisms exists, this thesis investigates one particular subset—the topological (spin) Hall effect. The essential ingredient for its emergence is the existence of skyrmions, special localized magnetic structures. This section briefly summarizes the research and properties of skyrmions, additional information can be obtained from the many reviews as for example Ref. [3].

The term "skyrmion" is relatively old and originates from Tony Skyrme who found several quantized solution in a classical field theory [23]. Back then, they were used to describe mesons and baryons in the field of high-energy physics. More recently, Skyrme's model attracted substantial interest since a similar problem exists in solid state physics when describing magnetic textures. Consequently, the name "skyrmion" was coined when Bogdanov and Hubert found a set of magnetic interactions and parameters which indeed allow for the formation of such "vortex-like structure" [24, 25]. With the experimental discovery of skyrmion lattices [26] they finally entered the solid-state physics mainstream eliciting numerous theoretical and experimental studies scrutinizing their exciting properties in search for useful applications.

First, the defining topological features of skyrmions are described which is followed by possibilities for theoretical descriptions, experimental realizations and their potent properties. Subsequently, their peculiarities in antiferromagnetic materials are summarized after which this chapter is concluded with a description of the skyrmion-interpolations utilized in later parts of this thesis.

2.1 Skyrmion properties

Skyrmions are usually characterized as topologically non-trivial, particle-like excitations in the magnetic texture. This first section describes these characteristic properties starting with the notion of magnetic textures.

In general, textures describe the large-scale variation of a basic order parameter. In case of magnetic textures this basic parameter is the magnetic order parameter. In magnetism several basic phases exist: dia-, para-, ferro-, ferri-, and antiferromagnetism. The latter three can serve as basis for the subsequent considerations as they include long-range order even in

absence of applied field. The concept of a magnetic order parameter is naturally included in the intuitive picture of having spins within the unit cell pointing in a distinguished direction. In the ferromagnetic case, where all spins in the unit cell point into one direction, the order parameter is chosen as those spin's direction. Similarly, the order parameter of collinear ferrimagnets and antiferromagnets can be defined by the direction of the spin, the only difference is that a consistent choice of either direction is necessary due to their antiparallel aligned spins. For non-collinear magnets, i.e. systems including spins within the unit cell that are neither parallel nor antiparallel, the order parameter can be chosen by selecting one arbitrary superposition of the spins as a reference state. Afterwards, different spin directions can be expressed as solid rotations from the reference state.

With the notion of a distinct magnetic order parameter it is to imagine its variation over scales much larger than atomic unit cell. Mathematically, such variations can be understood as a vector field defining the local spin orientation in real space. One of the simplest possible long-scale variations is the rotation of the order parameter along one direction which results in a spin wave in case of ferromagnets. In general, a multitude of different phases or textures exists such as large domain walls, helical and conical spin spirals, bubbles, and skyrmions.

2.1.1 Topological character

The essential question addressed in this section is what distinguishes a skyrmion from other possible structures. The answer to that question is the topological non-triviality of skyrmions which is described in this section and which causes the exotic properties outlined in the following sections. In simple words, the topological non-triviality means that it is impossible to deform a skyrmion by smooth transformations, instead drastic changes are necessary to transform the skyrmion into the background state.

An instructive analogue is a double domain wall in a one-dimensional spin-chain. For example, such a system could be constructed with the outer spins pointing into the up-direction while the middle spins point downwards. The vector field describing the spin orientations has to be smooth to allow sensible topological classifications so that the spin directions of neighboring spin may only differ slightly. Consequently, 180° flips are forbidden as they are drastic changes, instead smooth spin rotations may constitute the domains walls. Two distinct possibilities for such structures exist, either both domain walls rotate into the same or into opposite direction. The difference becomes obvious when moving the domain walls towards each other. If the domain walls have opposite rotational sense, the approaching wall can be smoothly rotated until reaching the up-direction since no large angles appear between them. Thus, such domain walls can be trivially annihilated or created by topologically allowed operations. In the other case with the same rotational sense large relative spin angles appear when trying to push the domain walls into each other. Accordingly, the domain walls can only be annihilated by drastic measure such as a spin-flips which distinguishes such structures from the previous trivial ferromagnetic groundstate.

Skyrmions are analogues of the above, non-trivial type of domain wall in 2 dimensions meaning that that no transformations exist that smoothly transform the skyrmion structure into the ferromagnetic background state. Example skyrmion textures are shown in Fig. 2.2. Defining features are spins in the skyrmion core pointing opposite to the background direction

and spin spirals in slices intersecting the skyrmion. If such a one-dimensional intersection crosses the skyrmion core a full rotation is obtained in analogy to the previous paragraph's structure. However, crossing slices into opposite directions both express this characteristic so that the structure is now two-dimensional. As smooth deformations are allowed the overall shape of a skyrmion can change drastically from this idealized picture for example by elongation, however the opposite core and the spiraling property remain.

Skyrmions can be distinguished from the trivial structure using the stereographic projection. This projection is well-suited to map an isolated magnetic structure onto a sphere. Choosing the projection point in the particle's core, the core's spin direction is mapped onto the sphere's lowest point while the background state is mapped to the topmost point. In between, the texture specifics determine the spin directions. Whether a texture is a skyrmion is then determined by checking if this spin map covers the whole sphere or not. If the spins wrap the sphere more than once, the magnetic texture describes a skyrmion of higher number with similar properties.

A more rigorous distinctions between skyrmions and other textures is possible using topology. It provides a framework to distinguish functions through their homotopy classes [27]. In general, all maps from a base manifold to a given domain can be discriminated into different homotopy groups. Now each homotopy group discerns the functions in disjoint homotopy classes which are distinguished by their corresponding topological invariant of integer value. If two functions are homotopic to each other, their topological invariants are identical and they can be transformed into each other by smooth transformations.

The connection to skyrmions is given by treating the magnetic texture as a function mapping from $\mathbb{R}_2 \cup \{\infty\}$ to $\mathbb{S}_2$ where $\mathbb{S}_n$ denotes the n'th unit sphere [28]. Topologically different textures can now be distinguished by the mapping degree. This quantity is the integral over the topological charge density for all such smooth functions mapping $\mathbb{S}_n$ to $\mathbb{S}_n$. In the one-dimensional case ($n = 1$) the degree coincides with the classical winding number, in the skyrmion case ($n = 2$) it is the skyrmion number

$$Q(\boldsymbol{m}) = \frac{1}{4\pi} \int_{\mathbb{R}^2} d\boldsymbol{r}\ \boldsymbol{m} \cdot \left(\frac{\partial \boldsymbol{m}}{\partial r_1} \times \frac{\partial \boldsymbol{m}}{\partial r_2} \right). \tag{2.1}$$

While the $n = 1$ winding number measures how often a curve winds around the origin, the skyrmion number Q, often called ($\mathbb{S}_2$) winding number or skyrmion charge, measures how often the spin wraps the sphere as required from the initial considerations with the stereographic projection. Q can take integer values, i.e. $Q \in \mathbb{Z}$, and is the topological invariant used to discern the different magnetic texture's homotopy classes. We call all textures with $Q(\boldsymbol{m}) = 0$ topologically trivial, as they can be smoothly transformed into the magnetic background state. Conversely, all states with $Q(\boldsymbol{m}) \neq 0$ are called skyrmion although further kinds can be distinguished.

The defining topological invariant also causes the iconic properties of skyrmions. The most direct characteristic is the inferred stability. Since smooth deformations can not change the homotopy class and as drastic magnetization changes involve larger energy scales, real systems' skyrmions are expected to remain stable as long as the topological requirements are satisfied. This means that the order parameter field has to be a valid approximation on

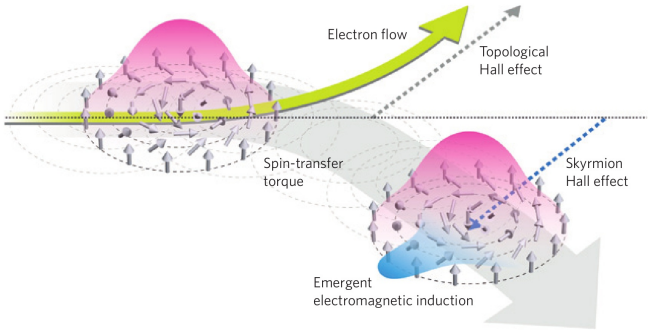

Figure 2.1: Sketch of physical phenomena causing skyrmion and topological Hall effect. Picture taken from Ref. [3]

the atomic scale so that the texture variation is much smaller than the inter-atomic spacing of the constituting magnetic atoms. Otherwise, the skyrmions might vanish which one can imagine as further shrinking until the skyrmion is no longer resolved by the atomic grid and hence has effectively vanished. Alternatively, random noise as introduced by temperature might supply the energy to overcome, or tunnel, through the energy barrier to the trivial state. Other possibilities for skyrmion destruction include merging with the edges of magnetic domains, collision with huge impurities significantly changing the underlying energy parameter set, or annihilation with skyrmions of opposite charge. However, in most cases repelling forces prevent such annihilations, impurities can be prevented by improved production processes, and few systems allow for simultaneous existence of skyrmions with opposite charge.

Further effects caused by the skyrmion number are the skyrmionic Hall effect and the topological (spin) Hall effect (Fig. 2.1), the main subject of this thesis which is described in Secs. 4.1.1, 4.2.1 and calculated in the final chapters of this thesis.

2.1.2 Skyrmion types

From the previous chapter it is clear that skyrmions are textures with non-zero skyrmion number, yet more differentiations exist within this large subset of possible textures. A first distinction can be made with respect to their rotational direction. While it is required that the spin textures wrap the whole sphere in the stereographic projection, no rotational sense is enforced leaving freedom for further characterizations. Analogously to domain walls of Bloch- and Néel-type, skyrmions can be differentiated into Bloch- and Néel-type depending on their rotational direction. An archetypical Néel-skyrmion's spin rotates exactly in or against the direction of the skyrmion core when following a straight path through the skyrmion. Conversely, Bloch-skyrmion rotate in one of the perpendicular directions. Both possibilities are depicted in Fig. 2.2.

Another, more impacting distinction originates in the skyrmion number's sign. Two possibilities exist for switching $\mathrm{sgn}(Q)$ which naturally requires drastic modifications. The trivial alternative is inversion of all spin as in the case of the time-reversal operator. Since the

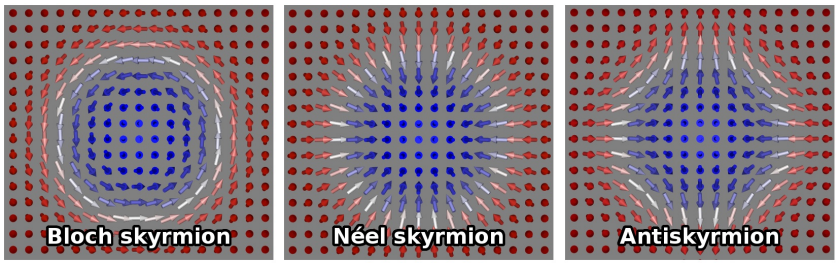

Figure 2.2: Magnetization visualization of different skyrmion types.

skyrmion number (Eq. 2.1) consists of an odd number of magnetization direction occurrences, time-reversal results in a skyrmion number sign change. As the background state is inverted as well, no pair of such $Q = \pm 1$ skyrmions is feasible in one magnetic domain. The other, more interesting possibility is the differentiation between skyrmions and antiskyrmions. Their background state magnetization is equivalent, but their $\mathbb{S}_1$ winding number enclosing the skyrmion core has opposite signs which causes a skyrmion number sign-change [29]. The descriptive difference between an antiskyrmion and a skyrmion is the direction of spin rotation (Fig. 2.2). While for some radial directions the antiskyrmion appears as a Néel-skyrmion, in other directions it has the rotational sense of a Bloch-skyrmion. If the in-plane spin-orientations constitute a different winding number than in case of a Bloch-skyrmion, the magnetic texture is an antiskyrmion with correspondingly inverted skyrmion number. Which types of skyrmions a system exhibits is determined by the DMI tensor and hence severely restricted by the systems symmetries [29].

Since the skyrmion charge is an integer number also higher order skyrmions with e.g. $Q = 2$ are possible. Such skyrmions' magnetizations wrap the unit sphere several times but retain the general skyrmion properties as topological "protection". Skyrmions with $Q = 2$ have to be distinguished from two independent $Q = 1$ skyrmions, which also have $Q = 2$ when integrating over the whole texture but behave as 2 independent particle-like excitations instead of 1 excitations that can not be separated by small forces. As many skyrmion properties are proportional to the skyrmion number, such systems for example exhibit a larger topological spin Hall effect. However, the material requirements for their existence are more restrictive so that few skyrmions of higher numbers have been found experimentally and applications are less likely.

While the previous considerations treated isolated skyrmions, skyrmion lattices have similar properties. They arise when creating more and more skyrmions in a system until it is energetically disadvantageous to spawn additional ones. These skyrmions then tend to from a regular lattice due to the skyrmion's mainly repulsive and only slightly attractive interactions. Such lattices are used in this thesis as basic magnetic texture whose topological spin Hall effect is investigated. The used interpolations are described in Sec. 2.4. Experimentally, a perfect, infinite domain is never created, instead several domains appear bordered by lattice imperfections caused by vacancies, step boundaries, or temperature. Typically, several skyrmions are found within a domain grain several but in some systems skyrmion lattice can

also fill large portions of domains.

Since the topological motivation (Sec. 2.1.1) heavily relies on the two-dimensionality of the base manifold, the three-dimensionality of real materials attenuates the previous strong arguments. In fact, several different magnetic structures in close resemblance of the 2D-skyrmion are possible. The most natural extension are skyrmion tubes, structures in which the 2-dimensional skyrmion texture does not change in the third dimension. This is a reasonable assumption for thin films, but they are expected to occur in thick materials as well although their phase-space extend is often reduced relative to their 2D counterpart. Yet, their energetic stability can be enhanced by slight deformed along the third direction especially in case of multilayers. Even attractive potentials may arise from such deformations keeping the tubes together [30]. Other related textures include chiral bobbers [31], skyrmion tubes connected to a surface that shrink down to a Bloch point with increasing depth, or even textures characterized by higher dimension nontrivial topology such as Hopfions [28]. Since this thesis restricts itself to very thin films, no such elaborate structures are taken into consideration. Instead, rigid skyrmion tubes analogous to the 2D skyrmion texture are assumed.

2.2 Skyrmions in practice

Given the previous theoretical prerequisites and characteristics of skyrmions, this chapter covers the theoretical means of describing skyrmion textures in realistic systems. Furthermore, experimental measurement methods and results demonstrating the existence of skyrmion are summarized after which propositions for their utilization are touched.

2.2.1 Theoreticaldescriptions

Many theoretical possibilities to describe magnetic textures exist. In this section they are shortly summarized demonstrating the requirements and realization possibilities of skyrmion textures. A more extensive overview over the described frameworks with further references is given in Ref. [32].

Since the basic constituents of magnetic textures, the magnetic moments, are quantum objects, the most precise descriptions require full quantum mechanical treatment. Consequently, the quantum Heisenberg model is a most accurate description. However, skyrmions require a smooth texture containing many atomic sites so that the necessary system sizes are not treatable on this level of accuracy.

Therefore, an approximation is necessary to obtain a numerically solvable description. A natural approximation is the classical limit which yields the atomistic Heisenberg model. There, the spins are considered as classical vectors arranged on a lattice. Instead of a complicated quantum Hamiltonian, the energy of a spin configuration is determined by an energy expression containing a multitude of magnetic interactions acting on vectorial spins. Typically, those interactions include the Heisenberg exchange, the Dzyaloshinsky-Moriya interaction (DMI) [33, 34], magneto-crystalline anisotropy, dipole-dipole interactions, and the Zeeman effect. For further calculations a choice of interaction parameters is necessary. While some calculations simply assume some interactions and scan large parameter spaces, other studies try to extract

effective parameters from experimental measurements or from detailed simulations of the system's Hamiltonian, for example by employing density functional theory (Sec. 7.1.1). Either way, approximations to the multiple-spin interactions, that sometimes fall off very slowly with increasing distance, are necessary. Different methods for obtaining its energetically preferable spin configurations exist. Either the spin dynamics can be tracked by solving the Landau-Lifshitz-Gilbert equations [35] or the energy can be directly minimized though several different procedures. Furthermore, the minimal energy path between spin configurations can be mapped by the geometric nudged elastic band method [36]. Thus, the energetic preference of skyrmions can be demonstrated for a multitude of interaction parameter sets and even their dynamics can be investigated with great precision.

While the previous framework allows precise calculations with atomic resolution, its applicability is limited to small-scale textures. However, skyrmions exist on different length scales even approaching radii of 300 nm [37] which is not reasonably resolvable within the atomistic Heisenberg model. Instead, the micromagnetic model is employed for such systems.

The further approximation of the micromagnetic model is that the microscopic details are averaged out so that the spin are no longer treated as vectors on a lattice but instead as a continuous magnetization field. Accordingly, the previous atomic interactions are combined into effective micromagnetic interactions that define the energy as a functional of the magnetization vector field. Subsequently, minimization methods can be used to determine the magnetic groundstate while the Landau-Lifshitz equations describe the magnetization dynamics .

The huge conceptional advantage of this approach is that the skyrmions are described by a continuous field analogous to the definition of skyrmions in Sec. 2.1.1. Since a multitude of micromagnetic energy functionals exist, describing various physical phenomena, a simple model is desirable to study skyrmion formation. Historically, the first theoretical description of magnetic skyrmions was done by Bogdanov and Hubert [24] with a relatively simple functional. There, the importance of the DMI for the formation of skyrmions was recognized. This antisymmetric interaction, originating in spin-orbit coupling, prefers orthogonal spin orientation with a distinct rotational sense introducing chirality. A most simple model can be formulated by adding exchange and Zeeman interaction. For this model it can be analytically proven that a single skyrmion of charge $Q = -1$ is energetically preferable over the topologically trivial state for a finite range of interaction parameters [38].

While the exhibition of skyrmions in such a simple system demonstrates their commonness, the necessity for DMI reduces the number of potential candidate materials. DMI is strongly dependent on symmetries which often restricts its original tensor property to vector or even scalar character and requires inversion symmetry breaking. Still, various inversion-symmetry broken bulk materials such as the B20 compounds [26] or thin multilayers with ideally constructive interfacial DMI were found to exhibit skyrmions. Especially the multilayer setup provides rich tuning potential allowing alterations the phase space of skyrmions and their shape [39].

A last theoretical aspect worth mentioning is the Thiele equation [40]. It describes the effective motion of rigid skyrmions and can be derived from the Landau-Lifshitz-Gilbert equation. Most notably, it includes a component which causes a transversal acceleration proportional to the skyrmion number. This intrinsic property similar to the Magnus effect

prevents skyrmions from moving along applied currents and is accordingly the source of the skyrmion Hall effect.

2.2.2 Experiments

This chapter shortly outlines experimental measurements of skyrmions to demonstrate that those structures are not theoretical physicist's phantasms but physical phenomena realized in various materials. A plethora of methods exist to experimentally verify the formation of skyrmions, some of which are described in the following.

The method most related to this thesis' topic is measurement of the topological Hall effect (Sec. 4.1.1). This indirect method relies on the transversal transport signal proportional to the skyrmion number. The simplicity of electron transport measurements requiring Hall bar geometry with attached leads makes it a convenient choice. However, the ordinary and anomalous Hall effects conceal the topological Hall effect due to their similar response. Involved procedures have to be undertaken to disentangle the different contributions. The ordinary Hall effect can be estimated by high temperature measurements in the paramagnetic phase and is subsequently subtracted using its linear dependence on the magnetic field. The anomalous Hall effect is more tricky but can be estimated by simultaneous measurements of the magnetization. Then, clear bumps in the Hall signals are observed when entering the skyrmion phase after subtraction of the alternative sources. This procedure has been successfully employed in case of $Mn_{1-x}Fe_xSi$ where the Hall signals were verified by supporting simulations reproducing the skyrmion transport characteristics [41]. The agreement between the measured signals and the theoretical estimations validate the applicability of the semiclassical approximations in combination with Boltzmann equations to estimate the topological Hall effect. This validation is important for further sections as the application of this method on degenerate antiferromagnetic skyrmions is the main topic of this thesis.

Alternatively, skyrmions can be verified by more direct experimental techniques summarized in the following.

The historically first method demonstrating the exhibition of skyrmion lattices is small angle neutron scattering [26]. It is based on elastic scattering of polarized or unpolarized neutrons from which the magnetic form factor is extracted. Then, it is possible to recover the magnetic texture by mathematical means with resolutions from nm to μm scales [42]. The initial experimental skyrmion study [26] investigating MnSi found an interference pattern indicating a magnetic texture consisting of a superposition of 3 spin spirals relatively tilted by 120°. This magnetic texture is interpreted as skyrmion lattice and called 3$\boldsymbol{q}$-texture (Sec. 2.4.1) in the following.

Alternatively, magnetic textures of thin films can be measured by Lorentz transition electron microscopy [43]. There, highly accelerated and focused electrons transverse thin sample while being slightly deflected by the sample's magnetic field. Afterwards, the texture can be reconstructed from tiny phase differences through numerical inversion. Its high resolution allows detection and characterization of small skyrmions [44].

Even smaller surface magnetic structures can be resolved by scanning tunneling microscopy. This method measures the tunneling currents between a probing tip and the sample thereby extracting information about the electronic structure at an atomic level. One possibility to

accurately resolve the magnetic texture is spin polarized scanning tunneling microscopy. It additionally uses a magnetic coating on the tip so that a spin projected signal is measured. The entire direction of the sample's spin can be naturally obtained by rotation of the tip's spin orientation. However, the magnetic texture can be resolved without magnetic coating as well. This is possible due to the non-collinear magnetoresistance which modifies the bandstructure in case of tilted neighboring spins so that tunneling signals depend on the local spin orientations [45]. Scanning tunneling microscopy provides extremely high resolution thus allowing the measurement of very small skyrmions at the surface of thin films [46]. Furthermore, the great resolution allows even direct measurement of antiferromagnetic alignments.

Using these experiments a multitude of materials were confirmed to exhibit skyrmions in bulk systems [26, 41, 47] such as the prominent B20-compounds as well as in various thin films [44, 48, 49]. Moreover, skyrmions were discovered in numerous multilayers [49–53] with large optimization potential due to stacking and thickness variations. Skyrmions are exhibited in a wide temperature range, from few degrees [48] to room temperature [5], and were even found in insulators [54]. Moreover, severely distorted skyrmions were created [55, 56], the relation to highly confined domains was investigated [57], and even the existence of antiskyrmions was verified [58]. Even the dynamics of skyrmion with respect to applied fields were assessed [7, 59]. Hence, skyrmions are under well experimental control so that their implementation into devices becomes conceivable.

2.2.3 Interesting properties

In recent times topological properties in reciprocal-space attracted great interest due to the exhibition of surface states and topological protection. While the spin-polarized surface states may be utilized in many experiments and applications, memory realizations are not as promising. Although the topological phases can be tuned by strain or magnetic fields [60–62], or by electric fields as in case of interfacial phase change materials [63], switching between the states requires relatively large energies. Hence, memory applications simply distinguishing the reciprocal-space topological characters benefit from long life-times in relatively small material structure-sizes, but switching of their global topological characters requires relatively large energies.

Skyrmions do not have this disadvantage due to their localization in real-space. Further advantages include the possibility to create and move skyrmions applying easily-implementable electric fields. Hence, memory-states can be switched efficiently by motion of skyrmions so that neither creation or annihilation of skyrmions are necessary. A popular proposition to harness these properties is the utilization as racetrack memory [10]. The use of skyrmions has several advantages over previous racetrack propositions utilizing domain walls [64]. Motion through corners and bends is easier due the skyrmions locality and repulsion from walls and other obstacles. Additionally, skyrmion implementations requires much smaller currents for similar accelerations of the information-carries compared to the domain-wall case. Hence, skyrmions have excellent prospects with respect to low-energy devices. Their 0-dimensionality, in contrast to the 1-dimensional domain walls, allows interesting concepts like multi-lane tracks [65]. Further propositions exist where the second state is not topologically trivial but the antiskyrmions state thus preventing memory faults due to different accelerations or pinning

in a chain of bits [29].

But skyrmions application propositions are not restricted to racetrack applications. Alternatively, they might be utilized as a multi-level memory due to their integer character. Furthermore, skyrmions ensembles can be considered whose statistical behavior allows for several computation tasks based on thermally driven dynamics [66]. Skyrmion-based transitions have been proposed paving the road towards hybrid skyrmionic-electronic devices [67]. Even direct computation with skyrmions is feasible since logical AND and OR gates, basic building blocks of electronic devices, are possible [12]. Another prospect of skyrmion applications are realizations in neuromorphic computing. Skyrmionic devices can naturally include properties necessary for artificial synapses such as "short-term plasticity long-term potential functionalities" which provides definite advantages over alternative electronic devices [13].

In conclusion, skyrmions provide various promising vistas for devices with distinct advantages over existing solutions. Realizations become increasingly probable due to the quickly increasing experimental expertise in many groups all over the world which necessitate numerous theoretical studies supporting existent experiments and devising new applications.

2.3 Antiferromagnetic skyrmions

So far, all skyrmionic system have been constructed from a ferromagnetic building block. Alternatively, one can construct skyrmionic textures whose bases have antiparallel coupling resulting in ferrimagnetic or antiferromagnetic skyrmions. The latter exhibit fundamentally different properties than their ferromagnetic counterpart. One origin of these differences are the doubly degenerate bands of antiferromagnetic systems in case of highly symmetric crystals, or time-reversal symmetry in general, causing entirely different electron dynamics (Sec. 3.2). This thesis considers the symmetric case so that notion of antiferromagnetic skyrmions is restricted in the following to skyrmion textures in such systems only.

Disappointingly, no natural antiferromagnetic skyrmion system has been discovered experimentally until now so that all antiferromagnetic skyrmion calculations performed in this thesis are based on hypothetical systems. A reason for this disparity might be the enhanced difficulty to observe textures in antiferromagnetic systems, also the groundbreaking discovery of skyrmions in ferromagnetic materials has attracted more attention to that variant. Still, antiferromagnetic systems with large DMI, an important ingredient for skyrmions formation, have been theoretically predicted [68], but the difficulty to stabilize skyrmions via external magnetic fields may further inhibit their discovery. However, ferromagnetic skyrmion were measured without external field [69] so that this constraint is a minor obstacle only. The general abundance of antiferromagnetic materials far exceeding the number of ferromagnetic systems makes the existence of antiferromagnetic skyrmion probable. Thus, soon discovery of real systems is likely so that methods for the theoretical estimation of their properties are in demand to verify measurements as in the case of ferromagnetic skyrmions [41].

In general, one can discern two distinct kinds of antiferromagnetic skyrmions depending on the kind of antiferromagnetic coupling, the synthetic and the intrinsic one (Fig. 2.3). The synthetic case can by understood as skyrmions in two ferromagnetic layers whose coupling is antiferromagnetic. Alternatively, the intra-layer coupling can be antiferromagnetic so that

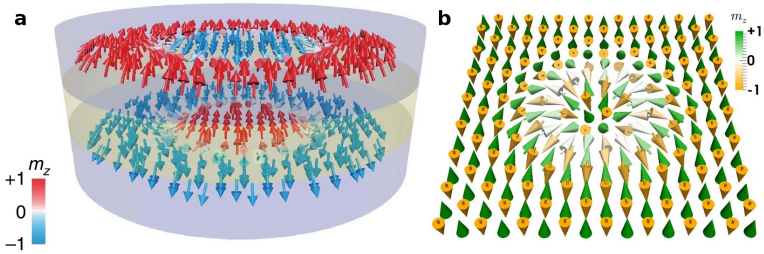

Figure 2.3: Schematic visualizations of synthetic (a) and intrinsic (b) antiferromagnetic skyrmions. The figures are takes from Ref. [19] and Ref. [18], respectively.

each layer's skyrmions contain both sublattices defining the case of intrinsic antiferromagnetic skyrmions. Both cases can be initially understood as a superpositions of 2 antiparallel ferromagnetic skyrmions, however new properties emerge due to coupling.

Considering skyrmion dynamics, the most significant difference is the absence of the skyrmionic Hall effect. Intuitively, this property is directly understandable within the picture of 2 coupled, time-reversed sublattices. As the skyrmionic Hall effect is proportional to the time-reversal odd skyrmion number (Eq. 2.1), the skyrmions of both sublattices have opposing transversal accelerations which cancel each other given sufficient magnetic coupling and equivalent magnetic parameters. This cancellation has been verified by several theoretical studies for synthetic and intrinsic skyrmions utilizing the Landau-Lifshitz-Gilbert formalism to describe the dynamics of matching micromagnetic models [17–20, 70, 71]. There, straight movement has been observed which is evoked by either directly applied fields or spin currents utilizing the spin Hall effect, i.e. by devices with currents in and perpendicular to the plane. Skyrmion velocities exceeding the terminal velocity of ferromagnetic skyrmions by orders of magnitude are observed, an advantage originating not only in the skyrmion Hall effect absence preventing annihilation at the boundary, but furthermore due to the generally faster antiferromagnetic dynamics owing to the absence of the Walker breakdown also present in domain wall motion [14]. Hence, antiferromagnetic skyrmions have several advantages over their ferromagnetic relatives especially with respect to racetrack applications which far exceed the general advantage of antiferromagnet materials such as their indifference to alien magnetic fields.

One problem when considering antiferromagnetic skyrmions for racetrack applications is that the topological Hall effect, usually proposed as read-mechanism, is also proportional to the skyrmion number and vanishes accordingly. Fortunately, another Hall effect emerges in antiferromagnetic skyrmions, the topological spin Hall effect (TSHE). In the simplistic picture of decoupled skyrmions the transversal spin currents are not canceled as the spin part causes another flip under time-reversal resulting in constructive addition. Interestingly, the TSHE has an intricate relation with the texture resulting in an enhancement of the longitudinal skyrmion acceleration [72].

The detailed investigation of the TSHE is the main topic of this thesis. Its origin and properties are described in further detail in Sec. 4.2.1, calculation methods and material

estimations are given in the ensuing chapters.

2.4 Skyrmion interpolations

This thesis investigates the influence of an imprinted skyrmion texture on traversing electron wave-packets numerically, hence an accurate and efficient approximation of skyrmion structures is necessary. This section describes the two models providing such textures which are used in this thesis. For simplicity, the antiferromagnetic texture is expressed through ferromagnetic interpolations treating the magnetization direction as staggered order parameter.

Several different skyrmion-texture parameterizations have been proposed in recent times. A popular approximation for the radial component of single skyrmions is a 360° domain-wall profile including arcsin- and tanh-functions. Model parameters have been extracted from spin polarized scanning tunneling microscopy measurements of single skyrmions in PdFe/Ir(111) for which the model shape agrees very well with the measured skyrmion shape [48]. Different possibilities exist to smoothly combine such single skyrmions to a skyrmion-lattice parameterization as required for the following transport calculations.

Instead, two alternative possibilities are used to obtain skyrmion textures in this thesis. The first is the analytic 3$\boldsymbol{q}$-texture (Sec. 2.4.1), the second is the more general approach of numerically solving atomistic spin models with simple interactions that yield skyrmion lattices (Sec. 2.4.2). Implementation details further enhancing the efficiently of texture evaluations are described in Sec. 5.2.3.

2.4.1 3q-texture

The first and more simple utilized parametrization of a skyrmion lattice is the so-called 3$\boldsymbol{q}$-texture. Initially motivated by the small angle neutron scattering results showing 6-fold scattering intensities [26], a skyrmion lattice can be approximated as the Fourier transform of 3 reciprocal-space vectors of equal magnitude and relative 120°-angles. The simple construction from sines and cosines allows easy evaluation and ensures smoothness of the texture. This parameterization has been successfully used to investigate the DMI by means of semiclassical methods [73] so that this parameterization is a good initial choice for describing the skyrmionic texture.

The order parameter is the normalized expression of:

$$N(\boldsymbol{r}) = B_0\hat{\boldsymbol{e}}_z + B_1 \sum_{n=0}^{2} \left[(\hat{\boldsymbol{e}}_z \times \boldsymbol{\xi}_n) \sin\left(q_0 \boldsymbol{\xi}_n \cdot \boldsymbol{R}\right) + \hat{\boldsymbol{e}}_z \cos\left(q_0 \boldsymbol{\xi}_n \cdot \boldsymbol{R}\right)\right], \tag{2.2}$$

with $\boldsymbol{\xi}_n = \cos(2\pi n/3)\hat{\boldsymbol{e}}_x + \sin(2\pi n/3)\hat{\boldsymbol{e}}_y$, $B_0 = 1$, $B_1 = -1.5$, and $q_0 = 2\pi/(190\,\text{Å})$ as taken from Ref. [73]. The $\boldsymbol{\xi}_n$ define the skyrmion lattice orientation and the 190 Å give the lattice periodicity as measured for MnSi. The corresponding magnetic unit cell contains one skyrmion, as can be verified through calculation of the skyrmion number. The texture direction is visualized in Fig. 2.4 showing well localized skyrmions with clearly defined clockwise Bloch-type rotational sense. The background magnetization is pointing in $\hat{\boldsymbol{e}}_z$ direction, but

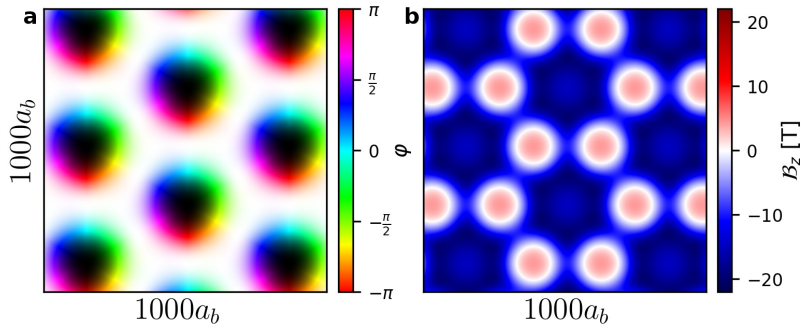

Figure 2.4: 3$\boldsymbol{q}$-state skyrmion texture: a) shows the magnetization direction $\hat{\boldsymbol{N}}$ using the hsv colormap. The hue visualizes the polar angle of the in-plane magnetization while the brightness encodes the $\hat{N}_z$ component. The saturation is linear between 0 and 1 for $\hat{N}_z \geq 0$ and 1 otherwise, the value is linear between 0 and 1 for $\hat{N}_z \leq 0$ and 1 otherwise (e.g. white corresponds to $+\hat{e}_z$ and black to $-\hat{e}_z$). b) Corresponding emergent magnetic field (Eq. 3.16). Each magnetic unit cell contributes one magnetic flux quantum. a_B denotes the Bohr radius.

the skyrmions are so large that the average $\hat{N}_z$ component $\langle \hat{N}_z \rangle \approx 0.38$. The averaged emergent magnetic field is $\langle \mathcal{B}_z \rangle \approx -9.92\,\mathrm{T}$ as can be calculated from the magnetic unit cell size and the skyrmion number $Q = -1$. This is verified by numerical calculations of the emergent magnetic field shown in Fig. 2.4. Furthermore, the figure glaringly visualizes the inhomogeneity of $\mathcal{B}_z$ with extrema of approximately $-19.7\,\mathrm{T}$ and $4.3\,\mathrm{T}$.

The easy implementation and evaluation makes this parameterization a perfect initial approximation which is used throughout the results parts of this thesis (Secs. 6, 8, 9). It is possible to modify the magnetic texture by changing q_0 which results in variations of the $\mathcal{B}_z$-magnitude, alternatively increase and decrease of the $|B_1|/|B_0|$-ratio can be used to grow and shrink the skyrmion, respectively. Nevertheless, more tuning potential with enhanced control over the texture is highly desirable, properties found in the more general following model.

2.4.2 Atomistic model

The atomistic framework (Sec. 2.2.1) allows a more realistic description of magnetic systems whose parameters can be extracted from experiments or theoretical descriptions such as density functional theory (Sec. 7.1.1). So far, it is not sensible to extract real parameters from realistic material descriptions as no antiferromagnetic system exhibiting a skyrmion texture has been found yet. Hence, simulations are unlikely to result in skyrmion lattices. While such a search for antiferromagnetic skyrmions is definitively possible, it is out of the scope of this thesis. Instead, simple, conveniently chosen magnetic-interaction model parameters are used to describe a more realistic texture with more tuning potential than in case of the 3$\boldsymbol{q}$-state.

The model employed here is an atomistic spin lattice Heisenberg model (Sec. 2.2.1)

including nearest neighbor exchange J, anisotropy $\boldsymbol{K}$, external magnetic field $\boldsymbol{B}$, and DMI $\boldsymbol{D}_{ij}$. Consequently, the Hamiltonian can be expressed as:

$$H = -\sum_{<ij>} J\hat{\boldsymbol{S}}_i \cdot \hat{\boldsymbol{S}}_j - \sum_{<ij>} \boldsymbol{D}_{ij} \cdot (\hat{\boldsymbol{S}}_i \times \hat{\boldsymbol{S}}_j) - \sum_{i\alpha} K_\alpha (\hat{\boldsymbol{K}}_\alpha \cdot \hat{\boldsymbol{S}}_i)^2 - \sum_i \mu_i \boldsymbol{B} \cdot \hat{\boldsymbol{S}}_i, \tag{2.3}$$

where $\hat{\boldsymbol{S}}_i$ is the normalized spin at lattice site i. For simplicity, the model is restricted to isotropic nearest-neighbor exchange J and the magnetic moments are always assumed as $\mu = 2\mu_B$. Since the DMI is only considered for neighboring spins on a rectangular grid, $\boldsymbol{D}_{ij}$ is expressed as $D_{\alpha\beta}$ in the following where β labels the real-space direction from lattice site i to j and α denotes the vector component of $\boldsymbol{D}_{ij}$. Exemplary values are supplied in Tab. 2.1.

A subset of the functionality of the SPIRIT code [74] is used to find the magnetic ground state properties through iteration of the Landau-Lifshitz-Gilbert equation. Starting from a random distribution, the magnetization dynamics are followed until a ground state is found. Alternatively, an approximate skyrmion lattice distribution is chosen as initial state either by inverting the spin of spherical sections at suspected skyrmion positions in a ferromagnetic background or by reusing the final state of a previous calculation with the wanted skyrmion number. Both possibilities results in faster, more reliable convergence than starting from a random configuration. The removal and addition of skyrmions is occasionally necessary to achieve the most favorable skyrmion density in the computations cell and to allow the formation of a well-fitting skyrmion lattice. Stability can be checked by energetic comparison with different textures such as the ferromagnetic state and simulation cells including more or less skyrmions. Any existing skyrmion would effectively describe a skyrmionic lattice due to periodic boundary conditions, however in most considered systems several skyrmions are contained in the computational cell. As long as an adequate number of skyrmions is in the simulation cell, the skyrmions arrange themselves in a triangular lattice after long enough convergence so that the final structure is comparable to the $3\boldsymbol{q}$-texture and experimentally measured skyrmion lattices. Small changes of the magnetic texture are easily accessible by slight modifications of the magnetic parameters and subsequent energy minimization of the previous ground-state which allows systematic studies of the shape variation impact on transport properties (Sec. 9.4.3).

As transport properties are investigated in the limit of smooth textures, the lattice spacings are scaled to unphysical large values in order to effectively describe a skyrmion lattice of the wanted size without excessive computational demand. This is reasonable as the SPIRIT textures do not describe the actual systems parameters but are only used as realistic example shape. Yet, it is probable that magnetic parameters exist exhibiting a similar texture to the rescale lattice.

An example texture utilizing the atomistic model is shown in Fig. 2.5. The lattice constant is chosen to match the averaged emergent magnetic field of the previously plotted $3\boldsymbol{q}$-state skyrmion lattice ($\langle \mathcal{B}_z \rangle \approx -9.92\mathrm{T}$) and the external magnetic field is chosen so that $\langle \hat{N}_z \rangle \approx 0.38$ in agreement to the texture of Fig. 2.4. The signs and directions of the DMI are selected to yield a Bloch-skyrmion with the same rotational sense as in case of the $3\mathbf{q}$-texture. Hence, this example is constructed to have close resemblance to the previous texture to allow direct comparison. Still, the chosen parameters do not reproduce the $3\boldsymbol{q}$-texture ideally as for example the radial change is more abrupt here. Furthermore, the lattice is rotated

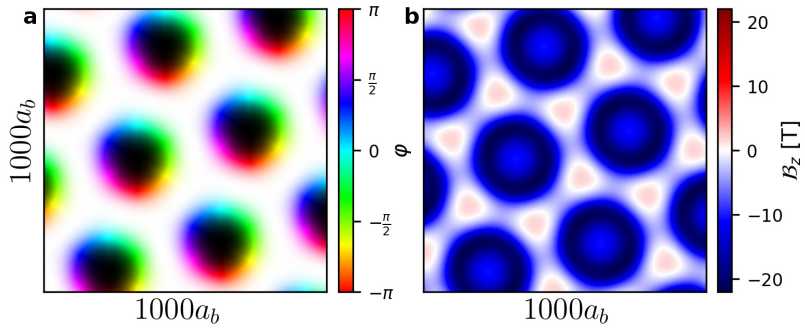

Figure 2.5: Example SPIRIT texture with 14 skyrmions forming a lattice in a 200×200 square lattice using the parameters of Tab. 2.1. The lattice-spacing was scaled to $\sim 7.47\, a_B$ in order to have the same average emergent magnetic field as the 3$\boldsymbol{q}$-state in Fig. 2.4. a) shows the magnetic texture with the same colormap as in Fig. 2.4 and b) is the corresponding emergent magnetic field.

as determined by the number of skyrmions and the computational unit's shape and size. While the magnetization-distributions seem very similar, significant differences appear in the emergent magnetic field. The extrema are quite different with $-21.64\,\mathrm{T} < \mathcal{B}_z < 1.9\,\mathrm{T}$ (SPIRIT) and $-19.69\,\mathrm{T} < \mathcal{B}_z < 4.32\,\mathrm{T}$ (3$\boldsymbol{q}$-texture) where especially the significantly larger latter $\mathcal{B}_z$ are noticeable. The maxima arise from the distinct positive, spherical contributions between 3 neighboring skyrmions. The circular property is not recovered in the atomistic texture and might be an artifact of the 3$\boldsymbol{q}$-texture, however with increasing skyrmion size $\mathcal{B}_z$ reaches increasingly large positive contributions at those positions so that the previous texture is still a reasonable approximation. Comparison of the evoked transport between both textures is given in Sec. 9.4.

J[meV]	D_{xx}[meV]	D_{yy}[meV]	K_z[meV]	B_z[T]
15	−2	−2	0.05	0.7

Table 2.1: SPIRIT-parameters corresponding to the texture displayed in Fig. 2.5.

Tuning of the parameters drastically alters the textures which includes diverse skyrmion-setups but also entirely different phases such as spin spirals. The huge variability is utilized in Sec. 9.4 where the transport effects caused by different skyrmion-types and shape variations are investigated.

In conclusion, the atomistic model is a suitable method to efficiently describe periodic magnetic structures with great tunability so that its inclusion into the computational procedure of this thesis allows the study of arbitrary but smooth periodic textures.

3

Wave-packet dynamics

This chapter covers a very intuitive method of describing electron dynamics under applied fields and in magnetic textures—the semiclassical wave-packet dynamics. Its main feature are the "equations of motion" which describe the evolution of a wave-packet's center through phase space. One of its salient properties is the possibility to include various general perturbations such as lattice distortions or magnetic textures. The principles of the electron motion in degenerate and non-degenerate systems is described in this chapter, the ensuing procedure to calculate transport properties within the Boltzmann formalism follows in Sec. 4.3.

This chapter primarily compiles established results from multiple sources (Refs. [75–77]) focused on the subject of this thesis and rephrases them in an uniform notation. A more general review of wave-packet dynamics and associated Berry phase effect with intuitive explanations of basic physical phenomena is given in Ref. [78].

First, the well-established equations of motion of non-degenerate systems are derived considering applied fields and magnetic textures. They were already employed to calculate the transport responses in ferromagnetic skyrmions analogous to this thesis's investigation of antiferromagnetic skyrmions and thus serve as comparison to the ensuing derivation in degenerate systems. The second part of this chapter starts with an overview of the differences that emerge when considering twofold-degenerate states. Most importantly, the isospin enters as a dynamical quantity which describes the sublattice localization. Afterwards, possibilities to simplify the equation of motions are discussed uncovering the relation between spin and isospin for collinear and non-collinear degenerate antiferromagnets.

3.1 Non-degenerate systems

In this section the dynamics of non-degenerate electrons are investigated considering magnetic textures and applied electric fields. While the electric field is understood as an external perturbation to the Hamiltonian, the magnetic texture is incorporated through system rotations keeping the spin quantization axis aligned with the texture. The later concept was successfully employed to describe the influence of textures as mediated by real-space dependent *sd*-exchange [8]. The goal of this section is to attain a framework which describes electron motion through phase-space in such environments.

A basic obstacle for such a description is the basic quantum mechanical principle which forbids simultaneous knowledge of the electron's precise position and velocity. Fortunately, the wave-packet formalism has been developed which allows to circumvent this problem by consideration of wave-packets with small but finite extend in real- and reciprocal-space [79]. In this section, the derivation of the wave-packet's equations of motion is demonstrated for the non-degenerate case loosely following the general Ref. [75].

3.1.1 General formalism

The theory as laid out in Ref. [75] starts from a general Hamiltonian $\hat{H}$ dependent on $\hat{\boldsymbol{r}}$, $\hat{\boldsymbol{p}}$, and small modulation functions $\beta_i(\hat{\vec{r}}, t)$. The local Hamiltonian of a wave-packet localized at $\boldsymbol{r}_c$ in real-space is approximated as

$$\hat{H} = \hat{H}_c + \sum_i (\hat{\boldsymbol{r}} - \boldsymbol{r}_c) \nabla_{\boldsymbol{r}_c} \beta_i(\boldsymbol{r}_c, t), \tag{3.1}$$

where $\hat{H}_c = H(\hat{\boldsymbol{r}}, \hat{\boldsymbol{p}}; \beta_i(\boldsymbol{r}_c, t))$ is the Hamiltonian with its linearized perturbations evaluated at $\boldsymbol{r}_c$. Since H_c is lattice periodic, the crystal momenta $\boldsymbol{q}$ can be used to define the Bloch-wave eigenstates $|\psi_{\boldsymbol{q}}(\boldsymbol{r}_c, t)\rangle$ valid around $\boldsymbol{r}_c$. Thus, the local Hamiltonian is a good choice describing the immediate vicinity of $\boldsymbol{r}_c$. The conceptional trick of this formalism is the construction of a wave-packet with small spread in both real and reciprocal space. Hence, only the local texture and environment matter when a bunch of electrons with slightly smeared real- and reciprocal-space localization is conflated to a wave-packet. As long as the smearing is small enough on the scale of the real-space texture, all constituting electrons are well described using H_c's Bloch vectors $|\psi_{\boldsymbol{q}}(\boldsymbol{r}_c, t)\rangle$. The second necessity of sufficient localization in reciprocal space becomes important when following the electron trajectories. If the wave-packet's spread is too large, the constituent electrons will soon move into different directions as their group velocities differ. Accordingly, the wave-packet would quickly loose its coherence so the H_c is not longer applicable for all constituent states. However, if the wave-packet diffusion is prevented by sufficient localization in both real and reciprocal space, the wave-packet center-of-motion effectively describes the dynamics of the entire wave-packet. Accordingly, the wave-packet is defined as:

$$|W\rangle = \int d\boldsymbol{q}\ w(\boldsymbol{q}, t)\, |\psi_{\boldsymbol{q}}(\boldsymbol{r}_c, t)\rangle\,, \tag{3.2}$$

where $w(\boldsymbol{q}, t)$ is a normalized enveloping function enforcing reciprocal-space localization. This distribution determines the crystal momentum average of the wave-packet $\boldsymbol{q}_c$ which specifies the wave-packet position in phase space together with $\boldsymbol{r}_c$. The localization in real and reciprocal space are connected by the Heisenberg principle. As $w(\boldsymbol{q}, t)$ has to be very localized on the scale of the reciprocal-space lattice vectors in order to ensure similar reciprocal-space properties, the minimal real-space localization has to include several unit cells. Hence the scale of the magnetic textures has to be much larger than the unit cell so that it is reasonable to describe the wave-packet by its center's properties.

In the following all effects caused by the "non-center" properties and the wave-packet shape are neglected so that the wave-packet's dynamics are governed entirely by the dynamics of

the wave-packet averages $\boldsymbol{r}_c$ and $\boldsymbol{q}_c$. In general, other wave-packet properties apart from the center have been shown to contribute to important phenomena and provide further corrections [80, 81].

The wave-packet dynamics are derived using the variational principle formulated in terms of the Lagrangian $\mathcal{L} = \langle W | \mathrm{i}\frac{d}{dt} - \hat{H} | W \rangle$. The relevant parts of the Lagrangian are:

$$\mathcal{L} = -\mathcal{E}_{\mathcal{W}} + \boldsymbol{q}_c \cdot \dot{\boldsymbol{r}}_c + \dot{\boldsymbol{q}}_c \cdot \left\langle u \middle| \mathrm{i}\frac{\partial u}{\partial \boldsymbol{q}_c} \right\rangle + \dot{\boldsymbol{r}}_c \cdot \left\langle u \middle| \mathrm{i}\frac{\partial u}{\partial \boldsymbol{r}_c} \right\rangle + \left\langle u \middle| \mathrm{i}\frac{\partial u}{\partial t} \right\rangle . \tag{3.3}$$

In this equation $|u\rangle$ denotes the periodic part of the Bloch-wave

$$|u(\boldsymbol{r}_c, \boldsymbol{q}_c, t)\rangle = \mathrm{e}^{-\mathrm{i}\boldsymbol{q}_c \cdot \boldsymbol{r}_c} |\psi_{\boldsymbol{q}_c}(\boldsymbol{r}_c, t)\rangle . \tag{3.4}$$

The wave-packet energy $\mathcal{E}_{\mathcal{W}}$ includes terms of the additional gradient function

$$\mathcal{E}_{\mathcal{W}} \approx \langle \Psi | \hat{H}_c | \Psi \rangle + \langle \Psi | \Delta\hat{H} | \Psi \rangle . \tag{3.5}$$

The $\langle \Psi | \Delta\hat{H} | \Psi \rangle$-term describes further corrections such as the effect of orbital magnetization, but $\Delta\hat{H}$ is neglected for simplicity in the following so that $\mathcal{E}_{\mathcal{W}}$ is the band energy only. The other parts originate in the total time derivative. The latter 3 terms include the different Berry connections

$$A_{\boldsymbol{r}} = \mathrm{i}\left\langle u \middle| \frac{\partial u}{\partial \boldsymbol{r}_c} \right\rangle , A_{\boldsymbol{q}} = \mathrm{i}\left\langle u \middle| \frac{\partial u}{\partial \boldsymbol{q}_c} \right\rangle , A_t = \mathrm{i}\left\langle u \middle| \frac{\partial u}{\partial t} \right\rangle , \tag{3.6}$$

which are constructed from the periodic part of the Bloch-waves. Alternatively, they can be cast into the single term $\langle u | \mathrm{i} du/dt \rangle$ which is the "net rate of change of Berry phase" [75]. Notice that the real- and reciprocal-space Berry connections are vectors in the respective space as indicated by the boldface indices. The "A" is not bold to keep consistency with the degenerate case (Sec. 3.2).

Henceforth, the index c, denoting the wave-packet center, is omitted as the following derivations consider the center-of-motion real- and reciprocal-space dynamics only. The Euler-Lagrange equations,

$$\begin{aligned} \frac{\partial \mathcal{L}}{\partial r_i} - \frac{d}{dt}\frac{\partial \mathcal{L}}{\partial \dot{r}_i} &= 0, \\ \frac{\partial \mathcal{L}}{\partial q_i} - \frac{d}{dt}\frac{\partial \mathcal{L}}{\partial \dot{q}_i} &= 0, \end{aligned} \tag{3.7}$$

are used to obtain the wave-packet's general equations of motion [75, 78]:

$$\dot{r}_\mu = \quad \frac{\partial \mathcal{E}_{\mathcal{W}}}{\partial q_\mu} - \Omega_{q_\mu r_\nu}\dot{r}_\nu - \Omega_{q_\mu q_\nu}\dot{q}_\nu - \Omega_{q_\mu t}, \tag{3.8a}$$

$$\dot{q}_\mu = -\frac{\partial \mathcal{E}_{\mathcal{W}}}{\partial r_\mu} + \Omega_{r_\mu r_\nu}\dot{r}_\nu + \Omega_{r_\mu q_\nu}\dot{q}_\nu + \Omega_{r_\mu t}. \tag{3.8b}$$

$\Omega_{\boldsymbol{xy}}$ denotes the different Berry curvatures:

$$\Omega_{\boldsymbol{xy}} = \frac{\partial}{\partial \boldsymbol{x}} A_{\boldsymbol{y}} - \frac{\partial}{\partial \boldsymbol{y}} A_{\boldsymbol{x}}, \tag{3.9}$$

with $\{\boldsymbol{x}, \boldsymbol{y}\} \in \{\boldsymbol{r}, \boldsymbol{q}, t\}$. $\Omega_{\boldsymbol{rr}}$, $\Omega_{\boldsymbol{rk}}$, and $\Omega_{\boldsymbol{kk}}$ are matrices in their respective space and are called real-space, mixed, and reciprocal-space Berry curvature, respectively. For convenience and due to their antisymmetry, the pure Berry curvatures, i.e. $\Omega_{\boldsymbol{rr}}$ and $\Omega_{\boldsymbol{kk}}$, can be expressed through a vector form: $\Omega_{\boldsymbol{xx}} \cdot \dot{\boldsymbol{y}} = \dot{\boldsymbol{y}} \times \Omega_{\boldsymbol{x}}$ with $\Omega_{x_i} = 1/2 \varepsilon_{ijl} \Omega_{x_j x_l}$. The dot product denotes multiplication with the latter index of $\Omega_{\boldsymbol{xx}}$ as commonly encountered in the equations of motion. The latter quantities of Eq. 3.8, $\Omega_{t\boldsymbol{x}}$, are different from the other curvatures since t in not a vector and their presence requires time dependent perturbations. The merit of Eq. 3.8 is that it supplies a general scheme of wave-packet dynamics where all system-dependent properties are encoded in the different Berry curvatures. Various physical effects can be recovered from these equations providing an intuitive picture with iteratively solvable equations[75, 78].

3.1.2 Electromagnetic fields

Having established the general formalism, it is necessary to treat the influence of an external electromagnetic field [82]. It may be understood as general perturbations of the form $\hat{H} = \hat{H}_0[\boldsymbol{q} + \mathrm{e}\boldsymbol{A}(\boldsymbol{x}_c, t)] - e\phi(\hat{\boldsymbol{x}}, t)$ expressed by its gauge potential. Such perturbations are perfectly suited for this formalism, hence equations of motion can be derived either directly from the equations of motion (Eq. 3.8) or via re-evaluating the Lagrangian (Eq. 3.3) [75]. It is instructive to look at the electromagnetic field's influence without texture, i.e. when only $\boldsymbol{x}_c$-dependence arises from the applied fields. In that case the equations of motion simplify to

$$\dot{\boldsymbol{r}} = \frac{\partial \mathcal{E}_M}{\partial \boldsymbol{k}} - \dot{\boldsymbol{k}} \times \boldsymbol{\Omega}_{\boldsymbol{k}}, \tag{3.10a}$$

$$\dot{\boldsymbol{k}} = -\boldsymbol{E} - \dot{\boldsymbol{r}} \times \boldsymbol{B}. \tag{3.10b}$$

The crystal momentum is now expressed as $\boldsymbol{k} = \boldsymbol{q} + e\boldsymbol{A}$ and the wave-packet energy includes the orbital magnetization $\mathcal{E}_M = \mathcal{E}_{\mathcal{W}} - \boldsymbol{M} \cdot \boldsymbol{B}$. The reciprocal-space Berry curvature $\Omega_{\boldsymbol{kk}}$ depends on the initial Hamiltonian $\hat{H}_0$ only and is thus unaffected by the applied fields. Originating in the real-space and time-dependent gauge field, the electromagnetic fields $\boldsymbol{E} = -\nabla_{\boldsymbol{r}}\phi - \partial \boldsymbol{A}/\partial t$ and $\boldsymbol{B} = \nabla_{\boldsymbol{r}} \times \boldsymbol{A}$ enter the equations via the $\frac{\partial \mathcal{E}}{\partial \boldsymbol{r}} + \Omega_{\boldsymbol{rr}} \cdot \dot{\boldsymbol{r}} + \Omega_{\boldsymbol{r}t}$ parts of Eq. 3.8 [75, 78]. The negative sign arises from the electron charge which is -1 in chosen unit system.

3.1.3 Magnetic texture

The remaining necessary ingredient is the influence of a magnetic texture whose spins are assumed to be of constant magnitude. When excluding spin-orbit coupling, all Berry curvatures containing $\boldsymbol{k}$ vanish despite the introduction of the texture. Hence, the texture's impact on the wave-packet dynamics is described by $\Omega_{\boldsymbol{rr}}$ and $\Omega_{\boldsymbol{r}t}$ only. Those quantities acquire intuitive

analytic expressions derived in the following. Initial descriptions of this effect were given in Refs. [8, 83], this section's derivations loosely follow Ref. [76].

Rotating the Bloch basis state in real space to have its spin axis aligned with the texture, the Bloch-wave can separated in an orbital and a spin-dependent part: $|u(\boldsymbol{r},\boldsymbol{k},t)\rangle = |\eta(\boldsymbol{k})\rangle\,|\uparrow(\boldsymbol{r},t)\rangle$. The $\boldsymbol{k}$-dependent orbital part $|\eta(\boldsymbol{k})\rangle$ describes the solutions of the original Hamiltonian while $|\uparrow(\boldsymbol{r},t)\rangle$ encodes the direction of the texture accounting for the entire $\boldsymbol{r}$-dependence under the given assumptions (especially neglecting spin-orbit coupling). As the local spin direction describing the texture is of constant magnitude, it can be conveniently described by its azimuthal θ and polar ϕ angles. Accordingly, its direction is given by

$$\boldsymbol{n} = \begin{bmatrix} \sin(\theta)\cos(\phi) \\ \sin(\theta)\sin(\phi) \\ \cos(\theta) \end{bmatrix}. \tag{3.11}$$

The Bloch-wave's real-space part thus takes the form:

$$|\uparrow\rangle = \begin{bmatrix} \mathrm{e}^{-\mathrm{i}\frac{\phi}{2}}\cos(\frac{\theta}{2}) \\ \mathrm{e}^{\mathrm{i}\frac{\phi}{2}}\sin(\frac{\theta}{2}) \end{bmatrix}. \tag{3.12}$$

Explicit calculations for that state show that the real-space Berry connection becomes

$$A_{\boldsymbol{r}} = \frac{\cos\theta}{2}\frac{\partial\phi}{\partial\boldsymbol{r}}. \tag{3.13}$$

Utilizing Eq. 3.9, the real-space Berry curvature can be expressed as

$$\Omega_{r_\mu r_\nu} = -\frac{\sin(\theta)}{2}\left(\frac{\partial\theta}{\partial r_\mu}\frac{\partial\phi}{\partial r_\nu} - \frac{\partial\theta}{\partial r_\nu}\frac{\partial\phi}{\partial r_\mu}\right) \tag{3.14}$$

for the spin-up state of Eq. 3.12. Reformulating $\Omega_{r_\mu r_\nu}$ in terms of $\boldsymbol{n}$ yields the convenient form:

$$\Omega_{r_\mu r_\nu} = -\frac{1}{2}\boldsymbol{n}\cdot\left(\frac{\partial\boldsymbol{n}}{\partial r_\mu}\times\frac{\partial\boldsymbol{n}}{\partial r_\nu}\right). \tag{3.15}$$

This equations demonstrates the distinct relationship between this wave-packet dynamics effect and skyrmion textures as $-\Omega_{r_\mu r_\nu}/\pi$ corresponds to the skyrmion number density (Eq. 2.1).

Similar to its electromagnetic relative—the magnetic field—the impact of the real-space Berry curvature originating in the magnetic texture can be interpreted as consequence of a field owing to the cross-product with $\dot{\boldsymbol{r}}$. This field is commonly called the *emergent magnetic field* and is defined in this thesis as:

$$\mathcal{B}_i = -\frac{1}{2}\varepsilon_{ijl}\Omega_{r_j r_l} = \frac{1}{4}\epsilon_{ijl}\boldsymbol{n}\cdot\left(\frac{\partial\boldsymbol{n}}{\partial r_j}\times\frac{\partial\boldsymbol{n}}{\partial r_l}\right). \tag{3.16}$$

ϵ_{ijl} is the Levi-Civita symbol whose antisymmetry causes the additional $1/2$-factor relative to Eq. 3.15. The impact of $\boldsymbol{\mathcal{B}}$ is illustrated in Fig. 3.1. The -1 is introduced so that the emergent field enters the equations of motion with the same sign as the external fields.

Analogous to external magnetic fields, the emergent magnetic field causes a transversal transport effect—the *topological Hall effect*. It is described in further detail in Secs. 4.1.1, 4.4.1. A distinct difference with respect to the electromagnetic fields exists. As Eqs. 3.13-3.15 have been derived from the spin-up state (Eq. 3.12), slight modifications are necessary for the spin down state. When replacing $\boldsymbol{n} \to -\boldsymbol{n}$ in order to effectively describe the down state, $\Omega_{\boldsymbol{rr}}$ (Eq. 3.15) reverses sign. Thus, the impact of the emergent magnetic field is spin-dependent. As $\mathcal{B}$ is constructed to be spin-independent, the spin-dependence has to be included in the equations of motion (Eq. 3.18) through the $(\boldsymbol{s} \cdot \boldsymbol{n})$-term. This artificial spin-dependence transfer from $\boldsymbol{\mathcal{B}}$ into the equation of motion enables better analogies with the later treatment of antiferromagnetic textures (Sec. 3.2).

In addition to the emergent magnetic field, the emergent electric field $\boldsymbol{\mathcal{E}}$ describes the effect of time-dependent variations of the texture. It originates in the general equation's Ω_{rt}-term (Eq. 3.8) which is exactly like Eq. 3.14 with the replacement $\boldsymbol{r}_\nu \to t$:

$$\mathcal{E}_i = \frac{1}{2}\boldsymbol{n} \cdot \left(\frac{\partial \boldsymbol{n}}{\partial r_i} \times \frac{\partial \boldsymbol{n}}{\partial t} \right). \tag{3.17}$$

Naturally, it is also spin-dependent and has a potential to invoke interesting transport effects in time-dependent systems. However, this thesis is constricted to the effect of static textures so that $\boldsymbol{\mathcal{E}}$ is neglected in the following sections.

The mixed Berry curvatures vanish when assuming that the previously used decomposition $|u\rangle = |\eta(\boldsymbol{k})\rangle\,|\uparrow(\boldsymbol{r}, t)\rangle$ into orbital- and spin-parts is possible since that implies that $A_{\boldsymbol{r}}$ and $A_{\boldsymbol{k}}$ are $\boldsymbol{k}$- and $\boldsymbol{r}$-independent, respectively. Hence, features of a texture-independent Hamiltonian not breaking the above requirement may enter the equations of motion through $\Omega_{\boldsymbol{kk}}$ only. For systems without even such reciprocal-space features, which are commonly caused by

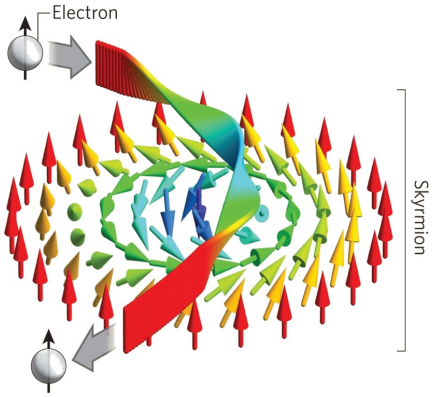

Figure 3.1: Schematic picture of spin alignment and influence of the emergent magnetic field on electrons caused by skyrmions. The figure is taken from Ref. [84].

spin-orbit-coupling or intra-cell non-collinearity, the equations of motion are:

$$\dot{\boldsymbol{r}} = \frac{\partial \epsilon}{\partial \boldsymbol{k}}, \tag{3.18a}$$

$$\dot{\boldsymbol{k}} = -(\boldsymbol{s} \cdot \boldsymbol{n}) \left(\boldsymbol{\mathcal{E}} + \dot{\boldsymbol{r}} \times \boldsymbol{\mathcal{B}} \right). \tag{3.18b}$$

3.1.4 Combined equation of motion

Next Eqs. 3.10 and 3.18 have to be combined since the dynamics of electrons will be studied that are influenced by static magnetic skyrmion textures and applied electric fields. Further effects caused by non-trivial reciprocal-space characteristics, in general manifested through $\Omega_{\boldsymbol{kk}}$ or $\Omega_{\boldsymbol{rk}}$, are neglected here. For analogy with the degenerate case (Sec. 3.2), the wave-packet's spin in the global frame is explicitly included into the equations of motion. As non-degenerate wave-packets consist of localized states of one band only, and since the construction assumes that its spin always stays aligned with the texture (Fig. 3.1), the "spin-up" or "spin-down" wave-packet character in the local frame is respectively expressed by $\boldsymbol{n}$ and $-\boldsymbol{n}$ in the global frame [76]. Accordingly, the following equations of motion are obtained:

$$\dot{\boldsymbol{s}} = (\boldsymbol{s} \cdot \boldsymbol{n}) \dot{\boldsymbol{n}}, \tag{3.19a}$$

$$\dot{\boldsymbol{r}} = \frac{\partial \epsilon}{\partial \boldsymbol{k}}, \tag{3.19b}$$

$$\dot{\boldsymbol{k}} = -\boldsymbol{E} - (\boldsymbol{s} \cdot \boldsymbol{n}) \dot{\boldsymbol{r}} \times \boldsymbol{\mathcal{B}}. \tag{3.19c}$$

It is important to consider the bounds of their validity in the ensuing interpretations. Throughout the derivation only one band is considered while the influence of other bands may only enter through the mixed or reciprocal-space Berry curvature since explicit transitions to other bands are impossible in this formalism. This rough approximation excludes all scattering to other states. Hence, this framework breaks down when the states approach each other. These equations are especially inapplicable at points of band degeneracy owing to their $U(1)$ nature and corresponding curvatures describing single bands only. Still, general corrections including horizontal mixing are possible within the semiclassical formalism [81]. A special case including a second band is described in the following section where degenerate bands of antiferromagnetic textures are considered.

Another restriction is the imperative alignment of the spin with the texture which limits this framework's applicability especially in the presence of spin-orbit coupling and spin scattering. It impedes the consideration of spin dephasing and corresponding torques. Moreover, within this branch of the formalism back-action on the texture is not included although resulting charge and spin currents could certainly modify the magnetic texture. Another simplification is the fundamental assumption that the decomposition $|u\rangle = |\eta(\boldsymbol{k})\rangle \, |\uparrow (\boldsymbol{r}, t)\rangle$ is possible, i.e. the texture's impact on the Hamiltonian can be described by a simple coupling term like $-J\boldsymbol{n} \cdot \boldsymbol{\sigma}$ [78] which has no further influence on other Hamiltonian parts. In general, the energy levels can change significantly depending on the magnetization direction, an effect visible via the non-collinear magnetoresistance when measuring skyrmions via scanning tunneling microscopy [46]. In principle, this effect is included in the most general equations of motion

(Eq. 3.8) through the $\frac{\partial \mathcal{E}_{\mathcal{W}}}{\partial \boldsymbol{r}}$ part, but it is neglected in employed Eq. 3.19 as its treatment would be difficult especially from an *ab-initio* perspective. Furthermore, the possibility that the wave-packet smears out due to its spread in real- and reciprocal-space (Sec. 3.1.1) is a perpetual restriction to this formalism's applicability.

Despite all these inaccuracies, the wave-packet's equations of motion are an intuitive method to describe physical effects and obtain insights into their origin. Given the right circumstances, this method provides good estimates and is readily expandable to include further phenomena. Eq. 3.19 fulfills this section's aim of describing the impact of applied electric fields and magnetic textures on the motion of electrons, its application to study the topological Hall effect is continued in Sec. 4.4.1.

3.2 Twofold-degenerate systems

In contrast to the previous ferromagnetic systems, antiferromagnets most often have twofold-degenerate states due to combined time-reversal and crystal symmetries. Since the aim of this thesis is the description of antiferromagnetic skyrmion systems with degenerate bands canceling the topological Hall effect, the previously derived wave-packet dynamics have to be generalized. Several references have studied how the wave-packet formalism has to be modified for degenerate states [76, 77, 85–87]. This section describes the derivation of general twofold-degenerate wave-packets dynamics following Ref. [76].

The basic components of this derivation are Hamiltonian $\hat{H}$, its degenerate band ϵ_i, and the corresponding eigenstates $|\psi_i\rangle$. For simplicity, the derivation is restricted to a single band which allows to drop the index i. The wave functions corresponding to ϵ are denoted as $|\psi_{1,2}\rangle = \mathrm{e}^{\mathrm{i}\boldsymbol{k}\cdot\boldsymbol{r}}\,|u_{1,2}\rangle$ using the Bloch-waves $|u_{1,2}\rangle$. Since the states are degenerate, a sensible choice of eigenstates has to be made. For example, the states of collinear antiferromagnets are distinguished by their spin so that $|u_1\rangle$ and $|u_2\rangle$ correspond to spin-up and -down, respectively. Analogous to the non-degenerate case (Eq. 3.2), a wave-packet localized in real- and reciprocal-space is constructed:

$$|W\rangle = \int d\boldsymbol{k}\; w(\boldsymbol{k}, t)\,[c_1\,|\psi_1\rangle + c_2\,|\psi_2\rangle]\,. \tag{3.20}$$

Again, the enveloping function w is chosen so that $\boldsymbol{k}_c = \int d\boldsymbol{k}\;\boldsymbol{k}|w|^2$ while $\boldsymbol{r}_c$ is the real-space wave-packet center as described in Sec. 3.1.1. Consequently, $\boldsymbol{k}_c$ and $\boldsymbol{r}_c$ are the wave-packet's center-of-motion coordinates in phase space. The major difference to the ferromagnetic case is that the wave-packet is constructed as a superposition of two states. Contrary to the $\mathcal{U}(1)$ character of the ferromagnetic wave-packets, where a general phase factor to the wave-packet will not affect the equation of motion, the variables $c_{1,2}$ encode the $\mathcal{SU}(2)$ character whose evolution has to be included into the equations of motion. At this point the initial choice of the basis vectors becomes important as it can simplify further transformations. In case of collinear magnets, the basis states are ideally defined so that the $c_{1,2}$ trivially determine the wave-packet weight on the respective magnetic sublattice. Consequently, a relation exists between the expectation values of $c_{1,2}$ and the spin of the wave-packet. The complex variables $c_{1,2}$ are of $\mathcal{SU}(2)$ character due to the general phase freedom and the wave-packet

normalization, i.e. $|c_1|^2 + |c_2|^2 = 1$. Using the isomorphism between $\mathcal{SU}(2)$ and $\mathcal{O}(3)$, a convenient notation of the $c_{1,2}$ is the isospin $\boldsymbol{\mathcal{C}}$:

$$\boldsymbol{\mathcal{C}} = \begin{bmatrix} 2\Re(c_1 c_2^*) \\ -2\Im(c_1 c_2^*) \\ |c_1|^2 - |c_2|^2 \end{bmatrix}. \tag{3.21}$$

In principle, $\boldsymbol{\mathcal{C}}$ can be understood as the expectation values of the Pauli matrices in $c_{1,2}$ space which leads to a convenient notation as the Pauli matrices are generators of the $\mathcal{SU}(2)$ group. Thus, the evolution of the relative wave-packet weight on the sublattices can be conveniently included into the equation of motion through the dynamics of $\boldsymbol{\mathcal{C}}$.

The general equations of motion are again deduced from the Lagrangian [76] (compare Eq. 3.3)

$$\mathcal{L} = -\mathcal{E}_{\mathcal{W}} + \boldsymbol{k}_c \cdot \dot{\boldsymbol{r}}_c + \mathrm{i}\boldsymbol{c}^\dagger \boldsymbol{c} + \boldsymbol{c}^\dagger \left(A_{\boldsymbol{ccr}} \cdot \dot{\boldsymbol{r}} + A_{\boldsymbol{cck}} \cdot \dot{\boldsymbol{k}} \right) \boldsymbol{c}. \tag{3.22}$$

The wave-packet energy $\mathcal{E}_{\mathcal{W}}$ is approximated by the band energy ϵ and the explicitly time-dependent corrections like $\langle u | \mathrm{i} \frac{\partial u}{\partial t} \rangle$ are neglected. The major difference to the non-degenerate case is the appearance of the isospinor $\boldsymbol{c} = [c_1, c_2]^T$. The originally $\mathcal{U}(1)$ Berry connections have become 2×2 matrices in isospinor space since the derivatives of both $|u_1\rangle$ and $|u_2\rangle$ enter the equations. Hence, the Berry connections in the Lagrangian expression are:

$$A_{\boldsymbol{cc}x_\mu} = \mathrm{i} \begin{bmatrix} \langle u_1 | \partial_{x_\mu} | u_1 \rangle & \langle u_1 | \partial_{x_\mu} | u_2 \rangle \\ \langle u_2 | \partial_{x_\mu} | u_1 \rangle & \langle u_2 | \partial_{x_\mu} | u_2 \rangle \end{bmatrix}. \tag{3.23}$$

The equations of motion have been derived meticulously in appendix A of Ref. [76] using the variational principle. These general derivations finally provide the following equations of motion valid in twofold-degenerate systems:

$$\dot{\boldsymbol{\mathcal{C}}} = 2\, \boldsymbol{\mathcal{C}} \times \left[\boldsymbol{A}_{r_\mu} \dot{r}_\mu + \boldsymbol{A}_{k_\mu} \dot{k}_\mu \right], \tag{3.24a}$$

$$\dot{k}_\mu = -\frac{\partial \epsilon}{\partial r_\mu} + \boldsymbol{\mathcal{C}} \cdot \left[\boldsymbol{\Omega}_{r_\mu r_\nu} \dot{r}_\nu + \boldsymbol{\Omega}_{r_\mu k_\nu} \dot{k}_\nu \right], \tag{3.24b}$$

$$\dot{r}_\mu = \frac{\partial \epsilon}{\partial k_\mu} - \boldsymbol{\mathcal{C}} \cdot \left[\boldsymbol{\Omega}_{k_\mu r_\nu} \dot{r}_\nu + \boldsymbol{\Omega}_{k_\mu k_\nu} \dot{k}_\nu \right]. \tag{3.24c}$$

Here, the Berry connections and curvatures are vectors in isospin space so that the explicit cross and scalar product with $\boldsymbol{\mathcal{C}}$ are meant in isospin space with the respective connections and curvatures. This is possible since the isospin matrices $A_{\boldsymbol{cc}x_\mu}$, like $c_{1,2}$, can be naturally expressed as vector in the basis of the generators of $\mathcal{SU}(2)$ since both quantities exist in that space. Analogously, all $\mathcal{SU}(2)$-matrices can be handily written as $X_{\boldsymbol{ccx}} = \boldsymbol{X}_{\boldsymbol{x}} \cdot \boldsymbol{\sigma}_{\boldsymbol{cc}}$. The curvatures $\Omega_{\boldsymbol{xx'}}$ obey the same rules which demonstrates the convenience of the previous construction of $\boldsymbol{\mathcal{C}}$. Using the explicit properties of $\boldsymbol{\sigma}$, the vectorial form of an $\mathcal{SU}(2)$ matrix $X_{\boldsymbol{cc}}$ can be constructed via:

$$\boldsymbol{X}_{\boldsymbol{x}} = \begin{bmatrix} \Re(X_{c_2 c_1 \boldsymbol{x}}) \\ \Im(X_{c_2 c_1 \boldsymbol{x}}) \\ X_{c_1 c_1 \boldsymbol{x}} \end{bmatrix}. \tag{3.25}$$

Hence, $\boldsymbol{\mathcal{C}} \cdot \boldsymbol{A}_{x_\mu}$ yields the correct Berry connection experienced by a wavepacket whose sublattice localization is expressed via $\boldsymbol{\mathcal{C}}$. Therefore, the impact of the matrix connections and curvatures on the wave-packet can be conveniently expressed as the scalar product of the isospin with the corresponding vectorial form as used in Eq. 3.24.

Eq. 3.9 is no longer applicable to calculate the Berry curvatures since the Berry connections are matrices in the $\boldsymbol{c}$-space due to the degeneracy and are thus non-abelian. In general the Berry curvatures are defined as:

$$\Omega_{\boldsymbol{ccxy}} = \frac{\partial}{\partial \boldsymbol{x}} A_{\boldsymbol{ccy}} - \frac{\partial}{\partial \boldsymbol{y}} A_{\boldsymbol{ccx}} - \mathrm{i}\left[A_{\boldsymbol{ccx}}, A_{\boldsymbol{ccy}}\right], \tag{3.26}$$

which in case of connections with $\mathcal{SU}(2)$-character can be recast into the vectorial form

$$\boldsymbol{\Omega}_{\boldsymbol{xy}} = \frac{\partial}{\partial \boldsymbol{x}} \boldsymbol{A}_{\boldsymbol{y}} - \frac{\partial}{\partial \boldsymbol{y}} \boldsymbol{A}_{\boldsymbol{x}} + 2\boldsymbol{A}_{\boldsymbol{x}} \times \boldsymbol{A}_{\boldsymbol{y}}. \tag{3.27}$$

A significant difference to the $\mathcal{U}(1)$-case is that the Berry curvatures in the degenerate case are gauge dependent. Only the product $\boldsymbol{\mathcal{C}} \cdot \boldsymbol{\Omega}_{\boldsymbol{xy}}$ is gauge independent. This property arises from the general freedom of choice for the degenerate eigenstates $|\psi_{1,2}\rangle$. Changes in the basic eigenstates are compensated by the product $\boldsymbol{\mathcal{C}} \cdot \boldsymbol{\Omega}_{\boldsymbol{xy}}$ so that the general formalism is valid irrespective of $|\psi_{1,2}\rangle$-variations throughout the wave-packet evolution. For actual numerical or analytical solutions of the dynamics a smooth choice is nevertheless highly advantageous with respect to computational cost or analytic solvability.

Note that all terms containing $\boldsymbol{A}_t$ have been neglected in the "general" equation of motion (Eq. 3.24) and that the wave-packet energy might be different from ϵ. In the following $\partial_{r_\mu}\epsilon$ is omitted as well, nevertheless the general equations provide rich enough physics to describe the phenomena under investigation here.

Alternative references contain differences in the derivations. For example, in Ref. [85] the Hamiltonian is allowed to have a further non-degenerate perturbation and the evolution of the $c_{1,2}$ in presented in a slightly different form. A notation in terms of gauge covariant derivatives is given as well. In Ref. [86] a different derivation of the equations of motion for an arbitrary-fold degeneracy is described. There, the equations of motion are derived in through the Ehrenfest theorem as the derivatives of observables. Ref. [87] derives the similar dynamics from an action without explicitly referring to wave-packets, the resulting equations are presented in a very general scheme of generalized coordinates in a compact notation.

The influence of electromagnetic field can still be treated on the general level irrespective of the kind of degeneracy covered here. With the restriction to constant uniform magnetic fields, the derivation of the equations of motion has been performed [85]. There, the orbital dynamics simplify to:

$$\dot{\boldsymbol{k}} = -(\boldsymbol{E} + \dot{\boldsymbol{r}} \times \boldsymbol{B}). \tag{3.28}$$

Obviously, further Hamiltonian modifications yielding additional non-vanishing Berry curvatures have been neglected so that exactly the same equations arise as in Eq. 3.10. Their impact in degenerate and non-degenerate systems is equivalent since external fields do not distinguish between the degenerate states of different sublattices.

3.2.1 Collinear Antiferromagnets

Having established the general wave-packet dynamics of degenerate systems, practical equations of motion have to be derived for concrete systems. The major part of this thesis treats the effect of electron motion through locally collinear antiferromagnets with imprinted skyrmionic texture. In this section all antiferromagnets are locally collinear which means that the $\boldsymbol{k}$-dependent part of the Hamiltonian stems indeed from a collinear system while the texture is included via the wave-packet formalism. Hence, antiferromagnetic systems are implicitly assumed to be of collinear type in this section. This is different from later considerations (Sec. 3.2.2) where the basic constituents are already non-collinear. Hence, this section derives the equations of motion in twofold degenerate, locally collinear antiferromagnetic systems considering impact of skyrmion textures. This sections follows closely the derivations of Ref. [76].

Culcer et al. [85] stated that one cannot "assume" that the "local spin quantization axes are parallel" due to interaction with "neighboring bands", meaning that the decomposition into spin and orbital part is not applicable especially in the case of spin-orbit coupling. Later however, Cheng, Culcer, et al. [76] further investigated wave-packet dynamics including this assumption as it leads to great insight into the influence of magnetic textures while being analogous to the treatment of ferromagnetic textures. Hence, expressing the eigenstates $|\psi_{1,2}\rangle = \mathrm{e}^{\mathrm{i}\boldsymbol{k}\cdot\boldsymbol{r}}\,|u_{1,2}\rangle$ through the Bloch-waves $|u_{1,2}\rangle$ and decomposing them into orbital- and spin-part is a necessary approximation for the following derivations:

$$|u_1\rangle = |\eta_1(\boldsymbol{k})\rangle\,|\uparrow(\boldsymbol{r},t)\rangle\,, \tag{3.29a}$$
$$|u_2\rangle = |\eta_2(\boldsymbol{k})\rangle\,|\downarrow(\boldsymbol{r},t)\rangle\,. \tag{3.29b}$$

Without SOC, a clear distinction into spin-up and -down is possible. The collinearity of the states furthermore allows to construct the Bloch-wave $|u_1\rangle$ so that it contain spin-up states only. Analogously, $|u_2\rangle$ covers the spin-down states. This exhausts the ambiguity of choosing the eigenstates and supplies a practical, smooth basis which ultimately allows a simple relation between the isospin and the spin.

In order to obtain the equations, it is necessary to explicitly calculate the Berry connections and curvatures of the general case (Eq. 3.24). Assuming the absence of spin-orbit coupling, the reciprocal-space Berry connection and curvature vanish. Since only the spin parts of the Bloch-waves are spin-dependent, solely their real-space derivatives encode the texture into $\boldsymbol{A}_{\boldsymbol{r}}$. When expressing the spin part's $\boldsymbol{r}$-dependence through the spherical coordinates θ and ϕ analogous to Eq. 3.12,

$$|\uparrow\rangle = \begin{bmatrix} \mathrm{e}^{-\mathrm{i}\frac{\phi}{2}}\cos(\frac{\theta}{2}) \\ \mathrm{e}^{\mathrm{i}\frac{\phi}{2}}\sin(\frac{\theta}{2}) \end{bmatrix} \quad |\downarrow\rangle = \begin{bmatrix} -\mathrm{e}^{-\mathrm{i}\frac{\phi}{2}}\sin(\frac{\theta}{2}) \\ \mathrm{e}^{\mathrm{i}\frac{\phi}{2}}\cos(\frac{\theta}{2}) \end{bmatrix}, \tag{3.30}$$

the derivatives necessary for calculating the real-space Berry connection can be expressed as:

$$\begin{bmatrix} \langle\uparrow|\partial_{\boldsymbol{r}}|\uparrow\rangle & \langle\uparrow|\partial_{\boldsymbol{r}}|\downarrow\rangle \\ \langle\downarrow|\partial_{\boldsymbol{r}}|\uparrow\rangle & \langle\downarrow|\partial_{\boldsymbol{r}}|\downarrow\rangle \end{bmatrix} = \frac{1}{2}\begin{bmatrix} -\mathrm{i}\cos(\theta)\frac{\partial\phi}{\partial\boldsymbol{r}} & -\frac{\partial\theta}{\partial\boldsymbol{r}} + \mathrm{i}\sin(\theta)\frac{\partial\phi}{\partial\boldsymbol{r}} \\ \frac{\partial\theta}{\partial\boldsymbol{r}} + \mathrm{i}\sin(\theta)\frac{\partial\phi}{\partial\boldsymbol{r}} & \mathrm{i}\cos(\theta)\frac{\partial\phi}{\partial\boldsymbol{r}} \end{bmatrix}. \tag{3.31}$$

Since the off-diagonal parts do no vanish, the orbital overlap $\langle u_1|u_2\rangle$ enters $A_{\boldsymbol{ccr}_\mu}$. $\langle \eta_x|\eta_x\rangle = 1$ holds by construction as $|\psi_i\rangle$ and the spin parts are orthonormal. Conversely, the overlap parameter

$$\xi(\boldsymbol{k}) = \langle \eta_1|\eta_2\rangle = \langle \eta_2|\eta_1\rangle \tag{3.32}$$

is not fixed and depends on the collinear system's orbital properties. All terms in Eq. 3.31 are expressible in the basis of the Pauli matrices due to its $\mathcal{SU}(2)$ character so that the Berry connection, originally defined through Eq. 3.23, can be expressed in the isospin space as:

$$\boldsymbol{A_r} = \frac{1}{2}\begin{bmatrix} -\xi\sin(\theta)\frac{\partial\phi}{\partial \boldsymbol{r}} \\ \xi\frac{\partial\theta}{\partial \boldsymbol{r}} \\ \cos(\theta)\frac{\partial\phi}{\partial \boldsymbol{r}} \end{bmatrix}. \tag{3.33}$$

Using Eq. 3.26, the real-space Berry curvature is:

$$\boldsymbol{\Omega}_{r_\mu r_\nu} = -(1-\xi^2)\frac{\sin(\theta)}{2}\left(\frac{\partial\theta}{\partial r_\mu}\frac{\partial\phi}{\partial r_\nu} - \frac{\partial\theta}{\partial r_\nu}\frac{\partial\phi}{\partial r_\mu}\right)[\hat{\boldsymbol{\tau}}]_z. \tag{3.34}$$

Only the z-component is non-vanishing due to the convenient choice of $|u_{1,2}\rangle$ distinguishing spin-up and -down. Moreover, the z-component is very similar to the ferromagnetic $\Omega_{\boldsymbol{rr}}$ expression (Eq. 3.14). The only difference is the additional factor $(1-\xi^2)$ caused by the coupling between the states. While the description of misaligned states is impossible in the ferromagnetic case, in the antiferromagnetic case the real-space Berry curvature exerts force only on the $\mathcal{C}_3$ components of the wave-packet. Therefore, the $\mathcal{C}_3$-component is understood as a measure for spin alignment with the texture. For intuitive comparison with the emergent magnetic field, and to demonstrate the previously mentioned relation to skyrmion textures, it is instructive to finally express $\boldsymbol{\Omega_{rr}}$'s texture-dependence through $\boldsymbol{n}$ instead of θ and ϕ:

$$\boldsymbol{\Omega}_{r_\mu r_\nu} = -(1-\xi^2)\frac{1}{2}\boldsymbol{n}\cdot\left(\frac{\partial \boldsymbol{n}}{\partial r_\mu}\times\frac{\partial \boldsymbol{n}}{\partial r_\nu}\right)[\hat{\boldsymbol{\tau}}]_z. \tag{3.35}$$

Hence, the real-space Berry curvature's effect is again expressed in terms of the emergent magnetic field (Eq. 3.16) similar to the ferromagnetic case.

The presence of $\xi(\boldsymbol{k})$ in $\boldsymbol{A_r}$ has a further effect. Although the orbital part is assumed to be trivial (meaning $\boldsymbol{A_k} = 0$), the mixed Berry curvature does not vanish since ξ is $\boldsymbol{k}$-dependent so that $\partial_{\boldsymbol{k}}\boldsymbol{A_r}$ leads to:

$$\boldsymbol{\Omega_{rk}} = -\boldsymbol{\Omega_{kr}} = \frac{1}{2}\frac{\partial\xi}{\partial \boldsymbol{k}}\begin{bmatrix} \sin(\theta)\frac{\partial\phi}{\partial \boldsymbol{r}} \\ -\frac{\partial\theta}{\partial \boldsymbol{r}} \\ 0 \end{bmatrix}. \tag{3.36}$$

Neglecting again all time-dependent changes which might enter through $\boldsymbol{\Omega_{xt}}$, the above

simplifications result in the following general equations of motion:

$$\dot{\boldsymbol{\mathcal{C}}} = \boldsymbol{\mathcal{C}} \times \begin{bmatrix} -\xi \sin(\theta) \frac{\partial \phi}{\partial r_\mu} \\ \xi \frac{\partial \theta}{\partial r_\mu} \\ \cos(\theta) \frac{\partial \phi}{\partial r_\mu} \end{bmatrix} \dot{r}_\mu, \tag{3.37a}$$

$$\dot{k}_\mu = -(1-\xi^2)\mathcal{C}_3[\dot{\boldsymbol{r}} \times \boldsymbol{\mathcal{B}}]_\mu, \tag{3.37b}$$

$$\dot{r}_\mu = \frac{\partial \epsilon}{\partial k_\mu} - \frac{1}{2}\frac{\partial \xi}{\partial k_\mu}\left(\sin(\theta)\frac{\partial \phi}{\partial r_\nu}\mathcal{C}_1 - \frac{\partial \theta}{\partial r_\nu}\mathcal{C}_2\right)\dot{r}_\nu. \tag{3.37c}$$

The $\boldsymbol{\Omega_{rk}}$ contribution to $\dot{k}_\mu$ vanishes as $\boldsymbol{\Omega}_{rk_\nu}\dot{k}_\nu \propto \partial_{k_\nu}\xi\partial_t k_\nu = \partial_t \xi = 0$ so that the $\dot{k}$ evolution is determined entirely by the emergent magnetic field with the isospin component corresponding to spin-z in the local frame for the collinear case. In addition to the group velocity, the mixed Berry curvature gives rise to an additional term proportional to the $\boldsymbol{k}$-derivative of the overlap ξ and determined by texture derivatives and the isospin expectation value. The evolution of the isospin has a convoluted form determined by the texture and velocity.

In principle, Eq. 3.37 is sufficient to track the wave-packet evolution numerically. However, more insight with respect to the isospin equation of motion part and the additional velocity term can be acquired by replacing the isospin with the wave-packet's spin expectation value $\boldsymbol{s} = \langle W|\boldsymbol{\sigma}|W\rangle$ in the "laboratory frame". This derivation is explained in great detail in appendix B of Ref. [76] and shall not be repeated here. Still, it is instructive to remark that the previous $\mathcal{C}_3$ component appearing with the emergent magnetic field is indeed the wave-packet's spin component along the local texture, i.e. $\mathcal{C}_3 = \boldsymbol{s}\cdot\boldsymbol{n}$. Furthermore, the explicit $\dot{\boldsymbol{r}}$ can be included into the general texture time derivative $\dot{\boldsymbol{n}} = \partial_t \boldsymbol{n} + (\dot{\boldsymbol{r}}\cdot\partial_{\boldsymbol{r}})\boldsymbol{n}$. The orbital dynamics can be compactly expressed as $\dot{k}_\mu = -\boldsymbol{n}\cdot(\partial_{r_\mu}\boldsymbol{n}\times\dot{\boldsymbol{s}})/2$. A better comparison with the non-degenerate case is possible when expressing $\dot{\boldsymbol{k}}$ as function of $\boldsymbol{s}$ and the emergent fields. Excluding $\boldsymbol{\Omega_{rk}}$, only the previously obtained $(1-\xi^2)$ factor discerns the resulting antiferromagnetic equations from the ferromagnetic ones (Eq. 3.18). However, the equations of motion are significantly more complicated in the antiferromagnetic case due to the non-trivial spin evolution (Fig. 3.2). The anomalous velocity part in the real-space dynamics can be expressed by a function of $\boldsymbol{s}$ and $\dot{\boldsymbol{n}}$ and the anomalous velocity's $\partial_{\boldsymbol{k}}\xi$-term becomes $\partial_{\boldsymbol{k}}\ln(\xi)$ when replacing $\boldsymbol{\mathcal{C}}$ by $\boldsymbol{s}$. Since this diverges for $\xi = 0$, the following equations of motion can treat finite ξ only. This problem does not appear in the original equations of motion (Eq. 3.37) but is a consequence of the ill-defined transformation from $\boldsymbol{\mathcal{C}}$ to $\boldsymbol{s}$ in case of $\xi \to 0$. Hence, special care is necessary when evaluating Eq. 3.38 with small ξ as the vanishing of the the anomalous term in case of $\xi = 0$ has to considered. The final equations of motion of Ref. [76] for collinear antiferromagnetic textures in terms of $\boldsymbol{s}$ instead of $\boldsymbol{\mathcal{C}}$ are:

$$\dot{\boldsymbol{s}} = (1-\xi^2)(\boldsymbol{s}\cdot\boldsymbol{n})\dot{\boldsymbol{n}}, \tag{3.38a}$$

$$\dot{\boldsymbol{k}} = -(1-\xi^2)(\boldsymbol{s}\cdot\boldsymbol{n})(\boldsymbol{\mathcal{E}} + \dot{\boldsymbol{r}}\times\boldsymbol{\mathcal{B}}), \tag{3.38b}$$

$$\dot{\boldsymbol{r}} = \frac{\partial \epsilon}{\partial \boldsymbol{k}} - \frac{1}{2}\left((\boldsymbol{s}\times\boldsymbol{n})\cdot\dot{\boldsymbol{n}}\right)\frac{\partial \ln\xi}{\partial \boldsymbol{k}}. \tag{3.38c}$$

These equations allow further interpretation of the wave-packet dynamics.

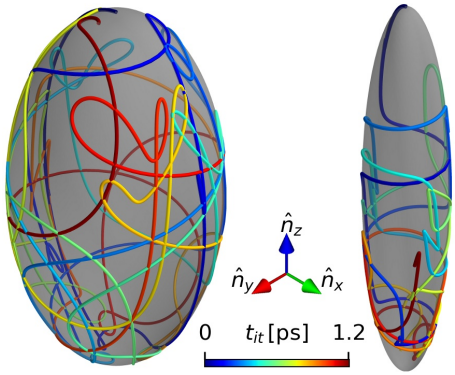

Figure 3.2: Exemplary spin evolutions in the local frame for $\xi \approx 0.53$ (left) and $\xi = 0.2$ (right).

At first, it is sensible to consider the limits $\xi = 0$ and $\xi = 1$. As ξ (Eq. 3.32) encodes the overlap of the Bloch function's orbital parts of different magnetic sublattices, it determines how easily the wave-packet's localization can shift between the sublattices. In case of $\xi = 0$ it is impossible to change the sublattice so that a wave-packet localized on one sublattice will remain there. The equations simplify to the non-degenerate analogue (Eq. 3.19) as the spins always follow the texture, the additional anomalous velocity vanishes, and the emergent magnetic field has the maximal effect always. Hence, such systems can be seen as 2 independent non-degenerate equations of motion with opposite spin. The other limit is $\xi = 1$ which corresponds to a perfectly coupled system. The spin of the wave-packet does not change anymore when traversing the texture, instead it simply changes the magnetic sublattice to keep its initial spin direction. Since such wave-packets ignore the texture entirely, no emergent fields act on the wave-packets and $\dot{\boldsymbol{r}}$ is determined solely by the group velocity. The $\xi \in (0, 1)$ region describes an intermediate wave-packet evolution with the additional anomalous velocity. A spin initially aligned with $\boldsymbol{n}$ appears to follow the texture but lags behind so that at some point $(\boldsymbol{s} \cdot \boldsymbol{n})$ changes the sign (Fig. 3.2). If so, the wave-packet will act as anti-aligned with the texture and consequently experience opposite effects from the emergent fields. Interestingly, the wave-packet spin's codomain is not the unit sphere but a prolate spheroid whose major axis points into the direction of $\boldsymbol{n}$ with unit length while the semi-major axis' length is ξ. In other words, $\boldsymbol{s}$ obeys

$$\tilde{s}_3^2 + \frac{\tilde{s}_1^2 + \tilde{s}_2^2}{\xi^2} = (\boldsymbol{s} \cdot \boldsymbol{n})^2 + \frac{(\boldsymbol{s} \times \boldsymbol{n})^2}{\xi^2} = 1, \tag{3.39}$$

where $\tilde{\boldsymbol{s}}$ is the spin in the local frame so that the general expression for $\boldsymbol{s}$ in the laboratory frame requires $\boldsymbol{n}$ explicitly. Example spin evolutions are shown in Fig. 3.2 demonstrating the restriction to the prolate spheroid. Notably, the spin evaluation is purely geometric and can be associated with a t'Hooft-Polyakov monopole which generates the $\mathcal{SU}(2)$ Berry phase [76].

As the impact of the emergent field is proportional to $\boldsymbol{s} \cdot \boldsymbol{n}$, its impact on $\dot{\boldsymbol{k}}$ varies tremendously in addition to the real-space dependent change of $\boldsymbol{\mathcal{B}}$. The additional anomalous

velocity only appears when the spin is misaligned with the texture and is maximal if the spin is perpendicular to $\boldsymbol{n}$. Hence, the spin character of a wave-packet in collinear antiferromagnets changes from aligned to anti-aligned respective to $\boldsymbol{n}$ throughout a long evolution which results in dynamics much more complicated than those of their non-degenerate counterparts solely caused by their non-abelian nature. In the ferromagnetic case similar deviations between spin and texture would require non-adiabatic corrections but here this feature arises in entirely adiabatic dynamics. Ultimately, the wave-packet equation of motion with applied external electric field and static magnetic texture:

$$\dot{\boldsymbol{s}} = (1-\xi^2)(\boldsymbol{s}\cdot\boldsymbol{n})\dot{\boldsymbol{n}}, \tag{3.40a}$$

$$\dot{\boldsymbol{k}} = -\boldsymbol{E} - (1-\xi^2)(\boldsymbol{s}\cdot\boldsymbol{n})(\dot{\boldsymbol{r}}\times\boldsymbol{\mathcal{B}}), \tag{3.40b}$$

$$\dot{\boldsymbol{r}} = \frac{\partial\epsilon}{\partial\boldsymbol{k}} - \frac{1}{2}\left((\boldsymbol{s}\times\boldsymbol{n})\cdot\dot{\boldsymbol{n}}\right)\frac{\partial \ln\xi}{\partial\boldsymbol{k}}, \tag{3.40c}$$

are studied in the following transport calculations.

3.2.2 Noncollinear Antiferromagnets

The wave-packet formalism can been applied to non-collinear antiferromagnets with twofold degenerate states analogously to the previous dynamics considering collinear antiferromagnets. In this section the basic derivations leading to the corresponding equations of motion are presented following Ref. [77]. While the part about the magnetic texture description adheres very closely to the reference, the latter section, which covers the terms appearing in the equations of motion, describes generalized expressions of the Berry connections and curvatures which are applied to a particular Hamiltonian in the source material [77].

Texture parametrization

A non-collinear antiferromagnet requires at least 3 atoms in the unit cell to fulfill the requirements of vanishing net magnetization and noncollinear magnetization angles. In contrast to the collinear case it is no longer sufficient to supply the magnetization direction of the unit cell and to define which atoms are of spin-up or -down character, instead the atoms and their corresponding spins form a two- or three-dimensional object. Hence, textures have to be described as solid angle rotations from a definite initial state instead of the simple definition of the staggered order parameter $\boldsymbol{n}$. A multitude of methods for describing such rotations exist. Here a vectorial parametrization is used where a vector $\boldsymbol{\phi}$ describes the solid rotation entirely, its direction determines the rotation axis while its magnitude encodes the rotation angle. In general, arbitrary parameterizations connecting the $\boldsymbol{\phi}$s with the rotation axis and angle exist and have different advantages [88], here the Caylay-Gibbs-Rodrigues parameterization is used [77]. In this case the rotation angle θ is defined via $|\boldsymbol{\phi}| = \tan(\theta/2)$ and the matrix $\mathfrak{R}$ can be parametrized as:

$$\boldsymbol{S}_j = \mathfrak{R}\boldsymbol{S}_j^{(0)} = \frac{1-\boldsymbol{\phi}^2}{1+\boldsymbol{\phi}^2}\boldsymbol{S}_j^{(0)} + \frac{2}{1+\boldsymbol{\phi}^2}\left[\boldsymbol{\phi}\times\boldsymbol{S}_j^{(0)} + (\boldsymbol{\phi}\cdot\boldsymbol{S}_j^{(0)})\boldsymbol{\phi}\right], \tag{3.41}$$

where j labels the atoms in the unit cell. Accordingly, all calculation steps to yield the solidly rotated spins $\boldsymbol{S}_j$ can be expressed as vector operations based on the chosen initial spin configuration $\boldsymbol{S}_j^{(0)}$. The symmetric terms of the rotation are expressed as scalar products while the skew part is denoted via cross products. The huge advantage of this parameterization is the simple form of the rotation matrix derivative

$$\frac{\partial \mathfrak{R}}{\partial \boldsymbol{x}} = \boldsymbol{\omega_x} \times \mathfrak{R}, \tag{3.42}$$

where a possible second symmetric part of the "space" angular velocity [77] $\boldsymbol{\omega_x}$ vanishes:

$$\boldsymbol{\omega_x} = 2\frac{\frac{\partial \boldsymbol{\phi}}{\partial \boldsymbol{x}} + \boldsymbol{\phi} \times \frac{\partial \boldsymbol{\phi}}{\partial \boldsymbol{x}}}{1 + \boldsymbol{\phi}^2}. \tag{3.43}$$

In other parameterizations it is generally impossible to express the derivative in this vector form with a cross product. Hence, the Caylay-Gibbs-Rodrigues parameterization is especially suited for this formalism since $\boldsymbol{\omega_x}$ appears in the real-space Berry curvature where the vector form allows similarities to the emergent magnetic field expression of the collinear case. $\mathfrak{R}$ and $\boldsymbol{\omega}$ replace $\boldsymbol{n}$ and $\partial_{\boldsymbol{r}}\boldsymbol{n}$ and are sufficient to describe the influence of the texture. $\mathfrak{R}^{-1}(\boldsymbol{\phi}) = \mathfrak{R}(-\boldsymbol{\phi})$ and $\mathfrak{R}^{-1}(\boldsymbol{\phi})\boldsymbol{\omega}(\boldsymbol{\phi}) = -\boldsymbol{\omega}(-\phi)$ hold as $\mathfrak{R}$ is a rotation matrix. Another extremely useful property is:

$$\frac{\partial \boldsymbol{\omega}_{r_\nu}}{\partial r_\mu} - \frac{\partial \boldsymbol{\omega}_{r_\mu}}{\partial r_\nu} = \boldsymbol{\omega}_{r_\mu} \times \boldsymbol{\omega}_{r_\nu}, \tag{3.44}$$

which allows to avoid higher order derivatives of $\boldsymbol{\phi}$ in antisymmetric setups and later proves to be helpful when calculating the antisymmetric $\boldsymbol{\Omega_{rr}}$.

Equations of motion

Although the wave-packet is constructed in the usual degenerate way (Eq. 3.20), several simplifications used in the collinear case are not applicable which ultimately leads to more general wave-packet dynamics expressions. The major difference is that the basis Bloch-waves $|u_{1,2}\rangle$ cannot be chosen as corresponding to a particular sublattice. Instead, basis states with weight on both spin parts will appear due to the noncollinearity even when choosing the quantization axis along one atom's spin direction. Hence, the Bloch states can no longer be decomposed into orbital- and spin-part as in Eq. 3.29 but take the form:

$$|u_1(\boldsymbol{k}, \boldsymbol{r}, t)\rangle = |\eta_{1\uparrow}(\boldsymbol{k})\rangle\,|\uparrow(\boldsymbol{r}, t)\rangle + |\eta_{1\downarrow}(\boldsymbol{k})\rangle\,|\downarrow(\boldsymbol{r}, t)\rangle\,, \tag{3.45a}$$

$$|u_2(\boldsymbol{k}, \boldsymbol{r}, t)\rangle = |\eta_{2\uparrow}(\boldsymbol{k})\rangle\,|\uparrow(\boldsymbol{r}, t)\rangle + |\eta_{2\downarrow}(\boldsymbol{k})\rangle\,|\downarrow(\boldsymbol{r}, t)\rangle\,. \tag{3.45b}$$

Accordingly, the overlaps $\langle \boldsymbol{u}|\boldsymbol{u}\rangle$ become more complicated and the orbital overlaps $\langle \boldsymbol{\eta}|\boldsymbol{\eta}\rangle$ are no longer 1 and ξ as in the collinear case, instead they depend on the actual system and vary with the choice of initial Bloch-waves. $\boldsymbol{\eta}$ contains the orbital parts of all sublattice and spin direction. $\langle \boldsymbol{\eta}|\boldsymbol{\eta}'\rangle$ is a hermitian 4×4 matrix and as such has 6 independent complex and 4 real diagonal components in general. Several simplifications are possible depending on the

choice of basis vectors and the symmetry of the system. For example, choosing the basis so that $\langle \boldsymbol{u}|\sigma_z|\boldsymbol{u}\rangle$ is diagonal makes the 4 diagonal components real and causes 2 off-diagonal components and their hermitian partners to vanish. In the example systems of Ref. [77] even more parts cancel out leaving only 3 different real $\boldsymbol{k}$-dependent overlaps which are functions of a single parameter similar to ξ. These simplifications are made possible by $|\eta_{a\downarrow}\rangle = |\eta_{b\uparrow}\rangle$, in general cases without that equality more complicated overlaps will appear.

Next, the Berry curvatures have to be expressed in terms of the magnetization parametrization and the overlaps $\langle \boldsymbol{\eta}|\boldsymbol{\eta}'\rangle$ in order to simplify and specify the general equations of motion (Eq. 3.24). The Berry connection terms can be simplified similarly to the collinear case as the initial Bloch functions are assumed to be separable into $\boldsymbol{r}$-independent orbital-parts and $\boldsymbol{k}$-independent spin-part.

In the following it is convenient to rotate the Bloch states back into the reference magnetic configuration $|\boldsymbol{u}^0\rangle$ via $|\boldsymbol{u}\rangle = U_{\boldsymbol{c}}\,|\boldsymbol{u}^0\rangle$ so that the Berry connections take the form:

$$A_{\boldsymbol{ccx}} = \mathrm{i}\left\langle \boldsymbol{u}^0 \middle| U^\dagger \frac{\partial}{\partial \boldsymbol{x}} U \middle| \boldsymbol{u}^0 \right\rangle . \tag{3.46}$$

Thereby it is possible to restrict the orbital-dependence onto the reference states $|\boldsymbol{u}^0\rangle$ while all texture related real-space dependence is encoded into the U parts. In contrast to the collinear case, the Berry connections add not only a complex phase but can mix $|u_1^0\rangle$ and $|u_2^0\rangle$ into $|u_{1,2}\rangle$.

The $\Lambda_{\boldsymbol{ccr}} = U_{\boldsymbol{c}}^\dagger \partial_{\boldsymbol{r}} U_{\boldsymbol{c}}$ part of Eq. 3.46 requires scrutiny to arrive at convenient expressions for the real-space Berry connection $\mathcal{SU}(2)$-matrix $A_{\boldsymbol{ccr}}$. In Ref. [77] only model-dependent simplifications are given whereas the generalized expressions are given in the following. First, $\Lambda_{\boldsymbol{ccr}}$ can be expressed as $\Lambda_{\boldsymbol{ccr}} = -\mathrm{i}/2\boldsymbol{\omega}_{\boldsymbol{r}}(-\boldsymbol{\phi})\boldsymbol{\sigma}_{\boldsymbol{cc}}$. The $\boldsymbol{\sigma}_{\boldsymbol{cc}}$-term mixes the different $|u_{1,2}^0\rangle$ in $|u_{1,2}\rangle$ according to $\boldsymbol{\omega}_{\boldsymbol{r}}(-\boldsymbol{\phi})$ which describes the derivative of the inverse rotation. Due to the arising $\boldsymbol{\sigma}_{\boldsymbol{cc}}$-term, several $\boldsymbol{r}$-independent overlaps encoded through $\langle \boldsymbol{u}^0|\boldsymbol{\sigma}_{\boldsymbol{cc}}|\boldsymbol{u}^0\rangle$ enter the final expression for the Berry connection:

$$A_{\boldsymbol{ccr}} = \frac{1}{2}\,\langle \boldsymbol{u}^0|\boldsymbol{\omega}_{\boldsymbol{r}}(-\boldsymbol{\phi}) \cdot \boldsymbol{\sigma}_{\boldsymbol{cc}}|\boldsymbol{u}^0\rangle\,. \tag{3.47}$$

The isospin parameters $\boldsymbol{c}$ denote the two-dimensional matrix spanned by $\langle \boldsymbol{u}^0|$ and $|\boldsymbol{u}^0\rangle$. Since the Pauli matrices as generators of the $\mathcal{SU}(2)$ group appear in $A_{\boldsymbol{ccr}}$, it is obvious that $A_{\boldsymbol{ccr}}$ can be expressed in the vectorial form of the Berry connection $\boldsymbol{A}_{\boldsymbol{r}}$. $A_{\boldsymbol{ccr}}$ can obviously be expressed in the vectorial form of the Berry connection $\boldsymbol{A}_{\boldsymbol{r}}$ as the Pauli matrices, generators of the $\mathcal{SU}(2)$ group, appear explicitly. Using Eq. 3.25, $\boldsymbol{A}_{\boldsymbol{r}}$ is expressed as:

$$\boldsymbol{A}_{\boldsymbol{r}} = \frac{1}{2}\begin{bmatrix} \Re\,\langle u_2|\boldsymbol{\omega}_{\boldsymbol{r}}(-\boldsymbol{\phi}) \cdot \boldsymbol{\sigma}_{\boldsymbol{cc}}|u_1\rangle \\ \Im\,\langle u_2|\boldsymbol{\omega}_{\boldsymbol{r}}(-\boldsymbol{\phi}) \cdot \boldsymbol{\sigma}_{\boldsymbol{cc}}|u_1\rangle \\ \langle u_1|\boldsymbol{\omega}_{\boldsymbol{r}}(-\boldsymbol{\phi}) \cdot \boldsymbol{\sigma}_{\boldsymbol{cc}}|u_1\rangle \end{bmatrix} . \tag{3.48}$$

It is instructive to introduce $S_{i,\boldsymbol{cc}} = \langle \boldsymbol{u}^0|\sigma_{i\boldsymbol{cc}}|\boldsymbol{u}^0\rangle$ and its $\mathcal{SU}(2)$ vector form

$$\boldsymbol{\Sigma}_i = \begin{bmatrix} \Re(S_{i,c_2c_1}) \\ \Im(S_{i,c_2c_1}) \\ S_{i,c_1c_1} \end{bmatrix} . \tag{3.49}$$

All of $\boldsymbol{\Sigma}_i$'s components are $\boldsymbol{r}$-independent so that the expression

$$\boldsymbol{A}_{\boldsymbol{r}} = \frac{1}{2}\sum_i \omega_{i\boldsymbol{r}}(-\boldsymbol{\phi})\boldsymbol{\Sigma}_i \tag{3.50}$$

is particularly convenient as all $\boldsymbol{r}$-dependence is in the $\boldsymbol{\omega}_{\boldsymbol{r}}$ term while $\boldsymbol{\Sigma}$ contains all $\boldsymbol{k}$-dependent parts. Explicitly resolving the Pauli matrices, $S_{i,\boldsymbol{cc}}$ can be expressed in terms of the overlaps $\langle\boldsymbol{\eta}|\boldsymbol{\eta}\rangle$ so that only simple calculations based on the eigenstates are necessary. Omitting η as an abbreviation, $|1\uparrow\rangle := |\eta_{1\uparrow}\rangle$, $\boldsymbol{S}_{\boldsymbol{cc}}$ can be expressed as:

$$\boldsymbol{S}_{\boldsymbol{cc}} = \begin{bmatrix} \begin{bmatrix} 2\Re\langle 1\uparrow|1\downarrow\rangle \\ 2\Im\langle 1\uparrow|1\downarrow\rangle \\ \langle 1\uparrow|1\uparrow\rangle - \langle 1\downarrow|1\downarrow\rangle \end{bmatrix} & \begin{bmatrix} \langle 1\downarrow|2\uparrow\rangle + \langle 1\uparrow|2\downarrow\rangle \\ \mathrm{i}\langle 1\downarrow|2\uparrow\rangle - \mathrm{i}\langle 1\uparrow|2\downarrow\rangle \\ \langle 1\uparrow|2\uparrow\rangle - \langle 1\downarrow|2\downarrow\rangle \end{bmatrix} \\ \begin{bmatrix} \langle 2\uparrow|1\downarrow\rangle + \langle 2\downarrow|1\uparrow\rangle \\ \mathrm{i}\langle 2\uparrow|1\downarrow\rangle - \mathrm{i}\langle 2\downarrow|1\uparrow\rangle \\ \langle 2\uparrow|1\uparrow\rangle - \langle 2\downarrow|1\downarrow\rangle \end{bmatrix} & \begin{bmatrix} 2\Re\langle 2\uparrow|2\downarrow\rangle \\ 2\Im\langle 2\uparrow|2\downarrow\rangle \\ \langle 2\uparrow|2\uparrow\rangle - \langle 2\downarrow|2\downarrow\rangle \end{bmatrix} \end{bmatrix}. \tag{3.51}$$

Using the definitions for $\boldsymbol{S}_{\boldsymbol{cc}}$, $\boldsymbol{\Sigma}_i$, and $\boldsymbol{A}_{\boldsymbol{r}}$, the overlaps $\langle\boldsymbol{\eta}|\boldsymbol{\eta}\rangle$ contain the only model-dependent parameters while the texture-dependence is encoded entirely in $\boldsymbol{\omega}_{\boldsymbol{r}}(-\boldsymbol{\phi})$ which itself solely depends on the orientation defining $\boldsymbol{\phi}$ and its real-space derivatives $\partial_{\boldsymbol{r}}\boldsymbol{\phi}$ (Eq. 3.43). Accordingly, the numerical implementation and calculation $\boldsymbol{A}_{\boldsymbol{r}}$ is straightforward and computationally affordable as the $\boldsymbol{r}$- and $\boldsymbol{k}$-dependent parts are separated and since only few basis model parameters enter the expression.

The simplification of the orbital Berry connection $A_{\boldsymbol{cck}}$ starts from Eq. 3.46 as well. The U's cancel each other since U is $\boldsymbol{k}$-independent so that the reciprocal-space Berry connection is $A_{\boldsymbol{cck}} = \langle\boldsymbol{u}^0|\partial_{\boldsymbol{k}}|\boldsymbol{u}^0\rangle$. Hence, all components depend only on the spin-diagonal sum of $\langle\boldsymbol{\eta}|\partial_{\boldsymbol{k}}|\boldsymbol{\eta}\rangle$ by construction. All texture-dependence has dropped out so that the tensor itself is entirely independent of $\boldsymbol{r}$. Nevertheless, the actual influence of $A_{\boldsymbol{cck}}$ on the wave-packet dynamics changes throughout the evolution according to the isospin evolution which picks out differently-weighted tensor components. $|\eta_{1,2}\rangle$-vectors span the isospinor matrix so that the $\boldsymbol{k}$-space Berry connection can be expressed as:

$$A_{\boldsymbol{cck}} = \mathrm{i}\begin{bmatrix} \langle\eta_{1\uparrow}|\partial_{\boldsymbol{k}}|\eta_{1\uparrow}\rangle + \langle\eta_{1\downarrow}|\partial_{\boldsymbol{k}}|\eta_{1\downarrow}\rangle & \langle\eta_{1\uparrow}|\partial_{\boldsymbol{k}}|\eta_{2\uparrow}\rangle + \langle\eta_{1\downarrow}|\partial_{\boldsymbol{k}}|\eta_{2\downarrow}\rangle \\ \langle\eta_{2\uparrow}|\partial_{\boldsymbol{k}}|\eta_{1\uparrow}\rangle + \langle\eta_{2\downarrow}|\partial_{\boldsymbol{k}}|\eta_{1\downarrow}\rangle & \langle\eta_{2\uparrow}|\partial_{\boldsymbol{k}}|\eta_{2\uparrow}\rangle + \langle\eta_{2\downarrow}|\partial_{\boldsymbol{k}}|\eta_{2\downarrow}\rangle \end{bmatrix}. \tag{3.52}$$

Contrary to the collinear case, the mere presence of non-collinear magnetic structures causes non-vanishing $A_{\boldsymbol{cck}}$ even neglecting spin-orbit coupling. Thus, the non-collinearity takes over parts of the role which spin-orbit coupling plays in the collinear case [89].

A general property of Berry connections is their gauge-dependence present even in the non-degenerate case. There, non-vanishing Berry connections vary drastically when changing the initial gauge of the Bloch function $|\psi\rangle$ constituting the wave-packet (Eq. 3.2). In the degenerate noncollinear case we thus have the gauge freedom of choosing a complex phase to the $|\psi_{1,2}\rangle$ in addition to the usual $\mathcal{SU}(2)$ gauge of determining relative choice of the $|\psi_{1,2}\rangle$ in the wave-function, although finally this is of course only one $\mathcal{SU}(2)$ gauge freedom. This $\mathcal{U}(1)$ choice can influence the final connection due to the $\boldsymbol{k}$-derivative in $A_{\boldsymbol{cck}}$ and may conceal

convenient choices for the relative $|\psi_{1,2}\rangle$ gauge. Contrary to $A_{\boldsymbol{ccr}}$, no reason is immediately apparent which allows to express $A_{\boldsymbol{cck}}$ as an $\mathcal{SU}(2)$ vector. On the contrary, example systems demonstrated that some gauges cause $A_{\boldsymbol{cck}}$ to break the $\mathcal{SU}(2)$-symmetry. In principle, this presents no fundamental problem but complicates the general equations of motion since the weight between the $|\psi_{1,2}\rangle$ are no longer expressible by the isospin vector $\boldsymbol{\mathcal{C}}$. Instead, the complex variables $c_{1,2}$ would have to be track. In the interest of staying consistent with the collinear equations only cases where $A_{\boldsymbol{cck}}$ can indeed be expressed as

$$\boldsymbol{A_k} = \begin{bmatrix} \Im\left(\langle\eta_{2\uparrow}|\partial_{\boldsymbol{k}}|\eta_{1\uparrow}\rangle + \langle\eta_{2\downarrow}|\partial_{\boldsymbol{k}}|\eta_{1\downarrow}\rangle\right) \\ -\Re\left(\langle\eta_{2\uparrow}|\partial_{\boldsymbol{k}}|\eta_{1\uparrow}\rangle + \langle\eta_{2\downarrow}|\partial_{\boldsymbol{k}}|\eta_{1\downarrow}\rangle\right) \\ \Im\left(\langle\eta_{1\uparrow}|\partial_{\boldsymbol{k}}|\eta_{1\uparrow}\rangle + \langle\eta_{1\downarrow}|\partial_{\boldsymbol{k}}|\eta_{1\downarrow}\rangle\right) \end{bmatrix} \tag{3.53}$$

are considered in the following. This form differs from Eq. 3.25 due to the imaginary unit prefactor of Eq. 3.52. In the system of Ref. [77] $A_{\boldsymbol{cck}}$ vanishes for degenerate states as can be shown explicitly by differentiating the highly symmetric eigenstates $|\psi_{1,2}\rangle$ constituting the wave-packet. That calculation is simple, as the $|\psi\rangle$'s have only one $\boldsymbol{k}$ dependent parameter and since many components cancel out due to the symmetric structure of the eigenstates. An alternative set of $\psi_{1,2}$ which results in non-vanishing $A_{\boldsymbol{cck}}$ should be possible in that system, however the dynamical differences arising from that modification in the other terms would be canceled by the emerging $A_{\boldsymbol{cck}}$.

Furthermore, the non-abelian Berry curvatures enter the equations of motion. Their calculation is based on the general Eq. 3.27. As the curvatures are obtained via the derivatives of the connections, the separation into $\boldsymbol{r}$- and $\boldsymbol{k}$-dependent parts simplifies the curvature expressions again. For construction of $\boldsymbol{\Omega_{rr}}$ the real-space derivative of $\boldsymbol{A_r}$ is required. Fortunately, the only real-space dependent component of $\boldsymbol{A_r}$ is $\boldsymbol{\omega}(-\boldsymbol{\phi})$ whose derivative can be simply expressed using Eq. 3.44 and $\boldsymbol{\Omega_{rr}}$'s antisymmetric properties. Hence, the real-space Berry curvature simplifies to:

$$\boldsymbol{\Omega}_{r_\mu r_\nu} = -\frac{1}{2}\sum_i \left(\boldsymbol{\omega}_{r_\mu}(-\boldsymbol{\phi}) \times \boldsymbol{\omega}_{r_\nu}(-\boldsymbol{\phi})\right)_i \boldsymbol{\Sigma}_i + 2\boldsymbol{A}_{r_\mu} \times \boldsymbol{A}_{r_\nu}. \tag{3.54}$$

This equation can be easily implemented in numerical schemes and is related to the simpler real-space Berry curvatures in that its $\boldsymbol{r}$-dependence is covered by the texture defining parameter and its first derivative, expressed through $\boldsymbol{\omega_r}$ (Eq. 3.42), only. A topological charge related to the $\boldsymbol{\Omega}_{\mu\nu}$ exists [77] similar to the collinear, and especially the non-degenerate, case. The $\boldsymbol{k}$-dependence is much more complicated than in the collinear case as several $\boldsymbol{\Sigma_i}$ arise in contrast to the simple $(1-\xi^2)$-dependence of collinear antiferromagnets. Thus, noncollinearity adds another layer of complexity concealing the transports' topological origin.

Both real- and reciprocal-space Berry connections are necessary for the mixed Berry curvature. Since $\boldsymbol{A_k}$ is $\boldsymbol{r}$-independent and as the orbital derivatives of $\boldsymbol{A_r}$ act only on $\boldsymbol{\Sigma_i}$, the mixed Berry curvatures can be expressed as:

$$\boldsymbol{\Omega}_{r_\mu k_\nu} = \frac{1}{2}\sum_i \omega_{i r_\mu}(-\boldsymbol{\phi})\frac{\partial \boldsymbol{\Sigma}_i}{\partial k_\nu} + 2\boldsymbol{A}_{r_\mu} \times \boldsymbol{A}_{k_\nu}, \tag{3.55a}$$

$$\boldsymbol{\Omega}_{k_\mu r_\nu} = -\frac{1}{2}\sum_i \omega_{i r_\nu}(-\boldsymbol{\phi})\frac{\partial \boldsymbol{\Sigma}_i}{\partial k_\mu} + 2\boldsymbol{A}_{k_\mu} \times \boldsymbol{A}_{r_\nu}. \tag{3.55b}$$

Here, $\partial_{\boldsymbol{k}}\boldsymbol{\Sigma}_i$ appears which solely depends on the derivatives of the overlaps $\langle\boldsymbol{\eta}|\boldsymbol{\eta}\rangle$ (Eqs. 3.49, 3.51). Since $\langle\boldsymbol{\eta}|\boldsymbol{\eta}\rangle$ and their derivatives appear prominently in the Berry curvatures, a convenient choice for the eigenstates $\psi_{1,2}$ aiming for smoothness even in the overlap derivatives is advantageous. Finding such a basis state gauge is not trivial and very system dependent, but it is necessary as the equations of motion are most probably practically unsolvable due to numerical restrictions for unsuitable gauges although the equations are valid in general. Notice furthermore that Eq. 3.55 is only applicable if $A_{\boldsymbol{cck}}$ can be expressed as $\mathcal{SU}(2)$ vector. Otherwise, the more general Eq. 3.26 has to be used where the latter cross product is replaced by a commutator.

The reciprocal-space Berry curvature can be calculated using the reciprocal-space Berry connection $A_{\boldsymbol{cck}}$ (Eq. 3.52) and the general Eq. 3.26. Since all components of $A_{\boldsymbol{cck}}$ contain only $\langle\boldsymbol{\eta}|\partial_{\boldsymbol{k}}|\boldsymbol{\eta}'\rangle$-terms, the first 2 terms of Eq. 3.26 can be expressed through sums of $\langle\partial_{k_i}\boldsymbol{\eta}|\partial_{k_j}\boldsymbol{\eta}'\rangle$ terms using the relation:

$$\partial_{k_i}\langle\boldsymbol{\eta}|\partial_{k_j}|\boldsymbol{\eta}'\rangle - \partial_{k_j}\langle\boldsymbol{\eta}|\partial_{k_i}|\boldsymbol{\eta}'\rangle = \langle\partial_{k_i}\boldsymbol{\eta}|\partial_{k_j}\boldsymbol{\eta}'\rangle - \langle\partial_{k_j}\boldsymbol{\eta}|\partial_{k_i}\boldsymbol{\eta}'\rangle\,. \tag{3.56}$$

Again, $|\partial_{\boldsymbol{k}}\boldsymbol{\eta}\rangle$ has to be evaluated which leads to the same problems as in case of $A_{\boldsymbol{cck}}$. A smooth gauge of the basis is necessary to define meaningful derivatives. Still, no significant further effort is necessary to compute $\Omega_{c_ic_j\boldsymbol{kk}'}$ after having obtained $A_{\boldsymbol{cck}}$ so that the reciprocal-space Berry curvature can be directly evaluated using:

$$\Omega_{c_ic_j\boldsymbol{kk}'} = \sum_{s=\{\uparrow,\downarrow\}} \mathrm{i}\left(\langle\partial_{\boldsymbol{k}}\eta_{is}|\partial_{\boldsymbol{k}'}\eta_{js}\rangle - \langle\partial_{\boldsymbol{k}'}\eta_{is}|\partial_{\boldsymbol{k}}\eta_{js}\rangle\right) - \mathrm{i}\left[A_{\boldsymbol{cck}}, A_{\boldsymbol{cck}'}\right]\Big|_{ij}\,. \tag{3.57}$$

In conclusion, the noncollinear antiferromagnetic equations are similar to the collinear ones. The more involved 3-dimensional magnetic texture can be effectively described in the adequate Caylay-Gibbs-Rodrigues parameterization from which the respective Berry connection and curvatures can be obtained. The reciprocal-space structure is more problematic. While the relevant components vanish in the collinear case without SOC, the overlaps $\langle\boldsymbol{\eta}|\boldsymbol{\eta}\rangle$ and even $\partial_{\boldsymbol{k}}|\boldsymbol{\eta}\rangle$ are necessary to describe all components in noncollinear systems. Hence, straight forward application of the equations of motion is only possible when treating simple systems with smooth basis states. Otherwise, it is necessary to find smart expressions to describe $A_{\boldsymbol{cck}}$ and $\Omega_{\boldsymbol{cckk}}$.

4

Transport

Electron transport is a very broad topic in physics with an enormous number of applications. A multitude of physical effects, of classical and quantum mechanical origin, varyingly pronounced in different materials, measured by different experimental techniques, and described by different theoretical theories, exist. Examples include the general distinction based of the band theory in metals, semiconductors, and insulators, as well as more involved phenomena such as superconductivity and Mott-insulators. One of the earliest heuristically understood transport phenomena is the Hall effect. This thesis' aim is to calculate a specific kind of Hall effects in skyrmionic textures. As its discussion requires a general understanding of Hall effects, an brief overview of different Hall effects is given in the following sections.

The main method of this thesis is based on the combination of the semiclassical equations of motion, thereby incorporating the magnetic texture, with the Boltzmann formalism to describe the cumulative transport properties. Sec. 4.3 introduces different methods giving access to transport information which is followed by detailed descriptions of the main procedure used to obtain the transport properties.

In general, the multitude of linear and non-linear transport effects in response to applied electric fields or temperature gradients exist and might be described in similar frameworks. Since this thesis is restricted to the topological (spin) Hall effect causes by magnetic textures under applied external electric fields, only the lowest order longitudinal and the Hall transversal components are considered here.

With the exception of Secs. 4.2.1 and 4.4.2, which cover the physical origin and formalism of the here-discussed effect, this chapter summarizes established transport phenomena and methods that are necessary to assess and understand the advancements of this thesis.

4.1 Hall effects

Already in 1879 the emergence of additional currents caused by an applied external magnetic field was experimentally measured [90]. These transversal currents are perpendicular to both the original current caused by an applied electric field, i.e. potential difference, and the magnetic field. This phenomenon is called the ordinary Hall effect (OHE) in the following. Shortly afterwards the related anomalous Hall effect (AHE) was discovered [91]. There, the

magnetization of the specimen phenomenologically takes the role of the external magnetic field and causes the transversal currents. Consequently, the term "Hall effect" describes a family of phenomena with transversal current in case of applied electric fields inducing the initial currents.

Similar phenomena exist for currents caused by thermal gradients replacing the electric potential gradients. There, the descriptor "Hall" is replaced by "Nernst". The extensive similarities with the Hall effects are covered by the Onsager relations. Hence, the same formalism as used in the following could be applied to the Nernst analogue [92].

Phenomenologically, the Hall effects are conveniently described as the off-diagonal components of the conductivity tensor σ which describe the linear transport response of the electric field $\boldsymbol{E}$ to the charge currents $\boldsymbol{j}$:

$$\boldsymbol{j} = \sigma \cdot \boldsymbol{E} = \begin{bmatrix} \sigma_{xx} & \sigma_{xy} & \sigma_{xz} \\ \sigma_{yx} & \sigma_{yy} & \sigma_{yz} \\ \sigma_{zx} & \sigma_{zy} & \sigma_{zz} \end{bmatrix} \cdot \begin{bmatrix} E_x \\ E_y \\ E_z \end{bmatrix}. \tag{4.1}$$

Some components of σ describing distinctive effects are computational accessible for example through Eqs. 4.34 and 4.35. In experiments resistivities ρ are measured instead of conductivities. Both quantities are related through $\rho = \sigma^{-1}$ so that restriction of the non-vanishing Hall components to the xy-plane

$$\rho = \begin{bmatrix} \frac{\sigma_{yy}}{\sigma_{xx}\sigma_{yy}-\sigma_{xy}\sigma_{yx}} & \frac{-\sigma_{xy}}{\sigma_{xx}\sigma_{yy}-\sigma_{xy}\sigma_{yx}} & 0 \\ \frac{-\sigma_{yx}}{\sigma_{xx}\sigma_{yy}-\sigma_{xy}\sigma_{yx}} & \frac{\sigma_{xx}}{\sigma_{xx}\sigma_{yy}-\sigma_{xy}\sigma_{yx}} & 0 \\ 0 & 0 & \frac{1}{\sigma_{zz}} \end{bmatrix} \approx \begin{bmatrix} \frac{1}{\sigma_{xx}} & -\frac{\sigma_{xy}}{\sigma_{xx}\sigma_{yy}} & 0 \\ -\frac{\sigma_{yx}}{\sigma_{xx}\sigma_{yy}} & \frac{1}{\sigma_{yy}} & 0 \\ 0 & 0 & \frac{1}{\sigma_{zz}} \end{bmatrix} \tag{4.2}$$

is a reasonable approximation as long as the Hall conductivity magnitudes are much smaller than the longitudinal ones.

Experimentally, the ordinary and anomalous Hall effects are commonly described as:

$$\rho_{xy} = \rho_{xy}^{OHE} + \rho_{xy}^{AHE} = R^O B + R^A M, \tag{4.3}$$

with the ordinary and anomalous Hall constants R^O and R^A, while B and M are the external magnetic field and the magnetization, respectively. The ordinary Hall constant R^O can be expressed through the conductivities as:

$$R^O = -\frac{\sigma_{xy}^{OHE}}{\sigma_{xx}\sigma_{yy}B}. \tag{4.4}$$

While the origin of the OHE was readily understood as a consequence of the general laws of electromagnetism, i.e. Lorentz force exerted on traversing electrons, the AHE initially eluded concise theoretical description. Later, 3 main contributions to the AHE were identified. Two of them are scattering related and thus called extrinsic: the side-jump and skew-scattering terms. The other source is a direct consequence of the bandstructure and called the intrinsic contribution.

The first description of the AHE's intrinsic part was given in 1954 [93]. There, the AHE was attributed to inter-band matrix elements of the applied electric field mediated by

spin-orbit coupling. Its linear scaling with respect to the magnetization originates in the proportionality between the spin-orbit interaction and the electron spin polarization. Later, the intrinsic contribution was rewritten in term of the Berry curvature formalism [94]. Using the semiclassical wave-packet equations (Eq. 3.10), a transversal conductivity component was uncovered which is the integral of $\Omega_{\boldsymbol{kk}}$ weighted by the distribution function over the whole Brillouin zone (Eq. 4.29). The magnetization results in spin-split bands whose Berry curvature integrals do not cancel each other due to the shifted Fermi energy and respective different occupations.

The scattering-dependent AHE contributions require spin-orbit coupling as well. Skew-scattering was theoretically described in 1955 as anisotropy of the scattering rates [95, 96]. Hence, electrons are more readily scattered into one direction than the other, so that a net current is obtained. Spin-orbit coupling causes a transversal wave-packet polarization which, with off-center scattering, leads to a Hall current. The side-jump term was first recognized as significant contribution in 1964 [97]. It can be effectively described as real-space shift which naturally arises when evolving a wave-packet explicitly through a sufficiently smooth impurity potential. It depends on in- and outgoing $\boldsymbol{k}$ and its Hall impact can be understood as a further distortion of the electron distribution which, in case of applied $\boldsymbol{E}$ fields, causes transversal conductivities through the usual group velocities [98]. These contributions do no exhaust the anomalous Hall phenomena, also anomalous distribution and intrinsic skew scattering can play a role. For the ultimate evaluation of the AHE, all conductivity contributions have to be added [98].

The OHE and AHE also have quantized versions. Fortunately, the prerequisites of their exhibition are seldom fulfilled in systems where the main subject of this thesis, the topological (spin) Hall effect, is realized. Hence, only a short overview is given due to their similarities. The quantum Hall effect occurs in two-dimensional materials with low electron density under very strong applied magnetic fields. There, the bands form Landau levels which each contribute a transversal resistivity quantum. Depending on the Landau level occupation, their summed resistivity quanta replace the OHE. The exact quantization of this effect is a very remarkable property [99] whose discovery was awarded with a Nobel price. A fractional version of the quantum Hall effect caused by quasi-particle emergence exists as well. The quantum anomalous Hall effect is a special case of the intrinsic AHE [100]. The $\Omega_{\boldsymbol{kk}}$ Brillouin zone integral has to be quantized for thin, insulating films. This integral is called Chern number and can take any integer number in principle. Only perturbations closing the energy gap can change the Chern number rendering it a topological invariant. If the Chern number is not zero, chiral edge states at the boundary with materials of different Chern numbers, e.g. the vacuum, are formed and transversal charge currents proportional to the Chern number emerge. Since this special case of the anomalous Hall effect requires insulating systems and since the investigated topological Hall effect contains a Fermi surface integral, confusion of those effects is improbable.

As the Hall effects are of such diverse origin, yet appear as the same signal type, it is important to discern these different phenomena. One possibility is investigating the scaling relation between the transversal and longitudinal conductivities. For example, no direct relation should exist in the intrinsic case while skew-scattering has a linear relation in super-clean metals. Further insight can be gained by modifying the impurity density as the side-jump

contribution becomes increasingly important in the strong scattering case dominating the skew scattering impact. In contrast, the intrinsic contribution does not depend on the carrier lifetimes at all since it is independent of scattering. Another fundamental difference of the intrinsic term is its dependence on all occupied states in contrast to the usual Fermi surface integrals.

4.1.1 Topological Hall effect

The topological Hall effect (THE) causes another distinctively different Hall current whose origin is the formation of skyrmions [9, 41, 101]. Due to its similarity to the main topic of this thesis—the topological spin Hall effect—this section describes its origin and properties in more detail.

A sensible first definition of the THE is that it is the remaining Hall effect after deducing the OHE and AHE from a skyrmion system. Thus, another THE term is added to Eq. 4.3:

$$\rho_{xy} = \rho^{O}_{xy} + \rho^{A}_{xy} + \rho^{T}_{xy}. \tag{4.5}$$

A rough approximation of the THE term is $\rho^{T}_{xy} = PR^{O}B_{eff}$ closely related to the ordinary Hall effect. Indeed, the OHE constant R^{O} is retained while the emergent replaces the external magnetic field and the spin polarization P is added [3, 102]. This expression is particularly popular among experimentalists, as R^{O} has to be measured anyways when deducting the OHE from the transversal resistivity. By approximating P and the averaged emergent magnetic field as B_{eff}, an estimate for the THE is readily accessible. Through this effect the formation of skyrmions can be validated whose density is subsequently estimated experimentally by relation to the emergent magnetic field magnitude.

Theoretically, the THE is a charge Hall response caused by the topological properties of skyrmions. Intuitively, the impact of skyrmions on traversing electrons can be understood by 2 effects: Firstly, the spins stay aligned with the magnetic texture, i.e. the spin follows the skyrmion shape, and, secondly, the electrons get redirected as if influenced by a magnetic field. These effects are mathematically described in the magnetic texture wave-packet equations of motion (Eq. 3.18). As the dynamics are equivalent to those of applied fields (Eq. 3.10), the consideration of the THE as analogue to the OHE caused by the applied magnetic field is reasonable. The only difference is the spin-dependence of the emergent magnetic field in contrast to the external magnetic field's spin-independent. Using the Boltzmann formalism in combination with the ferromagnetic wave-packet equations of motion, the resulting conductivities are expressible through Eq. 4.35. The difference to the ordinary Hall effect is the $(\boldsymbol{s}\cdot\boldsymbol{n})$-term describing the spin-dependence of the emergent magnetic field which is explicitly included on the level of the equation of motion. Hence, the Hall constants of the OHE and THE are similar, but their respective spin-resolved contributions have to be added or subtracted respectively. Yet, their similarity in derivation and approximately similar magnitude explains the usage of PR^{O} as R^{T} at the beginning of the section. The Hall constants even become equivalent in case of fully polarized Fermi surface states with only one spin character, but such a setup is rare in reality. Similar to the equation for the ordinary Hall constant R^{O}

(Eq. 4.4), the THE's Hall constant R^T can be calculated according to

$$R^T = -\frac{\sigma_{xy}^T}{\sigma_{xx}\sigma_{yy}\overline{\mathcal{B}}}, \tag{4.6}$$

where the transversal and longitudinal conductivities from Sec. 4.4.1 and the spatially averaged emergent magnetic field $\overline{\mathcal{B}}$ is used. The additional resistivity is thus:

$$\rho_{xy}^T = R^T\overline{\mathcal{B}}. \tag{4.7}$$

While the magnetic field causing the OHE is usually assumed to be homogeneous, the emergent magnetic field is inhomogeneous and given by the skyrmion shape (eg. Fig. 2.5). As the emergent magnetic field (Eq. 3.16) is the integrand of the real-space integral defining the skyrmion number (Eq. 2.1), the emergent magnetic field, and hence the magnitude of the THE, scales with the skyrmion (area) density. Most concurrence with the OHE should be found in skyrmion lattices where $\boldsymbol{\mathcal{B}}$ is repeated periodically which thus effectively mimics an homogeneous field on larger scales.

The topological aspect of the THE comes from the topological distinction of skyrmions from trivial magnetic structures. In an usual sample several skyrmions are probed which all give a contribution so that the THE transport signal does not verify or negate the presence of a single skyrmion but probes their density. Usually, it is difficult to see quantized differences due to the large number of skyrmions in common samples. This is a profound difference to the phases associated to reciprocal-space topological invariants where only a small number of distinct states exists whose classification extend over the entire domain. Most comparable are probably Chern insulators (QAHE) which also have a $\mathbb{Z}$ topological class so that many edge states could constitute the final transport response. However, the QAHE's quantization levels are independent of small bandstructure details which is not the case for the THE. Instead, many variable prefactors vary the magnitude of the THE due to its Fermi surface property and lifetime-dependence (Eq. 4.35). It should be noted that the emergent magnetic field scales quadratically with skyrmion lattice constant as the emergent magnetic field is proportional to the number of skyrmion per area. As skyrmion sizes can vary over orders of magnitude depending on the magnetic parameters, extremely different emergent magnetic field magnitudes can be obtained.

The THE has been successfully used to validate the existence of skyrmion lattice phases. At first, the phase space extent of the skyrmion lattice was measured successfully in MnSi [9, 103]. Subsequently, great agreement between experiments and theoretical predictions for the THE was shown for $Mn_{1-x}Fe_xSi$ and $Mn_{1-x}Co_xSi$ alloys. There, the transversal resistivity and magnetization were measured crossing the skyrmion lattice phase whose formation is indicated by large changes of ρ_{xy} at the boundary. In order to quantify the THE, the other Hall effects have to be approximated. The OHE is estimated from the high temperature limit and the AHE is captured by interpolation from the field-polarized state to the zero-field state. Thereby, a rough disentanglement of the THE from the general signal is possible.

Transport calculations based on the semiclassical formalism (Sec. 4.4.1) utilized in this thesis were done in Ref. [41]. Comparison of the theoretical predictions with the measurements show great agreement for a skyrmion lattice with a wave-length of about 120 Å. Further

examined materials include $Mn_{1-x}Fe_xGe$ [104] and $Fe_{1-x}Co_xGe$ [105]. In the last case the agreement between the semiclassical formalism and the experimental measurements is not convincing although the adiabatic requirement of having large scale skyrmions is supposedly fulfilled.

In this thesis the THE is understood as being caused by the real-space topology, but a method exists in which the magnetic texture is transfered into reciprocal space so that the whole magnetic unit cell has to be considered in the Hamiltonian diagonalization (Sec. 4.3) [106]. In that case the real-space topology is necessarily trivial. This procedure requires mean free paths larger than the magnetic lattice size and is accordingly valid and applicable only for small magnetic unit cells. In that interpretation the THE is very similar to the intrinsic AHE with the difference that SOC is not required on the bandstructure level, the spin chirality causes non-vanishing contributions instead. Hence, SOC is only required to obtain magnetic interactions exhibiting skyrmions as described in Sec. 2.2.1. Furthermore, the Boltzmann lifetime τ does not enter the Hall conductivities due to their similarity to the AHE which is a huge difference to the τ^2-dependent σ_{xy} of the semiclassical wave-packet approach.

When considering the AHE as being proportional to the magnetization, the presence of skyrmions has to change the AHE response as they decrease the overall magnetization. This effect should be distinguished from the THE but makes experimental distinction relying on the presence or absence of skyrmions difficult.

The most solid experimental demonstration of the THE would be a resistivity measurement with simultaneous magnetic imaging tracking the skyrmions. In Ref. [107] the skyrmions of multilayer systems are simultaneously imaged via magnetic force microscopy which reveals a distinct Hall signal proportional to the number of measured skyrmions. But as the skyrmions are on the order of 100 nm, the corresponding emergent magnetic field is too small to have significant impact on the transport measurement. Hence, the transversal transport effect of the skyrmions is dominated by the AHE. Additionally, the magnetic texture was imaged through scanning transmission x-ray microscopy using the x-ray magnetic circular dichroism to track skyrmions of similar size in Ref. [102]. Again, a distinct dependence on the number of skyrmions is found, but the THE is orders of magnitude too small to explain the strong Hall response. In Refs. [52] and [108] Ir/Fe/Co/Pt-multilayers skyrmion structures are measured by X-ray microscopy or magnetic force microscopy and compared to consecutive transport measurement. As skyrmions are exhibited in a large temperature range up to room temperature, it is possible to relate the Hall signals to the skyrmion density of the strongly disordered and dilute skyrmion phase with radii down to 60 nm. When treating apparent line domains as queues of skyrmions separated on the imaging resolution scale, quantitative agreement between transport and imaging is found, but the THE signal is still 2 orders of magnitude too small.

A magnetic imaging technique on much smaller scales than previously employed with concurrent Hall measurements would be necessary to find convincing evidence through such an experiment, although even there the distinction into AHE and THE would be difficult as evident from the AHE dominance in large skyrmions. Still, from the technological point of view those experiments clearly show the possibility to measure skyrmions through their Hall response so that electronic detection as necessary for racetrack applications are feasible even with vanishing THE.

While parts of this systematic theoretical underestimation of the THE can be attributed to the experimentalist's usage of R^O instead of R^T and the strong impact of the AHE subtraction with relatively small remainders, this mismatch between theory and experiment indicates that the adiabatic formalism with its clear emergent magnetic field may be inapplicable to the considered systems, especially with large SOC as above. Instead, further corrections or other methods including the SOC's impact differently might have to be applied for respective systems. Nevertheless the established understanding of the THE in the semiclassical picture is valid in other systems so that its evaluation and that of the topological Spin Hall effect in antiferromagnetic skyrmions (Sec. 4.2.1) still provide important theoretical predictions.

4.2 Spin Hall effect

Some 20 years ago, the spin Hall effect (SHE) was proposed as a relative of the anomalous Hall effect in paramagnetic materials [109]. Instead of charge currents $\boldsymbol{j}$, spin currents

$$\boldsymbol{j}^{\boldsymbol{s}} = \frac{\langle \boldsymbol{s} \cdot \boldsymbol{v} + \boldsymbol{v} \cdot \boldsymbol{s} \rangle}{2} \tag{4.8}$$

are generated. The bracket denotes the expectation value of the symmetrized spin-velocity product. In contrast to the charge current, $\boldsymbol{j}^{\boldsymbol{s}}$ is a tensorial quantity since it depends on the current and the spin direction. In cubic systems the SHE generates such spin currents perpendicular to charge currents:

$$\boldsymbol{j}^{\boldsymbol{s}} = \alpha_{SH} \boldsymbol{j} \times \boldsymbol{s}. \tag{4.9}$$

α_{SH} is the spin Hall angle which denotes the charge to spin conversion and thus the SHE "strength". As the charge currents may be described through the longitudinal conductivity and applied electric fields, this effect is classified as a Hall effect. Additional to the usual creation of transversal currents, another feature arises due to having different physical quantities as cause and result. Namely, the very same mechanism inversely converts spin current into transversal charge currents. This phenomenon is called inverse spin Hall effect (ISHE).

The SHE has been measured in non-magnetic materials where the anomalous Hall effect vanishes. One source of the SHE are the spin-dependent scattering rates of the extrinsic AHE which persist despite the cancellation of the charge currents. Analogously, the charge currents caused by the intrinsic AHE vanish but the corresponding spin currents add up due to the additional sign change. In principle, the same effect appears in materials exhibiting the anomalous Hall effect, but there the up- and down-states do no cancel each other so that spin-polarized charge currents are expressed instead of a pure spin currents. Thus, the physical mechanisms creating the spin and anomalous Hall effect are identical [110]. In general, the SHE is much less studied than its charge counterpart, mostly due to its much more recent discovery, yet with respect to recent developments in spintronics further understanding is necessary [15].

One further well-understood contribution is the quantum spin Hall effect (QSHE) related to the quantum anomalous Hall effect [111]. Instead of spin split bands, the QSHE is present in spin-degenerate systems with a band gap at the Fermi energy. The Chern number is not

well-defined any more for the degenerate case, but analogous topological quantities can be defined such as the spin Chern number or the equivalent $\mathbb{Z}_2$ invariants in case of time-reversal symmetry. As deducible from its name, the $\mathbb{Z}_2$ invariant allows only 2 topologically distinct phases, the trivial and the nontrivial. In the non-trivial phase helical (i.e. polarized with opposite spin at opposite $\boldsymbol{k}$) edge states emerge and a transverse quantized spin conductivity is exhibited. Three-dimensional versions of this effect exists where different high-symmetry planes in the Brillouin zone carry topological invariants leading to a classification into weak and strong topological insulators [112]. Furthermore, the crystalline topological insulators exist where the classification according to time-reversal symmetry is replace by crystalline symmetries [113]. In contrast to the charge analogue, the topological classification does not only depend on the band-structure topology but also on the additional symmetries constituting the invariant. Hence perturbations changing that symmetries may also change the topological invariants or render them meaningless without band-gap closure.

A reason for the long delay between the discovery of the Hall and the spin Hall effect is the relative difficulty in measuring spin currents in contrast to conventional Hall measurements. Nowadays, several measuring possibilities exist: The spin accumulation can be directly measured by Kerr microscopy while the spin torques exhibited by the spin currents on the magnetization of adjacent ferromagnets provide indirect means of detection. Another possibility is the usage of the inverse spin Hall effect of well characterized materials so that induced spin currents can be measured by electric means [110].

4.2.1 Topological Spin Hall effect

The cancellation of the THE leads to the topological Spin Hall effect (TSHE) which is similar to the cancellation of the charge currents of the AHE that leads to the SHE [21, 114]. As the THE is a Fermi surface property, it is very unlikely to have a non-degenerate bandstructure where all the spin-up and -down, electron- and hole-like contributions cancel each other in the vicinity of the Fermi energy—or any other small energy domain. Instead, spin-degenerate states provide a feasible method to cancel the transversal charge currents. In that case each states' charge contributions immediately cancel with its spin reversed pair due to the spin-dependence of the emergent magnetic field. Such twofold degenerate states with well-defined spins are common in antiferromagnets (depending on the crystalline symmetries). Hence, the THE of ferromagnetic skyrmions is expected to become the TSHE when investigating degenerate antiferromagnetic skyrmions [21]. Note that having an antiferromagnet does not enforce those twofold degenerate states per se, hence antiferromagnetic skyrmions can exhibit the THE in general, especially if the sublattice symmetry is broken [115]. In this thesis antiferromagnetic skyrmions are always considered to be twofold degenerate unless specified otherwise.

Naively, the TSHE's spin current can be estimated as twice the ferromagnetic skyrmion's charge Hall current with an additional $\hbar/e$-prefactor as the antiferromagnetic skyrmions can be understood as 2 copies of a ferromagnetic skyrmion of which one is spin reversed [**Buhl**]. Since the ferromagnetic THE has been calculated using the wave-packet equations of motions, the degenerate wave-packet formalism of Sec. 3.2.1 has to be applied in case of collinear antiferromagnets for more rigorous estimations. The derivation of the resulting Boltzmann

conductivities with these dynamics is given in Sec. 4.4.2. Nevertheless, the interpretation as two spin-reversed, independent quantities is still instructive as it corresponds to the limit with vanishing coupling ($\xi \to 0$) in which case Eq. 4.38 is applicable.

Analogous to the ferromagnetic case, the topological Hall constant R^T and the topological spin Hall constant R^{TS} are suitable to quantify the transport properties. In the $\xi = 0$ and the singly degenerate case, it is possible to dividing the usual THE term (Eq. 4.6) into the spin-up and -down contributions [41]:

$$R^T = -\frac{\sigma_{xy}^{T,\uparrow} + \sigma_{xy}^{T,\downarrow}}{\sigma_{xx}\sigma_{yy}\overline{\mathcal{B}}}. \tag{4.10}$$

For degenerate antiferromagnetic materials the THE vanishes as the parameters comprising the conductivity, such as group velocity and effective masses, are the same for degenerate states while the emergent magnetic field's spin-dependence changes the sign, $\sigma_{xy}^{T,\uparrow} = -\sigma_{xy}^{T,\downarrow}$. On the contrary, in the topological spin Hall constant defined as:

$$R^{TS} = -\frac{\sigma_{xy}^{T,\uparrow} - \sigma_{xy}^{T,\downarrow}}{\sigma_{xx}\sigma_{yy}\overline{\mathcal{B}}}. \tag{4.11}$$

Hence, both spin bands contribute constructively and thereby constitute the TSHE.

This relation is not applicable if $\xi \neq 0$ as the spin character of each wave-packet changes throughout the iteration (Eq. 3.38a) so that a clear distinction into spin-up and -down states is impossible. Thus, the wave-packet spin dynamics have to be directly included into the transport calculations obstructing the simple picture with 2 states of opposite spin. Hence, Eq. 4.44 has to be employed so that the topological spin Hall constant becomes:

$$R^{TS} = -\frac{\sigma_{xy}^{(2,s_z)}}{\sigma_{xx}\sigma_{yy}\overline{\mathcal{B}}}, \tag{4.12}$$

where $\sigma_{xy}^{(2,s_z)}$ describes the time- and space-averaged spin Hall conductivity including the momentary spin direction in the local frame during iterations from initial spin-up and -down states [21]. Explicit expressions for $\sigma_{xy}^{(2,s_z)}$ are derived in Sec. 4.4 and numerical details for its calculations are covered in Sec. 5.

4.3 Transport formalism

A multitude of methods exists that are suitable for estimating transport properties such as the Hall effects described above [116]. Depending on the physical setup, they can be more or less applicable. Three major methods exist for theoretically calculating the anomalous Hall effect: the Boltzmann [98], the Kubo [117] and the Keldysh formalism [118]. In the remainder of this thesis the Boltzmann formalism is used to estimate the T(S)HE, hence the Boltzmann case is this section's main topic. But firstly the latter 2 frameworks are shortly summarized followed by detailed derivations of the former method used to calculate the T(S)HE in this thesis

One major disadvantage of the Boltzmann formalism is that it is not quantum-mechanical but semi-classical. In order to include full quantum mechanics, the Kubo formalism can

be used for calculating linear responses [119]. There, the conductivities are related to the current-current correlation function so that the different Hall effects can be calculated via the Kubo-Streda formula expressed in terms of advanced and retarded Greens functions. This formalism is greatly suited for the disorder driven components, i.e. extrinsic AHE, as it is based on Greens functions which can readily include disorder through diagrammatic expansions and solution of the Dyson equation. Yet, the intrinsic AHE is automatically included as well through the zeroth order diagrams. The THE enters the Kubo-Streda equation similarly. The Keldysh formalism is a further generalization where non-equilibrium quantum states are used. Hence, more Greens functions are necessary and the diagrammatic technique becomes more complicated [118].

Specifically the transport fingerprint of skyrmions, and magnetic structures in general, can be calculated using the Landauer-Büttiker formalism [120]. Semi-infinite leads are attached in Hall bar geometry to a tight-binding system modeling skyrmionic textures. Via Greens functions the transmission coefficients between the leads are obtained that directly relate to the topological Hall angles and thus to the THE [114]. This method shows the emergence of the THE even without adiabaticity which is required when using wave-packet dynamics and allows to study its stability with respect to disorder effects [121]. This method has been applied to antiferromagnetic skyrmions exhibiting the TSHE and used to study the feedback of the spin currents to the texture via the non-adiabatic torque [72]. So far however, this method is restricted to simple Hamiltonians characterizing the underlying material thus preventing its application to realistic systems.

Another method for calculating the THE utilizes the Kubo equation directly [106, 122]. By treating the magnetic unit cell as unit cell for the entire Hamiltonian, all real-space topology and skyrmion characteristics are transformed into the reciprocal space. Thereby, the THE is effectively described as the intrinsic part of the AHE. Those Hamiltonians and the corresponding Berry curvature can be numerically solved for small system sizes and simple models. Since the Brillouin zones is small and many bands are folded back, a complicated Berry curvatures emerges which results in large cumulative conductivities. Ribbons of such structures exhibit edge states as expected for Chern insulators [106], but those edge states are seldom the only states at the Fermi energy which obstructs a quantized versions of the THE. Instead, many bands can contribute and many partially filled bands will influence the intrinsic contributions especially in the case of metals. This method was applied to the case of antiferromagnetic skyrmions as well [115]. In that study the bands are split since the antiferromagnetic pairs have slightly different spin directions due to the consideration of intrinsic antiferromagnetic skyrmions and the computational restriction to small skyrmions. Hence, the $\mathcal{U}(1)$ Berry curvatures can be applied similar to the ferromagnetic case. Using the Kubo equation, the expected emergence of the THSE for symmetric and THE for asymmetric AFM skyrmions is validated thus providing a reasonable computational scheme for the limit of small skyrmions [115].

Since the Boltzmann formalism is a well-established method several introductions can be found in the scientific literature [98, 123, 124]. This section reviews the basic properties to provide a basis for the Hall effect equations of Sec. 4.4.

4.3.1 Boltzmann formalism

The method used in this thesis, the Boltzmann formalism, is described in the following. In general, it is applied in various branches of physics and describes the evolution of distributions under external forces, diffusion, and scattering. Originally, it was developed to describe the progression of thermodynamic systems but since has been applied to a multitude of different physical problems. Here, it is used to extract the electronic transport properties from the evolution of the electron distributions in case of applied fields and scattering.

The Boltzmann equation is a so-called "semi-classical" equation which means that it combines classical with quantum-mechanical concepts. The classical part comprises the evolution between scattering which itself is treated quantum-mechanically in general. This necessity of intermediate classical validity defines this formalism's range of applicability as $\boldsymbol{k}$ has to be a sensible quantity for describing the evolution between the scattering events. Hence, the product of the material's Fermi wave vector with the mean free path l should be much larger than 1, i.e. $\boldsymbol{k}_F l \gg 1$. Here, the evolution between scattering is described by the wave-packet equations of motion (Sec. 3) while the scattering is treated in constant relaxation time approximation—a most simplistic choice.

The huge advantage of the Boltzmann formalism is the straightforward procedure to obtain expressions compared to the previously mentioned alternatives. Usually, the different terms can be interpreted immediately with respect to their physical origin. Furthermore, multiple drastic simplifications are possible so that the formalism can be applied to more complicated basic systems than other computational approaches.

The main quantity in the Boltzmann formalism is the distribution function $f(\boldsymbol{r}, \boldsymbol{k}, t)$ which, in this case, describes the electron occupation in real and reciprocal space. The following derivations of applicable simplifications of the Boltzmann equation loosely follow Ref. [125]. In general, the electron distribution is susceptible to a multitude of physical quantities such as applied electromagnetic fields, scattering, thermal gradients, or even variations in the chemical potential. The Boltzmann equation states that the change of f with respect to all those possible sources is implicitly described through their spatial, orbital, and temporal dependence:

$$\frac{df}{dt} = \frac{\partial f}{\partial \boldsymbol{r}}\frac{d\boldsymbol{r}}{dt} + \frac{\partial f}{\partial \boldsymbol{k}}\frac{d\boldsymbol{k}}{dt} + \frac{\partial f}{\partial t}. \tag{4.13}$$

All different causes of disturbance have to be modeled after which a solution of the nonlinear integro-differential equation for f has to be found. Several simplification have been proposed over the years due to the complicated structure of the general Boltzmann equation. In the following, the most blunt approximations are used to reach a basic understanding of the emerging transport phenomena caused by magnetic structures.

The goal is to yield a new equilibrium distribution incorporating perturbations caused by the external fields. Due to the equilibrium condition, the last term of Eq. 4.13 vanishes. Afterwards the Boltzmann distribution function is expanded around the original Fermi-Dirac distribution f_0:

$$f = f_0 + \delta f. \tag{4.14}$$

δf is the perturbation of f caused by external fields and has to be approximated in the following. Since we have a homogeneous system, the first term of the Boltzmann equation

describing diffusion due to spatial inhomogeneities is neglected.

Hence, the Boltzmann equations simplifies to

$$\left(\frac{d(f_0+\delta f)}{dt}\right)_{scatter} = \frac{\partial(f_0+\delta f)}{\partial \boldsymbol{k}}\frac{d\boldsymbol{k}}{dt}, \tag{4.15}$$

when restricting the perturbations from f_0 to scattering terms and the $\dot{\boldsymbol{k}}$ part. The term on the right describes the influence of the applied external electric field via the $\dot{\boldsymbol{k}}$-term as appearing in the equation of motion (e.g. Eq. 3.19). The left term covers the scattering via momentum transfer which counteracts the constant acceleration of the $\boldsymbol{E}$ field resulting in the new equilibrium. Many mechanisms could be included into the scattering term as for example the AHE, caused by scattering effects such as skew-scattering and side-jump, which would complicate the transport calculation significantly [98]. In general, the scattering term is described via scattering rates from occupied to unoccupied states and vice versa as determined by the distribution f. When using the relaxation time approximation, all those scattering rates are approximated as:

$$\left(\frac{d(f_0+\delta f)}{dt}\right)_{scatter} = -\frac{\delta f}{\tau}, \tag{4.16}$$

where τ is the $\boldsymbol{k}$-dependent, averaged relaxation time. Hence, only scattering terms are included that result in a relaxation towards the Fermi-Dirac distribution. As the scattering rates depend on the initial and final $\boldsymbol{k}$, already the assumption of $\tau(\boldsymbol{k})$ is an approximation. In the remainder of this thesis the even rougher constant relaxation time approximation is used which neglects τ's $\boldsymbol{k}$-dependence altogether. When instead keeping the $\boldsymbol{k}$-dependence, the following equations are modified slightly as τ appears only as linear and quadratic prefactor in the following derivations leading to the (spin) conductivities. Yet, a further term would arise from the $\boldsymbol{k}$-derivatives leading to Eq. 4.19 which would give corrections to the T(S)HE. Accurate predictions for τ including its $\boldsymbol{k}$-dependence, and furthermore $\boldsymbol{k}_{in}$- and $\boldsymbol{k}_{out}$-dependent scattering rates, can be obtained for example from Korringa–Kohn–Rostoker *ab-initio* calculations for specific defects in the studied materials. Those have the potential to significantly increase the accuracy of the (spin) conductivity prediction. In order to minimize the dependence on τ, and thus the impact of possible $\boldsymbol{k}$-dependent modifications, the τ independent topological (spin) Hall constants (Eq. 4.6) are ultimately used to characterize the T(S)HE.

The distribution perturbation can thus be expressed as

$$\delta f = -\tau\frac{\partial(f_0+\delta f)}{\partial \boldsymbol{k}}\cdot\frac{d\boldsymbol{k}}{dt}, \tag{4.17}$$

when assuming the constant relaxation time approximation in the expanded Boltzmann equations and keeping only $\dot{\boldsymbol{k}}$ and scattering parts. As δf is assumed to be small compared to f_0, it can be iteratively solved using this above equation expanded in orders of τ. The first-order term is conveniently expressed as

$$\delta f^{(1)} = -\tau\frac{\partial f_0}{\partial \boldsymbol{k}}\cdot\frac{d\boldsymbol{k}}{dt} = -\tau\frac{\partial f_0}{\partial \epsilon}\frac{\partial \epsilon}{\partial \boldsymbol{k}}\cdot\frac{d\boldsymbol{k}}{dt}. \tag{4.18}$$

Notably, the first correction to f_0 is a Fermi surface property due to the partial $\boldsymbol{k}$-derivative of the distribution function originating in the Boltzmann equations. This agrees nicely with the assumption that the distribution function changes only marginally away from f_0. The distribution function correction in second order in τ is obtained by inserting $\delta f^{(1)}$ into the right side of Eq. 4.17:

$$\delta f^{(2)} = -\tau \frac{\delta f^{(1)}}{\partial \boldsymbol{k}} \cdot \frac{d\boldsymbol{k}}{dt} = \tau^2 \frac{\partial f_0}{\partial \epsilon} \frac{\partial \left(\frac{\partial \epsilon}{\partial \boldsymbol{k}} \cdot \frac{d\boldsymbol{k}}{dt} \right)}{\partial \boldsymbol{k}} \cdot \frac{d\boldsymbol{k}}{dt}. \tag{4.19}$$

A $\partial_{\boldsymbol{k}} \tau$ term arises in general but vanishes here due to the constant relaxation time approximation. Therefore, the equilibrated electron distribution caused by simplest scattering counteracting an applied $\boldsymbol{E}$ field can be approximated by:

$$f \approx f_0 - \tau \frac{\partial f_0}{\partial \epsilon} \frac{\partial \epsilon}{\partial \boldsymbol{k}} \cdot \frac{d\boldsymbol{k}}{dt} + \tau^2 \frac{\partial f_0}{\partial \epsilon} \frac{\partial \left(\frac{\partial \epsilon}{\partial \boldsymbol{k}} \cdot \frac{d\boldsymbol{k}}{dt} \right)}{\partial \boldsymbol{k}} \cdot \frac{d\boldsymbol{k}}{dt}. \tag{4.20}$$

After a short consideration about means of obtaining observables with this description, the above distributions function is used in combination with the equations of motion to calculate charge and spin currents (Sec. 4.4).

The expansion of f in second order of τ and the following direct application of the equations of motion (Seq. 4.4) is not the only possibility to describe the transport impact of skyrmions through the Boltzmann equation. In fact, one disadvantage of the following derivations is the necessity for adiabaticity. The wave-packet's strict alignment with the magnetic texture requires strong exchange coupling especially in the ferromagnetic case. An alternative approach valid for weak exchange interactions still utilizing the Boltzmann equation has been developed to describe dilute magnetic semiconductors [126]. There, the explicit scattering from skyrmions in combination with non-magnetic impurities is investigated in the limit of impurity densities much larger than the skyrmion density. Then, the skyrmions cause asymmetric differential cross sections so that the asymmetric scattering creates the THE even for non-polarized electrons. Accordingly, the effect of the topological non-triviality is included in left side of Eq. 4.16 and not explicitly in the evolution of $\dot{\boldsymbol{r}}$. This method even uncovers oscillatory behavior between charge and spin responses relative to exchange-interaction and skyrmion size variations [127].

4.3.2 Obtaining observables

While the Boltzmann distribution function will be used to obtain observables, it is instructive to first consider evaluation of observables based only of the wave-packet formalism. In case of Bloch waves an observable $\boldsymbol{O}$ is calculated according to

$$\boldsymbol{O} = \sum_{n\boldsymbol{k}} f_{n\boldsymbol{k}} \boldsymbol{O}(\boldsymbol{k}), \tag{4.21}$$

where the $\boldsymbol{k}$-sum becomes a simple $\boldsymbol{k}$-integral over the Brillouin zone divided by its volume [78]. The phase-space is larger in case of wave-packet dynamics as the real space has to be included as well. The semiclassical limit for calculating a general observable becomes:

$$\boldsymbol{O}(\boldsymbol{R}) = \int d\boldsymbol{k} d\boldsymbol{r}\ D(\boldsymbol{r}, \boldsymbol{k}) f(\boldsymbol{r}, \boldsymbol{k}) \boldsymbol{O}(\boldsymbol{k}, \boldsymbol{r}) \delta(\boldsymbol{r} - \boldsymbol{R}), \tag{4.22}$$

when neglecting finite wave-packet size contributions. D is the density of states replacing the previous Brillouin zone volume division. As $\boldsymbol{k}$ and $\boldsymbol{r}$ are not a canonical set in general, the density of states gets modified so that the covered phase-space volume remains conserved, i.e. the Liouville theorem is satisfied. This correction is expressed as:

$$D = \frac{1}{(2\pi)^d}\sqrt{\det\left(\overleftrightarrow{\Omega} - \overleftrightarrow{I}\right)} \tag{4.23}$$

with

$$\overleftrightarrow{\Omega} = \begin{bmatrix} \Omega_{\boldsymbol{rr}} & \Omega_{\boldsymbol{rk}} \\ \Omega_{\boldsymbol{kr}} & \Omega_{\boldsymbol{kk}} \end{bmatrix}, \quad \overleftrightarrow{I} = \begin{bmatrix} 0 & \mathbb{1} \\ -\mathbb{1} & 0 \end{bmatrix}, \tag{4.24}$$

and is a necessary modification when treating full wave-packet dynamics. As long as either $\Omega_{\boldsymbol{rr}} = 0$ or $\Omega_{\boldsymbol{kk}} = 0$, the diagonal components of $\overleftrightarrow{\Omega}$ do not enter D so that the usual $D = (2\pi)^{-d}$ is recovered in case of $\Omega_{\boldsymbol{rk}} = 0$. More general, the curvature dependent parts are usually smaller than 1, hence the square root of Eq. 4.23 can be expanded as $1 + c \cdot x + \ldots$ so that $D = (2\pi)^{-d}$ is a sensible, albeit rough, approximation.

Several physical effects have been derived directly using this approach [78, 128] and direct calculation of the currents using that formalism is possible in principle. Starting from an initial distribution, the wave-packet's phase-space evolution would have to be tracked directly using the equations of motion including the applied fields and the modified density of states. Scattering would have to be included in the evolution as well, hence direct application is impracticable.

The Boltzmann equation provides a more feasible approach where the reciprocal-space variation is directly included on the Boltzmann level so that the phase-space of the actual evolution is reduced to the real space only. Using the approximate equilibrium distribution of the Boltzmann equation (Eq. 4.20), a general observable is given as:

$$\boldsymbol{O} = \frac{V}{(2\pi)^d}\int_{Bz.} d\boldsymbol{k}\ (f_0(\boldsymbol{k}) + \delta f^{(1)}(\boldsymbol{k}) + \delta f^{(2)}(\boldsymbol{k}))\boldsymbol{O}(\boldsymbol{k}). \tag{4.25}$$

V is the real-space unit-cell volume which usually cancels with the $1/V$-factor from the real-space integral. Charge currents are calculated as the expectation value of the wave-packet velocity

$$\boldsymbol{j} = \langle \dot{\boldsymbol{r}} \rangle \tag{4.26}$$

similar to its spin current analogue (Eq. 4.8). Note that the units are chosen so that $e = \hbar = 1$ throughout this thesis unless otherwise stated so that different e- and $\hbar$- dependent prefactors for charge and spin currents appear only in different atomistic units for the transport quantities. As velocity and spin commute in this semiclassical treatment using the equations of motion, the currents take the form:

$$\boldsymbol{j} = \frac{V}{(2\pi)^d}\int_{Bz.} d\boldsymbol{k}\ (f_0(\boldsymbol{k}) + \delta f^{(1)}(\boldsymbol{k}) + \delta f^{(2)}(\boldsymbol{k}))\dot{\boldsymbol{r}}, \tag{4.27a}$$

$$\boldsymbol{j}^{s_\alpha} = \frac{V}{(2\pi)^d}\int_{Bz.} d\boldsymbol{k}\ (f_0(\boldsymbol{k}) + \delta f^{(1)}(\boldsymbol{k}) + \delta f^{(2)}(\boldsymbol{k}))s_\alpha\dot{\boldsymbol{r}}. \tag{4.27b}$$

As the skyrmion lattice introduces a spatial inhomogeneity, it is furthermore necessary to average over the magnetic unit cell. Hence, the observables still depend on the remaining wave-packet equations of motion ($\dot{\boldsymbol{s}}$ and $\dot{\boldsymbol{r}}$) while $\dot{\boldsymbol{k}}$ is already included in the static $\boldsymbol{k}$-distribution. Inserting the expression for δf (Eq. 4.20) and the respective equations of motion, more explicit expressions for the currents can be obtained. Expanding those expressions in $\boldsymbol{E}$ the (spin) Hall conductivities are obtained through

$$\sigma_{lm}^{(s)} = \frac{1}{V} \int d\boldsymbol{r} \left(\frac{\partial j_l^{(s)}}{\partial E_m} \right)_{\boldsymbol{E}=0}, \tag{4.28}$$

which includes only linear $\boldsymbol{E}$ term in accordance with Eq. 4.1. The next section derives the conductivities caused by δf using the ferromagnetic and the antiferromagnetic equations of motion.

Still, the Fermi-Dirac distribution part of the current equations gives rise to scattering-independent transport phenomena. When including a nonzero reciprocal-space topology, corresponding to the intrinsic AHE, non-vanishing transport contributions arise from $\boldsymbol{\Omega}_{\boldsymbol{k}}$ through $\dot{\boldsymbol{r}}$ even without magnetic fields of topological or external origin:

$$\boldsymbol{j} = \frac{V}{(2\pi)^d} \int_{Bz.} d\boldsymbol{k}\ f_0(\boldsymbol{k}) \boldsymbol{E} \times \boldsymbol{\Omega}_{\boldsymbol{k}}. \tag{4.29}$$

The Berry curvature vanishes in the collinear case without SOC, hence this contributions vanishes for most cases covered here. Further scattering independent transport effects caused by the magnetic texture arise from those terms if $\boldsymbol{\Omega}_{\boldsymbol{k}}$ and $\boldsymbol{\Omega}_{\boldsymbol{r}}$ do not vanish. Since those term vanish for most considered systems, the f_0 parts of Eq. 4.27 are omitted in the following to focus on the δf terms.

All lower order changes will occur near the Fermi energy since the distribution function starting point is of Fermi-Dirac type. Indeed, both $\delta f^{(1)}$ and $\delta f^{(2)}$ are proportional to $\partial_\epsilon f_0$ (Eqs. 4.18-4.19) which restricts the Brillouin zone integral to the Fermi surface. In the limit of vanishing broadening temperature, $\partial_\epsilon f_0$ can be replaced by a Dirac distribution which results in the transformation to a surface integral:

$$\begin{aligned} \int_{Bz} d\boldsymbol{k}\ \frac{\partial f_0}{\partial \epsilon} &= \int_{Bz} d\boldsymbol{k}\ \delta(E_F - \epsilon(\boldsymbol{k})) \\ &= \int_{Bz} d\boldsymbol{k}\ \frac{\delta(\boldsymbol{k} - \boldsymbol{k}_F)}{|\partial_{\boldsymbol{k}} \epsilon|} \\ &= \int_{S(E_F)} ds_{\boldsymbol{k}}\ \frac{1}{|\partial_{\boldsymbol{k}} \epsilon|}. \end{aligned} \tag{4.30}$$

Here, $S(E_F)$ denotes the iso-energy surfaces at the Fermi energy and $ds_{\boldsymbol{k}}$ is the corresponding differential for the Fermi surface integral. The Fermi surfaces are actually 1-dimensional lines as thin films with 2-dimensional Brillouin zones are considered in this thesis. The procedure to numerically evaluate the above integrals by interpolation of the Fermi iso-energy lines is described in Sec. 5.2.1.

4.4 Hall conductivity

In this section the Hall conductivities are extracted from the current expectation values using the distribution corrections (Eq. 4.20) and the equations of motion of the underlying systems. Explicit expressions are derived for the ferromagnetic and the collinear antiferromagnetic case keeping the linear terms in $\boldsymbol{E}$ in accordance with Eq. 4.28.

While the ferromagnetic case can be derived analogously to the ordinary Hall effect [8, 41], the related degenerate antiferromagnetic case is new and the evaluation of the resultant equations is the main effort of this thesis [21].

4.4.1 Ferromagnetic case

First, the wave-packet equations of motion of non-degenerate ferromagnets are considered assuming trivial reciprocal-space topology (Eq. 3.19). Their $\dot{\boldsymbol{k}}$-term is included into the δf parts which become:

$$\delta f^{(1)} = \tau \frac{\partial f_0}{\partial \epsilon} \sum_i \frac{\partial \epsilon}{\partial k_i} E_i, \tag{4.31a}$$

$$\delta f^{(2)} = \tau^2 \frac{\partial f_0}{\partial \epsilon} \sum_{ij} \frac{\partial^2 \epsilon}{\partial k_i \partial k_j} E_i \left(E_j + (\boldsymbol{s} \cdot \boldsymbol{n})(\dot{\boldsymbol{r}} \times \boldsymbol{\mathcal{B}})_j \right). \tag{4.31b}$$

The $\boldsymbol{\mathcal{B}}$-term vanishes in the first correction as:

$$\frac{\partial \epsilon}{\partial \boldsymbol{k}} \cdot (\dot{\boldsymbol{r}} \times \boldsymbol{\mathcal{B}}) = \frac{\partial \epsilon}{\partial \boldsymbol{k}} \cdot \left(\frac{\partial \epsilon}{\partial \boldsymbol{k}} \times \boldsymbol{\mathcal{B}} \right) = 0. \tag{4.32}$$

Since only linear terms in E are sought, the second correction simplifies to :

$$\delta f^{(2)} = \tau^2 \frac{\partial f_0}{\partial \epsilon} (\boldsymbol{s} \cdot \boldsymbol{n}) \sum_{ij} \frac{\partial^2 \epsilon}{\partial k_i \partial k_j} E_i \sum_{lm} \varepsilon_{lmj} \dot{r}_l \mathcal{B}_m. \tag{4.33}$$

Inserting the first-order correction $\delta f^{(1)}$ into the conductivity expression (Eq. 4.27) yields:

$$\sigma_{ij}^{(1)} = \frac{\tau}{(2\pi)^d} \int d\boldsymbol{k} \int d\boldsymbol{r} \frac{\partial f}{\partial E} \frac{\partial \epsilon}{\partial k_j} \dot{r}_i. \tag{4.34}$$

This is the normal current contribution which does not create a Hall effect due to its $i \leftrightarrow j$-symmetry. It describes the lowest order longitudinal conductivity which is used as denominator in the topological Hall constant expression (Eq. 4.4). The topological Hall effect appears in the second-order term:

$$\sigma_{ij}^{(2)} = \frac{\tau^2}{(2\pi)^d} \int_{Bz.} d\boldsymbol{k} \int d\boldsymbol{r} \frac{\partial f_0}{\partial \epsilon} (\boldsymbol{s} \cdot \boldsymbol{n}) \frac{\partial \epsilon}{\partial k_i} \sum_{lmn} \varepsilon_{lmn} \frac{\partial^2 \epsilon}{\partial k_j \partial k_n} \frac{\partial \epsilon}{\partial k_l} \mathcal{B}_m. \tag{4.35}$$

When assuming $\boldsymbol{E} = E\hat{\boldsymbol{e}}_2$ and $\boldsymbol{\mathcal{B}} = \mathcal{B}\hat{\boldsymbol{e}}_3$, the antisymmetric tensor ε_{lmi} can be evaluated explicitly so that the transversal conductivity becomes:

$$\sigma_{12} = \frac{\tau^2}{(2\pi)^d} \int_{Bz.} d\boldsymbol{k} \int d\boldsymbol{r} \frac{\partial f_0}{\partial \epsilon} (\boldsymbol{s} \cdot \boldsymbol{n}) \mathcal{B} \frac{\partial \epsilon}{\partial k_1} \left(\frac{\partial^2 \epsilon}{\partial k_2 \partial k_1} \frac{\partial \epsilon}{\partial k_2} - \frac{\partial^2 \epsilon}{\partial k_2 \partial k_2} \frac{\partial \epsilon}{\partial k_1} \right). \tag{4.36}$$

Since neither of the constituents depends on both $\boldsymbol{k}$ and $\boldsymbol{r}$, the integrals can be separated into:

$$\sigma_{ij}^{(2)} = \frac{\tau^2}{(2\pi)^d} \sum_{lmn} \varepsilon_{lmn} \left(\int d\boldsymbol{k} \; \frac{\partial f_0}{\partial \epsilon} \frac{\partial \epsilon}{\partial k_i} \frac{\partial \epsilon}{\partial k_l} \frac{\partial^2 \epsilon}{\partial k_j \partial k_n} \right) \left(\pm \int d\boldsymbol{r} \; \mathcal{B}_m \right). \tag{4.37}$$

The $\boldsymbol{k}$-integral includes the group velocities and effective masses at the Fermi surface which are easily accessible even for complicated Hamiltonians. The $\boldsymbol{r}$-integral is simply the emergent magnetic field's flux. The $(\boldsymbol{s} \cdot \boldsymbol{n})$-term has become ± 1, depending on whether the band is of spin-up or -down character, since the spin stays aligned with the magnetic texture in the ferromagnetic equations of motion.

The spin conductivity is calculated analogously by adding the spin in the local frame. Due to the permanent alignment, a further $\pm$-sign is obtained so that the final conductivity has exactly the same form as the charge conductivity caused by the ordinary Hall effect:

$$\sigma_{ij}^{s_z} = \frac{\tau^2}{(2\pi)^d} \sum_{lmn} \varepsilon_{lmn} \left(\int d\boldsymbol{k} \; \frac{\partial f_0}{\partial \epsilon} \frac{\partial \epsilon}{\partial k_i} \frac{\partial \epsilon}{\partial k_l} \frac{\partial^2 \epsilon}{\partial k_j \partial k_n} P_s \right) \left(\int d\boldsymbol{r} \; \mathcal{B}_m \right). \tag{4.38}$$

Furthermore the spin polarization P_s is included which decreases the magnitude of the transport in case of SOC relative to $P_s = 1$ without SOC. The alternative $\sigma_{ij}^{s_x}$ and $\sigma_{ij}^{s_y}$ vanish due to the spin's alignment with the z-axis.

4.4.2 Collinear antiferromagnetic case

Analogous to the previous ferromagnetic case, the transport properties of the TSHE of antiferromagnetic skyrmions is obtained by inserting the respective equations of motion (Eq. 3.40) into δf and σ. The first Boltzmann distribution correction is:

$$\delta f^{(1)} = \tau \frac{\partial f_0}{\partial \epsilon} \sum_i \frac{\partial \epsilon}{\partial k_i} (E_i + \sum_{lm} (1 - \xi^2)(\boldsymbol{s} \cdot \boldsymbol{n}) \varepsilon_{ilm} \dot{r}_l \mathcal{B}_m). \tag{4.39}$$

$\dot{\boldsymbol{r}}$ has an additional velocity term which is collinear to $\partial_{\boldsymbol{k}} \epsilon$ in simple models (e.g. Sec. 6 and Ref. [76]) but that does not vanish in the general $\delta f^{(1)}$ expression:

$$\delta f^{(1)} = \tau \frac{\partial f_0}{\partial \epsilon} \sum_i \frac{\partial \epsilon}{\partial k_i} \left(E_i + \frac{1}{2} \sum_{lm} (1 - \xi^2)(\boldsymbol{s} \cdot \boldsymbol{n}) \varepsilon_{ilm} ((\boldsymbol{s} \times \boldsymbol{n}) \cdot \dot{\boldsymbol{n}}) \frac{\partial \ln \xi}{\partial k_l} \mathcal{B}_m \right). \tag{4.40}$$

While the first component proportional to $\boldsymbol{E}$ is exactly analogous to the ferromagnetic case (Eq. 4.31), the $\mathcal{SU}(2)$-term complicates the calculation of the second distribution function correction term which causes the TSHE:

$$\begin{aligned} \delta f^{(2)} = \tau^2 \frac{\partial f_0}{\partial \epsilon} \sum_{ij} & \frac{\partial \left(\frac{\partial \epsilon}{\partial k_j} \left(E_j + (1 - \xi^2)(\boldsymbol{s} \cdot \boldsymbol{n}) \left(\sum_{lm} \varepsilon_{jlm} \dot{r}_l \mathcal{B}_m \right) \right) \right)}{\partial k_i} \times \\ & \times \left(E_i + (1 - \xi^2)(\boldsymbol{s} \cdot \boldsymbol{n}) \left(\sum_{lm} \varepsilon_{ilm} \dot{r}_l \mathcal{B}_m \right) \right). \end{aligned} \tag{4.41}$$

For convenience, the expression can be split into 2 parts, $\delta f^{(2)} = \delta f^{(2,1)} + \delta f^{(2,2)}$, since only terms proportional to $\boldsymbol{E} \cdot \boldsymbol{\mathcal{B}}$ are considered. $\delta f^{(2,1)}$ contains the electric field part to the derivative term multiplied with the $\mathcal{B}$-part of latter expression and $\delta f^{(2,2)}$ vice versa. Accordingly, $\delta f^{(2,1)}$ corresponds to the ferromagnetic expression (Eq. 4.33) while $\delta f^{(2,2)}$ is a correction only arising in the band-degenerate case. $\delta f^{(2,1)}$ still contains corrections due to the $\mathcal{SU}(2)$ character:

$$\delta f^{(2,1)} = \tau^2 \frac{\partial f_0}{\partial \epsilon} \sum_{ij} (1-\xi^2)(\boldsymbol{s}\cdot\boldsymbol{n}) \frac{\partial^2 \epsilon}{\partial k_j \partial k_i} E_j \sum_{lm} \varepsilon_{ilm} \dot{r}_l \mathcal{B}_m. \tag{4.42}$$

Analogously to the ferromagnetic case, this distribution correction yields the following Hall conductivity:

$$\sigma_{ij}^{(2,1)} \approx \frac{\tau^2}{(2\pi)^d} \int_{Bz.} d\boldsymbol{k} \int d\boldsymbol{r}\ \frac{\partial f_0}{\partial \epsilon} (1-\xi^2)(\boldsymbol{s}\cdot\boldsymbol{n}) \dot{r}_i \sum_{lmn} \varepsilon_{lmn} \frac{\partial^2 \epsilon}{\partial k_j \partial k_n} \dot{r}_l \mathcal{B}_m. \tag{4.43}$$

The only differences compared to Eq. 4.35 are the replacement of the group velocity by $\dot{\boldsymbol{r}}$ and the additional $(1-\xi^2)$-term decreasing the impact of the emergent magnetic field. Nevertheless, the evaluation of the Hall conductivity is significantly more complicated in the antiferromagnetic case as the wave-packet evolution in real space results in spin misalignment. Contrary to the ferromagnetic case, $\dot{\boldsymbol{r}}$ is real-space dependent and the spin deviates from the texture so that evaluation of the transport expression requires explicit solution of the remaining equations of motion. Yet, the ferromagnetic equations are recovered in the limit $\xi \to 0$ where the wave-packet equations of motion become identical. Since all states are degenerate and start with initially aligned and anti-aligned spins, the THE vanishes due to the spin-dependence of the emergent magnetic field's impact on the wave-packets dynamics as explained in Sec. 4.2.1.

The spin Hall conductivity

$$\sigma_{ij}^{(2,1,\boldsymbol{s}_\alpha)} \approx \frac{\tau^2}{(2\pi)^d} \int_{Bz.} d\boldsymbol{k} \int d\boldsymbol{r}\ \frac{\partial f_0}{\partial \epsilon} (1-\xi^2)(\boldsymbol{s}\cdot\boldsymbol{n}) \dot{r}_i s_{\alpha,\boldsymbol{n}} \sum_{lmn} \varepsilon_{lmn} \frac{\partial^2 \epsilon}{\partial k_j \partial k_n} \dot{r}_l \mathcal{B}_m \tag{4.44}$$

contains a further spin term, $s_{\alpha,\boldsymbol{n}}$, so that the corresponding TSHE survives. $\boldsymbol{s}_{\boldsymbol{n}}$ is the spin in the local frame as considered in the TSHE. $\sigma_{ij}^{(2,1,\boldsymbol{s}_\alpha)}$ also includes the spin polarization P_s which decreases the magnitude in case of SOC. This equation is the main contribution of the TSHE and thus the main quantity calculated in this thesis. The actual computational procedure for approximating $\sigma_{ij}^{(\boldsymbol{s}_\alpha)}$ is described in Sec. 5.

The second distribution correction complementary to Eq. 4.42 is

$$\begin{aligned} \delta f^{(2,2)} &= \tau^2 \frac{\partial f_0}{\partial \epsilon} \sum_{ij} \frac{\partial \left(\frac{\partial \epsilon}{\partial k_j} (1-\xi^2)(\boldsymbol{s}\cdot\boldsymbol{n}) \left(\sum_{lm} \varepsilon_{jlm} \dot{r}_l \mathcal{B}_m \right) \right)}{\partial k_i} E_i \\ &= -\frac{\tau^2}{2} \frac{\partial f_0}{\partial \epsilon} (\boldsymbol{s}\cdot\boldsymbol{n}) \sum_{ij} \sum_{lm} \varepsilon_{jlm} \frac{\partial \left(\frac{\partial \epsilon}{\partial k_j} (1-\xi^2) \left((\boldsymbol{s}\times\boldsymbol{n})\cdot\dot{\boldsymbol{n}} \right) \frac{\partial \ln \xi}{\partial k_l} \right)}{\partial k_i} E_i \mathcal{B}_m. \end{aligned} \tag{4.45}$$

As $\dot{\boldsymbol{n}} = \partial_t \boldsymbol{n} + (\dot{\boldsymbol{r}} \cdot \nabla)\boldsymbol{n}$ includes $\dot{\boldsymbol{r}}$, its $\boldsymbol{k}$ derivate does not vanish so that the product of 4 $\boldsymbol{k}$-dependent terms has to be differentiated. Due to the Levi-Civita symbol and $\partial_{\boldsymbol{k}}\xi \cdot \dot{\boldsymbol{k}} = 0$, several terms vanish so that only 2 terms remain:

$$\begin{aligned} \delta f^{(2,2,1)} = \tau^2 \frac{\partial f_0}{\partial \epsilon} \sum_{ij} (1-\xi^2)(\boldsymbol{s}\cdot\boldsymbol{n}) \frac{\partial^2 \epsilon}{\partial k_j \partial k_i} E_i \times \\ \times \sum_{lm} \varepsilon_{jlm} \left[-\frac{1}{2} \left((\boldsymbol{s}\times\boldsymbol{n})\cdot\dot{\boldsymbol{n}} \right) \frac{\partial \ln \xi}{\partial k_l} \right] \mathcal{B}_m \end{aligned} \tag{4.46}$$

and

$$\begin{aligned} \delta f^{(2,2,2)} = -\frac{1}{2}\tau^2 \frac{\partial f_0}{\partial \epsilon} \sum_{ij} (1-\xi^2)(\boldsymbol{s}\cdot\boldsymbol{n}) \frac{\partial \epsilon}{\partial k_i} E_j \sum_{lm} \varepsilon_{ilm} \mathcal{B}_m \frac{\partial \ln \xi}{\partial k_l} \times \\ \times \sum_{\alpha} (\boldsymbol{s}\times\boldsymbol{n}) \cdot \frac{\partial \boldsymbol{n}}{\partial r_\alpha} \frac{\partial^2 \epsilon}{\partial k_j \partial k_\alpha} + O\left(\left(\frac{\partial \xi}{\partial \boldsymbol{k}} \right)^2, \frac{\partial^2 \xi}{\partial \boldsymbol{k}^2} \right). \end{aligned} \tag{4.47}$$

The first correction is very similar to $\delta f^{(2,1)}$, just the $\dot{r}_l$-term has been replaced by its anomalous velocity part. Hence, the impact of the non-abelian correction is enhanced. $\delta f^{(2,2,2)}$ contains an infinite series with increasing order of ξ $\boldsymbol{k}$-derivatives in principle. Only the first order of the $\boldsymbol{k}$-derivative of ξ is explicitly states here which is similar to the previous terms but contains an additional group velocity term and has different derivative indices in the mass term connected to the $\dot{\boldsymbol{n}}$ expression.

5

T(S)HE calculation scheme

This chapter describes the computational procedures employed to calculate the topological (spin) Hall constant (Eqs. 4.6 and 4.12), i.e. the diagonal currents σ_{ii} (Eq. 4.34) and the (spin) Hall currents (Eqs. 4.37, 4.38, 4.43, and 4.44). Furthermore, this chapter scrutinizes the dependence on numerical parameters necessary for the transport calculations.

5.1 Calculation method

The general procedure to obtain transport properties relies on 3 basic ingredients: the wave-packet dynamics (Sec. 3), the Boltzmann formalism (Sec. 4.3), and the description of materials parameters. The latter relies on 2 independent parts, the skyrmionic real-space texture (Sec. 2.4) and the reciprocal-space Hamiltonian encoding the material properties (Secs. 6, 7). The wave-packet equations of motion combine both system descriptions from which transport expressions are obtained using the Boltzmann formalism. Here, the skyrmion texture and the material parameters are strictly separated as spin-orientation dependent Hamiltonian modification are neglected and since the skyrmion texture is artificially imprinted without considering magnetic parameters deduced from the material description. The former could arise due to variation of the quantization axis caused by SOC or the slight tilting of the magnetization of neighboring atoms, i.e. non-collinearity. While such effects could generally be included into the formalism, they would require significantly more preliminary calculations to extract the dependence of the reciprocal-space properties on the spin orientation and, more importantly, would render the separation into $\boldsymbol{r}$, $\boldsymbol{s}$ on the one side and $\boldsymbol{k}$ on the other side impossible since the dispersion would depend on $\boldsymbol{r}$. Hence, the reciprocal-space Hamiltonian as in the bilayer model or obtained from density-function theory contains only collinear, spin-direction agnostic information.

When including the wave-packet equations into the Boltzmann formalism, the above difference between $\boldsymbol{r}$, $\boldsymbol{s}$ and $\boldsymbol{k}$ is used extensively. The $\dot{\boldsymbol{k}}$-part is already included in Sec. 4.4 on the level of the Boltzmann equations to determine the deviation from the Fermi-Dirac equation. Hence, only the $\boldsymbol{r}$- and $\boldsymbol{s}$-dynamics still have to be included as described in this section.

All transport quantities related to the T(S)HE require a Fermi surface integral whose

computational implementation is described in Sec. 5.2.1. Here, it is sufficient to know that a sum over $\boldsymbol{k}$ is obtained with respective weights l_i. The $\boldsymbol{r}$- and $\boldsymbol{s}$-dependent parts of the integrand have to be calculated for each of those $\boldsymbol{k}$-points obeying the remaining dynamics given by $\dot{\boldsymbol{r}}$ and $\dot{\boldsymbol{s}}$. This has the conceptual and computational advantage that the $\boldsymbol{k}$-dependent parameters are evaluated only once.

The $\boldsymbol{s}$- and $\boldsymbol{r}$-dependent quantities are evaluated by considering several wave-packets initialized on a real-space grid whose initial spin is aligned or anti-aligned with the magnetic texture according to the corresponding Bloch state's spin. Subsequently, all wave-packets are iterated using to the remaining $\dot{\boldsymbol{r}}$ and $\dot{\boldsymbol{s}}$ differential equations for all given Fermi surface $\boldsymbol{k}$. The $\boldsymbol{r}$- and $\boldsymbol{s}$-dependent quantities of the transport expressions are continuously integrated over time during this iteration, i.e. finally averaged. A fourth-order Runge-Kutta scheme is used to iterate the wave-packets as described in Sec. 5.2.2. For further reference, this iteration, time-integration scheme is denoted by angle brackets. In the actual computational procedure it can be written as:

$$\langle X_{\boldsymbol{s},\boldsymbol{r}} \rangle_{it} = \frac{1}{t_{it} N_s N_{R^2}} \sum_{r_{\text{init}}}^{N_R^2} \sum_{s_{\text{init}}}^{N_s} \sum_{i}^{t_{it}} \Delta t_i X_{\boldsymbol{s},\boldsymbol{r}}(t_i). \tag{5.1}$$

The initial denominators normalize the iteration-time differences Δt_i, the starting from several initial spin states, and the initialization of a real-space grid. In case of the twofold-degenerate antiferromagnetic bands starting with spin-up and spin-down states N_s is still 1 to account for their degeneracy.

Convergence is usually reached after system-dependent iteration-times t_{it} (Sec. 5.3.3). As the traversed space necessary for convergence far exceeds the magnetic unit cell and because the convergence time is much larger than the Boltzmann relaxation time, this approach for calculating the Hall conductivities is only applicable when the spin scattering time is much larger that the momentum scattering. If the limit of extremely long spin scattering times is not sensible, these calculations still give insight into the THSE magnitude as those cases would correspond to the non-converged values after the respective spin-scattering associated time. Usually, very large spin scattering times are assumed in the following so that only the converged values are given unless stated otherwise.

A general problem when comparing 2D and 3D materials are dimensional differences. Here, conductances G [S] are obtained instead of conductivities σ [S/m] when applying the transport equations of Sec. 4. Since transport properties are usually given in conductivities or resistivities, it is helpful to introduce the material thickness d_z which allows to switch between these physical quantities. Hence, all 2D σ-expressions are divided by d_z to obtain conductivities.

Throughout this thesis, it is occasionally convenient to directly calculate the different conductivity contributions. This is particularly necessary when displaying the conductivity's $\boldsymbol{k}$-dependence (e.g. Fig. 6.3). In those cases τ does not cancel out as in case of the topological Hall constant but instead is assumed to be $\tau = 4000\,\hbar/E_h \approx 9.7\,\text{fs}$ unless otherwise stated.

Taking the numerical procedures into account, the transport expressions from Sec. 4 can be recast into forms more closely related to the actual computation scheme. Eq. 4.34 becomes

$$\sigma_{ij}^{(1)(s_\alpha)} = \frac{\tau}{(2\pi)^2 d_z} \sum_{k_i \in \text{FS}} l_i \frac{1}{|\partial_{\boldsymbol{k}_i} \epsilon|} \frac{\partial \epsilon}{\partial k_j} \langle (s_{\alpha,\boldsymbol{n}}) \dot{r}_i \rangle_{\text{it}}\,, \tag{5.2}$$

while Eqs. 4.35 and 4.43 take the form

$$\sigma_{ij}^{(2)(s_\alpha)} = \frac{\tau^2}{(2\pi)^2 d_z} \sum_{k_i \in \mathrm{FS}} l_i \frac{1}{|\partial_{\boldsymbol{k}_i} \epsilon|} (1-\xi^2) \sum_{lmn} \varepsilon_{lmn} \frac{\partial^2 \epsilon}{\partial k_j \partial k_n} \left\langle (s_{\alpha,\boldsymbol{n}})(\boldsymbol{s}\cdot\boldsymbol{n}) \dot{r}_i \dot{r}_l \mathcal{B}_m \right\rangle_{\mathrm{it}} . \tag{5.3}$$

(s_α) is included into both expression, but the analogue charge currents can be obtained by simply leaving out s_α. If some terms within the angle brackets are iteration independent, as is the case in simple equations of motion, further simplification are possible decreasing the computational effort. The following 2 sections cover the application of the predominantly used equations of motion.

5.1.1 Ferromagnet

In the ferromagnetic case, the conductivities can be evaluated without explicit wave-packet iterations since the equation of motion are extremely simple.

Starting from Eq. 4.37, the orbital and the real-space part of the (spin) Hall conductivities have already been separated while the spin does not appear explicitly at all. The orbital term can be calculated directly from the Hamiltonian at the Fermi surface which is similar to the necessary evaluation of $\boldsymbol{k}$-dependent quantities before starting the wave-packet iterations of the more general approach. Only the real-space integral over the emergent magnetic field, i.e. its flux, remains to be calculated. As described in Secs. 2.1.1 and 3.1.3, the emergent magnetic field's flux is quantized in skyrmionic textures to the skyrmion number. Hence, the real-space term of Eq. 4.37 is immediately given by the skyrmion density. The longitudinal conductivities depend only on trivial Fermi surface integrals (Eq. 4.34) where the $\dot{\boldsymbol{r}}$ are simply the group velocities. Accordingly, the THE and TSHE can be calculated without resorting to explicitly solving the wave-packet dynamics by following this paragraph's considerations and using Eqs. 4.10 and 4.11 .

Still, it is informative to apply the general scheme as that allows instructive comparison with the more complicated evaluation of degenerate systems. At first, the remaining wave-packet dynamics for $\dot{\boldsymbol{r}}$ and $\dot{\boldsymbol{s}}$ (Eq. 3.19) have to be combined with the conductivity expressions of Sec. 4.4.1. Only few term appear in the resulting expression which possibly depend on $\boldsymbol{s}$ or $\boldsymbol{r}$: $(\boldsymbol{s}\cdot\boldsymbol{n})$, $\dot{\boldsymbol{r}}$, and $\mathcal{B}_z$. The former 2 terms are independent of the wave-packet's position and spin as the equations of motion already state that $\dot{\boldsymbol{r}}$ is the group velocity depending only on $\boldsymbol{k}$ and since the spin dynamics identically follows the magnetic texture so that $(\boldsymbol{s}\cdot\boldsymbol{n}) = \pm 1$. Hence, $\mathcal{B}_z$ is the only appearing quantity which actually depends on the real-space position. Its contribution is evaluated by integrating $\mathcal{B}_z$ along the trajectories of wave-packets starting from a real-space grid for each $\boldsymbol{k}$. Since the wave-packet's velocity vector does not change, each $\boldsymbol{k}$'s states move on straight, parallel lines through the magnetic texture. In the limit of a dense initial real-space grid, at least dense in one direction not parallel to $\partial_{\boldsymbol{k}}\epsilon$, this is exactly the same as calculating the average emergent magnetic field. Hence, the flux of the emergent magnetic field is obtained as in the direct calculation above.

5.1.2 Collinear Antiferromagnet

Such tremendous simplifications are impossible in case of collinear antiferromagnets, instead the remaining equations of motion (compare Eq. 3.40)

$$\dot{\boldsymbol{s}} = (1-\xi^2)(\boldsymbol{s}\cdot\boldsymbol{n})\dot{\boldsymbol{n}} \tag{5.4a}$$

$$\dot{\boldsymbol{r}} = \frac{\partial\epsilon}{\partial\boldsymbol{k}} - \frac{1}{2}\left((\boldsymbol{s}\times\boldsymbol{n})\cdot\dot{\boldsymbol{n}}\right)\frac{\partial\ln\xi}{\partial\boldsymbol{k}} \tag{5.4b}$$

have to be solved for each $\boldsymbol{k}$-point of the Fermi surface integral. $\dot{\boldsymbol{r}}$, $(\boldsymbol{s}\cdot\boldsymbol{n})$, and $\mathcal{B}_z$ are the only $\boldsymbol{s}$- or $\boldsymbol{r}$-dependent terms in the conductivities of Sec. 4.4.2. Since $\dot{\boldsymbol{s}} = \dot{\boldsymbol{s}}(\boldsymbol{s},\boldsymbol{r},\dot{\boldsymbol{r}})$ and $\dot{\boldsymbol{r}} = \dot{\boldsymbol{r}}(\boldsymbol{s},\boldsymbol{r})$, the wave-packet dynamics are a coupled set of equations which prevents a direct separation of the integrated $\mathcal{B}_z$. This is intuitively clear as the wave-packets deviate from the straight trajectories of the ferromagnetic case. Hence, $\boldsymbol{n}$, $\partial_{\boldsymbol{r}}\boldsymbol{n}$ and $\mathcal{B}_z$ have to be calculated at each momentary position throughout the wave-packet evolution in order to evaluate $\dot{\boldsymbol{r}}$ taking the $\boldsymbol{s}$-dependence into account. Even when excluding the spin-trajectory dependence of $\dot{\boldsymbol{r}}$, corresponding to $\partial_{\boldsymbol{k}}\xi = 0$, it is impossible to simplify the evaluation of the $\mathcal{B}_z$-term. While the straight trajectory in real space is directly known as in the ferromagnetic case, the texture-dependent spin-trajectory modifies the impact of $\mathcal{B}_z$ through the $(\boldsymbol{s}\cdot\boldsymbol{n})$-term. Hence the whole mechanism as described in the beginning of this chapter (Sec. 5.1) has to be employed with above remaining wave-packet dynamics. This is the numerical procedure which is used in the majority of the calculations in this thesis.

5.2 Implementation details

While the computational scheme for estimating the transport is demonstrated in the previous section, further implementation details are necessary to characterize the ensuing calculations unambiguously. This section covers the majority of the implementation details, only the Hamiltonian setup and evaluation is summarized separately (Secs. 6, 7).

First, the implemented Fermi surface interpolation scheme is established which provides the $\boldsymbol{k}$-points and their respective weights to accurately approximate the $\boldsymbol{k}$-integral. Thus, the computational effort is reduced as less $\boldsymbol{k}$-points have to be investigated in the wave-packet iteration part. Next, the 4th-order Runge-Kutta iteration scheme is described considering the evaluation of the equations of motion. Throughout that wave-packet evolution, the magnetic texture has to be evaluated very often which can result in significant slowdown even with relatively simply texture descriptions. Hence, very efficient but accurate methods are required which are covered in Sec. 5.2.3. Finally, the employed parallelization procedures are summarized which, provided sufficient computational resources, enable timely evaluation of the transport expression despite their huge numerical effort.

5.2.1 Fermi-surface integral

In this section the implemented scheme for interpolating the Fermi surface is described. Since only 2-dimensional systems are treated in this thesis, the Fermi surface consists of

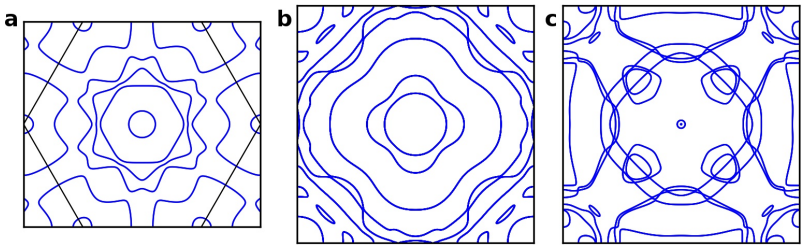

Figure 5.1: Example Fermi line interpolations of (a) $BiAg_2$ including SOC as published in Ref. [130], (b) $FeCu_5Fe$ as considered in Sec. 8.3, and (c) Fe/W(001) as plotted in Fig. 9.1c.

1D lines in the 2D Brillouin zone that are called Fermi lines henceforth. In principle, this implementation follows the 2-dimensional version of the tetrahedron method as described in Ref. [129]. $\epsilon(\boldsymbol{k})$ is evaluated very often during the interpolation, so that an efficient method is necessary to obtain the band energies. Ideally, simple model Hamiltonians are used whose diagonalization is simple and quick. Accordingly, the construction of a small, yet accurate, Wannier Hamiltonian is extremely advantageous when considering DFT-based system descriptions. Only this possibility is implemented to avoid direct interfacing with the DFT code. Example Fermi lines obtained through this method are shown in Fig. 5.1.

If the Fermi energy E_F is not externally chosen or taken from the DFT calculations, it has to be calculated for a given occupation before proceeding to the actual interpolation. Most often the DFT-based E_F is used in the following, alternatively the most simplistic implementation of a regular grid with counting of the occupied states is employable.

The utilized procedure to interpolate the Fermi lines for a given E_F is described in the remainder of this section. At first, the energies are calculated on a regular grid spanning the entire Brillouin zone. A reasonably large grid, depending on the number of bands near the Fermi energy, should be used to get a rough initial estimate of the Fermi lines' shape. Next, it is checked which bands cross the Fermi energy by comparing the indices of the bands with energies above and below $E_F \mp \delta E$, respectively. δE is a small numerical parameter accounting for possible crossings not resolved by the grid. All bands not crossing $E_F \mp \delta E$ are excluded from the following calculations in order to save memory, interprocessor communication, and CPU-cycles. Only one index of each degenerate pair is kept to similarly reduce computational effort. Their spin-reversed partners are reintroduced at the very end of this interpolation procedure.

Next, the number of occupied states is determined at each grid point in order to determine the path of Fermi lines with respect to the initial grid. If neighboring grid points have differing occupation numbers, a Fermi line has to cross the line connecting them (Fig. 5.2a). Non-overlapping triangles are formed to construct Fermi lines from that information. Here, the grid rectangles and the line between the lower left and the upper right corner of each rectangle are used (see Fig. 5.2a). If the occupations of the connected grid points differ, at least that many Fermi lines cross their connection. The occupation difference is not always equal to the number of crossed Fermi lines as two additional Fermi lines crossing a grid line

do not change the occupation numbers if their group velocities along the grid line direction have opposing signs. This effect is especially prominent near band crossing (Fig. 5.2b) where the 2 intersecting Fermi lines cancel the occupation difference so that the algorithm assumes that no crossing bands are between the corresponding grid points. Knowing which grid lines are crossed by Fermi lines, their intersections can be used to obtain an interpolation. Since the lines are all edges of triangles, the connections can be easily traces using that geometry. Each line entering a triangle has to leave it as well so that it is clear within the triangle which edge's crossing points have to be connected. After completing this procedure for each triangle, the Fermi line can be traced through the entire space (Figs. 5.2a,b) as the edges connect neighboring triangles. Obeying the symmetry boundary conditions, i.e. remaining in the first Brillouin zone, the whole line can be followed until returning to the first triangle. Hence, the path of each Fermi line can be traced and each crossing can be attributed to a numbered, closed Fermi line.

If a grid line is crossed by more than one Fermi line, the described algorithm may assume that there is no Fermi line crossing but that the other edges of the grid's triangle are connected instead (Fig. 5.2b). This can result in severe deviations from the true Fermi line especially in case of parallel lines. The obvious method to tackle that problem is to increase the grid density. Simply decreasing the grid spacing everywhere results in many more grid-points at positions without nearby Fermi lines and thus unnecessary waste of computational resources. Instead, it is more efficient to increase the grid spacing only at small areas of importance. Hence, additional grids with much finer spacings are computed at small areas where such problems may arise. The additional grids are also of rectangular shape in order to keep the connection to the triangles of the initial grid simple. The problematic regions that require further refinement are determined by judging the distance between distinct bands. Therefore, the indices of each Fermi line within a certain number of grid spacings (by default 3) are calculated for each grid point. It is advisable to increase that default value in case of sparse initial grids. Grid points are chosen to require further accuracy if they are associated with several Fermi-line indices and are connected to a Fermi lines. The mechanism of choosing areas of higher importance is depicted schematically in Fig. 5.2c with only 2 grid spacings in each direction and no additional enlargement while Fig. 5.2d shows the number of distinct neighboring Fermi lines for grid points connected to Fermi line intersections of a realistic $FeCu_6Fe$ DFT example system.

The refined areas are determined by rectangles which are laid around the grid points requiring enhanced accuracy. They are widened by 2 grid spacing in each direction to ensure enclosure of critical points. If rectangles overlap, they are divided into non-overlapping smaller rectangles of which only the ones containing grid points with occupation differences to neighbors are kept.

Within those rectangles, adaptive grids with a grid-spacing which are by default 10-times smaller than the initial grid are calculated following the above procedure to obtain the connections of the Fermi lines. Subsequently, the triangles of the adaptive grids are connected to the initial grid or neighboring adaptive grids so that it is possible to trace each Fermi lines through the entire Brillouin zone when following the triangles.

The intersections of the Fermi lines with the grid are obtained by successive bisection of the grid lines with occupation difference until the respective $\epsilon(\boldsymbol{k})$ corresponds to the Fermi energy

within a chosen accuracy. The resulting Fermi line interpolation for the previous $FeCu_6Fe$ example is shown in Fig. 5.2e. In principle, all necessary ingredients to define a Fermi-line interpolation have been obtained since many Fermi-line points are known whose connection is given by the triangles. The integral weights can be trivially obtained by calculating the distance of neighboring Fermi-line $\boldsymbol{k}$-point. Unfortunately, the distances between these points are vastly different, either due to crossings nearer or farther away from the grid points or, more extremely, due to the usage of the adaptive grid. Hence, direct integration of Fermi

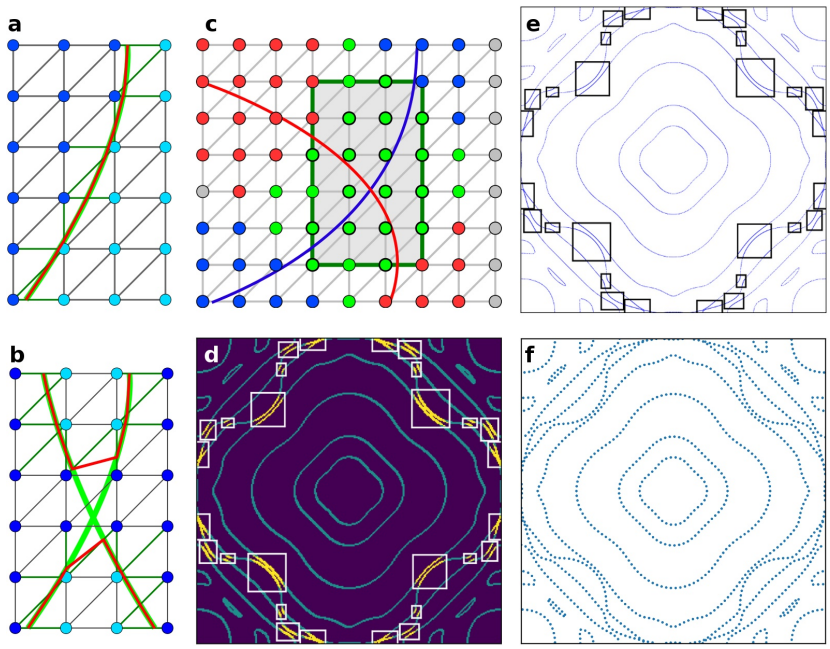

Figure 5.2: a,b) Schematic picture showing the interpolation procedure. Different blue colors denote different occupations at the grid points, the green line shows the true Fermi lines and the red line is the resulting interpolation. b) visualizes the problem of wrongly connected interpolation lines due to multiple crossings. c) Schematic choice of adaptive grid where red/blue grid points are within 2 lattice spacings of the red/blue Fermi line. Green grid points have both Fermi lines nearby, so that the dark green rectangle enclosing the green grid points with directly connected Fermi line intersections can be chosen as fine-grained adaptive grid. d-f) AFM degenerate $FeCu_6Fe$ example Fermi surface without SOC: d) shows the number of neighboring grid points (1: turquoise, 2: yellow) and the chosen adaptive grids as white rectangles. e) shows again the areas of refined grid usage and the Fermi line intersections with the initial and refined grid. f) displays the final integration grid with approximately equal weights for 1024 $\boldsymbol{k}$-points in each spin channel.

surface properties from this set is inefficient and a better interpolation is sought.

An equidistant interpolation is a sensible goal without further knowledge of the quantity that is to be calculated. As a good approximation for the length of each Fermi line is given by the previous interpolation, each line is alloted with the respective number of interpolation points so that their sum over all bands is a chosen number of $\boldsymbol{k}$-points while approximately similar spacings is ensured for all lines. The interpolation-algorithm starts from an arbitrary Fermi line point. At first, the target length to the next point is calculated. The former interpolation is followed until the target length minus the already traversed spacing is less than the length to the next intersection. Subsequently, the Fermi line is sought on a line at the target distance perpendicular to the difference vector. If this fails, the previously described grid mechanism is used to obtain a suitable Fermi line intersection with the aimed distance to the last intersection point. This procedure is repeated until the Fermi line is closed and the distances between connected points of the new interpolation mesh are known.

If more threads than Fermi lines are supplied, the usage of several initial positions in each Fermi lines provides a significant speedup since each line has to be tracked to the next thread's initial position only. Still, the threads are first distributed on the different Fermi lines since interpolations of single lines with many starting positions are prone to increased distance fluctuations. Accordingly, only excessive threads are distributed among the longest lines. The final interpolation of the example $FeCu_6Fe$ system with approximately equidistant spacings is shown in Fig. 5.2f. Overall, 2048 $\boldsymbol{k}$-points are used in that mesh but only 1024 $\boldsymbol{k}$-points are depicted since each state is twofold degenerate. An advantage of this setup is the possibility to simply change of the number of interpolation points by repetition of the last step as long as the grid- and the intersections-points of the refined grid are stored.

With the above information, the Fermi surface integral (Eq. 4.30) is conveniently expressed as the sum over all Fermi-line points with half the sum of the distances to the neighboring points as weight l_i:

$$\int_{\mathrm{Bz}} d\boldsymbol{k} \frac{\partial f_0}{\partial \epsilon} X(\boldsymbol{k}) = \sum_{k_i \in \mathrm{FS}} l_i \frac{1}{|\partial_{\boldsymbol{k}_i} \epsilon|} X(\boldsymbol{k}_i). \tag{5.5}$$

The additional $1/|\partial_{\boldsymbol{k}_i}\epsilon|$ originates in the transfer from $\delta(\epsilon - \epsilon_F)$ to $\delta(\boldsymbol{k} - \boldsymbol{k}_F)$ as described in Eq. 4.30.

Since a positive correlation between the effective masses and the $(1-\xi^2)$-prefactor exists, the spacing of the interpolation mesh could alternatively be construction to optimize with respect to those measures instead of the distance. Accordingly, the interpolation points would no longer be equidistant but more concentrated around high effective masses in combination with small ξ. Disadvantages include the fact that the new interpolation grid might be inefficient for other quantities such as the longitudinal conductivities and that the interpolation calculation would require additional information increasing the computational demand. Such different interpolation weights have not been implemented although they promise an auspicious, easy-to-implement possibility to decrease the computational demand of the actual transport calculation.

Other unimplemented possibilities to decrease the computational demand include the consideration of symmetries, i.e. calculating only the Fermi lines of the irreducible Brillouin zone, or improving the adaptive grid mechanism. The Delaunay triangulation provides an

interesting opportunity in the latter case: The greatest difficulty in the implementation of adaptive grids is the connection between the initial or other adaptive grids. This task can be passed to easily accessible, external libraries [131, 132] already interfaced in other parts of the code (adaptive grid for Brillouin zone integration of Berry curvatures). Thereby, the restrictive adherence to rectangular grids could be abolished allowing more efficient sampling directly around grid points with more than one nearby Fermi line. Moreover, it would be possible to implement a more systematical search for Fermi lines at the aimed distance and to enhance the grid resolution by including the numerous intermediary calculations.

Alternatively to this section's procedure of explicitly calculating the Fermi lines, the $\boldsymbol{k}$-integral can also be evaluated by summing over a regular grid spanning the entire Brillouin zone. Then, the Fermi surface character of the integral is implemented via the Fermi-Dirac distribution with a small, non-vanishing temperature regulating the impact of states relative to the Fermi energy. An advantage of that approach is the possibility to avoid extensive recalculations when computing small variations of the Fermi energy by simply modifying the Fermi-Dirac weights. Accordingly, the TSHE appears smoother when varying E_F, provided appropriate temperature broadening. On the downside, many $\boldsymbol{k}$-points will have vanishing impact on the sought physical quantity due to the lack of states near the Fermi level. In principle, those $\boldsymbol{k}$-points could be excluded from consideration, though the extreme of that approach yields the utilized implementation. This paragraph's method is well suited for the singly-degenerate case where no actual wave-packet iteration is needed so that the transport quantities are simply defined by easily obtainable group velocities and effective masses. Contrarily, the chosen method with direct Fermi surface interpolations is far better suited to tackle the TSHE calculation in AFM skyrmions as the computation effort required to obtain the $\boldsymbol{k}$-dependent transport part exceeds the computational power necessary to perform the Fermi-line interpolation by far.

5.2.2 Iteration scheme

This section describes the method and implementation details concerning the evolution of the remaining wave-packet dynamics such as Eq. 5.4. Mathematically speaking, the solution of a initial value problem of a coupled first-order differential equation in $\boldsymbol{s}$ and $\boldsymbol{r}$ is sought. An popular numerical procedure to tackle such tasks is the classical Runge-Kutta formalism [133]. This method discretizes the time into several steps which have to be solved consecutively. Here the 4th order Runge-Kutta formalism is used which requires 4 intermediate steps for each full iteration. The prefactors for summing the different contributions are chosen to cancel the errors in a Taylor-expansion scheme up to the 4th order.

Before performing the Runge-Kutta iteration, the differential equations have to be converted into the right form. It is necessary to express the time-derivative $\dot{\boldsymbol{x}}$ of a general variable $\boldsymbol{x}$ as a function $f_{\boldsymbol{x}}(t, \boldsymbol{x})$ and to define the initial state $\boldsymbol{x}(t_0) = \boldsymbol{x}_0$. Then, the iteration from the i-th time-step to the $(i+1)$-th time-step can then be obtained using the equation [133]:

$$\boldsymbol{x}_{i+1} = \boldsymbol{x}_i + h\left(\frac{1}{6}\boldsymbol{F}_1 + \frac{1}{3}\boldsymbol{F}_2 + \frac{1}{3}\boldsymbol{F}_3 + \frac{1}{6}\boldsymbol{F}_4\right), \tag{5.6}$$

where h is the time step size and $\boldsymbol{F}_i$ are the intermediate step derivatives:

$$\begin{aligned}
\boldsymbol{F}_1 &= f_{\boldsymbol{x}}(t_i, \boldsymbol{x}_i) \\
\boldsymbol{F}_2 &= f_{\boldsymbol{x}}(t_i + \frac{h}{2}, \boldsymbol{x}_i + \frac{h}{2}\boldsymbol{k}_1) \\
\boldsymbol{F}_3 &= f_{\boldsymbol{x}}(t_i + \frac{h}{2}, \boldsymbol{x}_i + \frac{h}{2}\boldsymbol{k}_2) \\
\boldsymbol{F}_4 &= f_{\boldsymbol{x}}(t_i + h, \boldsymbol{x}_i + h\boldsymbol{k}_3).
\end{aligned} \tag{5.7}$$

Following these equation from the initial state $\boldsymbol{x}_0$, the evolution can be tracked according to the differential equation. The issue of choosing an adequate step-size h is addressed in Sec. 5.3.1.

In all considered cases no explicitly time-dependent quantities are included so that the explicit time-dependence can be dropped: $\dot{\boldsymbol{x}} = f_{\boldsymbol{x}}(\boldsymbol{x})$. This could change when including e.g. breathing modes of the skyrmions, but such cases are not considered here. The next task is to bring the remaining equations of motion into the required form where the derivative depends only on $\boldsymbol{x}$ which corresponds to $\boldsymbol{s}$ and $\boldsymbol{r}$ in the considered equations of motion.

As the equations of motion are coupled in general, they are often given in an implicit form $\dot{\boldsymbol{x}} = f_{\boldsymbol{x}}(\boldsymbol{x}, \dot{\boldsymbol{x}})$ which violates the requirement $\dot{\boldsymbol{x}} = f_{\boldsymbol{x}}(\boldsymbol{x})$ initially. Simple transformations rearranging the equation system to satisfy the required dependences are possible since all covered equations of motion are linear in $\dot{\boldsymbol{x}}$. For example, the DGESV routine of the LAPACK library directly performs such transformations. As the Runge-Kutta iteration is at the core of the numerical procedure, a more efficient calculation of f can save significant amounts of the computational time. While the usage of LAPACK routines is most efficient when computing few large matrices, their application is inefficient when treating many small matrices. Fortunately, only simply 4-dimensional sets of equations have to be solved when considering 2-dimensional structures. Hence, several direct solutions of studied equations of motion have been implemented avoiding LAPACK calls.

In the ferromagnetic case the reformulation is trivial as Eq. 3.19b only depends on $\boldsymbol{k}$. Hence, this equation already satisfies the required dependencies, especially since $\boldsymbol{k}$ is treated as an external parameter. According to Eq. 3.19a, $\dot{\boldsymbol{s}}$ depends on $\boldsymbol{s}$, $\boldsymbol{r}$, and $\dot{\boldsymbol{r}}$ though the implicit dependences of $\boldsymbol{n}$ and $\dot{\boldsymbol{n}}$. But since an expression for $\dot{\boldsymbol{r}}$ independent of $\dot{\boldsymbol{s}}$ and $\dot{\boldsymbol{r}}$ is already obtained, $\dot{\boldsymbol{s}}$ is readily expressible through $\boldsymbol{s}$, $\boldsymbol{r}$, and the external $\boldsymbol{k}$ so that it obeys the above requirements for $f_{\boldsymbol{x}}$. Hence

$$f_{\boldsymbol{s}}^{FM} = (\boldsymbol{s} \cdot \boldsymbol{n}) \left(\frac{\partial \epsilon}{\partial \boldsymbol{k}} \cdot \nabla \right) \boldsymbol{n}, \tag{5.8a}$$

$$f_{\boldsymbol{r}}^{FM} = \frac{\partial \epsilon}{\partial \boldsymbol{k}} \tag{5.8b}$$

$$\tag{5.8c}$$

allows evaluation of the Runge-Kutta formalism $\boldsymbol{F}_{1..4}$ (Eq. 5.7). Actual calculations with these equations are not interesting as the transport properties can be directly deduced without iterations (Sec. 5.1.1). However, an interesting aspect is the verification of the iterative

solution and the necessary step-size, since it is clear from the wave-packet dynamics that the spin has to remain aligned with the magnetic texture. This is an easy measure to check if the Runge-Kutta step-size is sufficient (Sec. 5.3.1).

In the antiferromagnetic case Eq. 5.4 has the be considered. If $\partial_{\boldsymbol{k}}\xi = 0$, as in the case of the model Hamiltonian (Sec. 6), the rearrangement of the equations of motion is similar to the ferromagnetic case. The only difference is the misalignment from the magnetic texture, but, as there is no backtalk to $\dot{\boldsymbol{r}}$, it is only necessary to treat $\dot{\boldsymbol{s}}$ within the Runge-Kutta scheme. Again replacing $\dot{\boldsymbol{r}}$ by the group velocity, the equation obeys the necessary form $\dot{\boldsymbol{s}} = f_{\boldsymbol{s}}(\boldsymbol{s}, \boldsymbol{r})$.

In the general case ($\partial_{\boldsymbol{k}}\xi \neq 0$), $\dot{\boldsymbol{r}} = f_{\boldsymbol{r}}(\boldsymbol{r}, \boldsymbol{s}, \dot{\boldsymbol{r}})$ holds according to Eq. 5.4. Fortunately, $\dot{\boldsymbol{r}}$ is still independent of $\dot{\boldsymbol{s}}$ so that the $\dot{\boldsymbol{r}}$ equation can be solved independently before being inserted into $\dot{\boldsymbol{s}}$. Hence, $\dot{r}_x$ and $\dot{r}_y$ have to be obtained first when assuming a 2-dimensional system. Since the components $\dot{\boldsymbol{r}}$ are mixed in the equation of motion:

$$\dot{r}_i + \frac{1}{2}\sum_{jl}(\boldsymbol{s}\times\boldsymbol{n})_l \frac{\partial n_l}{\partial r_j}\frac{\partial \ln\xi}{\partial k_i}\dot{r}_j = \frac{\partial \epsilon}{\partial k_i}, \tag{5.9}$$

the 2×2-matrix in $\{\dot{r}_x,\dot{r}_y\}$-space has to be inverted and multiplied with the equation's right side. As all components are known and depend only on $\boldsymbol{r}$, $\boldsymbol{s}$, and the external $\boldsymbol{k}$, the analytic inversion of the matrix can be readily performed. Afterwards, the solution of $\dot{\boldsymbol{r}}$ is inserted into $\dot{\boldsymbol{s}}$ obtaining the set of equations required for the Runge-Kutta iteration.

The same procedure is also applicable for the general equations of motion (including $\dot{\boldsymbol{k}}$). Extracting transport properties out of those equations is more complicated, nevertheless numerical access to the motion of electron wave-packets in magnetic textures is physically interesting and allows to visualize e.g. their deflection in skyrmions. In the ferromagnet (Eq. 3.19) and the antiferromagnetic (Eq. 3.40) cases without SOC the solution is extremely similar as the calculated $\dot{\boldsymbol{r}}$ term just has to be included in $\dot{\boldsymbol{k}}$ as well. In the most general cases as Eq. 3.8 or Eq. 3.24 all equations are connected so that either an analytic or a numerical matrix inversion is necessary. While the latter requires more complicated implementations, it would speed up the code execution significantly.

5.2.3 Texture interpolation

The texture order parameter n has to be evaluated very often throughout the wave-packet iteration and the corresponding transport evaluation. In order to accelerate its computation, $\boldsymbol{n}$ is initially calculated on a grid from which the texture at the wave-packet position is interpolated. This is necessary in case of the atomistic model as the texture is given only on a grid anyways, yet this interpolation proved to be favorable in case of the analytic $3\boldsymbol{q}$-texture as well due to a significant computational speedup.

Since $\partial_{\boldsymbol{r}}\boldsymbol{n}$ and $\mathcal{B}$, and other texture related quantities in case of non-collinear textures, have to be evaluated almost as often, they are analogously interpolated from the same grid. Although the derivatives and the emergent magnetic field are directly accessible in simple parameterizations, the texture derivatives are calculated by numerical means preferably from the analytic $\boldsymbol{n}$-expression. The 8th order central finite difference method is used with a grid spacing either given by the atomistic lattice parameter or chosen as 0.1% of the

magnetic lattice parameters of analytic models. Accordingly, the interpolation parameters of the emergent magnetic field are obtained according to Eq. 3.16 from $\boldsymbol{n}$ and $\partial_{\boldsymbol{r}}\boldsymbol{n}$ on the grid.

The texture interpolation requires special care as small errors may tremendously change the results when tracking the wave-packets over very long distances. The most important requirements of the parameterization are continuity and smoothness. This is especially critical in case of degenerate antiferromagnetic wave-packets in which the spin deviates from the magnetic texture. The worst case in those iterations would be a discontinuity in the texture which breaks the adiabaticity requirement and thus would render the equations of motions inapplicable ($\boldsymbol{n}$ changes but $\boldsymbol{s}$ does not).

The most obvious applicable procedure is a bilinear interpolation between neighboring grid point which is easily implemented and very fast to evaluate. However, the derivatives of $\boldsymbol{n}$ are not smooth at the grid lines so that the previously described problems arise. Such

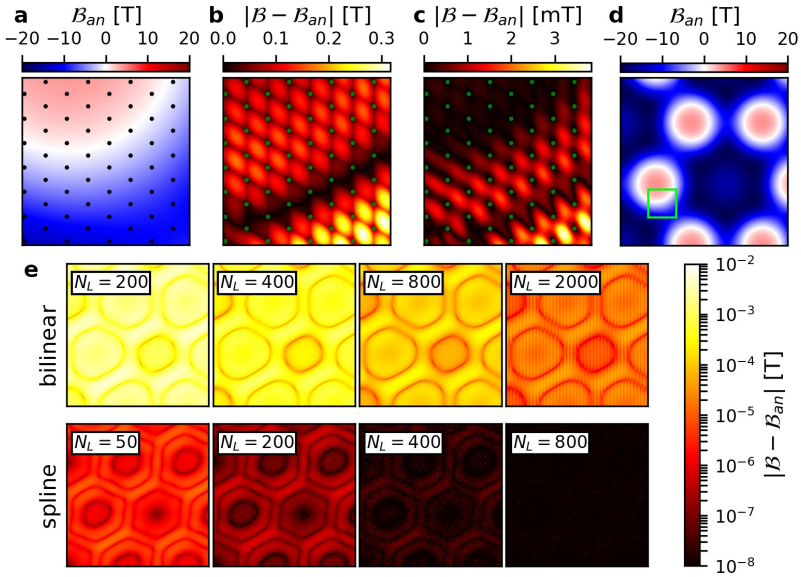

Figure 5.3: Emergent magnetic fields and differences to the analytic result for 5 nm × 5 nm (a-c) and 30 nm × 30 nm (d-e) texture sections. The green square of d) indicates the position of the smaller section. a) and d) show the emergent magnetic field $\mathcal{B}_{an}$ of the 3$\boldsymbol{q}$-structure numerically calculated from the analytic expression. In a) to c) the interpolation points ($N_L = 30$) are displayed which are used to obtain the interpolations. The absolute differences to $\mathcal{B}_{an}$ of a) are plotted for the bilinear and bicubic spline interpolation in b) and c), respectively. Analogously, the interpolation difference respective to d) are depicted in e). The upper plots show several N_L with the bilinear interpolation, while the lower displays the spline interpolation. Notice the different N_L in each line and the logarithmic scale.

discontinuities can lead to further numerical complications for example when using a δn_{max} to adaptively determine the Runge-Kutta step size h (Sec. 5.3.1). The difference between the analytic and the interpolated emergent magnetic fields is displayed in Fig. 5.3b for a very small $N_L = 30$, where N_L denotes the number of interpolation points in each magnetic lattice direction. Deviations of 3% are apparent in this rough approximation so that the interpolation is acceptable only in the direct vicinity of the interpolation grid. A straightforward enhancement can be achieved by increasing N_L as shown in the upper frames of Fig. 5.3e. Some orders of magnitude in accuracy can be gained when increasing N_L, yet the memory requirements for calculations with large N_L (e.g. $N_L = 2000$) become large. Moiré patterns are formed in the respective figure due to the extreme size of N_L and the smaller number of plotting points. While the slope of the kinks can be mitigated by enhanced N_L, their existence can not be entirely avoided when using the bilinear interpolation.

An alternative, slightly more complicated method is the bicubic spline interpolation. It still reproduces the interpolation points perfectly while the intermediate sections are much smoother than the bilinear ones. The differences in the analytic emergent magnetic field are plotted in Fig. 5.3c for $N_L = 30$ as comparison to the bilinear interpolation (Fig. 5.3b). The deviations are smaller by 2 orders of magnitude and the area with small errors extends farther around the interpolation points. The errors even vanish in some sections on the depicted range. The dependence of $|\mathcal{B} - \mathcal{B}_{an}|$ on N_L is again shown in Fig. 5.3e. Already the $N_L = 50$ calculation is better than the $N_L = 2000$ case of the bilinear interpolation. The deviation becomes very small on the scale of $\mathcal{B}$ itself already for $N_L = 200$, yet systemic changes are still visible. They become more erratic including noise of smaller deviations for $N_L = 400$ and even vanish in sections of the texture for $N_L = 800$. There, the emergent magnetic field is 9 orders of magnitude larger than the differences so that the limit of computer accuracy is approached when calculating the differences. This explains the vanishing of $|\mathcal{B} - \mathcal{B}_{an}|$ in several regions where both fields are represented by identical numbers.

In practice, the spline parameters are calculated prior to the main calculations using the external NAG libraries' E01DAF subroutine. Then, the spline interpolation can be efficiently evaluated in the main calculations with only slightly more effort than in case of the bilinear interpolation. For computers without the NAG library, and to save time when doing many small calculations, the spline coefficients can also be supplied through an automatically generated input file.

In conclusion, the spline interpolation is more accurate than the bilinear interpolation by orders of magnitude in case of the 3$\boldsymbol{q}$-structure and supplies a much smoother interpolation which enhances the numerically stability of the wave-packet iterations and resembles the skyrmion texture better. Hence, it is reasonable to assume that the spline interpolation is much better when interpolating the SPIRIT textures. Furthermore, the difference in computational effort between both interpolation methods is negligible, an example calculation of $\boldsymbol{n}$, $\partial_{\boldsymbol{r}}\boldsymbol{n}$, and $\mathcal{B}$ on a grid with $2.5 \cdot 10^7$ points took 6.6 s and 6.9 s for bilinear and spline interpolation, respectively. The same calculation takes 815.2 s when using the analytic expressions and numerical derivatives of the 3$\boldsymbol{q}$-texture, hence the spline interpolation is used for all transport calculations in the following. $N_L = 800$ is used by default to interpolate the 3$\boldsymbol{q}$-texture as it provides excellent reproduction with acceptable computational effort, in case of SPIRIT-textures N_l is necessarily given by the atomistic grid size.

5.2.4 Parallelization

The computationally expensive part of this thesis are the actual transport calculations. Fortunately, most required parameters can be separated easily from the bulk of the transport calculations. A huge part of this simplification originates in the fact, that the $\boldsymbol{k}$-part of the equations of motion has been separated into the Boltzmann part so that the evaluation of reciprocal-space properties is not necessary during the transport calculations. Instead, only the initial parameters depending of the Fermi-line $\boldsymbol{k}$-points have to be supplied at the start of the calculation. Although that part is also trivially parallelized in $\boldsymbol{k}$, the parameters can be calculated on a smaller machine and then supplied via an input file to the main calculation on a strongly parallelized machine. Similarly, the spline interpolation parameters describing the magnetic texture can be calculated in advance of the main calculations on a smaller machine that support the used NAG library.

The remaining steps necessary to estimate the transport properties are the evaluation of the magnetic texture using the spline interpolation, the solution of the Runge-Kutta scheme, and the merging of those parameters to the actual transport properties during the iteration. All of these steps are computationally simple and do no require further external libraries so that parallelization of those parts is easily possible. Since the transport calculations require a Fermi surface integral with independent $\boldsymbol{k}$-points, parallelization over this loop is possible in a simple way. Furthermore, each $\boldsymbol{k}$ requires a loop over initial real-space points which is used as a further parallelization level. Additional care is necessary for the $\boldsymbol{k}$-point parallelization since the computational effort of each $\boldsymbol{k}$ is different (Sec. 5.2.2) and as the computation times can only be estimated roughly based on the group velocities. Hence, each thread is initially allotted with only one $\boldsymbol{k}$ instead of distributing all $\boldsymbol{k}$ to the MPI-thread in the beginning. A new $\boldsymbol{k}$-point is only supplied by the master if the previous calculation is finished. While this creates communication overhead, this setup is advantageous as otherwise a single thread might be occupied with many long calculations while other threads with shorter tasks are idle most of the time.

Still, the parallelization causes idling as soon as no further $\boldsymbol{k}$ are available so that it is advantageous to introduction a second layer of parallelization. In that case less threads will be used in the $\boldsymbol{k}$ loop on the same machine so that idle time is reduced and less $\boldsymbol{k}$ points have to be calculated while others are finished already. The real-space initial-state grid, having the same form for all $\boldsymbol{k}$-points, is used as second layer of parallelization utilizing OpenMP. The only large arrays used within that loop are the spline interpolation parameters of the magnetic texture which are accordingly shared on the second layer. Hence, memory is saved as only one copy per MPI thread is necessary. This procedure allows the usage of highly parallelized computers for this thesis's computations..

Additional to the important parallelization of the transport properties, further parallelizations have been included at non-critical parts of the code aiming at smaller machines. These includes parallelizations in the interpolation of the Fermi lines (Sec. 5.2.1), calculation of the orbital parameters as effective masses and overlaps ξ, and evaluation of the magnetic texture. Most often explicit MPI routines, but also smaller openMP parallelizations, are used.

5.3 Convergence

From the previous sections it is clear that additional numerical parameters have to be chosen in order to apply the transport formalism or to solve the wave-packet iterations. These parameters include the iteration-time, the step sizes, the Fermi-line interpolation, and the real-space initial grid which are described in the previous parts of Sec. 5.1. All will be determined by successive calculations increasing the particular parameter until the transport is sufficiently converged.

5.3.1 Runge-Kutta step size

The choice of the time-step size h is an integral part of the Runge-Kutta iterations. If it is chosen too large, the numerical solution quickly deviated from the true path in phase space so that the solution becomes erroneous, if it is too small excessive computational effort will only provide meager results so that in principle solvable problems become inaccessible. A first upper bound is given by the necessity to resolve the scale of the investigated real-space texture. When requiring at least 100 intermediary steps to resolve the magnetic texture with lattice vectors of 190 Å (Sec. 2.4.1), $h = 3.8 \cdot 10^{-16}$ s is a sensible first approximation which corresponds to typical group velocities of 500 km/s. In the following the step size is given in atomic units, $[h] = 2.418884326505 \cdot 10^{-17}$ s so that the above preliminary approximation becomes $h \approx 16[h]$.

The transversal transport components of the TSHE investigated in this thesis converge approximately after iterations for about 1 ns. Using the above group velocity, this corresponds to 500 μm which is about 26000-times the magnetic lattice unit vector length. For these very long iteration times it is not clear how many steps are necessary to resolve the magnetic structure while retaining numerical stability, hence the above considerations are insufficient to select h. A better estimation on the necessary h can be obtained by solving the equations of motion with varying h. The simple structure of the ferromagnetic spin dynamics allows for an intuitive check of the accuracy. The analytic solution $\boldsymbol{s} = \boldsymbol{n}$ is known since the spin is supposed to follow the texture, and since the real-space path is a straight line whose evaluation is independent from h. Therefore, the deviation of $\boldsymbol{s}$ from $\boldsymbol{n}$ can be evaluated immediately. In Fig. 5.4a the deviation, expressed as $||\boldsymbol{s} - \boldsymbol{n}||_2$, is shown for an arbitrarily state with $\partial_k \epsilon = 500$ km/s over the iteration-time of 1 ns in the $3\boldsymbol{q}$-state texture. Since many evolutions are plotted over each other, the averaged deviation throughout the evaluation are depicted again in Fig. 5.4d (blue). As expected, the spin deviates very much from the converged evaluation in case of $h \gtrsim 100$ so that those calculations should be discarded immediately. For $h \gtrsim 10$ oscillating deviations are still visible so that the resulting conductivities are ultimately not reliable but will give a good approximation. The lower limit of this range corresponds to the previous estimation of the step size validating these considerations. For smaller h down to $h = 0.01$ no systematical differences are visible, so that $h = 10$ seems to be a sensible choice.

The fact that the spin is constricted to a prolate spheroid in the antiferromagnetic case can be used to further enhance the accuracy by rescaling the spin length to fulfill the analytic requirement. The corresponding iterations with spins forced onto their analytic codomain

are shown in Fig. 5.4b and d. Less oscillations are visible in the time evolution of $||\boldsymbol{s}-\boldsymbol{n}||_2$ compared to the previous case. Furthermore, $h \approx 1$ has even better accuracy than smaller h within the first 0.25 ns. This counterintuitive behavior most probably originated in the fact that fewer numerical steps are necessary to reach that iteration-time so that the accrued computer accuracy errors have lesser impact. Comparing the averaged deviations (Fig. 5.4d), the enforced unit sphere calculations show higher accuracy below $h \approx 20$ and decreasing h down to $h = 1$ seem to be advantageous.

Wave-packet trajectories with vastly different $\boldsymbol{k}$-dependent group velocities have to be evaluated in the TSHE-calculations of realistic materials. In the ferromagnetic case the spin evolution is geometrical and hence independent of the wave-packet velocity. Hence, $\boldsymbol{k}$-points with group velocity that are 10-times larger require 10-times smaller h and vice versa. Of course, 10-times larger or smaller distances have be traversed, but the spin iteration accuracy with respect to the texture changes. An obvious improvement of the computational velocity is the use of different h for each $\boldsymbol{k}$-point chosen according to their group velocity. However, velocity terms with changing magnitude appear in more complicated equations of motion so that the maximal velocity of a wave-packet is unknown at the beginning of the iterations. This problem is circumvented by defining a maximal real-space step-size δr_{max} which rejects iteration steps if the restriction is violated. h is adjusted after each accepted or rejected state

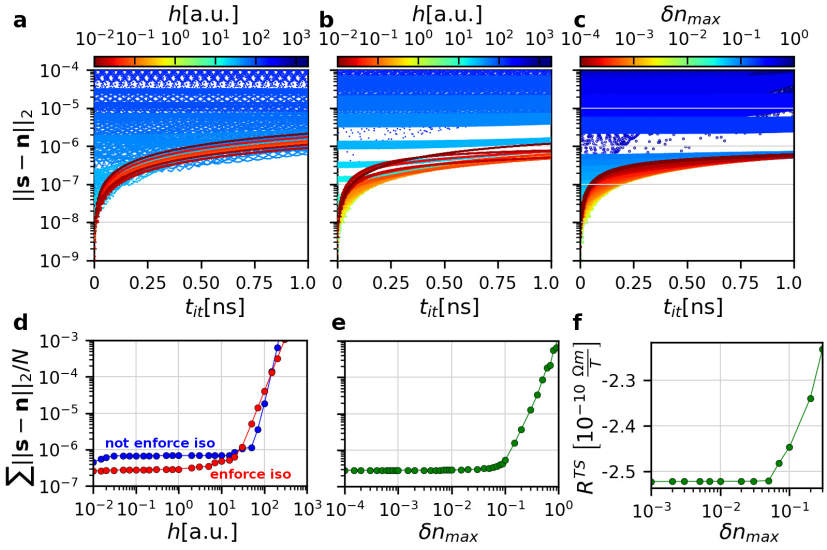

Figure 5.4: a-e) Ferromagnetic wave-packet evolution spin-alignment check for single iterations. a,b,d) are calculations performed with a constant time-step h, c,e) are calculated with a $\delta n_{\max}$. a-c) show full time dependent alignment, while d,e) display the averaged spin difference from the magnetic texture. f) shows the TSHE transport convergence of the model in Sec. 6.2.1 with varying $\delta n_{\max}$ using 48 k-points on an 3×3 real-space grid after 1 ns

to aim at a real-space change of $0.7\delta r_{max}$ per iteration to minimize the number of rejected calculations. This procedure proved to be a stable and efficient approach for the $3\boldsymbol{q}$-texture whose spin state is constantly changing. However, much computational time is still wasted in the collinear background when investigating more localized skyrmion textures.

Since the required accuracy is dominated by the spin structure changes, it is sensible to tune h with respect to the local change of $\boldsymbol{n}$. Hence, δn_{max} is defined and h is adjust after each step to aim for

$$||\boldsymbol{n}(\boldsymbol{r}_{i+1}) - \boldsymbol{n}(\boldsymbol{r}_i)||_2 \stackrel{!}{=} 0.7\delta n_{max} \tag{5.10}$$

while restricting the spin to the iso-surface. Fig. 5.4c shows the corresponding time-dependent deviations for various δn_{max}. The time evolution reveals a systematic enhancement similar to the constant h with enforced iso-surface. Judging from the computational times t_c on one example computer, the smallest constant h calculation with $t_c(h = 0.01) \approx 3500\,\mathrm{s}$ is comparable to the smallest δn_{max} calculation with $t_c(\delta n_{max} = 10^{-4}) \approx 1600\,\mathrm{s}$. In Fig. 5.4e the averaged deviations are shown for varying δn_{max} demonstrating that for $\delta n_{max} \lesssim 0.03$ good accuracy is reached that is comparable to the constant time step $h = 1$ calculations. Comparison of the computation times of the wave-packet iteration, $t_c(\delta n_{max} = 0.03) \approx 6\,\mathrm{s}$ and $t_c(h = 1) \approx 18\,\mathrm{s}$, demonstrates the extremely advantage of enforcing a δn_{max} instead of using a constant h when aiming for similar accuracies, even in case of the $3\boldsymbol{q}$-texture. For actual transport calculation

$$\delta n_{max} = 0.01 \tag{5.11}$$

is chosen in the following to be on the save side with respect to the wave-packet iteration accuracy. This is an affordable safety measure since $t_c(\delta n_{max} = 0.01) \approx 16\,\mathrm{s}$ is analogous to above calculations.

The question arises whether the previous convergence criteria of the ferromagnetic case are also sensible in the antiferromagnetic case. In the latter case the spin dynamics are slower and lag behind the magnetic texture changes due to the overlap ξ. Hence, the numerical accuracy necessary for tracking the ferromagnetic spin dynamics should be more than sufficient. The changes of the emergent magnetic field are determined by the changes of $\boldsymbol{n}$ which are very accurately resolved during the iterations so that its impact on the transport properties is sufficiently resolved. The additional velocity term should also be adequately resolved as it mainly depends on the nicely resolved spin evolution. Therefore, at least the reduced wave-packet dynamics solved in the transport calculations should be described sufficiently with the above choice of $\delta n_{max} = 0.01$.

Direct numerical convergence checks are more difficult in the antiferromagnetic case as no analytic solution is known. One possibility is comparison with a calculation employing much smaller numeric parameters but that result would still be less definite than in the ferromagnetic case. Instead, several small example TSHE-calculation with otherwise insufficient numerical parameters are performed with varying δn_{max}. The model system of Sec. 6.2.1 is described by only 48 $\boldsymbol{k}$-points, 24 of each spin channel, and only a 3×3 initial real-space grid is used. The resulting R_{xy}^{TS} after iterations for 1 ns are plotted in Fig. 5.4f. On the scale of this plot no variations are visible for $0.001 \leq \delta n_{max} \leq 0.04$ so that even $\delta n_{max} = 0.04$ seem reliable enough for antiferromagnetic transport calculations. This confirms the assumption that the

ferromagnetic accuracy level is sufficient for the antiferromagnetic transport calculations and that $\delta n_{max} = 0.01$ is a valid choice for the remaining transport calculations.

Finally, it should be noted that the $\boldsymbol{k}$-point's transport calculations can require very different iteration times as the group velocities differ while the wave-packets are iterated for a fixed time.

5.3.2 k-interpolation

The number of $\boldsymbol{k}$-points N_k is a further numerical quantity which has to be chosen appropriately. Naturally, a good choice for N_k is very system-dependent changing drastically between simple systems with few Fermi lines and large systems with many Fermi-lines or fine features which require many more $\boldsymbol{k}$-points to reach convergence. Nevertheless, it is instructive to study the $\boldsymbol{k}$-point convergence of the TSHE in simple example systems. The following calculations are done with $\xi = 0$ to reduce the influence of other numerical parameters and to lessen the computational effort (Sec. 5.1.1). Fig. 5.5a shows the N_k-convergence for the antiferromagnetic bilayer model of Sec. 6.2 choosing $\xi = 0$. The $FeCu_2Fe$ trilayer with $\xi = 0$ is chosen as second test system and its TSHE N_k-dependence is shown in Fig. 5.5b. Since $\xi = 0$, only short iteration-times ($t_{it} \approx 2.5\,\mathrm{ps}$) and small real-space grids (4×4) are necessary to obtain converged and reliable results.

In case of the model convergence is already reached with $N_k \gtrsim 60$ while $N_k \gtrsim 1000$ seems necessary for the trilayer. Large, albeit a bit smaller, differences between the systems are to be expected since the model has only 1 simple Fermi loop while the trilayer has 7 distinct Fermi lines. The more than linear increase with the number of Fermi lines can be attributed to the complicated shape of the trilayer's Fermi lines which have more bends and drastically changing effective masses. Hence, the equidistant choice of the Fermi line interpolation (Sec. 5.2.1) is suitable for the model calculation while another doubling of the resolution is necessary in case of the trilayer.

In conclusion, N_k has to be chosen with regard to the complexity of the Fermi lines and can easily exceed 1000. A small example variation of N_k with $\xi = 0$ is appropriate in order to validate the choice of N_k..

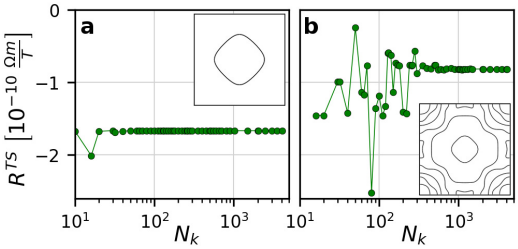

Figure 5.5: TSHE convergence with respect to the number of $\boldsymbol{k}$-points N_k. a) model system (Sec. 6.2.1) b) $FeCu_2Fe$ (Sec. 8.2) with $\xi = 0$ for simple convergence. The insets show the respective Fermi lines.

5.3.3 Iteration time

The iteration time t_{it} is another important numerical parameters. It has tremendous impact on the TSHE due to the iterative character of the transport procedure which starts from aligned and anti-aligned spins that have to be equilibrated. This section scrutinizes the impact of t_{it} to obtain a reasonable default choice.

It is sensible to first consider the limit of very small t_{it}. Intuitively, it is clear that calculations with very small t_{it} will not show the full features of the degenerate structures as long as the traversed space is small on the scale of the magnetic texture. This arises from the fact that the spin has not had the chance to misalign with the texture which otherwise would decrease the wave-packet's spin transport impact. If the initial $\boldsymbol{R}$-grid and the short iterations are sufficient to resolve the magnetic texture, the transport result is similar to the decoupled antiparallel ferromagnetic case as the spins are initially chosen to be aligned and antialigned with the magnetic texture. The only difference of this setup to the true ferromagnetic case is the $(1-\xi^2)$ prefactor (Eq. 4.43) of the TSHE.

For typical group velocities of 500 km/s, this behavior is to be expected for $t_{it} \leq 10^{-15}$ s corresponding to traversed spaces of less or equal 5 Å which is much smaller than conventional magnetic lattice parameters of 190 Å. Indeed, the transport impact remains constant up to 10^{-15} s as shown in Fig. 5.6a-b, in case of $\xi \leq 0.5$ no significant t_{it}-dependent transport alteration appear even up to $t_{it} = 10^{-14}$ s. Yet, it is still possible to approximate the TSHE with reasonable accuracy from large ξ in case of $t_{it} = 10^{-14}$ s using the $(1-\xi^2)$- relation as depicted by the red line in Fig. 5.7.

For larger iteration times the spin misalignment starts to modify the THSE until the transport converges eventually. The intermediate behavior is similar for all calculations with constant ξ's irrespective of the underlying Hamiltonian. Increasing t_{it}, the R^{TS} reacts with a relatively continuous decrease until it approaches the converged value with small fluctuations only. These fluctuations are slightly stronger in case of the $FeCu_2Fe$ system which most probably originates in the more complicated reciprocal-space structure with a wider range of group velocities. The faster convergence of the systems with larger ξs can be attributed to the faster spin misalignment with increasing ξ as determined by the equations of motion (Eq. 3.38). Accordingly, the transport decreases more rapidly as the spin equilibrates faster with respect to the texture. This property is clearly visible in the different slopes of Fig. 5.6a-b as well as when comparing the shapes of the $t_{it} = \{10^{-13}, 10^{-12}\}$ s calculations to the spin-polarized $t_{it} = 10^{-14}$ s line of Fig. 5.7. There, the problem of approaching $\xi = 0$ is especially apparent since the convergence becomes slower and slower until the spin no longer deviates from the texture for $\xi = 0$ so that no transport modification caused by spin variation can appear. This is a problem for real calculations as very small ξ can definitively appear near the Brillouin zone boundary. Still, infinitely long iterations are neither computationally feasible nor physically sensible so that the iteration has to be terminated at some point with fairly converged transport properties. Hence, those states with very small ξ are effectively treated similar to 2 antiparallel ferromagnetic states which physically makes sense as small ξ correspond to weakly coupled states.

Furthermore, the $FeCu_2Fe$ t_{it}-convergence with the true $\boldsymbol{k}$-dependent ξ is given in Fig. 5.6b. Two glaring differences arise when comparing to the previous calculations with constant ξ.

Firstly, the convergence is much slower than in the other depicted example systems and, secondly, $|R^{TS}|$ does no longer decrease monotonously but has intermediate increases. The first feature can be readily attributed to the Fermi line parts with $\xi \ll 0.1$ (Fig. 8.4d) due to the increased convergence time with decreasing ξ as explained in the previous paragraph. The second feature originates in the varying ξ-distribution on the Fermi surface which results in a much faster transport contribution decrease of sections with larger ξ compared to the sections with small ξ. Since different parts of the Fermi lines contribute to the overall transport with different signs (Fig. 8.5c), the overall transport increases if the decrease of the destructive sections supersedes its constructive counterpart.

The last regime of t_{it} is the converged part with only small variations oscillating around the converged values. The t_{it} of the systems with constant ξ can be clearly extracted from Fig. 5.6, for example the system with $\xi = 0.1$ requires approximately 10^{-11} s while the $\xi = 0.75$-system converges already after about 10^{-13} s. A remarkable relation is revealed by the t_{it}-converged values for $\xi \geq 0.1$ in Fig. 5.7: the dependence of the converged R^{TSH} on ξ can be described by a $c \cdot (1 - \xi^2)$-function analogous to the non-converged $t_{it} = 10^{-14}$ s calculation. This means that the $s_{z,\boldsymbol{n}}$ real-space averaged product with the emergent magnetic field $\boldsymbol{\mathcal{B}}$ decreases the TSHE by a constant factor c relative to the spin-fixed calculations since a $(1 - \xi^2)$-factor directly appears in the TSHE expressions (Eq. 4.44). It is very plausible that this constant decrease demonstrates that $s_{z,\boldsymbol{n}}$ equilibrates to the same fraction of initially-chosen maximal $s_{z,\boldsymbol{n}}$ irrespective of ξ. Alternatively, this relation could still be influences by the correlation between the spin evolution and the real-space dependence of the emergent magnetic field.

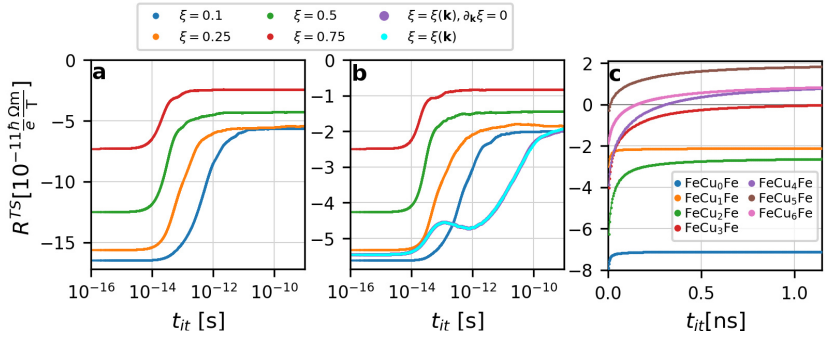

Figure 5.6: TSHE convergence with respect to the iteration-time t_{it}. a) and b) are small example calculations resolving several t_{it} orders of magnitude for (a) the model system (Sec. 6.2.1) and (b) $FeCu_2Fe$ (Sec. 8.2). In both cases constant $\xi = \{0.1, 0.25, 0.5, 0.75\}$ is enforced, while the inherent ξ of $FeCu_2Fe$ is included as well. Only few $\boldsymbol{k}$-points resolving the Fermi lines, $N_{k,\text{model}} = 64$ and $N_{k,FeCu_2Fe} = 300$, and an initial $\boldsymbol{R}$-grid of $N_R = 8$ are used, since these calculations only demonstrate the general mechanism. In c) the THSE convergence of several $FeCu_nFe$-trilayers (Sec. 8.3) with different thicknesses and their inherent ξ are displayed in the relevant timescale of 1ns. The calculations otherwise are well converged with $N_k = 32786$ and $N_R = 10$.

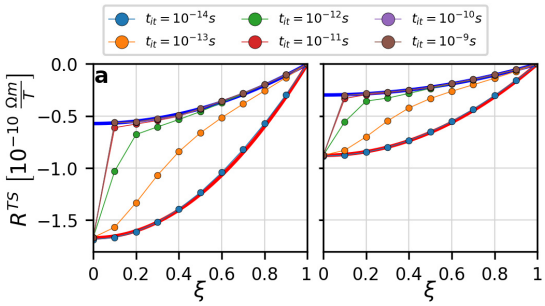

Figure 5.7: TSHE convergence with respect to ξ for various color-coded t_{it}. a) shows calculations for the model system (Sec. 6.2.1) and b) is the $FeCu_2Fe$ (Sec. 8.2) analogue with enforced ξ. To reduce the computational demand only rough Fermi line interpolations, $N_k = 64$ for the model and $N_k = 300$ for $FeCu_2Fe$, with an 8×8 initial $\boldsymbol{R}$-grid are used. The functions $a(1-\xi^2)$ are depicted, where a is either chosen to match the mean $R^{TS}(\xi = 0)$ over all iteration-times (red) or obtained from fitting the function to the 1 ns line excluding $\xi = 0$ (blue).

Still, it is more probable that the effect of the emergent magnetic field averages out so that the first interpretation is true. This conjecture could be checked assuming an homogeneous emergent magnetic field while retaining the previous spin dynamics.

Fitting the $c \cdot (1-\xi^2)$ function to the converged values (blue line) results in $c_\cdot \approx 0.343 c_0$ and $c_\cdot \approx 0.340 c_0$ for the model and the $FeCu_2Fe$ calculation, respectively. c is the prefactor of the converged R^{TS} while c_0 is the prefactor of the initial red line. This similarity indicates that the uncovered relation is independent of bandstructure details (e.g. group velocities) as expected due to the geometrical properties of the spin equations of motion [76]. This simple relation might be broken in case of $\partial_{\boldsymbol{k}}\xi \neq 0$ as the anomalous velocity correction in the equations of motion (Eq. 3.38) modify the real-space path. However, TSHE-calculations of $FeCu_2Fe$ in- and excluding $\partial_{\boldsymbol{k}}\xi$ with the inherent ξ (Fig. 5.6b) reveal only minor differences so that the relation still holds. At this point the decrease to almost $1/3$ could depend on specific features of the $3\boldsymbol{q}$-texture but later calculation (Sec. 9.4) demonstrate the TSHE's topological independence on the skyrmion texture eliminating this possibility, too. Overall, this additional reduction to $1/3$ gives a simple rule of thumb for estimating the impact of the non-collinear properties.

In realistic systems ξ is $\boldsymbol{k}$-dependent so that the previous systematical decrease is not as apparent as in the previous example calculations with constant ξ. Instead, the different decreasing factors are well hidden in the $\boldsymbol{k}$-integral so that further scrutiny is necessary to obtain analogous results. As previously stated, it is difficult to obtain converged transport values for $\boldsymbol{k}$ with very small ξ. In Fig. 5.6c otherwise converged t_{it}-dependent TSHE calculations for FeCuFe trilayers with different Cu thicknesses are shown. Large changes are occurring up to 1 ns which is much larger than the 0.01 ns of the $\xi = 0.1$ example calculations and therefore indicates Fermi line sections with much smaller ξ's. Still, R_{TSH} is sufficiently converged after $t_{it} = 1$ ns which is used as default value in the following. Much larger t_{it}

are computationally very demanding when choosing the other computational parameters reasonably large. Nevertheless, few calculations up to 10 ns reaffirm the default t_{it} choice for realistic example systems.

Lastly, it is worthwhile to note a problem arising from the strict periodicity of the magnetic texture which emerges if the group velocity is parallel to a high-symmetry line of the magnetic texture. In that case the wave-packet is restricted to a 1-dimensional slice of the texture spanned by the group velocity and the initial real-space position unless significant spin- or texture-dependent transversal velocity components arise. The anomalous velocity term of the collinear antiferromagnetic case proportional to $\partial_{\boldsymbol{k}}\xi$ causes such modification and is often, but not always, of sufficient magnitude. Otherwise, and for equations of motion without such terms, the restriction of the trajectory results in very large t_{it}-requirements or even prevents reasonable convergence entirely if the setup is not ergodic. The likelihood for group velocities parallel to the magnetic lattice vectors is increased by the Fermi surface construction starting with the outmost $\boldsymbol{k}$-point along a unit direction as their group velocities often point along the high symmetry lines. Hence, the probability of restricted phase-spaces can be reduced by rotation of the magnetic texture so that the high-symmetry lines of the reciprocal space and the texture are tilted with respect to each other. Nevertheless, it is still likely that the group velocities of some $\boldsymbol{k}$-points are almost aligned to the rotated texture lattice-vectors increasing their t_{it}-requirements significantly. A reasonable approach to circumvent this problem is the combination of calculation with differently rotated textures excluding the few unconverged $\boldsymbol{k}$.

5.3.4 Initial real-space grid

The last remaining numerical parameter is the number of initial $\boldsymbol{R}$-grid points from which the iterations are started. The initial grid is spanned by the magnetic lattice vectors divided by N_R starting at $\boldsymbol{R} = 0$ as defined by the chosen texture. Hence, N_R denotes the number of inequivalent points along each lattice direction so that for $N_R = 8$ actually 64 initial wave-packet positions are used.

Physically, transport calculations are started from wave-packets with texture-aligned spins due to previous spin-scattering, the TSHE is then obtained from the ensuing wave-packet dynamics. Since a homogeneous electron distribution function is assumed, $\partial_{\boldsymbol{r}} f = 0$ (Sec. 4.3.1), all positions within the unit cell are equally probable as starting points. Accordingly, the use of a large initial grid covering the whole magnetic texture is strongly motivated from this physical picture.

On the other hand, the spin will go through the entire texture following a complicated spin evolution which results in alignment with the texture at other positions in the magnetic unit cell throughout the iteration. Hence, the remainder after each alignment can be interpreted as a calculation started at that position with a respective shorter t_{it}. Hence, in this interpretation only small N_R seem necessary since the previous chapter's convergence requires very large t_{it} which anyways results in the passage through many magnetic unit cells. Thus, it is likely that the spin equilibration is more important than a large N_R. Yet, large N_R are still advantageous as they certainly help resolving the magnetic texture and accordingly the emergent magnetic field, but, as the main convergence originates in spin equilibration and since all states start from aligned positions, large N_R will not enhance that convergence significantly. In principle

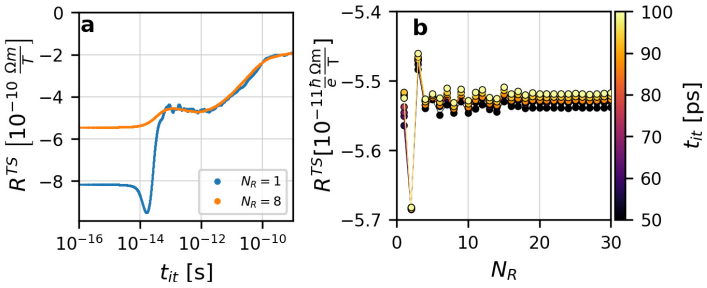

Figure 5.8: Impact of varying N_R. a) shows the convergence of R^{TS} over several orders of magnitude of t_{it} for $N_R = 1$ and $N_R = 8$ in case of the $FeCu_2Fe$ system with $N_k = 300$ and DFT-based ξ analogue to Fig. 5.6. In b) the convergence of R^{TS} of the model of Sec. 6.2.1 ($\xi = 0.25$) with $N_k = 64$ is displayed. Intermediate results with t_{it} between 50 ps and 100 ps are included through the color scale.

even an iteration from only one position should still reach a converged result equivalent to large N_R-calculations if iterated for an infinite time. Since the previous consideration provide no clear criterion for a good N_R-choice, the N_R-dependence of TSHE-calculations is tested from example systems in the following.

The t_{it}-dependence using different N_R is depicted in Fig. 5.8a where significant differences between $N_R = 1$ and $N_R = 8$ are apparent. For very small t_{it} the R^{TS} necessarily differ tremendously as the $N_R = 1$ calculations contains only the emergent magnetic field of its initial position and accordingly assumes a constant $\mathcal{B}$ everywhere in contrast to the average of the 8×8 texture grid of the second calculation. Since the initial R^{TS} of the $N_R = 1$ calculation is much larger, it has to start at a position with large $\mathcal{B}$. When approaching a t_{it} for which the magnetic unit cell is traversed, the $N_R = 1$ calculation has very strong oscillations while the other behaves very smooth on the shown scale. At $t_{it} \approx 10^{-13}$ the overall transport effect becomes comparable which corresponds to the crossing of few magnetic unit cells judging from the average group velocity. Yet, oscillations around the R^{TS} of the $N_R = 8$-calculation appear until the end of the iteration at $t_{it} = 1$ ns. The final difference at $t_{it} = 1$ ns is very small with approximately 0.3% which verifies the previous prediction that the texture details are sufficiently resolved due to the long iteration-times alone. Still, medium sized N_Rs should be used as their smoother t_{it}-dependence allows better judgment of the convergence.

A more systematic investigation of the R^{TS}'s convergence with respect to N_R is given in Fig. 5.8b. There, the R^{TS} N_R-dependence is shown for model calculations including the rough t_{it}-dependence. The transport seems converged on the chosen scale for $N_R \geq 18$ yet only the $N_R \leq 3$ show really large changes. In between, i.e. $3 < N_r < 18$, the final R^{TS} differ by less than 0.4%. Since the iteration-times from 50 ps to 100 ps are depicted, the smoothness of the convergence can furthermore deduced. For $N_R > 8$, R^{TS} is increasing less and less with increasing t_{it} which indicates a smooth, slowly convergent behavior. On the other side, the t_{it}-dependence becomes increasingly erratic with decreasing N_R. The behavior of $N_R = 2$ is especially dangerous as it coincidentally appears to be t_{it}-converged although it is a severe

outlier with respect to the other N_R.

In conclusion, t_{it} is a more important convergence parameter than N_R, yet the usage of intermediate values is definitively advantageous. Large N_R, such as $N_R = 30$, result in excessive computational demand due to the quadratic scaling originating in the definition of N_R as the number of points in each lattice direction. However, very small N_R such as $N_R = 2$ can lead to an unstable convergence or even wrong, pseudo-converged values. Accordingly, $N_R = 8$ or $N_R = 10$ are often chosen in the following which are neither excessive nor risky. In principle, the grid sizes could be chosen inequivalent along different directions but only equal spacings are used in this thesis since skyrmions are usually rather symmetric.

6

Antiferromagnetic bilayer model

This chapter introduces a simple antiferromagnetic bilayer model Hamiltonian and investigates its transport properties. Although this rough model is a poor approximation of realistic systems, it is a great starting point due to its transparency and tunability. Hence, it is mainly used to estimate the necessary size of numerical parameters in Sec. 5.3 . Furthermore, the detailed investigation of its transport properties, described in Sec. 6.2, allows a basic understanding of the TSHE.

6.1 Model setup

This section introduces an antiferromagnetically-coupled bilayer square-lattice model (Fig. 6.1a) which is based on the model initially used to investigate the degenerate wave-packet dynamics in Ref. [76]. It contains 3 principal parameters, the s-d exchange J and the intra- and inter-plane nearest-neighbor couplings T and t. Each atom, respectively denoted by A and B for the upper and lower layer, has one state for each spin. In the basis $\{|A\uparrow\rangle, |A\downarrow\rangle, |B,\uparrow\rangle, |B,\downarrow\rangle\}$ the Hamiltonian is expressed as the following matrix:

$$H(\boldsymbol{k}) = \begin{bmatrix} J + H_0(\boldsymbol{k}) & 0 & t & 0 \\ 0 & -J + H_0(\boldsymbol{k}) & 0 & t \\ t & 0 & -J + H_0(\boldsymbol{k}) & 0 \\ 0 & t & 0 & J + H_0(\boldsymbol{k}) \end{bmatrix}. \tag{6.1}$$

Hence, the antiferromagnetic character is included through the s-d exchange with spins along the z-axis where the spin of atom A is of down character and vice versa. The Hamiltonian's entire $\boldsymbol{k}$-dependence comes from the in-plane nearest neighbor hopping via H_0, which is a sum of cosines due to the square lattice structure:

$$H_0 = T \sum_{\boldsymbol{\delta}} \mathrm{e}^{\mathrm{i}\boldsymbol{k}\cdot\boldsymbol{\delta}} = 2T\left(\cos(k_x a) + \cos(k_y a)\right). \tag{6.2}$$

Here, a denotes the lattice constant so that the in-plane nearest neighbor vectors are $\boldsymbol{\delta} = (\pm a, 0, 0)$ and $(0, \pm a, 0)$.

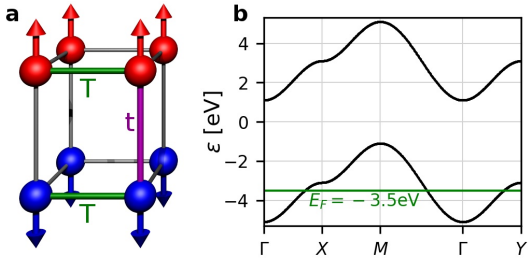

Figure 6.1: a) Schematic structure of the model system with colored interaction directions. b) Bandstructure corresponding to the parameters of Tab. 6.1 with the green line denoting the Fermi energy chosen in Sec. 6.2.1.

The bandstructure (Fig. 6.1) is given by 2 twofold-degenerate, non-crossing bands which have the dispersion:

$$\epsilon_{\pm} = 2T\left(\cos(k_x a) + \cos(k_y a)\right) \pm \sqrt{J^2 + t^2}, \tag{6.3}$$

where ϵ_+ and ϵ_- denote the upper and lower band, respectively. The energy branches are separated by $2\sqrt{J^2 + t^2}$ irrespective of $\boldsymbol{k}$. The eigenstates, obtained from direct diagonalization, are:

$$\begin{aligned}
|u_{-\uparrow}\rangle &= \left(\frac{t}{\sqrt{J^2 + t^2} - J}\,|A\uparrow\rangle + |B\uparrow\rangle\right)/\mathcal{N}_1,\\
|u_{-\downarrow}\rangle &= \left(\frac{t}{\sqrt{J^2 + t^2} + J}\,|A\downarrow\rangle + |B\downarrow\rangle\right)/\mathcal{N}_2,\\
|u_{+\uparrow}\rangle &= \left(\frac{-t}{\sqrt{J^2 + t^2} + J}\,|A\uparrow\rangle + |B\uparrow\rangle\right)/\mathcal{N}_2,\\
|u_{+\downarrow}\rangle &= \left(\frac{-t}{\sqrt{J^2 + t^2} - J}\,|A\downarrow\rangle + |B\downarrow\rangle\right)/\mathcal{N}_1.
\end{aligned}$$

The $\pm$ denotes the different energy branches and $\mathcal{N}_i$ is the respective normalization factor.

Subsequently, ξ can be calculated by evaluating $\langle\eta_1|\eta_2\rangle$ for each band as required by Eq. 3.32. Utilizing the explicit form of the eigenstates (Eq. 6.4), the expression of the lower band becomes

$$\xi_1 = \frac{1}{\sqrt{\mathcal{N}_1\mathcal{N}_2}} \cdot \sqrt{\frac{t}{\sqrt{J^2 + t^2} - J} \cdot \frac{t}{\sqrt{J^2 + t^2} + J} + 1}.$$

This equation can be severely simplified by explicitly evaluating the normalization factor which results in

$$\xi = \frac{|t|}{\sqrt{t^2 + J^2}} \tag{6.6}$$

for both bands. As the eigenstates are $\boldsymbol{k}$-independent, ξ is $\boldsymbol{k}$-independent as well. Hence its $\boldsymbol{k}$-derivatives vanish, i.e. $\partial_{\boldsymbol{k}} \ln(\xi) = 0$, so that the equations of motion are severely simplified as the additional velocity term (Eq. 3.38c) vanishes.

The in-plane hopping parameter T only determines the width of the bands which is given by $8T$. Band crossings are impossible as the bands are $\boldsymbol{k}$-independently split by $\sqrt{J^2 + t^2}$. Still, both bands can have states at the same energy although not at the same $\boldsymbol{k}$. As the bands differ only by a constant offset, each band's energy-adjusted transport contributions are the same. Consequently, and to keep the calculation simple, the parameters are subsequently chosen so that the band splitting is larger than the band's width. Hence, only one Fermi surface has to be considered, in the following the lower band is chosen.

The parameters J and t determine the overlap ξ and the band separation. At least one of them has to be non-zero to avoid fourfold degenerate states. That case would leave the scope of this thesis as the wave-packet dynamics of Sec. 3.2.1 would be inapplicable. When setting $t = 0$, both layers are totally decoupled resulting in $\xi = 0$, so that the antiferromagnetic transport equations become equivalent to two ferromagnetic transports expression with antiparallel spins. For $J = 0$ the opposite limit of $\xi = 1$ is obtained. In that limit no spin evolution occurs any more in the global frame and the effect of the emergent magnetic field vanishes together with the TSHE. This is understandable as the distinction between spin-up and -down states vanishes with the exchange coupling. For a given J, the overlap ξ can be selected by choosing t according to:

$$t = \frac{J\xi}{\sqrt{1 - \xi^2}}. \tag{6.7}$$

Due to the relation between t and ξ, the interpretation of the overlap ξ as the coupling between the both magnetic sublattices, i.e. the interlayer coupling, is validated. Since $t(\xi) \propto J$, strong exchange decreases ξ counteracting the direct coupling. This relation is to be expected as stronger exchange increases the tendency of the wave-packet's spin to follow the texture, i.e. the wave-packet's weight is impeded from shifting to the other magnetic sublattice.

6.2 Transport

This model allows for a simple calculation of the transport properties and intuitive interpretations of the relation to the bandstructure. Thereby, a basic understanding of the transport's dependence on the reciprocal-space structure is obtained before investigating more complicated, DFT-based systems as in Sec. 8. In the following, the $\boldsymbol{k}$-dependence of the different transport components is investigated for a constant Fermi energy to demonstrate the direct dependence on the $\boldsymbol{k}$-resolved group velocities and effective masses. This is followed by the Fermi energy dependence of the TSHE which allows to investigate the transport impact of varying Fermi surface averaged reciprocal-space properties.

In principle, the transport responses to modifications of the Hamiltonian parameters could be studied, but, since the only modification to the dispersion are constant shifts or band width variations, the transport impact is trivially predicable. The only interesting effect when varying the parameters is the variation of ξ which is already depicted in Fig. 5.7a and explained in the corresponding Sec. 5.3.3. Hence, this section is primarily focused to the parameters of Tab. 6.1. As the exchange J dominates the Hamiltonian, the bands are well separated with

J [eV]	T [eV]	t [eV]	a [a_B]
3	0.5	~ 0.77	4

Table 6.1: Model-Hamiltonian parameters used in this section. t is chosen such that $\xi = 0.25$ according to Eq. 6.7.

an indirect band gap of approximately 2.2 eV (see Fig. 6.2a). $d_z = 10a_b$ is chosen as layer thickness necessary for the calculation of conductivities. Due to the simplistic structure of the dispersion, the same bandstructure with $\xi = 0$ can be achieved by setting $t = 0$ and $J \approx 3.1\,\text{eV}$.

6.2.1 Constant Fermi energy

The Fermi surface at half filling consists of straight lines crossing in right angles at the Brillouin zone boundary due to the cosine structure of the energy dispersion (Eq. 6.3). Hence, $E_F = -3.5\,\text{eV}$ with a more typical Fermi surface is arbitrarily chosen for the following in-depth investigation of the $\boldsymbol{k}$-dependent dispersion and transport properties.

The group velocity and effective masses at the Fermi surface are depicted in Fig. 6.2. The group velocity is highly symmetrical and everywhere of comparable magnitude. While the off-diagonal effective masses vanish as is obvious from the dispersion (Eq. 6.3), the remaining diagonal masses are dominated by negative values although positive sections appear as well.

Assuming the $3\boldsymbol{q}$-texture (Sec. 2.4.1), the transport properties are calculated according to Sec. 5 in which the dependences on various numerical parameters for this system are described and depicted (e.g. Fig. 5.5a, Fig. 5.8a). Here, $N_k = 400$, $N_R = 8$, and $t_{it} = 1\,\text{ns}$ are used which ensures sufficient convergence. This setup results in $R^{TS} \approx -5.47 \cdot 10^{-11} \frac{\hbar}{e} \frac{\Omega\text{m}}{\text{T}}$ which is a realistic magnitude for such effects as the analogous THE of ferromagnetic skyrmion structures is of surprisingly similar magnitude (experimentally MnSi $R^T = -4.5 \cdot 10^{-11} \frac{\Omega\text{m}}{\text{T}}$ [41]).

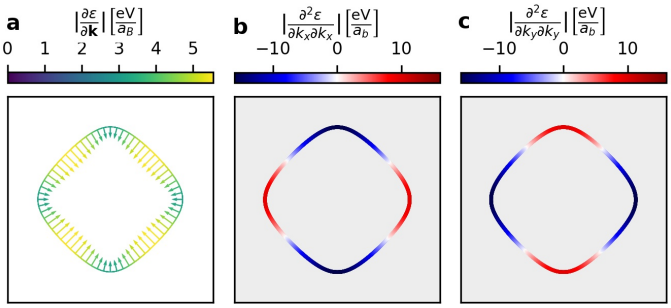

Figure 6.2: This figure shows the Fermi surface properties for $E_F = -3.5\,\text{eV}$ using the parameters of Tab. 6.1. a) displays the group velocity $\partial_{\boldsymbol{k}}\epsilon$. b) and c) visualize the diagonal effective masses $\partial^2_{\boldsymbol{k}}\epsilon$. The off-diagonal masses $\partial_{k_x}\partial_{k_y}\epsilon$ vanish due to the simple structure of the dispersion (Eq. 6.3).

Due to the Fermi surface integration in the calculation scheme, it is possible to associate each Fermi line point with a transport contribution using the definition

$$\sigma = \sum_i l_i \sigma(\boldsymbol{k}_i), \tag{6.8}$$

with the weights l_i from Eq. 5.5. Hence, different $\boldsymbol{k}$-resolved conductivity terms can be calculated independently and subsequently related to bandstructure properties.

The first component to the conductivity, $\sigma^1(\boldsymbol{k})$, is displayed in the first row of Fig. 6.3. The Fermi integrals of the transversal components σ^1_{xy} and σ^1_{yx} vanish due to very symmetric structure where each quadrant is canceled by its neighbor in either direction due to its relative minus sign. The diagonal elements describe the usual longitudinal conductivity determining the scale to quantify the effect of the following non-vanishing transversal conductivities. Accordingly, they do not vanish as expected from the $\dot{r}_i \dot{r}_j$ term in $\sigma_i^{(1)}$ due to the absence of a sign change. Likewise, the overall shape of σ^1 can be easily deduced from the group velocities in Fig. 6.2a. For example, $\sigma^1_{xx}(\boldsymbol{k})$ is minimal on the $\overline{\Gamma Y}$ line while $\sigma^1_{yy}(\boldsymbol{k})$ is maximal along that line since $\dot{\boldsymbol{r}}$ is pointing in y-direction. In case of $\xi = 0$ the first component of the spin conductivity, $\sigma^{1,s_z}(\boldsymbol{k})$, has almost the same behavior as $\sigma^1(\boldsymbol{k})$. The only differences are an additional $0.5\hbar/e$-prefactor for each initial spin alignment and reversed signs for one of the spins. The latter difference has tremendous impact as it leads to a cancellation of σ^{1s_z} when finally summing over the spin states. Conversely, $\sigma^{1s_z}(\boldsymbol{k})$ vanishes already at each point on the Fermi line in case of non-zero ξ. This originates in the fact, that the wave-packet's spin varies tremendously during the iteration which destroys the clear picture of initial spin-up and -down states resulting in a spin average already on that level. As the canceling sum of the

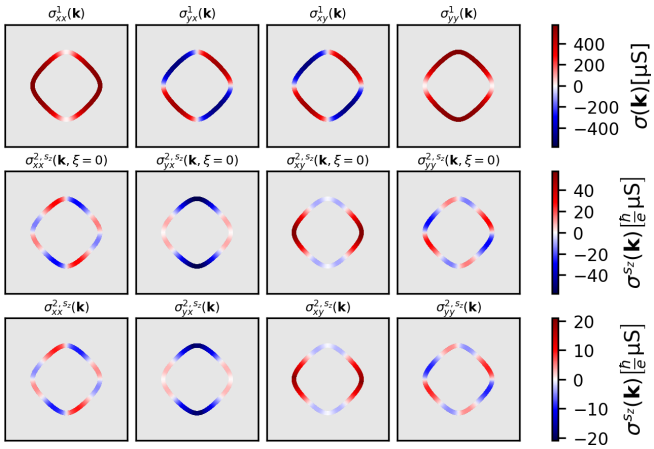

Figure 6.3: $\mathbf{k}$-resolved conductivities using parameters of Tab. 6.1 at $E_F = -3.5\,\mathrm{eV}$ with $\tau = 4000\,[\hbar/E_h]$. The columns denote the tensor elements in the 2D plane. The rows correspond to the conductivity components σ^1 (Eq. 4.34), σ^{2,s_z} with $\xi = 0$, and σ^{2,s_z} with the "inherent" $\xi = 0.25$ (Eq. 4.44).

different initial spin state calculations with $\xi = 0$ corresponds to such a spin average, the above direct cancellation for $\xi \neq 0$ is apprehensible.

The $\sigma^{2,s_z}(\boldsymbol{k})$ spin conductivity causing the TSHE is displayed in the second and third row of Fig. 6.3 for $\xi = 0$ and $\xi = 0.25$, respectively. Since ξ is $\boldsymbol{k}$-independent, only the conductivity magnitude changes between both rows. The charge conductivity contributions $\sigma^2(\boldsymbol{k})$ for each initial spin alignment would differ when comparing $\xi = 0$ and $\xi = 0.25$, but in the end they integrate to zero exactly analogous to the above case of $\sigma^{1,s_z}(\boldsymbol{k})$. Hence, the THE vanishes as expected. The Fermi surface integrated diagonal σ^{2,s_z} xx- and yy-components vanish due to the $k_x = 0$ and $k_y = 0$ mirror planes, respectively. One symmetry less than in case of σ^1 enforces the cancellation of the Fermi surface integral owing to the dependence on the effective masses (Fig. 6.3b,c) which each have one mirror symmetry each in contrast to the two mirror symmetries of the group velocity. Since the off-diagonal effective masses vanish due to the simple construction of this model, the origin of the off-diagonal $\sigma^{2,s_z}(\boldsymbol{k})$ components is very transparent. According to Eq. 4.44 $\sigma^2_{ij}(\boldsymbol{k}) \propto \dot{r}_i m_{jj} \varepsilon_{l3j} \dot{r}_l$ with m as the effective mass tensor. Hence, the diagonal conductivity terms vanish along the unit-direction high-symmetry lines as group velocity projections in both unit directions appear in the transport expression while the group velocities are parallel to the unit-directions. Furthermore, their Fermi surface integral vanishes due to high symmetry of the group velocity which results in an overall sign change when executing m's symmetry operation. Conversely, the transversal components $\sigma^{2,s_z}_{ij}(\boldsymbol{k})$ are proportional to $\dot{r}_i^2$ which prevents a respective sign change when applying the symmetry of m_{jj} so that their Fermi surface integral does not vanish. The net σ^{2,s_z}_{ij} is decreased by small sections with opposite sign, yet the simple structure permits a straight forward interpretation of the integrated transport for the $\boldsymbol{k}$-resolved case allowing predictions for parameter variations. Furthermore one should note that the ratio of σ^1 and σ^2, which have the same units and could be used to calculate the spin Hall angle, is not very realistic due to their different scaling with respect to the fairly arbitrarily chosen τ.

6.2.2 Varying Fermi energy

Variation of E_F has a very systematic impact on the transport properties due to the simple bandstructure evolution. Fig. 6.4a depicts the different iso-energy lines which allows simple association of E_F-dependent transport variations to bandstructure changes. When going through the whole band width from bottom to top, the bands first appear circular around Γ, then increase their radius and become more square-like until forming a square with corners at $\pm X$ and $\pm Y$. This is followed by a reversed symmetric repetition from the square back to the circle now centered at M where the Fermi line ultimately vanishes.

In order to interpret the transport effects, it is convenient to first describe the evolution of the reciprocal-space properties. Each $\boldsymbol{k}$'s group velocity has an inverse partner pointing into the opposite direction at $-\boldsymbol{k}$ and the group velocities along the high symmetry lines always point antiparallel to that direction (Fig. 6.2). $|\partial_{\boldsymbol{k}} \epsilon|$ vanishes at the edges of the band, i.e. $E_F \approx \{-5.1, -1.1\}$, and is maximal at half filling, yet for the majority of the covered energies the maximal values are of similar magnitude. While the group velocity is maximal for some $\boldsymbol{k}$ at half filling, it is actually vanishing for other $\boldsymbol{k}$. Since the group-velocity Fermi surface integral vanishes due to aboves inversion relation, it is sensible to directly look at the

Fermi surface average of $(\partial_{k_x}\epsilon)^2/|\partial_{\boldsymbol{k}}\epsilon|$. This quantity is directly related to $\sigma^{(1)}_{xx}$ (Eq. 5.2) and accordingly lies directly above the numerical results of Fig. 6.4b. In that plot all quantities are rescaled to have visually the same maximal value, hence the different prefactors to finally obtain the conductivity have no impact. When comparing the depicted Fermi surface length to the group velocity, differences are directly apparent. The overall group velocity is very small near the edges since the FS-length is larger, then the group velocity magnitude increases significantly enhancing the relative impact of the group velocity integral. Afterwards the FS-length drastically increases when forming the square in the Brillouin zone, yet many $\boldsymbol{k}$-sections have decreasing group velocity magnitude so that the diagonal transport increases only slightly near half filling. The upper half in energy is the exact mirror image of the lower half so that their interpretation is analogous.

The other necessary, non-vanishing quantity is the diagonal effective mass. Its Fermi surface integral dependence on E_F is shown in Fig. 6.4c. Its glaring properties are the fast initial increase despite the small FS-length and the zero crossing at half filling followed by a sign-reversed, mirror-symmetric upper half. When investigating the effective mass $\boldsymbol{k}$-resolved, this behavior can be readily understood. At the lowest E_F the effective masses are maximal and quickly decrease with increasing E_F. At first its Fermi surface integral is large despite the very small Fermi lengths as the $\boldsymbol{k}$-resolved masses are very large and uniform due to the band's approximately parabolic behavior near Γ and M (Eq. 6.3). After $\sim 1\,\mathrm{eV}$ some $\boldsymbol{k}$-points start to have negative contributions and m starts to decrease. Although the integration weight is rapidly increasing, the overall mass integral is ever decreasing until the negative and

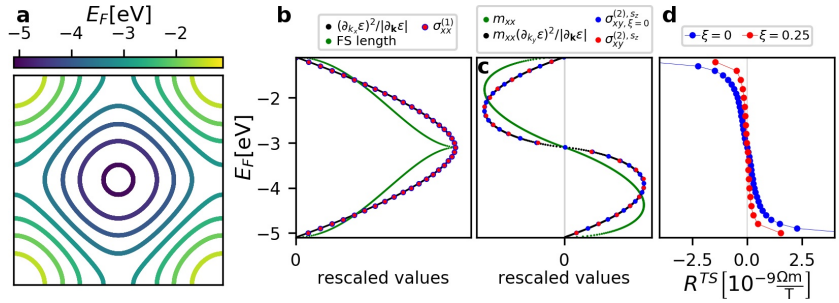

Figure 6.4: a) demonstrates the evolution of the Fermi surface from $E_F = -5\,\mathrm{eV}$ to $E_F = -1.5\,\mathrm{eV}$ in steps of $0.5\,\mathrm{eV}$.b-d) show the E_F-dependence of the transport properties and related Fermi-surface integrated bandstructure quantities. The longitudinal conductivity σ^1_{xx} is displayed together with its $\boldsymbol{k}$-dependent parameters as described in Eq. 5.2. Correspondingly, the transversal conductivities σ^2_{xy} for $\xi = 0$ and $\xi = 0.25$ are displayed with the $\boldsymbol{k}$-dependent parameters from Eq. 5.3 and the diagonal effective mass m_{xx}. Notice that all quantities displayed in b) and c) are scaled to fill the same range of the x-axis despite differences in their units. Especially σ^2_{xy} is of different magnitude for the different ξ. Finally, d) shows the E_F-dependence of the topological spin Hall constant R^{TS}. The transport calculations are done with $N_k = 400$, $N_R = 8$, and $t_{it} = 1\,\mathrm{ns}$ for $\xi = 0.25$.

positive contributions finally cancel each other at half filling. Afterwards, the negative parts of the Fermi surface are increasing even more ensuring the overall negative contributions of the upper half as they behave analogous to the previously positive sections.

As the final transport quantity is proportional to masses and velocities, $\sigma_{ij}^{2,s_z}(\boldsymbol{k}) \propto \dot{r}_i m_{jj} \varepsilon_{l3j} \dot{r}_l$ (Eq. 5.3), the E_F-dependences of the Fermi surface averaged $m_{xx}\dot{r}_y^2$ and σ_{ij}^{2,s_z} are expected to be similar (Fig. 6.4c). As ξ is constant, the numerical transport calculations with $\xi = 0$ and $\xi = 0.25$ match the Fermi surface average of $m_{xx}\dot{r}_y^2$ perfectly when neglecting the different prefactors. Hence, in this model it is possible to deduce the transport characteristics from group velocity and effective masses only. The main features of the transport's E_F-dependence are determined by m, yet the group velocities prominently shift the transport maxima towards the band's edges. Hence, the initial σ_{ij}^{2,s_z}-rise is less drastic, but the sign change has a significantly more dramatic effect due to the large group velocity impact near half filling.

The topological spin Hall constant R^{TS}, shown in Fig. 6.4d, quantifies the TSHE. It exhibits the usual decrease when increasing ξ, yet their overall shape is the same as both conductivity contributions are equivalent neglecting prefactors.

More remarkable is the large increase of R^{TS} (Eq. 4.12) near the band edges. There, $R^{TS} \propto \sigma_{xy}^{2,s_z}/(\sigma_{xx}^1)^2$ is exceptionally enhanced due to the relative smallness of the group velocities and the relatively large magnitude of the effective masses. This strong effect at the band boundary has already been demonstrated for similarly simple models, even antiferromagnetic skyrmions, through different means of computation [72]. Yet, such exceptional enhancement is only to be expected very near energy gaps so insulating E_F-ranges are required where the TSHE vanishes altogether. In the conventionally considered, more applicable metallic systems usually several bands appear at each E_F. In that case the σ_{xx}^1 contribution caused by one band still decreases significantly when E_F approaches that band's edge, but the overall $1/(\sigma_{xx}^1)^2$ variation is significantly less drastic since several other bands still supply non-vanishing longitudinal contributions. σ_{xy}^{2,s_z} can still be relatively large so that the edges of bands are clearly visible in the data, yet increases by more than an order of magnitude as in this model are unlikely. One slight variation of this effect is the impact of Dirac cones where, in contrast to the usual vanishing below the band edge, the reversed Hall effects are observed when crossing the cone. Hence, although their effective masses are decreasing near the crossing energy, potentially twice as large transport responses occur when crossing a Dirac point. This is further investigated in Sec. 8.2.2 where a Dirac cone with the above transport signature is found in a realistic system.

Another interesting feature of the R^{TS} plot is the relatively small impact of σ^{2,s_z}'s drastic sign change at half filling. This extreme variation is only possible due to the large size of the Fermi line and the total compensation of the $\boldsymbol{k}$-resolved masses at half filling. Even small changes in the mass distribution result in massive modifications of σ^{2,s_z} due to the large overall weight, yet the group velocities and accordingly the longitudinal conductivities scale with the Fermi length as well so that the net effect onto R^{TS} is rather diminishing. This gives a foretaste of the large possible variations to come in more complicated systems (e.g. Sec. 8) where several $\boldsymbol{k}$-dependent σ^{2,s_z} of the same and different bands keep each other in check yet offer the potential for drastic variations.

7

Description of realistic systems

After examination of the TSHE in the simplistic bilayer model, naturally interest of its behavior in more realistic systems arises. In principle, one could develop new models or utilize existing ones, yet these approaches require implementation effort for each possible setup which is neither time-efficient nor versatile. Instead, it is advisable to utilize existing methods to efficiently describe the reciprocal-space structure of thin films.

A very general, albeit computationally expensive, tool to describe the electronic structure is density function theory (DFT). It enables *ab-initio* calculations and as such is not restricted to the verification of experiments but can also make successful predictions of unknown materials. Here, DFT is used to obtain the reciprocal-space properties of complicated, collinear systems as required in Sec. 5.1. In principle, the predictive power of DFT could be harnessed to directly estimate all necessary parameters for the transport calculations, but an intermediate step is preferable since direct interfacing to DFT codes is a hurdle and evaluation of many $\boldsymbol{k}$-points (e.g. Sec. 5.2.1) is computationally very expensive. Therefore, maximally localized Wannier functions are constructed to obtain an effective model that accurately describes the vicinity of the Fermi level while allowing numerically efficient evaluation. From this interpolation the Hamiltonian and spin operators in the Wannier function basis are finally attained which allows to employ the usual, already implemented, and transparent diagonalization schemes. Hence, this procedure allows to transform relatively arbitrary, extremely complicated initial systems to manageable effective models whose THE and TSHE can be readily calculated using this thesis' method.

In the following, the theoretical background of DFT and Wannier interpolation is very briefly described, followed by a short overview of the practical application.

7.1 Theory

7.1.1 DFT

The holy grail of solid state physics is the precise prediction of electron and nuclei behavior in atomic systems. Considering the kinetic energy T and the Coulomb interaction V, the

Hamiltonian of such a system is

$$H = T_e + T_n + V_{ee} + V_{en} + V_{nn}, \tag{7.1}$$

where e and n denote the terms with electrons and nuclei, respectively. The next step would be the solution of the Schödinger equation for a given atomic configuration. In order to have a chance at solving this problem, the corresponding full-particle wave-functions have to be representable at least. Yet, even for relatively small systems the memory requirement easily exceeds the number of atoms in the galaxy so that an universal approach to the general problem is impossible. Instead, a series of sensible approximations has to be applied to yield a calculable problem.

The first straightforward simplification is the Born-Oppenheimer approximation which decouples the motion of the electrons from the nuclei motion. This is justified as the nuclei mass is orders of magnitude larger than the mass of electrons. Hence, the electron Hamiltonian can be expressed as:

$$H_e = T_e + V_{ee} + V_{en}, \tag{7.2}$$

where the nuclei positions enter as an external parameter only. Accordingly, the latter calculations demand either the atomic positions as input or require sampling of several arrangements to find the energy minimum.

Still, the above Hamiltonian requires an inconceivable amount of computational power to describe more than the simplest systems due to the 2-particle interaction and the expression in terms of many-particle wave-functions. DFT can circumvent both problems by considering an effective single-particle interaction in terms of the electron density instead of the wave-functions as described in the following.

The Hohenberg-Kohn theorem allows to describe the system in terms of the electron density n. It consists of 2 statements. Firstly, it states that the ground-state wave-function is a unique functional of the ground-state electron density n_0 and, secondly, that n_0 is unique and minimizes the energy functional. Hence, all information is contained in n_0 which can be obtained by minimizing the energy. Thus, the many-particle wave-functions are no longer strictly necessary to obtain the observables, but the Hamiltonian still contains 2-particle interaction terms which makes its evaluation difficult.

This second problem is circumvented by considering the Kohn-Sham system. Its Hamiltonian

$$H_s = T_s + v_s \tag{7.3}$$

contains only a single-particle kinetic term T_s and an effective single-particle potential v_s, the Kohn-Sham potential, which has to be constructed so that the system's n_0 is exactly the same as the ground-state density of the full Hamiltonian. This Kohn-Sham Hamiltonian is much simpler to solve while its solution still contains all ground-state information of the fully interacting system.

This raises the question how to obtain the Kohn-Sham potential corresponding to a given interacting system. When expressing the total energy of the Kohn-Sham system as

$$E[n] = T_s[n] + E_{ext}[n] + E_H[n] + E_{xc}[n], \tag{7.4}$$

the Kohn-Sham potential is the functional derivative of the latter terms:

$$v_s = \frac{\delta \left(E_{ext}[n] + E_H[n] + E_{xc}[n] \right)}{\delta n}. \tag{7.5}$$

Here, E_{ext} is the external energy containing the atomic positions. As it has become a single-particle expression, its functional derivative is the corresponding external potential v_{ext} giving rise to the V_{en} of Eq. 7.2. E_H is the Hartree energy and as such a classical approximation of the Coulomb exchange. Its functional derivative results in the simple potential term

$$v_H = \int d\boldsymbol{r}' \; \frac{n(\boldsymbol{r}')}{|\boldsymbol{r} - \boldsymbol{r}'|}. \tag{7.6}$$

The final term, E_{xc}, is the exchange-correlation energy which contains all remaining corrections such as the correlation terms appearing in the general many-particle expressions and the missing Coulomb interaction terms not covered by the simplistic Hartree term. The functional derivative of $E_{xc}[n]$ is the exchange-correlation potential v_{xc}, so that the whole Kohn-Sham potential take the form

$$v_s = v_{ext} + v_H + v_{xc}. \tag{7.7}$$

In principle, the last procedures have only transfered the inability of describing v_s over to v_{xc}. Yet, this rearrangement has several advantages. v_{xc} no longer contains information of the actual physical system as those have been split of into v_{ext}, hence the unknown potential has become a system-independent quantity. Furthermore, an approximation of v_{xc} has been made more feasible since a major part of the Coulomb exchange has been split off in form of the Hartree term. Until now, all modifications after the Born-Oppenheimer approximation have been exact, even the transition from the interacting to the non-interacting systems. Unfortunately, this exactness is no longer maintainable as no exact form of E_{xc} is known. Instead, one has to resort to one of the multiple approximations that have been developed over the recent decades.

The plethora of approximations can be divided into different classes. The simplest kind is the local density approximation (LDA) [134]. The term "local" refers to the assumed locality of the exchange-correlation functional, i.e. v_{xc} at a position $\boldsymbol{r}$ depends only on $n(\boldsymbol{r})$. Hence, a locally homogeneous electron gas is always assumes from which an expression for v_{xc} is extracted. A natural extension of this approach is the inclusion of $\boldsymbol{n}$'s spatial gradients into the functional expression of E_{xc}. This approach is called general gradient approximation (GGA) [135]. In that case the surrounding densities are no longer constant so that several possibilities, and accordingly various different approximations, for constructing E_{xc} exist. Some aim at satisfying certain analytical requirements, others are constructed to agree with empirical measurements. Both kinds, and LDA, have advantages and disadvantages so that often an educated choice is necessary to ideally describe the investigated system. Other classes of E_{xc} approximations, not utilized in this thesis, are LDA+U [136], meta-GGA [137], and hybrid functionals [138]. LDA+U adds an explicit Coulomb repulsion to selected bands in order to improve the description of strongly-correlated materials, meta-GGAs include the second derivate of n thus often describing a kinetic energy density, and hybrid functionals

mix Hartree-Fock exchange energies with e.g. LDA E_{xc} to enhance the Coulomb exchange accuracy.

With the above, n-dependent approximations for E_{xc}, and through its functional derivative v_{xc}, the Hamiltonian of the Kohn-Sham system (Eq. 7.3) has an explicit form. The next step is solving the Kohn-Sham equations associated to H_s:

$$\left(\hat{T}_s + \hat{v}_s\right) |\phi_i\rangle = \epsilon_i |\phi_i\rangle \,. \tag{7.8}$$

Since $|\phi_i\rangle$ are single-electron wave-functions instead of the previous, memory-intensive many-particle wave-functions, the above equation can be solved with a reasonable effort. The ultimate goal is to find the ground-state density that minimizes H_s. From the eigenvectors $|\phi\rangle$ the electron-density can calculate according to:

$$n = \sum_i \langle \phi_i | \phi_i \rangle \,. \tag{7.9}$$

As v_s of Eq. 7.8 is again dependent on n, the Eqs. 7.8 and 7.9 form a coupled set that has to be solved self-consistently. In practice, one has to start from a guessed initial n which then defines v_s so that one can calculate $|\psi\rangle$ (Eq. 7.8). From those v_s one updates n (Eq. 7.9) and the whole procedure is repeated until n is converged. The final electron density is the ground-state density n_0 of the Kohn-Sham system which accordingly contains information of the fully interacting system.

A further, general problem is the choice of adequate basis functions to efficiently describe the Hamiltonian. In principle, very localized core electrons can also be described in the DFT framework so that huge variations of the wave function are to be expected near the nuclei positions. Such features are difficult to describe within a plane-wave basis commonly used in simple, effective models. Two distinct possibilities exist circumventing this problem, either v_s is smoothened near the nuclei or a different basis is introduced. The first case introduces the so-called "pseudopotentials". The huge advantage of that approach is its computational simplicity, while the mandatory creation or selection of these not necessarily transferable potentials is a severe disadvantage as it includes further external parameters. Prominent examples for alternative basis sets are atomic orbitals or the FLAPW method. The latter uses augmented plane waves (APW). In that basis set the system is divided into "muffin-tins", spherical sections enclosing the nuclei positions, and the interstitial area where spherical harmonics and plane-waves are used as basis functions, respectively. The further "F" and "L" stand for "full potential" and "linearized" where the former tackles the energy-dependence of the radial part in the muffin-tins and the latter includes non-spherical parts of v_s within the muffin-tins. This procedure has the advantage that all electrons are included in the calculation so that less external parameters are necessary. Furthermore, FLAPW results are usually considered to be more reliable than pseudopotential calculations, yet the implementation is more complicated and the calculation are more demanding.

Over the times DFT in various forms and implemented in multiple codes has been used to describe many different material properties. Here, it is only used to construct an effective model in combination with Wannier interpolation that extracts basic quantities. The practical application of DFT is further described in Sec. 7.2.

7.1.2 Wannier interpolation

Large scale evaluations of the previous DFT calculations are computationally expensive, thus an efficient interpolation method is sought for quick and accurate evaluation at arbitrary $\boldsymbol{k}$. Wannier interpolation as described in this section fulfills these requirements and is hence utilized in thesis' Secs. 8 and 9.

In order to outline the interpolation procedure, it is necessary to first describe the properties and definitions of the underlying Wannier functions. The fundamental reason for their applicability is their mathematical equivalence to Bloch functions with respect to the description of electronic structure. The main difference between Wannier- and Bloch functions is their real-space localization and delocalization originating in their respective Fourier transformation relation. This relation is most obvious for a single, isolated band described by a Bloch function $|\phi_{i\boldsymbol{k}}\rangle$. In that case, the corresponding Wannier functions can be constructed as

$$|w_{i\boldsymbol{R}}\rangle = \frac{1}{N}\sum_{\boldsymbol{k}} \mathrm{e}^{-\mathrm{i}\boldsymbol{k}\cdot\boldsymbol{R}}\,|\phi_{i\boldsymbol{k}}\rangle\,, \tag{7.10}$$

labeled by the Bravais lattice vectors $\boldsymbol{R}$ denoting the respective Wannier functions' localization. In case of an equidistant $\boldsymbol{k}$-grid with a set number of grid points in one lattice direction, the Wannier functions are periodically repeated after said number of unit cells in the corresponding direction. Furthermore, the real-space dependence of the Wannier functions at different $\boldsymbol{R}$ are related to each other through translational symmetry.

The most important property of the Wannier functions is their non-uniqueness. While change of a Bloch function's phase has no physical impact, the Wannier functions obtained through Eq. 7.10 can vary drastically depending on the chosen Bloch function's gauge. This property allows sampling for very localized basis states for which the interpolation of the system parameters is much simpler since most information is contained in the directly neighboring shells.

In case of multiple, entangled bands the situation complicates. Then, the N_W Wannier functions are constructed as a superposition of N_B Bloch states according to

$$|w_{i\boldsymbol{R}}\rangle = \frac{1}{N}\sum_{\boldsymbol{k}} \mathrm{e}^{-\mathrm{i}\boldsymbol{k}\cdot\boldsymbol{R}}\sum_{j=1}^{N_B} U_{ij}(\boldsymbol{k})\,|\phi_{j\boldsymbol{k}}\rangle\,, \tag{7.11}$$

where $U_{ij}(\boldsymbol{k})$ is a $N_W \times N_B$ transformation matrix mixing the Bloch functions into the Wannier functions. While those Wannier functions are no longer necessarily eigenstates of the Hamiltonian, they still provide an excellent basis to obtain a localized model of the Hamiltonian. A requirement is $N_W \leq N_B$ where $U_{ij}(\boldsymbol{k})$ is a unitary matrix in case of equality. The Wannier function's localization can be tuned through the gauge of the Bloch functions, now given through $U_{ij}(\boldsymbol{k})$, analogous to the single-band case.

The next step is finding an $U_{ij}(\boldsymbol{k})$ for which the Wannier functions are localized. Fortunately, a general scheme was devised and implemented which allows a minimization procedure to iterate towards maximally localized Wannier functions [139]. Broadly speaking, this method works by minimizing the quadratic spread functionals around the Wannier function center which serves as a localization measure. The procedure is relatively quick as the explicit

calculation of Wannier functions is not necessary, instead it is sufficient to evaluate numerical derivatives on a regular grid. If $N_W < N_B$, the "disentanglement" procedure [140] is first applied to obtain a connected subset of the Bloch functions thereby enforcing $N_W = N_B$ and minimizing the part of the spread functional contingent on the subset choice. Afterwards, unitary transformations are applied to $U_{ij}(\boldsymbol{k})$ in order to minimize the remaining spread functional by a steepest-descent or conjugate-gradient minimization algorithm [139].

After attaining the optimal gauge choice for the Bloch functions, the Hamiltonian interpolation is straightforward. At first the initial, $\boldsymbol{k}$-dependent Hamiltonian has to be projected onto the Bloch states chosen in the disentanglement procedure. Afterwards, the $U_{ij}(\boldsymbol{k})$ obtained from the minimization procedure are applied which yields the Hamiltonian H^{rot} in the accordingly rotated Bloch basis. Subsequently, the Hamiltonian $H(\boldsymbol{R})$ in the basis of the Wannier functions can be calculated by a simple Fourier transformation

$$\langle i|H(\boldsymbol{R})|j\rangle = \frac{1}{N}\sum_{\boldsymbol{k}} \mathrm{e}^{-\mathrm{i}\boldsymbol{k}\cdot\boldsymbol{R}} \langle i|H^{\text{rot}}(\boldsymbol{k})|j\rangle \,. \tag{7.12}$$

$\langle i|H(\boldsymbol{R})|j\rangle$ are the Hamiltonian matrix elements between Wannier functions $|i\rangle$ and $|j\rangle$ whose unit cells containing the centers are separated by $\boldsymbol{R}$. Since the Wannier functions are constructed to be maximally localized, the magnitudes of the $\langle i|H(\boldsymbol{R})|j\rangle$-components decrease quickly with increasing $\boldsymbol{R}$. Therefore, even a rough approximation of $\langle i|H(\boldsymbol{R})|j\rangle$ with only few $\boldsymbol{R}$ still describes the entire system reasonably well. Accordingly, a good interpolation of $\langle i|H(\boldsymbol{k})|j\rangle$ at arbitrary $\boldsymbol{k}$ is given through the inverse transformation

$$\langle i|H(\boldsymbol{k})|j\rangle = \sum_{\boldsymbol{R}} \mathrm{e}^{\mathrm{i}\boldsymbol{k}\cdot\boldsymbol{R}} \langle i|H(\boldsymbol{R})|j\rangle \,. \tag{7.13}$$

Efficient interpolations of other operators initially described in the Bloch basis can be analogously obtained by following the same steps starting from the converged $U_{ij}(\boldsymbol{k})$ as obtained from the Hamiltonian treatment.

7.2 Application

In this thesis the FLEUR code [141] is used as implementation of DFT. It is an FLAPW code especially tuned towards magnetic properties and allows native two-dimensional calculations. A huge advantage is the already existing, versatile interface to the wannier90 code [139] that implements the construction of Wannier functions.

Here, the main use cases for FLEUR are the construction of the ground state density, the subsequent preparation of the input files for the Wannier function generation, and the final expression of the Hamiltonian and the spin operator in terms of the Wannier functions. Moreover, FLEUR is used to evaluate the bandstructure with DFT accuracy to verify the quality of the Hamiltonian interpolation. In between, wannier90 is used to obtain the $U_{ij}(\boldsymbol{k})$ (Eq. 7.11) which results in maximally localized Wannier functions. Finally, the attained operators in the Wannier basis are imported into this thesis' main code from which several parameters are deduced. In the following, this overall procedure is described in more detail.

At first a system has to be chosen whose TSHE is calculated. Since no antiferromagnetic skyrmions are known experimentally, this thesis investigates only example systems to study the general mechanism. Having chosen a particular atomic configuration, the lattice structure has to be ascertained. In many cases structural properties are known reasonably well so that they can be taken from literature, alternatively relaxation calculations could performed where the lattice parameters and atomic positions are adjusted according to calculated forces while comparing the total energies. The latter procedure requires a multitude of self-consistent DFT calculations and accordingly necessitates significant computational resources.

Before proceeding with the self-consistent solution of the Kohn-Sham equations, the exchange-correlation potential has to be chosen. In this thesis either LDA (Sec. 9) or Perdew-Burke-Ernzerhof GGA [135] (Sec. 8) is used. SOC can be handily included through second variation during the primary iteration or based on previously converged densities without SOC. While the derivations of the THSE neglects SOC corrections expressed through the Berry curvatures, it is interesting to consider its corrections on the bandstructure level (Sec. 8.2.3). Throughout the self-consistent calculation the magnetic moments should converge toward the ground-state configuration. Yet, it is possible to flip magnetic moments switching between ferro- or antiferromagnetic orientations. In the subsequent iterations the system often converges towards an at least local minimum keeping the chosen magnetic configuration. In case of more than one converged density, the preferred configuration is identified by comparison of the total energies. Still, the alternative minima allow to study the impact of magnetic structures that are not the true magnetic ground states. Since neither of the investigated structures are really expected to exhibit skyrmions, it is reasonable to consider densities corresponding to antiferromagnetic configurations that are only local minima in order to achieve a more systematic study (Sec. 8.3).

The next step is the construction of maximally localized Wannier functions. At first, a reasonable set of bands has to be selected from the DFT calculation to lessen the computation effort of the ensuing interpolation by excluding states very far from the investigated energy range. Since the TSHE calculation depends on the Fermi surface properties, only bands in the extended vicinity of the Fermi energy are included. Ideally, all states of an isolated set should be included, but in metals a clear distinctions is often impossible. Hence, for optimal accuracy it is advisable to include many states relatively far away from the finally interpolated bands. Their impact will be small, but it is advantageous to have many states as that ensures sufficient degrees of freedom in the disentanglement procedure. Afterwards, the number of Wannier functions has to be chosen. Considering that the outermost Wannier functions will only loosely reproduce the bandstructure, the choice depends highly on the number of bands in the extended energy range of interest. Two possibilities exist as initial choice for the Wannier functions, either random phases or trial functions obtained from angular-moment dependent projection on the Bloch states can be used. Here, the latter is always chosen. Afterwards, the trial projections and the overlap between the different Bloch functions are constructed by FLEUR on a regular $\boldsymbol{k}$-mesh. As described in Sec. 7.1.2, the size of the mesh corresponds to the unit cell extend of the resulting Hamiltonian so that the mesh has to be sufficiently large. In this thesis usually a 12×12 mesh is used. Next, a "frozen window" is generously chosen around the investigated energy range which ensured that bands within are entirely included after disentanglement. With these prerequisites the disentanglement procedure of

the wannier90 code can be employed. After convergence of the associated spread functional, the Wannier functions are iteratively localized until sufficient convergence is reached. Then, the interpolated bandstructure constructed from the wannier90 code is compared to the DFT results (Fig. 8.2). If the dispersions agree well, the spin operator in the basis of maximally localized Wannier functions is extracted by using the respective FLEUR routines.

When aiming for accurate maximally localized Wannier functions, a common tuning parameter is the choice of the initial projections. While it should not matter in principle, severe differences are common with respect to the localization functional and the interpolated bandstructure. Especially when investigating symmetry-related band-structure features, it is advantageous to start from initial projections obeying that symmetries. Hence, it is advisable to try several initial projections from which the most localized result is selected.

After performing the previous procedures applying the FLEUR and wannier90 codes, the Hamiltonian $\langle i|H(\boldsymbol{R})|j\rangle$ and the spin operator $\langle i|S(\boldsymbol{R})|j\rangle$ are attained fully describing the system in the Wannier basis. Then, the Hamiltonian is interpolated according to Eq. 7.13 at arbitrary $\boldsymbol{k}$. The subsequent diagonalization employing LAPACK routines allows direct access to the energies and eigenvectors. Since doubly-degenerate systems are investigated, the eigenvector choice is not unique. As long as SOC is neglected, the different spin channels do not mix so that each eigenstate contains only states of one spin channel directly identifiable when calculating the eigenstates' spin. For convenience and continuity, the eigenstates are reordered so that the eigenstate with negative spin always precedes its degenerate complement while keeping the ordering by energy. In case of SOC the eigenstates are not spin-diagonal states so that the eigenstates are first recombined by diagonalization the spin-z component.

For the transport calculations the evaluation of the derivatives of the bandstructure and ξ is necessary, which can be extracted using the interpolation scheme. Due to the Fourier transformation structure of the interpolation, it is straightforward to calculate the $\boldsymbol{k}$-derivatives of an operator $\langle i|O(\boldsymbol{R})|i\rangle$ in the Wannier basis. The n-th derivative is:

$$\left\langle i \left| \frac{\partial^n O(\boldsymbol{k})}{\partial \boldsymbol{k}^n} \right| j \right\rangle = \sum_{\boldsymbol{R}} (\mathrm{i}\boldsymbol{R})^n \mathrm{e}^{\mathrm{i}\boldsymbol{k}\cdot\boldsymbol{R}} \langle i \,|\, H(\boldsymbol{R}) \,|\, j\rangle \,. \tag{7.14}$$

For the evaluation of the relevant quantities it is necessary to evaluate the operators in basis of the Hamiltonian eigenstates $|\boldsymbol{\psi}\rangle$. Computationally, this basis change requires only left and right multiplication of the eigenstate matrices as provided from the diagonalization:

$$\left\langle \psi_i \left| \hat{O} \right| \psi_j \right\rangle = \sum_{lm} \langle \psi_i \,|\, l\rangle \left\langle l \left| \hat{O} \right| m \right\rangle \langle m \,|\, \psi_i\rangle \,. \tag{7.15}$$

Using the above relations, the group velocity can be computed as the diagonal elements of the Hamiltonian derivative:

$$\frac{\partial \epsilon_i}{\partial k_j} = \left\langle \psi_i \left| \frac{\partial H(\boldsymbol{k})}{\partial k_j} \right| \psi_i \right\rangle . \tag{7.16}$$

In case of the second derivative further terms arise due to derivatives of the eigenstates [142]:

$$\frac{\partial^2 \epsilon_i}{\partial k_l \partial k_m} = \left\langle \psi_i \left| \frac{\partial^2 H(\boldsymbol{k})}{\partial k_l \partial k_m} \right| \psi_i \right\rangle + 2\Re \left\{ \sum_{\epsilon_j \neq \epsilon_i} \frac{\left\langle \psi_i \left| \frac{\partial H(\boldsymbol{k})}{\partial k_l} \right| \psi_j \right\rangle \left\langle \psi_j \left| \frac{\partial H(\boldsymbol{k})}{\partial k_m} \right| \psi_i \right\rangle}{(\epsilon_i - \epsilon_j)} \right\} . \tag{7.17}$$

The spin operator $\langle i|S(\boldsymbol{r})|j\rangle$ is used to obtain spin-polarized eigenstates as described above, to estimate the spin polarization P_s as used in $\boldsymbol{s_n}$, and to calculate the overlap ξ. The former quantities can be trivially obtained from the diagonal components of the spin operator in the $|\psi\rangle$-basis. Conversely, ξ is calculated from the off-diagonal spin components. The σ_x and σ_y spin matrices contain the overlaps between the spin-up and -down parts, hence ξ of band i can be constructed as:

$$\xi_i = \frac{1}{2}\left(\langle\psi_i|S_x(\boldsymbol{k})|\psi_j\rangle + \mathrm{i}\,\langle\psi_i|S_y(\boldsymbol{k})|\psi_j\rangle\right), \tag{7.18}$$

where j is the degenerate partner of i. While it is in principle possible to obtain $\partial_{\boldsymbol{k}}\xi$ through analogous equations, in practice numerical derivatives proved to be more stable so that this approach is used.

In conclusion, the above expressions allow to efficiently calculate all reciprocal-space dependent quantities necessary for the transport calculation scheme of Sec. 5. This procedure is employed in the following chapters to predict the TSHE in different materials based on accurate, collinear DFT.

8

FeCuFe-trilayer

After calculating the TSHE for a model system (Sec. 6), the next step is the investigation of more realistic systems using the DFT- and Wannier-based approach described in Sec. 7. Copper layers of varying thickness sandwiched between 2 antiferromagnetically coupled iron layers are chosen as an example system. Accordingly, this chapter investigates synthetic antiferromagnets including a more complicated reciprocal-space structure than the analogous bilayer model while keeping its imprinted real-space texture. The alternative approach of an intrinsic antiferromagnet is investigated in Sec. 9. Many results of this chapter have already been published in Refs. [21, 22].

First, this chapter describes the general structural and electronic properties, followed by an in-depth investigation of the TSHE for fixed thickness, and concluded by the TSHE's dependence on the layer thickness.

8.1 General structure

Layered systems with magnetic films separated by e.g. a paramagnetic spacer have been investigated for a long time and proven to exhibit interesting physics. Most prominently, the giant magnetoresistance effect [1, 143] was even awarded with a Nobel price. It describes the dependence of the electron transport through the multilayer on the relative alignment or anti-alignment of the outer spins. Here however, we are interested in transport within the multilayer.

An interesting feature of such multilayer systems is an often observed oscillatory behavior between ferromagnetic and antiferromagnetic coupling depending on the spacer thickness. Physically, this is explained by the RKKY interaction [144]. Many different material compositions exhibiting these properties have been discovered [145–149], yet none has been verified to exhibit a skyrmion texture. Hence, in order to study the TSHE with realistic electronic properties it is only possible to investigate hypothetical systems with artificially imprinted skyrmion textures until a material exhibiting synthetic antiferromagnetic skyrmions is discovered.

In this chapter, body-centered cubic $FeCu_nFe(001)$ is chosen as example system. In 1990, antiferromagnetic coupling was experimentally demonstrated in case of 3 Fe-monolayers on

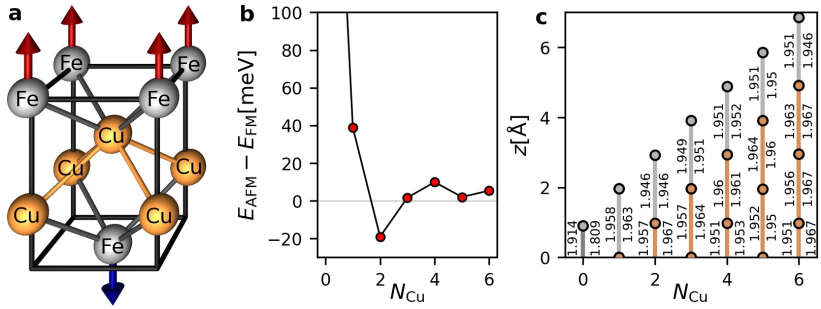

Figure 8.1: a) shows the $FeCu_2Fe$ structure as an example of the (001) bcc trilayer setup. b) displays the energy difference between the in z-direction relaxed ferro- and antiferromagnetic setups. In c) the rounded z-distances between the neighboring atoms are denoted left and right for the ferro- and antiferromagnetic structures, respectively.

each side using Kerr rotation [150]. Five years later, theoretical calculations with semi-infinite Fe crystals and varying Cu thickness examined the coupling in detail [151]. These early calculations utilize self-consistent Green's functions and the linear muffin-tin orbital method. One result of that early study is that the exchange coupling varies strongly with many sign changes even for very thick Cu thicknesses and that its magnitude decreases up to about 10 layers after which it increases again in agreement with RKKY model calculations.

Here, the freestanding trilayer with only 1 Fe-monolayer on each side is investigated. A schematic picture of the structure in case of 2 Cu-layers is given in Fig. 8.1a. In the following, copper thicknesses from 0, i.e. an iron double-layer, to 6 monolayers are considered. After preliminary calculations, the $FeCu_2Fe$ structure is identified as most promising with respect to antiferromagnetic coupling. The atomic positions are calculated starting from the iron bcc lattice-structure. By alternately varying the in-plane lattice constant and the atomic z-positions, the ground state structure is found to be antiferromagnetically coupled with a lattice parameter of $a \approx 4.59\, a_B$ significantly smaller than the bulk lattice structure. The calculations of the other layers use the same in-plane lattice parameter while the atomic z-positions are relaxed in both the antiferromagnetic and ferromagnetic case. The symmetric atom positions and the inter-atom z-distances are shown in Fig. 8.1c. Only the $n = 2$ configuration exhibits antiferromagnetic coupling as demonstrated in Fig. 8.1b. This is in contrast to the previous FeCuFe calculations, but some differences are to be expected since semi-infinite Fe layers were considered back then. One possible venue to obtain more antiferromagnetically coupled systems is the symmetric inclusion of further Fe layers. Instead, in the following the antiferromagnetic configurations are considered despite their energetic disadvantage for most thicknesses as investigation of the general feature evolution is sufficient.

The Wannier functions are constructed using s, p, d-states for the iron and copper atoms as initial projections. A 12×12 $\boldsymbol{k}$-grid is used to describe the Wannier functions with a frozen window from the lowest bands up to 2 eV above the Fermi level. Overall, the model Hamiltonian in the basis of the Wannier functions reproduces the DFT-bandstructure very

well. Within the frozen-energy window no deviations from the FLEUR bandstructure are visible on the resolved scale of Figs. 8.2a-c. Contrarily, the bands differ strongly above the frozen window. The great accuracy of the interpolation at the Fermi surface is visualized in Fig. 8.2d. Only deviations of $\sim 3\,\mathrm{meV}$ from the model Fermi energy appear when calculating the DFT energies at the model Fermi energy $\boldsymbol{k}$-points. Hence, the Wannier-based model is well-suited to describe the reciprocal structure of the studied systems.

8.2 $FeCu_2Fe$

Having established the general setup of the FeCuFe trilayer system, this section investigates one selected thickness in detail. The $FeCu_2Fe$ structure is chosen as an example system since it is the only found structure energetically preferring the antiferromagnetic configuration. The dispersion and the Fermi surface are shown in Fig. 8.2b,d from which many dispersive and non-dispersive bands near the Fermi energy are apparent. Overall, the Fermi surface contains 8 distinct lines that are relatively separated from each other and will be referenced in this section by using the enumeration of Fig. 8.2d.

When comparing the bandstructure of $FeCu_2Fe$ with those of FeFe and $FeCu_6Fe$ (Fig. 8.2a-c), the impact of increasing copper thickness is relatively straightforward. Especially along

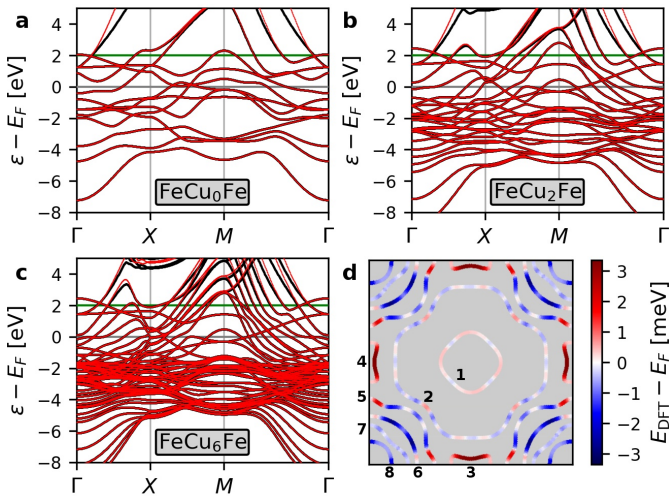

Figure 8.2: a-c) show the DFT (black) and Wannier (red) dispersions of $FeCu_nFe$ for the thicknesses $n = [0, 2, 6]$ in ascending order. The upper boundary of the Wannier interpolation frozen window is marked as green line. d) displays the Fermi-surface as obtained from the Wannier interpolation for the $FeCu_2Fe$ structure. The color encodes the energy difference between the DFT calculation and the Wannier interpolation. Furthermore, an enumeration is defined for further references to specific bands.

the $\overline{\Gamma M}$ and $\overline{\Gamma X}$ high-symmetry lines many copper-based electron states appear at the Fermi energy, while the immediate vicinity of M remains relatively unmodified. These considerations allow preliminary understanding of the origin of the respective states, yet more insight can be gained by employing the DFT-formalism which allows direct evaluation of the band character.

8.2.1 Properties at the Fermi energy

First, DFT is utilized to study the band-characters at the Fermi surface as plotted in Fig. 8.3. A glaring property is the large weight within the Fe muffin-tins that barely drops below 0.4 for all states at the Fermi energy. Contrarily, the weights in the copper muffin-tins only reach ~ 0.33 at few positions on the Fermi lines. Hence, the states at the Fermi surface are of significant iron-character so that the assumption of having spin-polarized states is reasonable. Numerically, this is enforced anyways due to negligence of SOC, yet the strong iron-character justifies that assumption even when including SOC on the DFT-level. The band-character attributions based on DFT calculations are in good agreement with the previous predictions based on the thickness-dependent bandstructure differences, as e.g. attributing the bands in the vicinity of M to iron. Accordingly, the overall band modifications are foreseeable in such a system. However, almost all bands have significant portions of non-iron muffin-tin character so that a more complicated structure than the simply synthetic antiferromagnetic model system is realized. Particular differences appear when considering the spin-up and -down character of the upper iron atom (Fig. 8.3). Especially the 8th band is almost exclusively of spin-up character while most other band are mainly of spin-down character. Of course,

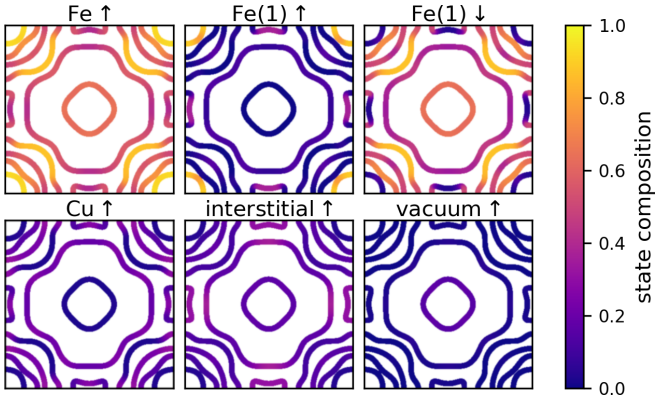

Figure 8.3: State composition of the $FeCu_2Fe$ structure at the Fermi surface as calculated from DFT. "Fe ↑" and "Cu ↑" denote the sum of the spin-up state-contributions within all muffin tins of the respective atoms. Analogously, "Fe(1) ↑" and "Fe(1) ↓" show the spin-up and -down weights of the upper Fe-atom only. The spin-resolved weights for the lower Fe-atom are exactly the reversed of the upper Fe-atom. Lastly, the remaining spin-up weights distinguished into interstitial and vacuum are plotted.

this distribution is reversed for the lower iron atom conserving the spin degeneracy, yet this property is different from the simple model approximation of having one spin state on one atom and reversed. Still, the collinear wave-packet mechanism as described in Sec. 3.2.1 is straightforwardly applicable due to the negligence of SOC which automatically results in Wannier-states whose spin-polarization is independent of their DFT origin.

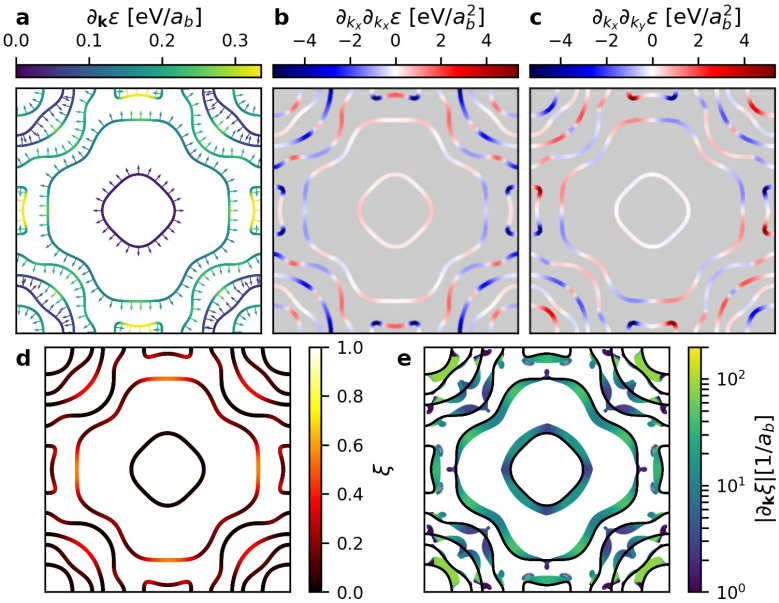

Figure 8.4: Collinear properties of $FeCu_2Fe$ at the Fermi surface. a) shows the group velocity with color-coded magnitude and indicated direction through arrows. b) and c) display the diagonal and off-diagonal second energy derivatives corresponding to the effective masses. Due to the symmetries of the structure $\partial_{k_y}\partial_{k_y}\epsilon$ is exactly the same $\partial_{k_x}\partial_{k_x}\epsilon$ rotated by 90°. d) shows the overlap ξ. In e) $\partial_{\boldsymbol{k}} \log \xi$ is plotted where the color denotes the magnitude logarithmically and densely plotted arrows indicate the direction.

Next, all necessary $\boldsymbol{k}$-dependent, collinear properties are calculated by employing the well-working Wannier-based model Hamiltonian as described in Sec. 7.2 and visualized in Fig. 8.4. While the dispersion derivatives can be easily understood from the overall bandstructure, so that their behavior is only interesting with respect to their transport impact, the origin of ξ's $\boldsymbol{k}$-dependent structure is not clear. Intuitively, one could suspect a relation to the atomic-characters of Fig. 8.3, yet no clear analogy can be drawn between the plots. Sections with relatively large ξ are exhibited in the 2nd and 6th Fermi line but neither has well correlated state-composition behavior. While the Fe ↑-composition of the 6th band has similar maxima as ξ, the Fe ↑-maxima of line 8 are certainly not reproduced in ξ and the ξ-maxima of the 3rd, 4th, and 5th lines correspond to minima of the iron-composition. Conversely, the

correspondence between the small maxima of the 2nd band's interstitial contribution with the ξ is rendered unimportant when considering the composition maxima of the 3rd band and the ξ maxima of the 6th band. Hence, ξ proves to be an intricate quantity that can not be understood from the band-character alone but requires explicit calculation, at least when considering the structure with 2 copper atoms. The $\partial_{\boldsymbol{k}} \log(\xi)$-distribution is similarly unpredictable. Its norm varies over several order of magnitude even within the same Fermi line. For some lines the direction is equally unstable, while some lines such as the 1st, 2nd, and 8th mainly point to either the inside or the outside. Comparison of transport calculations including and excluding the $\partial_{\boldsymbol{k}} \log(\xi)$-terms reveals no significant difference so that further scrutiny of $\partial_{\boldsymbol{k}} \log(\xi)$ would be superfluous.

Having obtained values for the collinear reciprocal-space properties, the TSHE is calculated assuming the $3\boldsymbol{q}$ skyrmion texture (Sec. 2.4.1) and using the formalism as described in Sec. 5. Different transport aspects are visualized in Fig. 8.5. Fig. 8.5a displays the iteration-time dependence of the topological spin Hall constant R^{TS} (Eq. 4.12). Overall, the calculation with generously chosen numerical parameters shows that sufficient convergence to $R^{TS} \approx -2.6 \cdot 10^{-11} \frac{\hbar}{e} \frac{\Omega \mathrm{m}}{\mathrm{T}}$ is reached after $\sim 1\,\mathrm{ns}$. This result is of similar magnitude as the topological Hall constant of the $3\boldsymbol{q}$-state exhibited by $Mn_{1-x}Fe_xSi$ [41] neglecting the $\frac{\hbar}{e}$-prefactor due to the different nature of the transport.

As R^{TS} depends mainly on the longitudinal charge and transversal spin current, more insight can be gained by investigation of their $\boldsymbol{k}$-resolved distribution shown in Fig. 8.5b,c. The other transport contributions not plotted here vanish due to the same reasons as in the bilayer model calculations (Sec. 6.2.1). Due to the simple computational structure of σ^1_{xx} (Eq. 4.34), its distribution can be directly correlated with the respective x-component of the group velocity (Fig. 8.4a) analogous to the model calculation. Furthermore, it is interesting to note that all bands have significant contributions to the integrated σ^1_{xx}.

More important for the TSHE is the transversal spin conductivity plotted $\boldsymbol{k}$-resolved in

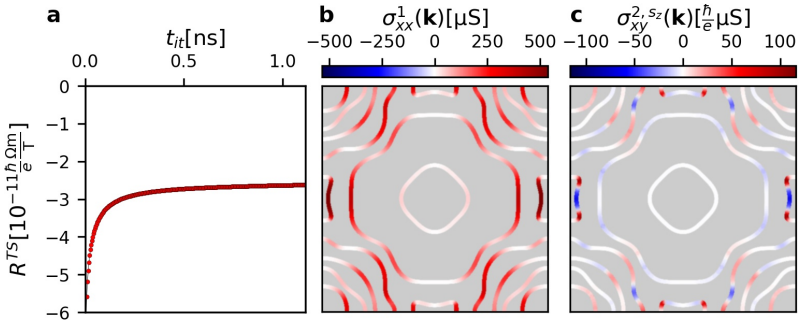

Figure 8.5: TSHE of $FeCu_2Fe$ as calculated with $N_k = 32772$, $N_R = 10$, and $h = 10$ [a.u.] (compare Sec. 5.3). a) shows the t_{it}-dependence of the topological spin Hall constant R^{TS}. b,c) show converged ($t_{it} \approx 1.16\,\mathrm{ns}$), $\boldsymbol{k}$-resolved conductivity contributions necessary to calculate the TSHE. The longitudinal conductivity is displayed in b) and the transversal spin conductivity is plotted in c).

Fig. 8.5c. Here, its attribution to reciprocal-space properties is more difficult than in case of the bilayer model (Sec. 6.2.1) due to the non-vanishing off-diagonal effective masses. Overall, $\sigma_{xy}^{2,s_z}(\boldsymbol{k})$ varies a lot in sign and magnitude, but still most bands, except for the 1st and the 7th band, have relevant $\boldsymbol{k}$-dependent contributions either due to their large magnitudes or because of the huge length of the underlying Fermi lines. Furthermore, most lines contain sections with positive and negative sign so that the integrated spin conductivity is highly compensated allowing for large modifications caused by small differences. While lines with neither large group velocities nor large effective masses indeed result in small $\sigma_{xy}^{2,s_z}(\boldsymbol{k})$ (line 1), lines exist which have large magnitudes in the effective masses but overall small $\sigma_{xy}^{2,s_z}(\boldsymbol{k})$ due to small group velocities and large ξ (line 6). In general, the spin conductivity's $\boldsymbol{k}$-dependence has become a complicated property depending on 4 reciprocal-space parameters and the spin evolution.

8.2.2 Fermi energy dependence

A natural extension to the TSHE study at the DFT-based Fermi energy is the variation of the Fermi energy as carried out in this section. For convenience, all energies are given relative to the DFT Fermi energy $E_{F,\mathrm{DFT}}$. While the Wannier-interpolation describes all bands up to 2 eV accurately, in this section the range from -1 to 0.5 eV is investigated only. This reduces the computation effort significantly and disregards only states so far from $E_{F,\mathrm{DFT}}$ that they are inaccessible in realistic application anyways. The calculations are performed with $N_k = 8192$, $t_{it} \approx 1$ ns, $h = 10$ [a.u.], and $N_R = 5$ which, though less than the $E_{F,\mathrm{DFT}}$-calculation, yields sufficiently well-converged results.

The bandstructure and energy dependence of the TSHE are shown in Fig. 8.6. The first

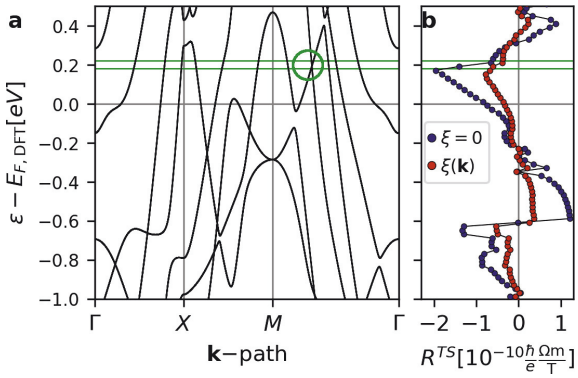

Figure 8.6: Comparison between bandstructure and TSHE energy-dependence of $FeCu_2Fe$. a) shows the bandstructure (compare to Fig. 8.2b) in the $[-1\,\mathrm{eV}, 0.5\,\mathrm{eV}]$ energy range around the DFT Fermi energy. b) displays the R^{TS} in the corresponding energy-range for $\xi = 0$ (blue) and $\xi(\boldsymbol{k})$ (red). The green circle indicates the Dirac cone investigated in Fig. 8.7, the horizontal lines correspond to the energy-planes in the cone-visualizations of that figure.

eye-catching property of R^{TS} is the dissimilarity between the full ξ-dependent calculation and the $\xi = 0$ case. While the $\xi = 0$-calculations yields larger magnitudes for most energies, in some cases near a R^{TS} sign-change this behavior can be reversed. For example, at $E_F \approx 0.31\,\text{eV}$ the $\xi(\boldsymbol{k})$-result ($R^{TS}_{\xi(\boldsymbol{k})} \approx 2.17 \cdot 10^{-11} \frac{\hbar}{e} \frac{\Omega_\text{m}}{\text{T}}$) is more than three times as large as the $\xi = 0$ calculation ($R^{TS}_{\xi=0} \approx 0.63 \cdot 10^{-11} \frac{\hbar}{e} \frac{\Omega_\text{m}}{\text{T}}$). Similarly, it is possible that the sign of $R^{TS}_{\xi=0}$ has already changed while the sign of $R^{TS}_{\xi(\boldsymbol{k})}$ has not (e.g. at $E_F \approx 0.33\,\text{eV}$). Hence, the inclusion of ξ can change even the direction of the TSHE.

In principle, the energy could be tuned so that $R^{TS}_{\xi=0}$ vanishes while $R^{TS}_{\xi(\boldsymbol{k})}$ retains non-vanishing contributions so that arbitrarily large enhancements relative to the naive approach are possible. Of course, the reverse is possible as well by tuning to $R^{TS}_{\xi(\boldsymbol{k})} = 0$. While these considerations serve no physical purpose as only $R^{TS}_{\xi(\boldsymbol{k})}$ can be measured, they emphasize the importance of including the full non-abelian wave-packet dynamic.

While the effect of the spin-evolution has been shown to yield a factor of 1/3 (Sec. 5.3.3), the degenerate properties still have major impact through the $\boldsymbol{k}$-dependence of ξ through the $(1 - \xi^2)$-prefactor (Eq. 5.3), which can significantly decrease $\sigma^{2,s_z}_{xy}(\boldsymbol{k})$ at Fermi-line sections with large ξ. Therefore, the many different relative magnitudes of R^{TS} in Fig. 8.6 point towards strongly changing ξ distributions. Hence, the transport signal can be severely misjudged if no ξ-distribution is supplied.

As the TSHE is a Fermi-surface property, strong variations are to be expected with respect to the Fermi energy. Indeed, in the small energy window of 1.5 eV the R^{TS}-sign changes several times. Fortunately, in case of $FeCu_2Fe$ the behavior near $E_{F,DFT}$ is relatively smooth so that transport predictions are stable. However, strong R^{TS}-variations around the Fermi energy are very likely for different materials in general. Therefore, further investigations of the origin of those variations are beneficial.

Since R^{TS} is constructed from quantities that strongly dependent on dispersion details, comparison of the TSHE transport with the bandstructure allows to uncover the origin of the strong variations (Fig. 8.6). Of course, more dispersive bands result in more rapid variations as their group velocities are larger and since the overall length of the Fermi lines is more sensitive to changing energies. Furthermore, band edges tend to have a strong influence as the rapid changes of R^{TS} usually coincide with band edges and crossings. An example is the strong variation near $E_F = -0.3\,\text{eV}$ which coincides with a crossing on $\overline{XM}$ and a band edge at M. The most drastic variations appear between $-0.7\,\text{eV}$ and $-0.6\,\text{eV}$ where several band edges and crossings are exhibited. Yet, not all crossings result in as drastic variations, for example the band edges on $\overline{XM}$ and $\overline{M\Gamma}$ around the Fermi energy result in relatively small magnitude changes.

In the following, this behavior is scrutinized for the exemplary Dirac cone between M and Γ near 0.19 eV which is indicated in Fig. 8.6a. When crossing the Dirac energy, $R^{TS}_{\xi=0}$ drops by $\sim 13 \cdot 10^{-11} \frac{\hbar}{e} \frac{\Omega_\text{m}}{\text{T}}$ corresponding to a decrease by 66% within only 0.04 eV. In contrast, $R^{TS}_{\xi(\boldsymbol{k})}$ drops by only $\sim 3 \cdot 10^{-11} \frac{\hbar}{e} \frac{\Omega_\text{m}}{\text{T}}$, although this still corresponds to a decrease by 43% due to overall smaller magnitudes. Judging from the bandstructure only, this strong change can be attributed to the Dirac cone since the other bands do not vary much, at least along the high-symmetry lines.

For confirmation, the energy-dependence of the transversal spin-conductivity (for $\xi = 0$) is

compared using either the full Fermi surface or a line originating from one Dirac line only (Fig. 8.7a). In both curves a significant drop is observed when crossing the Dirac energy. Since 4 symmetry-related Dirac points exist in the Brillouin zone, a drop by the 4-fold of the Dirac-only calculation difference is expected when including all Fermi lines. This expectations is approximately fulfilled as the full σ_{xy}^{2,s_z} drops by the 3.5-fold of the decrease including one Dirac cone only. This comparison validates the previous attribution to the Dirac cones convincingly when considering the relatively decreased $\boldsymbol{k}$-accuracy of the full calculation and the possibility of small variations in other bands.

Remarkably, σ_{xy}^{2,s_z} of the Dirac Fermi-line remains relatively constant when approaching the Dirac point despite the line's drastically decreasing length. This behavior can be understood from the $\sigma_{xy}^{2,s_z}(\boldsymbol{k})$-visualization at different Fermi lines around the Dirac point (Fig. 8.7b). Foremost, this plot shows predominately positive contributions below and negative contributions above the Dirac energy. The sign-change of σ_{xy}^{2,s_z} originates in the odd number of occurrences of group velocities and effective masses (Eq. 5.3) which change their sign when crossing a Dirac point. The decrease in length, which usually causes diminishing overall contribution, is counteracted by a very large increase in magnitude when approaching the Dirac energy. The largest $\sigma_{xy}^{s_z}(\boldsymbol{k})$-magnitude of Fig. 8.7b is more than 60-fold the maximal $\sigma_{xy}^{s_z}(\boldsymbol{k})$ at the Fermi surface shown in Fig. 8.5c (7284 $\frac{\hbar}{e}\mu$S to 116 $\frac{\hbar}{e}\mu$S). Therefore, the overall impact remains significant even in the immediate vicinity of the Dirac point due to the increasing effective mass contributions. Additionally, $\sigma_{xy}^{2,s_z}(\boldsymbol{k})$ appear to be symmetric up to a sign change around the Dirac energy when inverting $\boldsymbol{k}$ relative to the Dirac point positions and changing the sign of the energy relative to the Dirac point energy. This feature, arising from the large symmetry of the atomic structure, is not necessary for such drastic transport signatures, yet an overall sign-change is expected everywhere due to the above 3-fold occurrence.

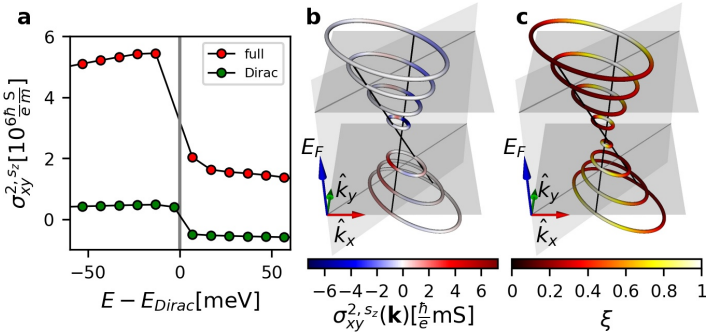

Figure 8.7: TSHE response to the Dirac cone indicated in Fig. 8.6a. a) shows the energy dependence of σ_{xy}^{2,s_z} in the immediate vicinity of the Dirac cone energy with $\xi = 0$ for the full Fermi-surface (red) and including the Fermi line of one Dirac cone only (green). b) and c) visualize $\sigma_{xy}^{2,s_z}(\boldsymbol{k})$ ($\xi = 0$) and $\xi(\boldsymbol{k})$ for the Fermi lines with $E_F = 0.16..0.23\,$eV (in (b) $E_F = 0.19\,$eV is excluded) so that the third from the bottom and second from top correspond to the green lines of Fig. 8.6a.

This rapid change in transport is apparently contradicted by the $R^{TS}_{\xi=0}$ data-point between the green lines in Fig. 8.6. It is approximately at half the difference so that one could assume that a continuous albeit steep connection exists which would be at variance with the previously worked out abrupt sign-change at the Dirac point. However, this data-point can be reconciled with above consideration as the Dirac-cones are excluded for this calculation due to insufficiencies in the Fermi line interpolation algorithm. Hence, this plot does not contradict a binary jump when passing the Dirac energy but rather enforces it by being in the middle including neither the positive nor the negative contribution.

The transport changes are much smaller in case of $\xi(\boldsymbol{k})$ compared to the $\xi = 0$ calculations as shown in Fig. 8.6. Since the majority of the modification originates from only 1 particular (or 4 considering the symmetric partners), small Fermi line, large ξ-contributions suppressing σ^{2,s_z}_{xy} are to be expected there. For larger Fermi lines one often has compensated contributions so that overall the decrease is not necessarily as large, yet here only small, insignificant sections of opposite sign appear at each energy. Hence, even relatively moderate ξ will straightforwardly cause significant transport decreases. The $\boldsymbol{k}$-resolved distribution of ξ (Fig. 8.7c) shows very large ξ directly at the positions of maximal σ^{2,s_z}_{xy}-magnitude. Hence, these large ξ cause the strong attenuation relative to the drastic $\xi = 0$ transport changes. Furthermore, Fig. 8.7c reveals that ξ varies strongly in this small $\boldsymbol{k}$-domain so that special numerical care is necessary for such bandstructure sections. In general, it should be possible to have Dirac cones where large ξ do not coincide with large σ^{2,s_z}_{xy} so that very strong variations are realized in the $\xi(\boldsymbol{k})$-case as well. Also, the transport variations near most band edges are still large relative to their scale.

Alternatively to the Dirac cones, similar features can appear at band edges. However, such band, and even crossings as exemplified at M near $-0.3\,\mathrm{eV}$, exhibit a parabolic bandstructure. While such features can still result in sign-changes of the transport, on similar energy scales they happen less abruptly as the group velocities vanish at the outmost energy. Yet, very large masses and associated small energy ranges with large Fermi-line shrinking can result in similar, or even more extreme, transport-variations despite the group-velocity vanishing and the absence of the sign-reversed cone in case of band edges.

In conclusion, this section has uncovered the extreme Fermi-energy dependence of the THSE. While such behavior is to be expected due to its Fermi surface character, different mechanisms in the transport expression are discussed that result in increased sensitivity with respect to Dirac cones or alternative band edges. Furthermore, ξ is shown to exhibit drastic signatures, which overall emphasizes the necessity for extreme numerical care in such calculations.

8.2.3 Influence of SOC

Although SOC has been neglected on the wave-packet level and is accordingly not included in the transport considerations, a small grasp of its effect can be obtained by including SOC on the DFT level (Sec. 7.2). Since neither iron ($Z = 26$) nor copper ($Z = 29$) are heavy atoms, the influence of SOC is expected to be very small. Indeed, the properties of the collinear calculation barely change as for example the magnetic moments change by less then $0.005\,\mu_B$. Consequently, the bandstructure does not change much and noticeable differences

occur only at $-3\,\mathrm{eV}$ relative to the Fermi energy. In the previously investigated energy range near the Fermi energy ($[-1\,\mathrm{eV}, 0.5\,\mathrm{eV}]$ as in Fig. 8.6a) only minor modifications appear as shown in Fig. 8.8a. The only visible differences are the expected gap openings at the band crossings of which the previously investigated Dirac cone is the most unaffected. From these considerations, only minimal modifications to the TSHE are to be expected when including SOC which mainly lessen the abruptness of the energy-dependent variations near crossings.

As the Fermi energy is far from band crossings, the Fermi surface changes only minimally. This is shown in Fig. 8.8b, where the black lines denoting the states without SOC are barely visible as boundary of some SOC-states. Since the dispersion at the Fermi energy is that similar to the previous calculations, the properties depending on the $\boldsymbol{k}$-derivatives are almost identical to the ones displayed in Fig. 8.4a-c. Hence, one does not expect many differences to the calculations without SOC. Indeed, the iteration-time dependence of R^{TS} is only sightly affected by the inclusion of SOC (Fig. 8.8c). The final value including SOC is only 4% smaller than the result without SOC. A further difference is the faster convergence of the SOC calculations, at least its initial decline is visibly steeper.

One reason for this difference is the decrease of the spin polarization when including SOC due to state-mixing in the DFT calculations. It results in a straightforward decrease of the transport impact (Sec. 4.4.1), but fortunately most states at the Fermi surface are unaffected as demonstrated in Fig. 8.8. Only the 8th line has s_z as low as 0.9 while the 7th band as second smallest band has minimal contributions of $s_z \approx 0.97$, the other bands are virtually unaffected. As the 8th line is small and has only moderate $\boldsymbol{k}$-dependent contributions to the TSHE (Fig. 8.5c), this effect has minor overall impact.

Still, the overlap ξ might change despite the unchanged bandstructure details. Hence, ξ and $\partial_{\boldsymbol{k}}\xi$ are plotted in Fig. 8.9 as comparison to Fig. 8.4d,e. In case of ξ no differences are visible, both the magnitudes and the distribution are extremely similar although the Fermi-lines are slightly shifted. When comparing the ξ of the SOC calculation to ξ without SOC, but using the same $\boldsymbol{k}$ and band indices as in the SOC case, the difference is within ± 0.015 and averages to less than 0.001 so that the overall impact of the ξ-variation is negligible. Yet, these minor

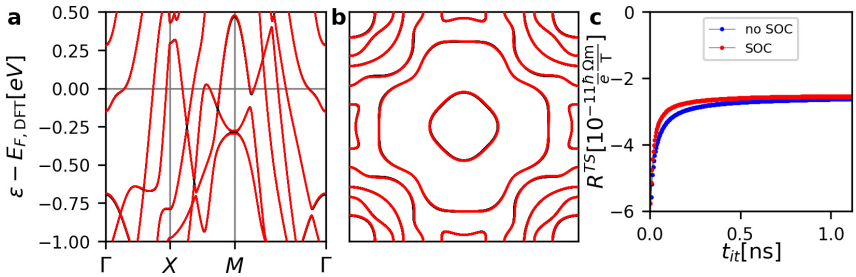

Figure 8.8: Modifications due to inclusion of SOC in $FeCu_2Fe$. a) and b) show the bandstructure and Fermi surface including (red) SOC on top of bands without (black) SOC so that black lines denote differences. c) displays the time-dependence of R^{TS} with SOC calculated with $N_k = 8192$, $N_R = 10$, and $h = 10\,[\mathrm{a.u.}]$ relative to the case without SOC as shown in Fig. 8.5a.

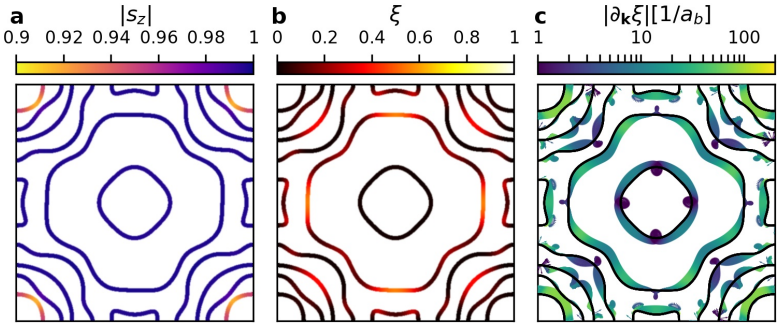

Figure 8.9: Collinear properties of $FeCu_2Fe$ at the Fermi surface including SOC. a) shows the magnitude of the spin-expectation value as obtained from the Wannier model. b) and c) display ξ and $\partial_{\boldsymbol{k}}\xi$ corresponding to Figs. 8.4d,e here including SOC.

differences between the cases with and without SOC are visible as small variations of $\partial_{\boldsymbol{k}}\xi$. Overall its distribution is very similar and the magnitude changes rarely. Different directions appear for example at the 1st band, but only at irrelevant magnitudes, and at the Brillouin zone edges as in the case of the 8th band. However, since no systematic transport effect caused by $\partial_{\boldsymbol{k}}\xi$ has been found, it is unlikely that these small change of $\partial_{\boldsymbol{k}}\xi$ can explain the minimal TSHE variations.

Hence, in the case of $FeCu_2Fe$ only minor variations of the spin polarization and even smaller modifications of the dispersion and overlap are found as possible sources for TSHE modification when including SOC. Since R^{TS} is only very slightly effected by SOC this result is consistent and demonstrates the negligibility of SOC for $FeCu_2Fe$ at the Fermi surface. Furthermore, the general applicability of SOC on the DFT level for the TSHE calculations is demonstrated which in different energy ranges or different materials certainly has dramatic impact.

8.3 FeCuFe thickness dependence

After having investigated the case with 2 copper layers in detail, this section treats the dependence of the THSE on the Cu-thickness of the Fe/Cu/Fe-trilayer. The THSE can be calculated straightforwardly using the Wannier-basis Hamiltonian as constructed from the atomic structures shown in Fig. 8.1. It should be noted that the topological spin constant R^{TS} is based on conductivities instead of conductances, which would be the more natural transport characteristic in 2D materials. Hence, all conductivities are divided by the thickness d_z as described in Sec. 5.1. Thereby, R^{TS} is kept comparable and conceptually less dependent on the number of Cu layers, yet the decrease of $\sigma_{xy}^{s_z}(\boldsymbol{k})$ with increasing thickness has to be considered. d_z is taken as the sum of the distance between the outmost atomic positions (Fig. 8.1c) and their muffin-tin radii (here $2.18\,a_B$). The resulting d_z are noted in Tab. 8.1.

Including these prefactors, the dependence of R^{TS} is shown in Fig. 8.10a. The maximal

#Cu layers	0	1	2	3	4	5	6
$d_z[a_b]$	7.78	11.78	15.43	19.16	22.84	26.52	30.30

Table 8.1: Thickness of $FeCu_nFe$ layers as obtained from Fig. 8.1

.

magnitude is obtained in case of the Fe double-layer with a negative sign, then R^{TS} becomes very small for $n = 3$ and has smaller positive R^{TS} for thicker systems . This increase is not monotonous as R^{TS} decreases between $n = [1, 2]$ and $n = [5, 6]$ and might be coincidental.

The $\xi(\boldsymbol{k})$ calculations show a systematic decrease in magnitude relative to the $\xi = 0$-case as expected due to the decrease to $1/3$ originating in the spin equilibration on the prolate spheroid (Sec. 5.3.3). Further variations occur due to the $\boldsymbol{k}$-dependent $(1 - \xi^2)$-factor. Since the $(1 - \xi^2)$-factor reduces the Hall-conductivity contributions $\boldsymbol{k}$-dependently, in general a decrease to even less than $1/3$ is expected. As shown in Fig. 8.10b, this is the case for the thicknesses $n = 0, 1, 2, 6$ while for $n = 4, 5$ the ratio is larger than $1/3$. Hence, the $(1 - \xi^2)$-distribution causes the TSHE to shrink in the former case while it increases in the latter case. A further decrease is generally more probable as even the limit of an isotropic ξ-distribution would result in less than $1/3$ remaining magnitude. Conversely, in the latter case it is necessary to have a ξ-distributions which reduces the minority $\sigma_{xy}^{2,s_z}(\boldsymbol{k})$ (state at $\boldsymbol{k}$ which decrease the magnitude of σ_{xy}^{2,s_z}) more strongly than the majority $\sigma_{xy}^{2,s_z}(\boldsymbol{k})$. Since by definition the integral over the majority $\sigma_{xy}^{2,s_z}(\boldsymbol{k})$ is larger than that of the minority conductivities, this requires a ξ-distribution strongly preferring the minority $\boldsymbol{k}$.

A necessary condition for such relative enhancements is a strong compensation of $\sigma_{xy}^{2,s_z}(\boldsymbol{k})$ at the Fermi surface. Otherwise, it would be impossible to sufficiently decrease the few minority $\sigma_{xy}^{2,s_z}(\boldsymbol{k})$ in order to counter the decrease of the majority conductivity. Such behavior has already been demonstrated in case of $FeCu_2Fe$ (Sec. 8.2.1) and is summarized in Fig. 8.10c

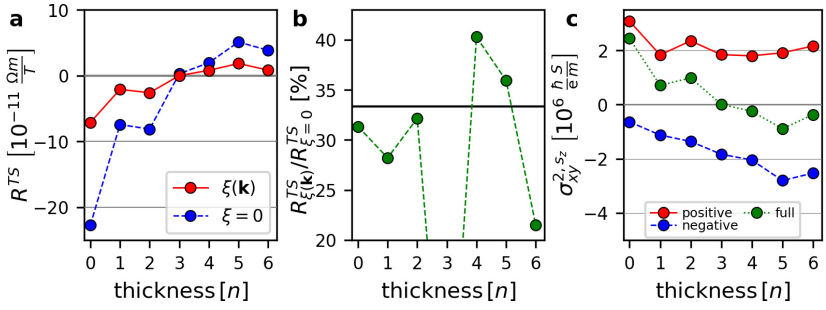

Figure 8.10: Thickness dependent transport properties of the Fe/Cu/Fe-trilayer using $t_{it} \approx 1.16$ ns, $N_k = 32786$, and $N_R = 10$ convergence parameters. a) displays R^{TS} in case of $\xi = 0$ and the inherent $\xi(\boldsymbol{k})$. b) clarifies the decrease due to $\xi(\boldsymbol{k})$ through the percentaged difference compared to the $\xi = 0$ (not shown: $FeCu_3Fe$ with -4%). c) shows σ_{xy}^{2,s_z} for the inherent ξ calculations in green in comparison to the σ_{xy}^{2,s_z} including only the positive and the negative $\sigma_{xy}^{2,s_z}(\boldsymbol{k})$.

for the investigated thicknesses. That figure shows the positive and the negative $\sigma_{xy}^{2,s_z}(\boldsymbol{k})$ integrated separately as well as their sum which allows direct judgment of the cancellations. Strong compensations are immediately apparent since the positive integral does not change much, while the previously described R^{TS}-increase originates in a strong magnitude-increase of the negative integral starting from very small magnitudes in the Fe double-layer case. Since the positive contributions are relatively constant, that behavior might be naively attributed to the Fe-dominated bands. However, σ_{xy}^{2,s_z} scales with $1/d_z$ so that the newly appearing bands, originating in additional copper atoms, have to contribute substantially to the majority $\sigma_{xy}^{2,s_z}(\boldsymbol{k})$.

An overall increase due to the ξ-distribution is very unlikely as the compensation is small for small thicknesses. Accordingly, all R^{TS}-fractions of the thinner systems are smaller than $1/3$. Furthermore, Fig. 8.10c demonstrates a strong sensitivity with respect to small changes for the thicker systems as relatively small alterations of one integral can yield large-percentage changes in the net TSHE. Indeed, the thicker systems experience more drastic variations than a small decrease in the R^{TS}-fraction from $1/3$. Instead, enhancements up to 40.3% ($FeCu_4Fe$) and decreases down to 21.5% ($FeCu_6Fe$) are observed.

An extremal case of these considerations is $FeCu_3Fe$. There, already $R_{\xi=0}^{TS}$ is very small due to cancellation of $\sigma_{xy}^{2,s_z}(\boldsymbol{k})$. In principle, this could allow large percentage enhancements of $R_{\xi(\boldsymbol{k})}^{TS}$ over $R_{\xi=0}^{TS}$ in case of unbalanced ξ-distributions. Instead, the ξ-distributions results in an even greater cancellation which remarkably culminates in a sign change and is accordingly the opposite of greatly diminished minority contributions. While of no practical use due to its small magnitude, this sign change demonstrates the huge potential impact of the overlap ξ.

Comparison of the previous conclusions with the overall ξ-distribution (Fig. 8.11) demonstrates the intricate nature of the relation between R^{TS} and ξ as well as the necessity for detailed investigation. For example, the ξ-distributions of $FeCu_5Fe$ and $FeCu_6Fe$ are very similar, however their R^{TS}-fractions caused by the $\boldsymbol{k}$-resolved ξ are very different. In contrast, $FeCu_0Fe$ and $FeCu_2Fe$ have very similar R^{TS}-fractions while their ξ-distributions are extremely different. Furthermore, large R^{TS}-fraction changes do not necessitate many large ξ as could be a naively expected, instead the extreme cases $FeCu_3Fe$ and $FeCu_4Fe$ even have the least large ξ. Hence, reliable conclusions can only be drawn from $\boldsymbol{k}$-resolved distributions of both ξ and $\sigma_{xy}^{2,s_z}(\boldsymbol{k})$ as done at the end of this chapter.

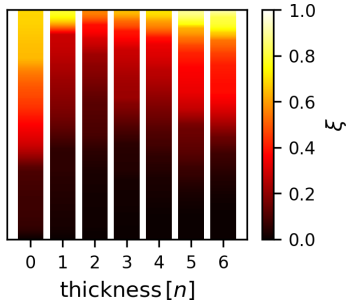

Figure 8.11: ξ-distribution for each thickness as a bar where each horizontal slice represent Fermi points with the color-coded ξ and height-encoded Fermi-line weight.

The inability to estimate TSHE properties purely from the $\boldsymbol{k}$-independent ξ-distribution is further demonstrated by comparison to the iteration-time dependence (Fig. 5.6c). There, very slow convergences are found for $n = \{3, 4, 5\}$ while $n = \{0, 1\}$ converge very quickly. In general, longer iteration-times t_{it} are necessary to converge $\boldsymbol{k}$ with small ξ as shown in Fig. 5.6a-b. Here however, this relation is violated most prominently in the case of the iron double-layer. There, the Fermi lines have many intermediate ξ, yet the overall convergence is relatively fast. Furthermore, the quickly converged $FeCu_1Fe$

system has similarly many $\xi \in [0, 0.2]$ as the slowly convergent $FeCu_4Fe$ system. Hence, the ξ-distribution is insufficient to infer information about the iteration-time dependence, instead detailed knowledge of the $\boldsymbol{k}$-dependence of included parameters is necessary for sensible predictions. Still, it is clear from the t_{it}-dependence that thicker systems require larger t_{it} which originates from the ever increasing number of sections with relevant $\sigma_{xy}^{2,s_z}(\boldsymbol{k})$-contributions that will have slightly different t_{it}-dependences due to different group velocities and overlaps.

More details of the thickness dependence can be uncovered by plotting the $\boldsymbol{k}$-resolved $\sigma_{xy}^{2,s_z}(\boldsymbol{k})$ for all investigated systems (Fig. 8.12). In case of the Fe double-layer, most $\boldsymbol{k}$ yield positive $\sigma_{xy}^{2,s_z}(\boldsymbol{k})$-contributions while the few negative contributions originate mainly in the near-crossings of Fermi-lines where large TSHE-magnitudes appear due to strong dispersion variations. When increasing the Cu-thickness, more and more Fermi lines emerge in the outer Brillouin-zone parts naturally resulting in an increasingly dense Fermi surface.

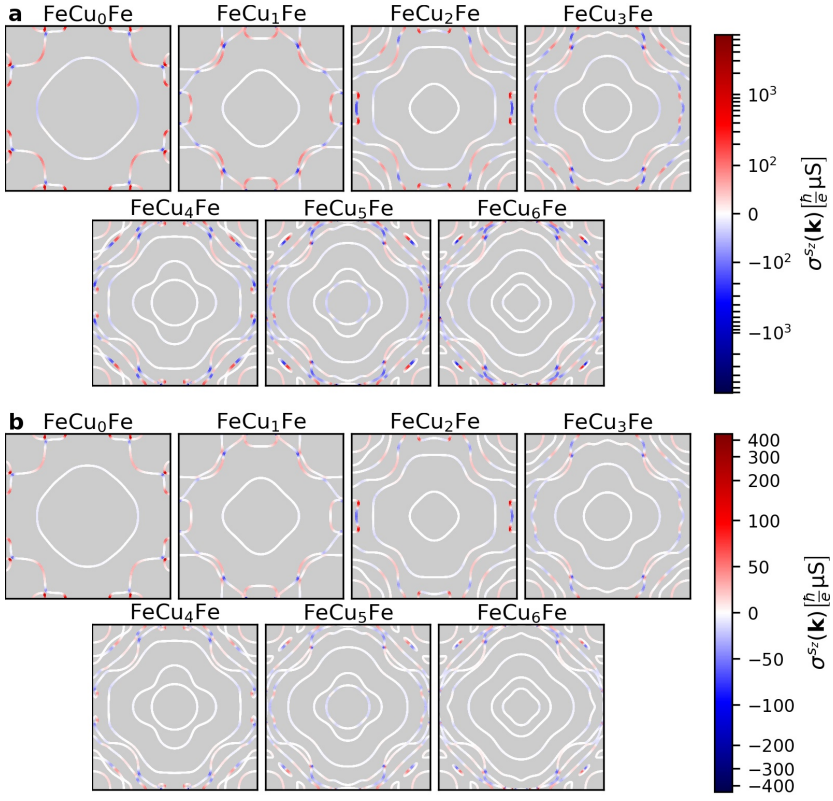

Figure 8.12: $\sigma_{xy}^{2,s_z}(\boldsymbol{k})$-distribution for different thicknesses of $FeCu_nFe$ at the respective Fermi surface with $\xi = 0$ (upper, a) and including $\xi(\boldsymbol{k})$ (lower, b). Notice the change to logarithmic scales at $\pm 100 \frac{\hbar}{e} \mu S$.

Although many of those lines are parallel, more crossings appear and constitute the majority of the transport contributions. As line-crossing can cause $\sigma_{xy}^{2,s_z}(\boldsymbol{k})$-increases by orders of magnitude (Sec. 8.2.2), the computational demand increases strongly with increasing thickness. Furthermore, Fermi lines with unusual shape appear due to hybridization with the numerous, densely-packet Fermi-lines as for example for $FeCu_4Fe$ near X. In general, SOC can lessen the computational demand as energy-gaps increase so that the Fermi lines become more separated (Sec. 8.2.3), yet only small modifications are to be expected due to the lightness of the constituting atoms.

The cumulated contribution of long, well-separated Fermi lines decreases with increasing thickness due to the $1/d_z$ prefactor which is only partially countered by the increasing number of Fermi lines. This decrease is clearly expressed in the Fermi line directly enclosing M whose shape is relatively unaffected from $n = 2$ to $n = 6$ but whose magnitude is ever decreasing. Conversely, the line enclosing Γ has a very erratic behavior with respect to the thickness. While this line foreseeably yields relatively large magnitudes in case of $n = 0$ (only for $\xi = 0$), visible contributions are also appearing for $FeCu_5Fe$ where the innermost bands are in close proximity. In contrast, the transport contributions for the systems with neighboring thickness are negligible. Although these central bands are long, their $\sigma_{xy}^{2,s_z}(\boldsymbol{k})$-magnitudes are minor which demonstrates the advantage of an alternative criteria for the Fermi line interpolation instead of constant length (Sec. 5.2.1).

One further merit of the systematic investigation of the thickness dependence is the ability to study the evolution of the enigmatic overlap ξ. The naive expectation is that ξ will decrease with increasing thickness as the iron states become increasingly separated in real space. However, such a decrease is not observed as the states at the Fermi surface include significant contributions from the Cu-atoms as well. Instead, even larger ξ are expressed with increasing thickness as summarized in Fig. 8.11. This effect could be studied better by intercalating an insulator instead of copper thereby preventing the emergence of new Fermi lines when increasing the spacer thickness. Still, antiferromagnetic coupling would have to be ensured and the overall transport would decrease with d_z-increases as the insulator layers would not supply any transport contributions while the ξ-decreases only have limited potential for increasing the transport signal. Hence, the here-investigated trilayer setup results in more interesting properties.

In more detail, this evolution is visualized in Fig. 8.13 $\boldsymbol{k}$-dependently. The previous simple picture is violated already in case of the Fe double-layer where small ξ appear even without intercalated Cu-layers. Still, the line enclosing Γ consists of relatively large ξ which decrease drastically when including even one copper layer. As this Fermi line is separated from the other bands, its evolution with increasing thickness can be tracked until it is approached by a second line at $n = 4$, the prevalent Fe-character is further supported by Fig. 8.3. The line retains a very small ξ throughout the investigated thicknesses so that the bands in its vicinity still have $\xi < 0.2$ even at $n = 6$. The Fermi line's TSHE contribution is diminishing (Fig. 8.12) despite its small ξ due to the small effective masses and group velocities. The other kept characteristic Fe double-layer feature is the bend of the second line going from Γ to M. For $n = 2$, its Fe-character is verified by Fig. 8.3 (5th line Fig. 8.2) and its supposed monotonous decrease of ξ is not violated since the small initial ξ is retained for all thicknesses. The remaining double-layer Fermi lines are not that easily tracked and might even disappear due

to shifts in the Fermi energy and band bending effects from the appearing copper states. Yet, small remainders of the initial Fe double-layer with small ξ are identifiable for all thicknesses.

The ξ-evolution of the newly appearing states is not as comprehensible since Fermi lines with small, large, and even strongly fluctuating ξ appear. Although ξ is relatively constant for some of the long Fermi lines, for others it changes drastically despite absence of other nearby Fermi lines. The ξ-behavior is relatively comprehensible at Fermi line crossings as it mainly exhibits large variations only if the crossing bands have different ξ. However, such crossings become more numerous with increasing thickness due to the correspondingly increasing number of bands. Moreover, drastic ξ variations are to be expected in the immediate vicinity of Dirac cones, as shown in Fig. 8.7c, that are not resolved on the scale of Fig. 8.13 and might require different Fermi energies. Since hitherto long Fermi lines traversing the whole Brillouin zone start to form smaller lines from $n = 5$ onwards, more extreme ξ-changes on short reciprocal-space length scales appear in these newly formed lines. A further property of ξ is its decrease to 0 at the Brillouin zone boundary [76]. Since lines with large ξ appear for $n \geq 4$ at the Brillouin zone boundary, localized sections with large ξ variations appear in its vicinity.

Having $\boldsymbol{k}$-resolved information about ξ (Fig. 8.13) and $\sigma_{xy}^{2,s_z}(\boldsymbol{k})$ for both $\xi = 0$ and $\xi(\boldsymbol{k})$ (Fig. 8.12) for all investigated thicknesses, it is interesting to study their relations and search for validations of previous findings. Foremost, the large difference in magnitude of $\sigma_{xy}^{2,s_z}(\boldsymbol{k})$ between $\xi = 0$ and $\xi(\boldsymbol{k})$ is immediately apparent. The first, obvious relation between all 3 plots is the $(1-\xi^2)$-decrease in addition to the 1/3 decrease due to the spin expectation value. However, direct comparison is difficult since $\sigma_{xy}^{2,s_z}(\boldsymbol{k})$ varies on several orders of magnitude so that many positions of large ξ vanish already in case of $\xi = 0$. Still, in some cases the expected relation are directly visible as for example in case of the Γ-encircling state of the iron double-layer. The opposite case with large remaining $\sigma_{xy}^{2,s_z}(\boldsymbol{k})$ due to small ξ is more apparent as for example in case of the Fe-dominated state encircling M. Another property is the attenuation of large magnitude sign-changes of $\sigma_{xy}^{2,s_z}(\boldsymbol{k})$ within one Fermi line due to

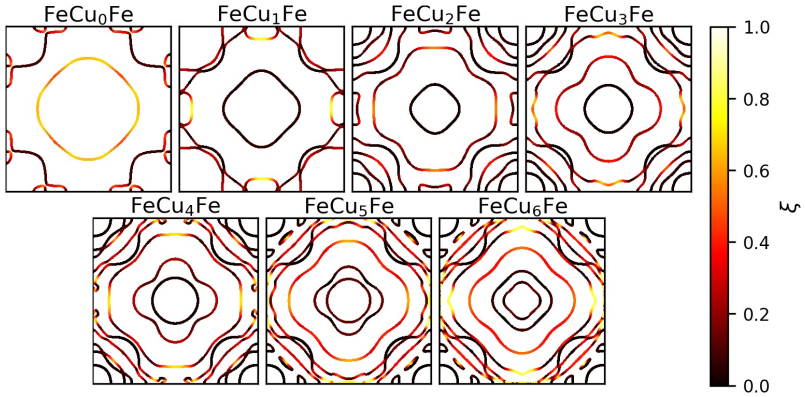

Figure 8.13: ξ-distribution for different thicknesses of $FeCu_nFe$ at the respective Fermi surface.

ξ-peaks as for example near M in case of $FeCu_5Fe$ and $FeCu_6Fe$. While some $\sigma_{xy}^{2,s_z}(\boldsymbol{k})$-peaks at avoided Fermi-line crossings are lessened by these ξ-spikes, others do no coincide at all with ξ-maxima resulting in relatively strong transport impact when considering the inherent $\xi(\boldsymbol{k})$.

One further interesting case is $FeCu_4Fe$ which experiences the lowest TSHE-decrease when going from $\xi = 0$ to the inherent $\xi(\boldsymbol{k})$ (Fig. 8.10b). Despite having a final R^{TS}-percentage much larger than $1/3$, comparison between ξ and $\sigma_{xy}^{s_z}$ is surprisingly inconclusive. The overall $\sigma_{xy}^{s_z}$ is negative since R^{TS} is positive and as $\overline{\mathcal{B}}$ is negative so that the positive $\sigma_{xy}^{s_z}(\boldsymbol{k})$-sections have to be affected more strongly by ξ. However, many line sections with large ξ do not have large Hall contributions and other major ξ-features, such as the 3rd band from M, decrease minority- and majority-$\sigma_{xy}^{s_z}(\boldsymbol{k})$ symmetrically. Only few of the significant ξ directly coincide with positive $\sigma_{xy}^{s_z}(\boldsymbol{k})$ (e.g. near Y) while some occur at $\boldsymbol{k}$ with clearly negative $\sigma_{xy}^{s_z}(\boldsymbol{k})$. This demonstrates the huge compensation and intricacy of the TSHE while pointing towards the possibility of much more significant enhancements in case of more selective ξ-distributions.

In conclusion, it is shown that the chosen method is well-suited to describe thicker systems although the TSHE-calculation becomes more involved as even small Fermi-lines and small avoided crossings have to be resolved. The relation between the thickness, ξ, and $\sigma_{xy}^{2,s_z}(\boldsymbol{k})$ is investigated which invalidates naive assumptions and exposes the complicated structure of the relevant parameters. Moreover, the sensitivity with respect to small bandstructure-changes is reinforced which demonstrates the necessity for precise calculations.

9

Chromium thin films

As described in Sec. 2.3, two distinct kinds of antiferromagnetic skyrmions are viable. The first kind, the synthetic AFM skyrmion, has already been investigated extensively in the bilayer model (Sec. 6) and the Fe/Cu/Fe-trilayer (Sec. 8). In contrast, this section examines the alternative possibility—the intrinsic AFM skyrmion.

Initially, we aimed to study this possibility in an iron monolayer on W(001). This is a sensible choice since its checkerboard antiferromagnetic structure is well established from theoretical and experimental studies also utilizing the here-used DFT code [152]. Moreover, small-scale domain-walls were discovered in this system through spin-polarized scanning tunneling microscopy [153], which, though oriented along high-symmetry lines, is a first step towards skyrmionic textures. Even the expression of a ferromagnetic anti-skyrmion phase was theoretically predicted for the related Fe double-layer on W(110) [29] for which the exhibition of domain walls was already shown experimentally [154].

Consequently, DFT calculations were performed based on previous structures [152]. The

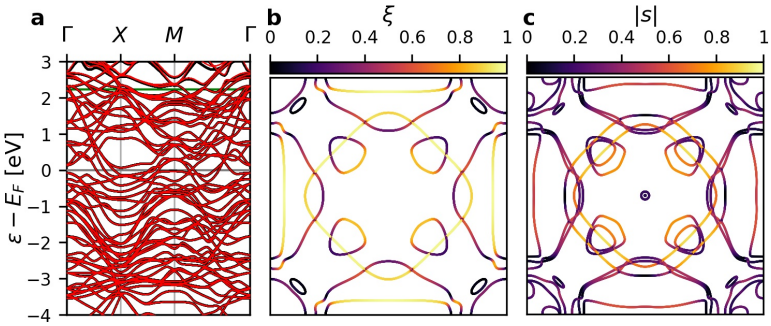

Figure 9.1: Band properties of antiferromagnetic Fe/W(001) with 6 W-layers. a) shows good agreement between the DFT (black) and Wannier-Hamiltonian (red) bandstructure without SOC up to the boundary of the "frozen" window (green). b) displays ξ at the Fermi surface without SOC while c) visualizes the spin magnitude $|s|$ including SOC in z-direction.

FLEUR code was employed to describe an iron-monolayer on 6 tungsten layers using the PBE-functional. Energetic comparison of the ferro- and antiferromagnetic structure verified the antiferromagnetic preference. Afterwards, Wannier functions were constructed based on initial projections on *s*-,*p*-, and *d*-orbitals in case of Fe and *s*-, and *d*-orbitals in case of W (in sum 180 states). The resulting model Hamiltonian reproduces the DFT-bandstructure very well (Fig. 9.1a). From the corresponding Fermi-surface, which shows a huge ξ-variety (Fig. 9.1b), the TSHE can be straightforwardly calculated using this thesis' method. However, the previously degenerate bands split up when introducing SOC (Fig. 9.1c) which ultimately results in the emergence of the THE when considering a skyrmion texture. While the treatment of such systems is easier in this thesis' approximations due to the simplification to non-degenerate wave-packet equations of motion (Secs. 3.1, 5.1.1), such studies are not the main focus of this thesis and are hence not pursued.

Instead, this chapter investigates the TSHE of intrinsic antiferromagnetic skyrmions in thin chromium films. Similarly to the last chapter, at first the reciprocal-space properties and TSHE-characteristics are depicted for different thicknesses with and without SOC on the DFT-level. Afterwards, the dependence of the obtained TSHE on the spin-texture is explored.

9.1 General structure

While antiferromagnets are abundant in nature, only few elemental antiferromagnets exist. Bulk chromium is a well-studied, appealing realization due to its metallic phase and simple, body-centered cubic structure. Furthermore, thin Cr(001)-films were shown to exhibit antiferromagnetic behavior as overlayer on metals [155] and directly as mono- and trilayers [156]. However, layers along (001)-direction are not suitable for our purpose since each layer contains either spin-up or spin-down atoms, never both. Accordingly, depending on the number of layers, either the top- and bottom-layer have opposite, pure spin character or an overall spin moment remains. Neither of these possibilities complies with the intended intrinsic antiferromagnetic setup, thus the (110)-surface is chosen instead. That orientation results in a centered rectangular unit cell whose longer edge has the $\sqrt{2}$-fold length of the shorter edge.

Previous studies of Cr(001) as monolayer on Cu(111) demonstrated an energetic preference of an 120° noncollinear antiferromagnetic over the row-wise antiferromagnet [157]. Here however, we investigate free-standing Cr-layers and assume the row-wise, collinear antiferromagnetic setup (Fig. 9.2a). For simplicity, the bulk lattice parameters (291 pm) are used so that $a \approx 5.50\, a_b$ and $b \approx 7.78\, a_b$. The centered and the corner atoms have opposite spins and the neighboring layers are translated relative to each other by half the longer lattice unit vector. Accordingly, each layer has compensated spin and the system is PT-symmetric.

In the following, both the monolayer and the trilayer are investigated based on a DFT-description using LDA. As expected, both cases prefer the antiferromagnetic order energetically and the bandstructures remain doubly-degenerate (Fig. 9.2b,c) irrespective of the inclusion of SOC. Wannier functions are constructed using *s*-,*p*-, and *d*-orbitals as initial guesses on a 12×12-grid which reproduce the bandstructure well.

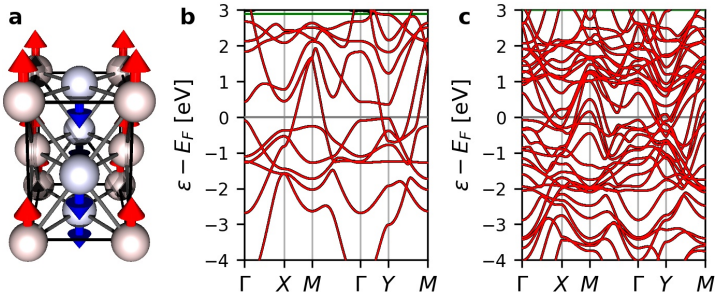

Figure 9.2: a) visualizes the structure of trilayer (110)-chromium with color-coded spin directions. b,c) show the bandstructure without SOC for monolayer (110)-chromium (b) and trilayer (110)-chromium (c) which demonstrates excellent agreement up to the boundary of the "frozen" window (green) between the DFT (black) and Wannier-Hamiltonian (red) bandstructure.

9.2 Monolayer

The most simple system with the (110)-structure is a monolayer consisting of just one spin-up and one spin-down atom arranged in the rectangular structure. The bandstructure (Fig. 9.2a) is relatively simplistic so that the Fermi-surface of the DFT Fermi-level consists of only 2 distinct lines respectively enclosing the Y- and M-point. Consequently, the bandstructure derivatives (Fig. 9.3a-c) are simple as well so that only few sign-changes appear in the effective masses. Likewise, the ξ-distribution has very few features, however the overall very small magnitude with $\xi < 0.15$ and ξ's even smaller than 10^{-4} demonstrates good separation between the degenerate bands. This is a major difference to the synthetic antiferromagnetic Fe double-layer (Fig. 8.13) were some bands even reach $\xi \approx 0.69$ though parts with comparably small ξ exist. Hence, judging from these 2 data points only, the very thin intrinsic antiferromagnets are more decoupled than their synthetic counterparts which should result in a smaller difference in R^{TS} compared to 1/3 of the decoupled $\xi = 0$ calculations. One disadvantage of the overall small ξ is that $|\partial_{\boldsymbol{k}} \ln(\xi)|$ is very large in parts due to the $1/\xi$-denominator. Hence, rapid changes of $\partial_{\boldsymbol{k}} \ln(\xi)$ occur especially at the positions of minimal ξ on the line enclosing the Y-point despite the overall simple Fermi-surface structure.

Next, the TSHE is calculated assuming the $3\boldsymbol{q}$-skyrmion texture and using the previous reciprocal-space description. The resulting iteration-time dependence of R^{TS} is shown in Fig. 9.4a. After iteration for 1 ns, the transport expressions converge to $R^{TS}_{xy} \approx 2.45 \cdot 10^{-11} \frac{\hbar}{e} \frac{\Omega \mathrm{m}}{\mathrm{T}}$ and $R^{TS}_{yx} \approx -2.41 \cdot 10^{-11} \frac{\hbar}{e} \frac{\Omega \mathrm{m}}{\mathrm{T}}$. While crystal symmetries enforced equality between R^{TS}_{xy} and $-R^{TS}_{yx}$ in the previous systems, in case of the Cr(110) no such symmetry is directly apparent. Nevertheless, in case of the monolayer $R^{TS}_{yx} \approx -R^{TS}_{xy}$ holds within the accuracy of the $\boldsymbol{k}$-interpolation despite entirely different $\sigma^{2,s_z}(\boldsymbol{k})$-distributions and accordingly different t_{it}-convergence paths. Surprisingly, this relation holds at different Fermi energies as well.

Since only 2 well-separated Fermi-lines exist at the DFT Fermi-energy, the $\boldsymbol{k}$-resolved conductivities are relatively smooth with significant contributions arising from both bands

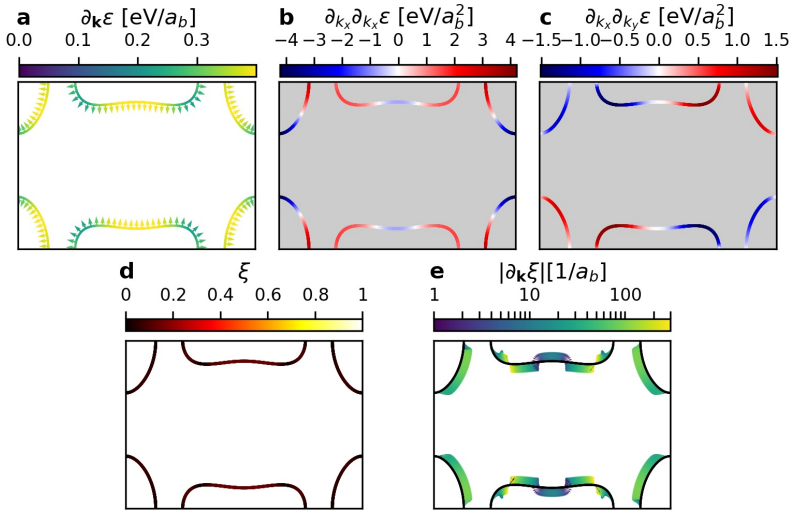

Figure 9.3: Collinear properties of Cr(110) monolayer at the Fermi surface without SOC. a) shows the group velocity with color-coded magnitude and indicated direction through arrows. b) and c) display the diagonal and off-diagonal second energy derivatives corresponding to the effective masses. d) shows the overlap ξ. In e) $\partial_{\boldsymbol{k}} \log \xi$ is plotted where the color denotes the magnitude logarithmically and densely plotted arrows indicate the direction.

(Fig. 9.4b,c). Their magnitudes are large in comparison to those of the FeCuFe-trilayer (Figs. 8.5, 8.12b). Since the dispersion derivatives are of similar magnitude, this mainly originates in the small magnitude of $d_z = 4.52\, a_B$. Contributions with positive and negative $\sigma^{2,s_z}(\boldsymbol{k})$ appear in both directions so that the R^{TS} is more compensated than in case of very thin FeCu$_n$Fe-layers but significantly less than in case of thicker systems. Here, σ^{2,s_z} is 46% (xy) and 40% (yx) of the majority sum compared to 79% in case of the iron double-layer (Fig. 8.10b).

The R^{TS} are quite near to 1/3 of the $\xi = 0$ calculations with 35.6% and 35.0%. However, since the $(1 - \xi^2)$-prefactor with the maximal ξ only yields an overall reduction to 97.8% the previous interpretation of preferred attenuation of the minority $\sigma^{2,s_z}(\boldsymbol{k})$ is insufficient to describe that deviation. Furthermore, the $\boldsymbol{k}$ of maximal ξ have small $\sigma^{2,s_z}(\boldsymbol{k})$-magnitudes so that this explanation is even less convincing. Alternatively, this effect could be caused by the large $\partial_{\boldsymbol{k}}\xi$. However, comparing calculation with $\partial_{\boldsymbol{k}}\xi = 0$ yielded even slightly larger R^{TS} with reductions to 35.7% and 35.1% which eliminates this possible explanation. Since the percentages are still quite near to 1/3, a systematical modification due to the different setup (intrinsic skyrmions) is unlikely so that insufficient t_{it}-convergence is the most probable cause. As many $\boldsymbol{k}$ have very small ξ, this explanation is also convincing as small ξ increase the necessary t_{it} significantly (Fig. 5.6) due to increased tracking of the texture changes (Eq. 3.38a).

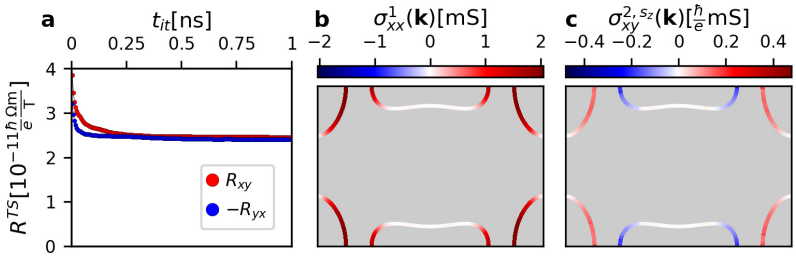

Figure 9.4: TSHE of Cr(001) monolayer as calculated with $N_k = 1024$, $N_R = 10$, and $\delta n_{max} = 0.01$ (compare to Sec. 5.3). a) shows the t_{it}-dependence of the topological spin Hall constant R^{TS}. b,c) show exemplary, converged ($t_{it} = 1\,\text{ns}$), $\boldsymbol{k}$-resolved conductivity contributions. The longitudinal conductivity in x-direction is displayed in b) and the transversal spin conductivity corresponding to R^{TS}_{yx} is plotted in c).

In conclusion, the Cr(110) monolayer intrinsic AFM skyrmion is a simple system without huge differences to the previous synthetic AFM skyrmions. A remarkable property is the extreme smallness of ξ, but the overall decrease due to the $\mathcal{SU}(2)$-character is surprisingly similar to previous calculations so that all computations can be performed analogously, though larger t_{it} are necessary. This setup could be used to further investigate the properties of intrinsic AFM skyrmions, instead the Cr(110) trilayer is chosen for further investigations due to the monolayer's extreme Fermi-surface simplicity and smallness of ξ.

9.3 Trilayer

Since the chromium monolayer is relatively simplistic, the main emphasis of this chapter is laid onto the trilayer (Fig. 9.2a) as investigated in this section. Here, its TSHE is studied assuming the $3\boldsymbol{q}$ skyrmion texture which demonstrates huge similarities with the synthetic AFM-skyrmion. The extension to different textures is covered in the next section.

9.3.1 TSHE at the Fermi surface

Analogous to the previous chapter, the TSHE is investigated first without SOC and assuming the $3\boldsymbol{q}$-texture.

The main reciprocal-space properties are displayed in Fig. 9.5. Many new Fermi lines emerge compared to the monolayer. As the number of atoms is tripled, the tripling of the bands around M is self-evident. The other monolayer line encircling Y is quadrupled which is not surprising as the monolayer has another flat band almost reaching the Fermi energy at Y (Fig. 9.2b,c). Furthermore, 3 bands emerge near the X-point so that overall 3 separate sets of Fermi lines are exhibited. While the set encircling M is relatively simple, the other set has crossings which complicate the interpolation and result in localized enhancement of the effective masses and large $|\partial_{\boldsymbol{k}}\xi|$. Excluding these sections, the magnitudes of the group

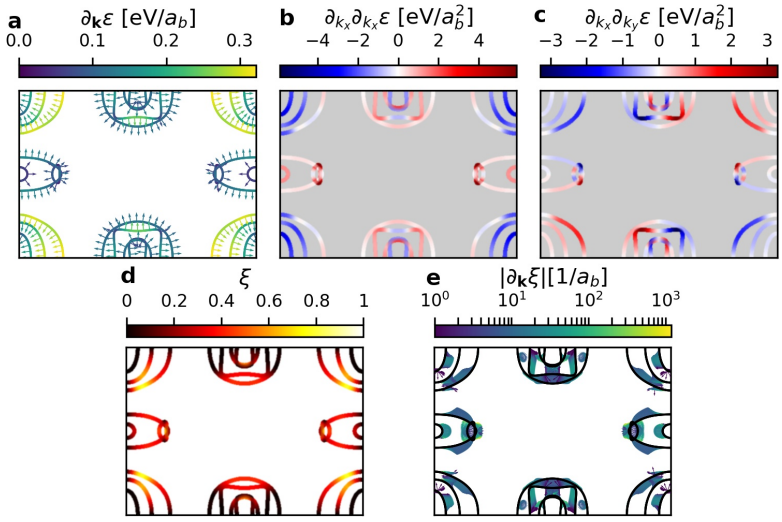

Figure 9.5: Collinear properties of Cr(110) trilayer at the Fermi surface without SOC. a) shows the group velocity with color-coded magnitude and indicated direction through arrows. b) and c) display the diagonal and off-diagonal second energy derivatives corresponding to the effective masses. d) shows the overlap ξ. In e) $\partial_{\boldsymbol{k}} \log \xi$ is plotted where the color denotes the magnitude logarithmically and densely plotted arrows indicate the direction.

velocities and effective masses are relatively comparable and do not include extreme variations. The most significant modification is the largely increased variation of ξ. Here, ξ reaches almost 0.8 which is a drastic difference to the monolayer with $\xi < 0.15$. Some bands still have small ξ, but the overall distribution is similar to that of the FeCuFe-trilayer. Hence, more features are expected due to the $\mathcal{SU}(2)$-character and smaller $\partial_{\boldsymbol{k}} \ln(\xi)$ are expressed.

The TSH-properties at the Fermi surface are displayed in Fig. 9.6. The R^{TS}-convergence is slower than in case of the monolayer which, at first glance, is surprising due to the decreased average ξ. Still, many Fermi line sections also have small ξ which explains this behavior in combination with the significantly decreased group-velocity magnitudes. R^{TS}_{xy} and $-R^{TS}_{yx}$ are surprisingly equal despite the absence of enforcing symmetries similar to the monolayer. At different E_F this relation is approximately satisfied for a surprisingly large range, yet many E_F show clear violation so that without further study this property has to be regarded as accidental. Compared to the $\xi = 0$-case, R^{TS} is reduced to approximately 31.5% which is slightly below $1/3$ so that the $\boldsymbol{k}$-dependence of ξ has no surprising effects. Considering the slow convergence, the percentage might even decrease further which would still be within expectable ranges but is different from the monolayer case with percentages slightly above $1/3$.

The Fermi line sets have relatively different characteristics (Fig. 9.6b,c). The longitudinal component has relevant contributions from the M- and Y-set while the X-set is of small

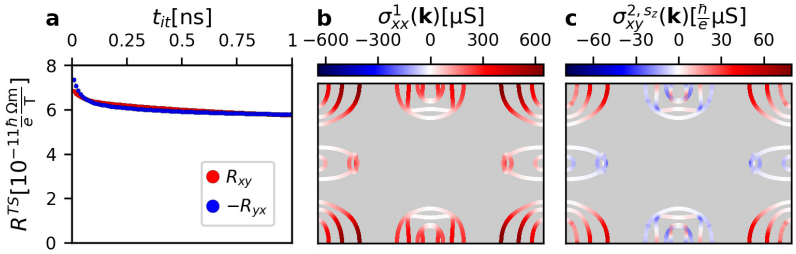

Figure 9.6: TSHE of Cr(110) trilayer as calculated with $N_k = 8196$, $N_R = 10$, and $\delta n_{max} = 0.01$ (compare Sec. 5.3). a) shows the t_{it}-dependence of the topological spin Hall constant R^{TS}. b,c) show exemplary, converged ($t_{it} = 1$ ns), $\boldsymbol{k}$-resolved conductivity contributions. The longitudinal conductivity in x-direction is displayed in b) and the transversal spin conductivity corresponding to R^{TS}_{yx} is plotted in c).

integrated magnitude. The transversal components are even more diverse due to the small, negative contributions from the X-set, strongly alternating and compensating contributions from the Y-set, and dominating monotonously positive contributions from the M-set. Compared to the monolayer, the compensation of the $\sigma^{2,s_z}_{xy}(\boldsymbol{k})$ has decreased so that the σ^{2,s_z} are $\sim 61\%$ of the majority $\sigma^{2,s_z}_{xy}(\boldsymbol{k})$-integral (monolayer on average $\sim 43\%$). This change can be mainly attributed to the remaining large contributions of the M-lines in combination to the emergence of small positive contributions near X so that the small integrals of the X-sets become irrelevant.

Overall, the total TSHE-magnitude is slightly larger than that of most FeCuFe-trilayers. The magnitudes of $\sigma^{2,s_z}(\boldsymbol{k})$ vary less which, in combination with fewer line-intersections, allows the usage of less N_k. Furthermore, the decreased symmetry allows differences between R^{TS}_{xy} and R^{TS}_{yx} which results in more volatility with respect to texture variations. Hence, the Cr(110) trilayer supplies a great platform for further examination of the intrinsic AFM-setup.

9.3.2 Influence of SOC

While the previous trilayer setup has many useful properties, line crossings at the Fermi energy still complicated the TSHE evaluation. SOC generally adds level repulsion through symmetry breaking so that crossings are often avoided (as in case of the FeCuFe-trilayer in Sec. 8.2.3). Since Cr is a light atom ($Z = 24$), only few modifications are to be expected near the intersections. Still, SOC results in significant modifications of the Fermi surface as shown in Fig. 9.7. The extreme splitting of the bands near Y is most noticeable, but also intersections of the lines near X are lifted. Unfortunately, 4 symmetry-related crossings within the Brillouin zone are split very weakly so that some numerical intersection problem remains.

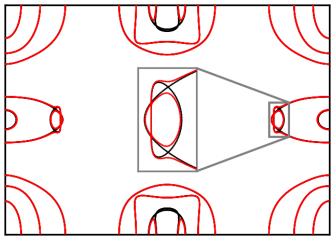

Figure 9.7: Cr(110) Fermi surface including (red) and excluding (black) SOC.

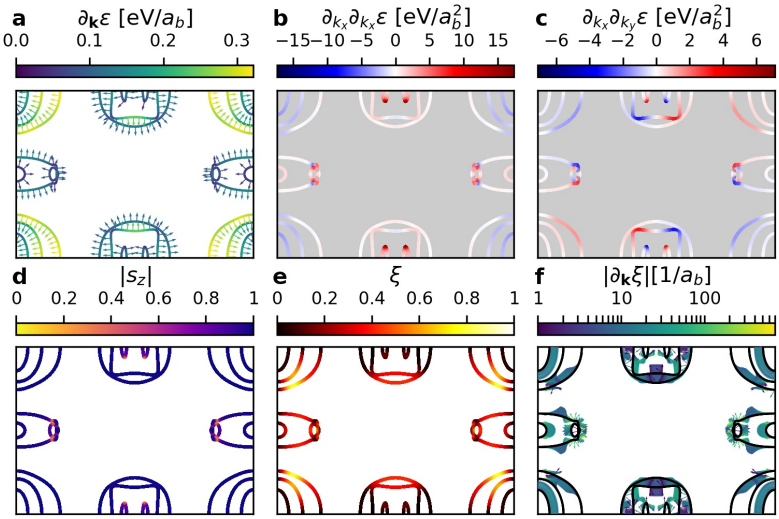

Figure 9.8: Collinear properties of Cr(110) trilayer at the Fermi surface including SOC. a) shows the group velocity with color-coded magnitude and indicated direction through arrows. b) and c) display the diagonal and off-diagonal second energy derivatives corresponding to the effective masses. d) shows the magnitude of the spin-expectation value as obtained from the Wannier model. e) visualizes the overlap ξ. In f) $\partial_{\boldsymbol{k}} \log \xi$ is plotted where the color denotes the magnitude logarithmically and densely plotted arrows indicate the direction.

The reciprocal-space Fermi surface properties are displayed in Fig. 9.8. Consideration of SOC barely affects the band properties as can be seen by comparison to the analogous plot without SOC (Fig. 9.5). The group velocities are barely affected while the maximal magnitudes of the 2nd derivatives grow to more than the twofold of the previous maxima. These spikes at the edges linearly affecting the TSHE could severely complicate the necessary $\boldsymbol{k}$-interpolation which would counteract the previous intention of simplification through opening the intersections. Fortunately, SOC diminishes the spin-polarizations $|s_z|$ significantly around those $\boldsymbol{k}$ reaching almost 0 so that $\sigma_{xy}^{2,s_z}(\boldsymbol{k})$ has small minima instead of spiky maxima (Fig. 9.9c). ξ decreases slightly around the avoided crossing in principle enhancing the TSHE contributions again, but this effect is entirely superseded by the $|s_z|$-decrease. Since the affected line-sections ultimately have minor contributions, the effect of ξ increasing the necessary t_{it} for convergence is negligible as well. The enhanced variations of ξ increase the variability of the directions of $\partial_{\boldsymbol{k}}\xi$ as well, but no systematic effect on the transport is found.

The TSHE is calculated and displayed analogously to the case without SOC (Fig. 9.6) in Fig. 9.9. Few modifications caused by the consideration of SOC have a huge impact on the TSHE, most notably the clear lifting of the $R_{xy}^{TS} = -R_{yx}^{TS}$-relation. While R_{yx}^{TS} decreases by 5.3% relative to the calculation without SOC, the magnitude of R_{yx}^{TS} increases by 10.3% to $-6.35 \cdot 10^{-11} \frac{\hbar}{e} \frac{\Omega \mathrm{m}}{\mathrm{T}}$. Similar differences are found at different Fermi energies. Furthermore,

the t_{it}-convergence is accelerated as no trend is visible from at least 0.5 ns onwards, whereas R^{TS} is still slightly decreasing for larger times when excluding SOC (Fig. 9.6a).

The modification of R^{TS} has its origins in the modifications of both σ^1 and σ^{2,s_z}. The adjustments of the former is straightforward. The group-velocities have relatively small magnitudes in the vicinity of the crossing so that the initial $\sigma^1(\boldsymbol{k})$ have only minor contributions (Fig. 9.6b). This does not change with the introduction of SOC so that some positive sections are effectively removed from the Fermi surface thereby shrinking the integrated value (Fig. 9.6b).

	$\sigma^1_{xx}\left[10^5\frac{\mathrm{S}}{\mathrm{cm}}\right]$	$\sigma^1_{yy}\left[10^5\frac{\mathrm{S}}{\mathrm{cm}}\right]$	$\sigma^{2,s_z}_{xy}\left[10^4\frac{\hbar}{e}\frac{\mathrm{S}}{\mathrm{cm}}\right]$	$\sigma^{2,s_z}_{yx}\left[10^4\frac{\hbar}{e}\frac{\mathrm{S}}{\mathrm{cm}}\right]$
without SOC	5.16	4.43	1.31	−1.31
including SOC	4.86	4.14	1.27	−1.63

Table 9.1: Effect of SOC on relevant (spin) conductivities for R^{TS}-calculation.

The modifications of $\sigma^{2,s_z}(\boldsymbol{k})$ are different. Only few differences are apparent when comparing the xy-case with (Fig. 9.9c) and without (Fig. 9.6c) SOC. Of course, contributions from the lines around Y disappear, but this change has minor overall impact since those bands had positive and negative contributions of similar magnitude. The modifications near X have even less impact as only very localized and minor modifications are visible. Consequently, σ^{2,s_z}_{xy} changes only insignificantly with a minor decrease in magnitude (Tab. 9.1). σ^{2,s_z}_{yx} behaves differently. The initial positively dominated Y-states are replace by a smaller but more concentrated positive contributions around the edges. More importantly, negative $\sigma^{2,s_z}_{yx}(\boldsymbol{k})$ appear in the X-states counteracting the previously positive sections. Accordingly, σ^{2,s_z}_{yx} decreases significantly enhancing the R_{yx}-magnitude.

In conclusion, SOC has a strong impact on the TSHE though considering its effect on the collinear-DFT level only. As the computation after construction of the Wannier-functions is identical, its inclusion allows major accuracy improvements with only minor computational

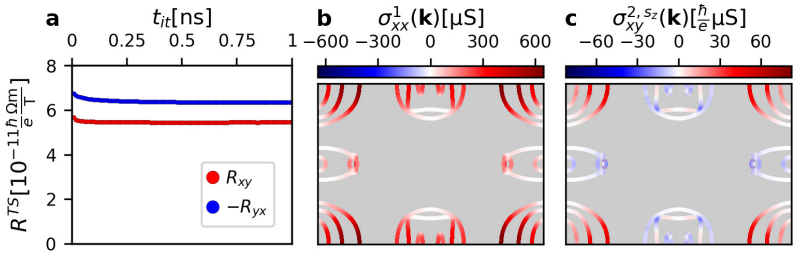

Figure 9.9: TSHE of Cr(110) trilayer as calculated with $N_k = 8196$, $N_R = 10$, and $\delta n_{max} = 0.01$ (compare Sec. 5.3). a) shows the t_{it}-dependence of the topological spin Hall constant R^{TS}. b,c) show exemplary, converged ($t_{it} = 1$ ns), $\boldsymbol{k}$-resolved conductivity contributions. The longitudinal conductivity in x-direction is displayed in b) and the transversal spin conductivity corresponding to R^{TS}_{yx} is plotted in c).

effort. In case of the chromium trilayer, SOC simplifies the Fermi surface properties and results in better converged and direction-dependent R^{TS}. Hence, the following investigation of texture modifications is based on the calculations including SOC.

9.4 Variation of the skyrmion texture

After detailed study of the transport properties evoked by the 3**q**-texture, the question arises whether the obtained TSHE is indeed a topological quantity, meaning that it is independent of the skyrmion shape but depends only on the skyrmion number. While the few parameters of the 3**q**-texture could be varied to obtain slight modifications, the more viable option is the employment of the SPIRIT-code as described in Sec. 2.4.2. This section accordingly considers the TSHE of various different textures.

9.4.1 3q-state versus similar SPIRIT texture

First, it is sensible to investigate the similarity between the previously used 3**q**-texture and the atomistic parameterization. Fortunately, an alternative texture with great similarity to the 3***q***-texture is already described in Sec. 2.4.2.

Consequently, the TSHE is calculated with the atomistic parameters from Tab. 2.1 in order to compare the resulting TSHE with that of similar 3***q***-state calculations in Fig. 9.9. The differences between both calculations, encoded in the t_{it}-dependence of R^{TS}, are shown in Fig. 9.10. Only minimal differences between the converged results are to be expected due to the topological nature of the TSHE and the similarity of the textures. Indeed, for R^{TS}_{xy} this equality is well satisfied with differences of only 0.13%, however for R^{TS}_{yx} the final values are visibly different with 0.78%. Comparing the overall t_{it}-dependence their similarity is most convincing. R^{TS}_{xy} converges quicker than R^{TS}_{yx} in both cases and the shape of the convergence is relatively texture-independent. While the differences between the textures decrease in case of R^{TS}_{xy}, it is relatively constant for R^{TS}_{yx}. The slower convergence of the SPIRIT-texture in case of R^{TS}_{xy} might originate in the more abrupt radial change of the skyrmions which can delay the $|s_z|$-convergence, however this explanation is weak considering the similar convergence of R^{TS}_{yx}. The reason for that difference most probably lies hidden in the transport weights and corresponding ξ-distributions.

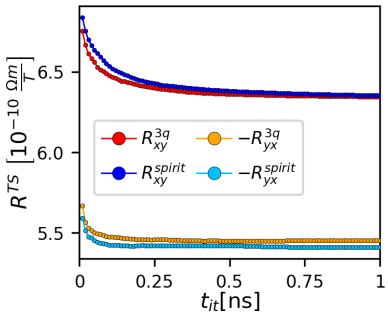

Figure 9.10: TSHE comparison between 3**q**-texture (Fig. 2.4) and similar SPIRIT texture (Fig. 2.5)

Nevertheless, the applicability of the SPIRIT-textures is demonstrated and a first confirmation of the topological character is obtained as the final R^{TS}-differences are quite small. In the following, the topological property is challenged by more drastic variations of the skyrmion lattice.

9.4.2 Isolated Skyrmions

The most trivially achievable skyrmionic texture in the atomistic setup are isolated skyrmions. Starting from a small spherical section with reversed spins, the magnetization quickly converges to a skyrmion groundstate given suitable parameters. While such isolated skyrmions are disadvantageous from the viewpoint of the TSHE iterative solution, they allow great variability and easy modification of the skyrmion types. Here, Bloch-, Néel-, and anti-skyrmions as most basic skyrmion types (Sec. 2.1.2) are investigated in square-lattices with very far separated skyrmions.

The skyrmion type can be easily tuned by changing the DMI-direction. The here-used parameters and chosen DMI-tensors are denotes in Tab. 9.2.

type	J[meV]	D_{xx}	D_{xy}	D_{yx}	D_{yy}	K_z[meV]	B_z[T]
Bloch	15	2	0	0	2	0.4	1
Neel	15	0	-2	2	0	0.4	1
Anti	15	0	2	2	0	0.4	1

Table 9.2: SPIRIT-parameters corresponding to the texture displayed in Fig. 9.15. The DMI is given in meV.

The corresponding textures are shown in Fig. 9.11. The size of the magnetic lattice-spacing is scaled to match the averaged emergent magnetic field of the 3$\boldsymbol{q}$-texture. Due to the increased B and K (Tab. 2.1) the skyrmion radius ($\sim 30\,a_B$) got much smaller than in the previous case ($\sim 115\,a_B$). Furthermore, the long distances between neighboring skyrmions enhances the $\mathcal{B}_z$-magnitude. Hence, the emergent fields become very large and localized with up to $-380\,\mathrm{T}$ (Fig. 9.12b) in comparison to the $-19.7\,\mathrm{T}$ of the 3$\boldsymbol{q}$-texture (Fig. 2.4b). A further difference is that almost no positive $\mathcal{B}_z$-contributions appear in the isolated case ($\mathcal{B}_z < 0.01\,\mathrm{T}$) while in the 3$\boldsymbol{q}$-case positive contributions emerged with more than 20% magnitude of the maximal negative $\mathcal{B}_z$. Since the different types of the isolated skyrmions are very similar except for their defining differences, the emergent magnetic fields are equivalent except for the sign-reversal in case of the anti-skyrmion.

The evoked TSHE of the isolated skyrmion lattice is surprisingly independent of the skyrmion type (Fig. 9.12a). While the topological character suggests equivalent final values,

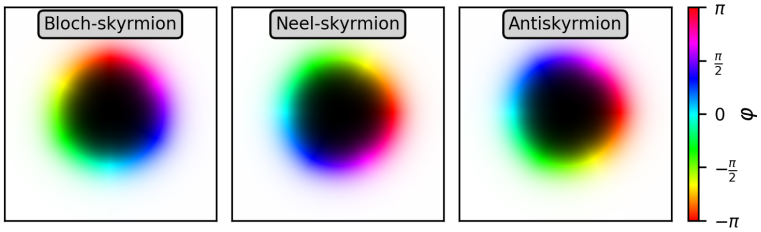

Figure 9.11: Skyrmion textures of the 3 investigated types as given in Tab. 9.2. The colormap is chosen analogously to Fig. 2.4

the intermediate values might vary due to the different spin-evolution. Yet, their R^{TS} have only very minor differences at very small t_{it} and become almost identical for intermediate t_{it}. The final R^{TS}_{xy} are virtually indistinguishable as their difference is less than 0.04%, the R^{TS}_{yx}-differences are even smaller. Note that the anti-skyrmion is distinguishable due to the reversed σ^{2,s_z}_{xy}-sign, the previous equivalence originates from the division by the averaged emergent magnetic field $\overline{\mathcal{B}}$ which also changes sign (Eq. 4.12). Comparison to the previous 3$\boldsymbol{q}$-texture verifies the expected behavior. The R^{TS} are very different for small t_{it} as the 3$\boldsymbol{q}$-calculation starts with larger magnitudes while the isolated textures start with smaller magnitudes. This difference is easily understandable as the 3$\boldsymbol{q}$-texture has skyrmionic behavior everywhere so that all initial states with perfect spin polarization describe the maximal contributions. Conversely, the initial-state real-space grid resolves the isolated skyrmion texture very poorly in the isolated skyrmion case as many states are in the antiferromagnetic background. Coincidentally, the initial grid is skewed towards the background so that R^{TS} starts from a significantly smaller magnitude. After sufficient t_{it} the previous inaccuracies are resolved and the R^{TS} converge towards similar values. Ultimately, the R^{TS} differ by less than 0.8% despite their entirely different shape. As this difference is only marginally larger than the difference to the atomistic texture of Sec. 9.4.1, the topological character of the TSHE is confirmed for drastically different magnetic textures.

9.4.3 Skyrmion lattice variation

After demonstrating R^{TS}'s independence with respect to the skyrmion type and drastic skyrmion-size changes, this section explores a more systematical approach to variations of the skyrmion's size and shape in a lattice.

At first, it is necessary to obtain a convenient skyrmion lattice description within SPIRIT. In principle, it is possible to start again from the 3$\boldsymbol{q}$-alike texture of Sec. 2.4.2. However, one disadvantage of that texture is that the skyrmion lattice does not perfectly fit into the 200 × 200 unit-cell which results in unexpected distortions and lattice rearrangement

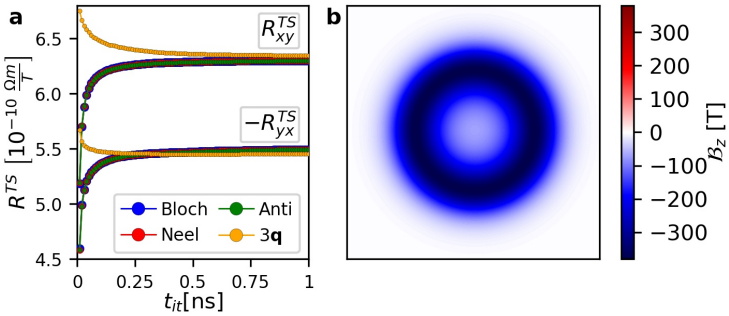

Figure 9.12: a) Comparison of R^{TS} between the different type isolated skyrmions types and the 3$\boldsymbol{q}$-lattice texture. b) Emergent magnetic field corresponding to the isolated Néel-type skyrmion (Fig. 9.11b).

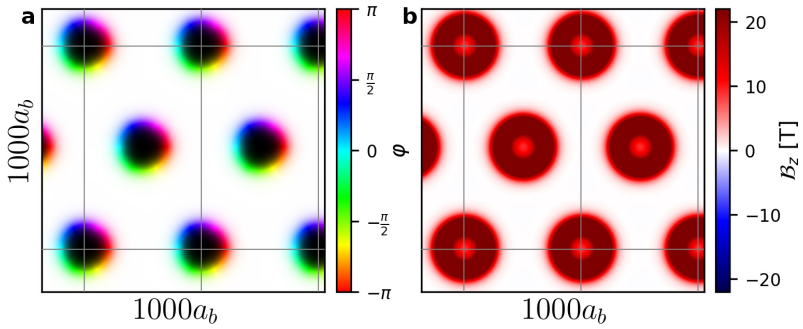

Figure 9.13: Magnetic texture (a) and emergent magnetic field (b) of this section's skyrmion lattice model. The atomistic parameters are given in Tab. 2.1 . The gray lines denote the possible minimal unit-cells. The unit-cell of this texture contains 4 of the minimal ones.

despite systematically changing parameters. Furthermore a large number of skyrmions (14) is necessary to arrange the skyrmions in a lattice through energy minimizations. Obviously, this reduces the accuracy of the ensuing spline-interpolation (Sec. 5.2.3) as less atomistic sites constitute one skyrmion.

This problem can be circumvented by adjusting the SPIRIT-grid to the expected lattice-symmetry. Since the SPIRIT-description requires a rectangular lattice while the skyrmions form a triangular lattice, the most simplistic congruent choice is a rectangle whose lattice-ratio is $a = (2/\sqrt{3})b$. Under these conditions a perfect triangular structure could be constructed by skyrmions centered on the corners and in the center. However, it is impossible to exactly satisfy the ratio with equidistant lattice-spacing as the fraction is an irrational number. Nevertheless, a 153×265-grid satisfies the relation sufficiently well with an error of 0.38% which is a definite improvement over the 200×200 grid with only minor increase of computational demand.

For convenience, the same parameters as for the isolated skyrmions are used (Tab. 9.2). Based on an arbitrary choice, the bulk of the ensuing calculations is only done for the antiskyrmion texture since the TSHE is independent of the skyrmion type. Indeed, calculations of the basic texture simply switching to Bloch- and Néel-type show R^{TS}-differences of less than 0.03%. The small skyrmion size determined by the chosen parameter set requires the inclusion of 4 minimal triangular unit cells into the used unit cell. Although this decreases the accuracy of each skyrmion (8 instead of 2), still significantly more sites describe each skyrmion and the lattice-ratio condition remains satisfied. The magnetic order parameter and the corresponding emergent magnetic field is visualized in Fig. 9.13. At the given parameters, the skyrmions are well separated so that their shape closely resembles that of the isolated case (Fig. 9.11). Analogous to the isolated case, the emergent magnetic field contains very small negative contributions only (positive in Fig. 9.12b), but due to the lattice arrangement the magnitudes do not differ much from those of the $3\boldsymbol{q}$-texture.

J[meV]	D_{xy}[meV]	D_{yx}[meV]	K_z[meV]	B_z[T]
15	2	2	0.4	1

Table 9.3: SPIRIT-parameters corresponding to the texture displayed in Fig. 9.13

The TSHE's t_{it}-evolution of this texture is shown in Fig. 9.14. As expected, the R^{TS} converge on similar time-frames and the final values are very near to those of the previous calculations based on the 3$\boldsymbol{q}$-texture and the isolated skyrmions. Incidentally, the converged R^{TS} are between those of the comparative calculations. This section's lattice has a smoother convergence as it starts from a more suitable initial-grid and has a smoother $\mathcal{B}_z$ than the 3$\boldsymbol{q}$-texture.

Hence, this setup is nicely suited for TSHE calculations following this thesis's method so that it can be conveniently used in the following to study the dependence on size- and shape-variations.

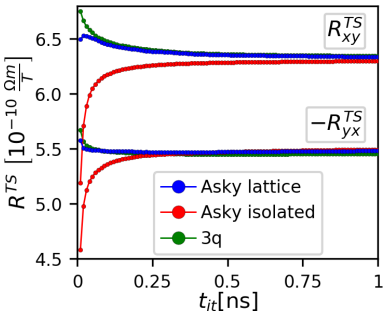

Figure 9.14: TSHE comparison of anti-skyrmion lattice (Fig. 9.13) with 3**q**-texture and isolated anti-skyrmion (Fig. 9.12)

Variation of radius

Firstly, the TSH-response to variations of the skyrmion radius is investigated. One simple possibility to achieve such systematical changes is the variation of the applied B-field within the atomistic model. Larger B correspond to an increased energetic preference of the background state so that the skyrmions shrink and vice versa. Example emergent magnetic fields demonstrating growth and shrinking of the skyrmions depending on B are shown in Fig. 9.15. The relation between the applied field B and the skyrmion radius r_{sky} is visualized in Fig. 9.16a. r_{sky} is defined as the distance between the skyrmion core with maximal n_z-magnitude and the surrounding positions where $n_z = 0$. This distance can depend on the direction as skyrmions are not necessarily spherical . Hence, minimal and maximal distances are displayed. From the atomistic input parameters, this sections' skyrmion texture should be spherical which is accurately confirmed by the vanishing difference between minimal and maximal radii. Hence, the great numerical accuracy of the skyrmion lattice on this interpolation grid is reaffirmed. The monotonous, non-linear relation between B and r_{sky} demonstrates the expected tuning applicability.

With the same numerical parameters as in previous calculations, the TSHE is calculated for $B = 0.6..1.6\,\mathrm{T}$ in steps of $0.1\,\mathrm{T}$. The final R^{TS} after $t_{it} = 1\,\mathrm{ns}$ are shown in Fig. 9.16b. Most remarkably, a clear, almost linear dependence between B and R^{TS} is observed. When changing r_{sky} from $60\,a_B$ to $114\,a_B$, i.e. almost quadrupling the skyrmion size, R^{TS}_{xy} and $-R^{TS}_{yx}$ increase by 1.1% and 3.3%, respectively. Although this size change is much smaller than the previous comparison of isolated skyrmions and the 3$\boldsymbol{q}$-state (Sec. 9.4.2), this sections' R^{TS}-variation is much more drastic than the previous section's 0.8%. One possible explanation is insufficient

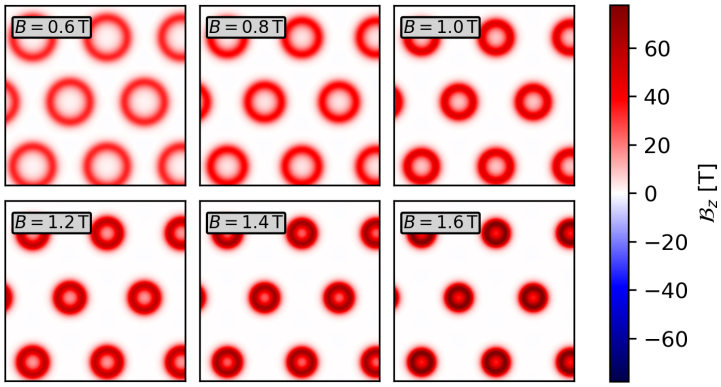

Figure 9.15: Anti-skyrmion lattice with changing applied B-field. The other parameters are shown in Tab. 9.3.

t_{it}-convergence, however Fig. 9.16c demonstrates similar behavior with relatively flat but offset curves for different B. This possibility can be excluded as R^{TS}_{yx} has an significantly flatter t_{it}-dependence though having a stronger B-dependence. Furthermore, the differences between the $R^{TS}(B)$ slopes in the xy- and yx-case excludes simple reasons such as wrongly calculated $\overline{\mathcal{B}}$ or direct changes of $|s_z|$.

Hence, the topological character of the TSHE is unexpectedly violated with respect to the skyrmion-radius variations. Overall, this effect is not overly severe with at most 3.3% in the here-investigated, quite large range, but it is definitively an interesting result entirely impossible in the trivial ferromagnetic formalism.

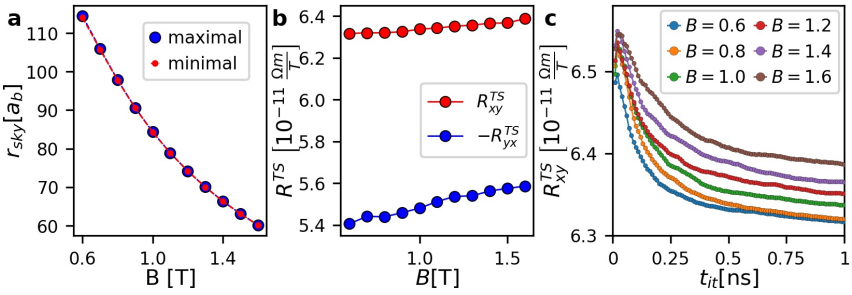

Figure 9.16: THSE properties of Cr(110) trilayer with varying skyrmion radii. a) shows the skyrmion radii r_{sky} depending on the applied field B with the remaining parameters from Tab. 9.3. b) demonstrates the dependence of R^{TS} on B. In c) the iteration-time t_{it}-dependence for R^{TS}_{xy} is shown for several B in units of T.

9.4.4 Variation of shape

Alternatively, the shape of the skyrmions can be changed through variation of the DMI. Choosing D's with different magnitudes distorts the skyrmions away from the spherical shape and thus allows systematic investigation.

Again, the basic texture of the previous section (Tab. 9.3) is used. Severe distortions are introduced by varying D_{yx} from 1.9 meV to 2.1 meV, thus investigating the vicinity of the previously chosen $D_{yx} = 2.0$ meV. Exemplary emergent magnetic fields of this series are visualized in Fig. 9.17. Strong distortions are immediately visible especially in y-direction for larger D_{yx}. Further increase results in the formation of stripe domains. Conversely, the skyrmions enlarge in x-direction but shrink in y-direction for smaller D_{yx}. Yet, the overall skyrmion shape remains well distinguishable and the $\mathcal{B}$-magnitudes do not change drastically. The skyrmion radii are plotted in Fig. 9.18a reaffirming the previous observations. For the largest D_{yx}, the maximal radius exceeds its counterpart from the B-variations while the minimal radius becomes relatively small. Hence, strong skyrmion-distortions are observed in the chosen range of parameters, although smaller D_{yx} could be chosen to further enlarge the range investigated distortions.

The TSHE-dependence on this texture variations is shown in Fig. 9.18b. Contrary to the variation of B, no strong dependences are expressed. While $-R_{yx}^{TS}$ decreases with decreasing D in most cases, the overall change is only 0.88% instead of the previous 3.3%. Considering the change of the skyrmion size with variations of D, this minimal trend could be a further manifestation of the previously discovered dependence on the radius. However, for the R_{xy}^{TS} calculations no dependence is visible anymore, instead the previous trend of increasing magnitudes is entirely replaced by small, unsystematic variations. The t_{it}-dependence of R_{yx}^{TS} (Fig. 9.18c) shows the previous behavior where most contributions are horizontally shifted and not converging towards a similar value. In comparison, the t_{it}-dependent variations are less systematical than in case of R_{xy}^{TS} analogous to the variation of B.

In conclusion, this calculation confirms the topological independence on the shape, only

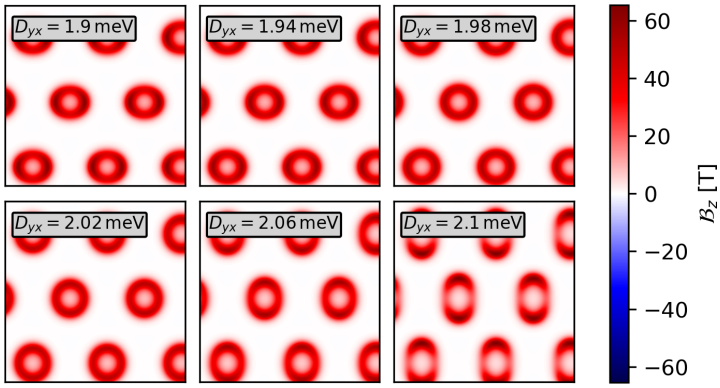

Figure 9.17: Anti-skyrmion lattice with changing D_{yx}. The other parameters are shown in Tab. 9.3

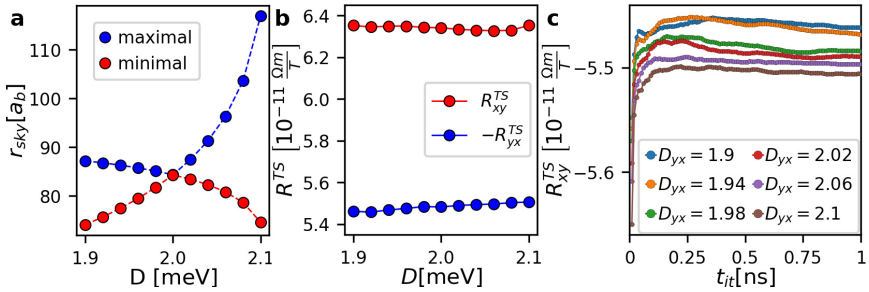

Figure 9.18: THSE properties of Cr(110) trilayer with varying skyrmion shape. a) shows the minimal and maximal skyrmion radii r_{sky} depending on D_{yx} with the remaining parameters from Tab. 9.3. b) demonstrates the dependence of R^{TS} on D_{yx}. In c) the iteration-time t_{it}-dependence for R^{TS}_{xy} is shown for several D_{yx} in meV.

remnants of the previous, unexpected dependence of the size are recovered.

10

Conclusion

In summary, a computational method has been developed which allows the estimation of the topological spin Hall effect in the adiabatic limit as exhibited by degenerate antiferromagnetic skyrmions, based on collinear density functional theory.

It is demonstrated that the arising spin-dynamics of the wave-packet equations of motion, caused by the non-abelicity of the Berry curvatures and connections, have tremendous impact on the resulting topological spin Hall effect.

A main part of this thesis is the development and implementation of a computational scheme for calculating transport effects based on semiclassical equations of motions and the Boltzmann formalism, as well as embedding of this procedure into existing numerical frameworks. Practically, the spin- and real-space dynamics of wave-packets in magnetic textures are solved iteratively using the Runge-Kutta method while transport characteristics are extracted using simple approximations of the Boltzmann equations. Convergence with respect to numerical parameters is carefully examined and several procedures are employed to balance numerical accuracy and computational effort. While the majority of the performed calculations use a basic skyrmion lattice approximation, various periodic magnetic textures can be imported from an atomistic spin dynamics code. Smoothness between the sites, as required from the semiclassical equations of motion, is ensured by spline interpolation which also accelerates the computational evaluation of analytical skyrmion-models. Simple and versatile application to various materials is guaranteed by an interface to well-established density functional theory utilizing Wannier functions from which all necessary collinear reciprocal-space properties are obtained accurately and efficiently.

Realistic estimations of the topological spin Hall effect are attained for FeCuFe(001)-trilayers and thin Cr(110)-layers demonstrating the universality of the calculation procedure irrespective of the distinction into synthetic and intrinsic antiferromagnets. Sizeable magnitudes of the topological spin Hall effect are predicted similar to previous studies of the topological Hall effect. Furthermore, extreme sensitivity with respect to reciprocal-space properties is uncovered which promises great tuning potential especially in the presence of Dirac cones. Consideration of spin-orbit coupling on the DFT-level has lead to minor corrections only, yet entwining with topologically non-trivial reciprocal definitively possible in the chosen framework provides interesting vistas for further studies.

Contrary to the sensitivity with respect to reciprocal-space changes, the topological char-

acter of the arising transport is verified by study of diverse skyrmion textures. Only minor systematic variations are discovered when slightly modifying an example skyrmion structure while consideration of vastly different textures resulted in almost identical responses.

A great advantage of the employed method is the great adaptability on the level of the semiclassical equations of motion and ensuing approximations in the Boltzmann formalism. While further corrections of the studied transport effects could be systematically included, a particular interesting possibility is the consideration of textures in degenerate non-collinear antiferromagnets whose rich dynamics promise exciting phenomena.

List of Figures

Bibliography

[1] G. Binasch, P. Grünberg, F. Saurenbach, and W. Zinn. "Enhanced magnetoresistance in layered magnetic structures with antiferromagnetic interlayer exchange". In: *Phys. Rev. B* 39.7 (1989), pp. 4828–4830. DOI: 10.1103/PhysRevB.39.4828 (cit. on pp. 1, 103).

[2] F. D. Natterer, K. Yang, W. Paul, P. Willke, T. Choi, T. Greber, A. J. Heinrich, and C. P. Lutz. "Reading and writing single-atom magnets". In: *Nature* 543.7644 (2017), pp. 226–228. DOI: 10.1038/nature21371 (cit. on p. 1).

[3] N. Nagaosa and Y. Tokura. "Topological properties and dynamics of magnetic skyrmions". In: *Nat. Nanotech.* 8.12 (2013), pp. 899–911. DOI: 10.1038/nnano.2013.243 (cit. on pp. 1, 5, 8, 44).

[4] R. Wiesendanger. "Nanoscale magnetic skyrmions in metallic films and multilayers: a new twist for spintronics". In: *Nat. Rev. Mater.* 68 (2016), p. 16044. DOI: 10.1038/natrevmats.2016.44 (cit. on p. 1).

[5] Y. Tokunaga, X. Z. Yu, J. S. White, H. M. Rønnow, D. Morikawa, Y. Taguchi, and Y. Tokura. "A new class of chiral materials hosting magnetic skyrmions beyond room temperature". In: *Nat. Commun.* 6.1 (2015), p. 7638. DOI: 10.1038/ncomms8638. arXiv: 1503.05651 (cit. on pp. 1, 13).

[6] P.-J. Hsu, A. Kubetzka, A. Finco, N. Romming, K. von Bergmann, and R. Wiesendanger. "Electric-field-driven switching of individual magnetic skyrmions". In: *Nat. Nanotech.* 12.2 (2016), pp. 123–126. DOI: 10.1038/nnano.2016.234 (cit. on p. 1).

[7] K. Litzius, I. Lemesh, B. Krüger, P. Bassirian, L. Caretta, K. Richter, F. Büttner, K. Sato, O. A. Tretiakov, J. Förster, R. M. Reeve, M. Weigand, I. Bykova, H. Stoll, G. Schütz, G. S. D. Beach, and M. Kläui. "Skyrmion Hall effect revealed by direct time-resolved X-ray microscopy". In: *Nat. Phys.* 13.2 (2016), pp. 170–175. DOI: 10.1038/nphys4000 (cit. on pp. 1, 13).

[8] P. Bruno, V. K. Dugaev, and M. Taillefumier. "Topological Hall Effect and Berry Phase in Magnetic Nanostructures". In: *Phys. Rev. Lett.* 93.9 (2004), p. 096806. DOI: 10.1103/PhysRevLett.93.096806 (cit. on pp. 1, 21, 25, 56).

[9] A. Neubauer, C. Pfleiderer, B. Binz, A. Rosch, R. Ritz, P. G. Niklowitz, and P. Böni. "Topological hall effect in the a phase of MnSi". In: *Phys. Rev. Lett.* 102.18 (2009), p. 186602. DOI: 10.1103/PhysRevLett.102.186602. arXiv: arXiv:0902.1933v2 (cit. on pp. 1, 44, 45).

[10] A. Fert, V. Cros, and J. Sampaio. "Skyrmions on the track". In: *Nat. Nanotech.* 8.3 (2013), pp. 152–156. DOI: 10.1038/nnano.2013.29 (cit. on pp. 1, 13).

[11] A. Rosch. "Skyrmions: Moving with the current." In: *Nat. Nanotech.* 8.3 (2013), pp. 160–1. DOI: 10.1038/nnano.2013.21 (cit. on p. 1).

[12] X. Zhang, M. Ezawa, and Y. Zhou. "Magnetic skyrmion logic gates: Conversion, duplication and merging of skyrmions". In: *Sci. Rep.* 5 (2015). DOI: 10.1038/srep09400. arXiv: 1410.3086 (cit. on pp. 1, 14).

[13] Y. Huang, W. Kang, X. Zhang, Y. Zhou, and W. Zhao. "Magnetic skyrmion-based synaptic devices". In: *Nanotechnology* 28.8 (2017), 08LT02. DOI: 10.1088/1361-6528/aa5838 (cit. on pp. 1, 14).

[14] O. Gomonay, T. Jungwirth, and J. Sinova. "High Antiferromagnetic Domain Wall Velocity Induced by Néel Spin-Orbit Torques". In: *Phys. Rev. Lett.* 117.1 (2016), p. 017202. DOI: 10.1103/PhysRevLett.117.017202 (cit. on pp. 1, 15).

[15] V. Baltz, A. Manchon, M. Tsoi, T. Moriyama, T. Ono, and Y. Tserkovnyak. "Antiferromagnetic spintronics". In: *Rev. Mod. Phys.* 90.1 (2018), p. 015005. DOI: 10.1103/RevModPhys.90.015005 (cit. on pp. 1, 47).

[16] P. Wadley, B. Howells, J. Elezny, C. Andrews, V. Hills, R. P. Campion, V. Novak, K. Olejnik, F. Maccherozzi, S. S. Dhesi, S. Y. Martin, T. Wagner, J. Wunderlich, F. Freimuth, Y. Mokrousov, J. Kune, J. S. Chauhan, M. J. Grzybowski, A. W. Rushforth, K. W. Edmonds, B. L. Gallagher, and T. Jungwirth. "Electrical switching of an antiferromagnet". In: *Science* 351.6273 (2016), pp. 587–590. DOI: 10.1126/science.aab1031. arXiv: 1503.03765 (cit. on p. 2).

[17] J. Barker and O. A. Tretiakov. "Static and Dynamical Properties of Antiferromagnetic Skyrmions in the Presence of Applied Current and Temperature". In: *Phys. Rev. Lett.* 116.14 (2016), p. 147203. DOI: 10.1103/PhysRevLett.116.147203. arXiv: 1505.06156 (cit. on pp. 2, 15).

[18] X. Zhang, Y. Zhou, and M. Ezawa. "Antiferromagnetic Skyrmion: Stability, Creation and Manipulation". In: *Sci. Rep.* 6 (2016), p. 24795. DOI: 10.1038/srep24795. arXiv: 1504.01198 (cit. on pp. 2, 15).

[19] X. Zhang, Y. Zhou, and M. Ezawa. "Magnetic bilayer-skyrmions without skyrmion Hall effect." In: *Nat. Commun.* 7 (2016), p. 10293. DOI: 10.1038/ncomms10293. arXiv: 1504.02252 (cit. on pp. 2, 15).

[20] C. Jin, C. Song, J. Wang, and Q. Liu. "Dynamics of antiferromagnetic skyrmion driven by the spin Hall effect". In: *Appl. Phys. Lett.* 109.18 (2016), p. 182404. DOI: 10.1063/1.4967006 (cit. on pp. 2, 15).

[21] P. M. Buhl, F. Freimuth, S. Blügel, and Y. Mokrousov. "Topological spin Hall effect in antiferromagnetic skyrmions". In: *Phys. status solidi - Rapid Res. Lett.* 11.4 (2017), p. 1700007. DOI: 10.1002/pssr.201700007. arXiv: 1701.03030 (cit. on pp. 3, 48, 49, 56, 103).

[22] G. Bihlmayer, P. M. Buhl, B. Dupé, I. L. Fernandes, F. Freimuth, J. Gayles, S. Heinze, N. Kiselev, S. Lounis, Y. Mokrousov, and S. Blügel. Ψ *k Scientific Highlight of the Month Magnetic skyrmions: structure, stability, and transport phenomena*. Tech. rep. 2018 (cit. on pp. 3, 103).

[23] T. Skyrme. "A unified field theory of mesons and baryons". In: *Nucl. Phys.* 31 (1962), pp. 556–569. DOI: 10.1016/0029-5582(62)90775-7 (cit. on p. 5).

[24] A. Bogdanov and A. Hubert. "Thermodynamically stable magnetic vortex states in magnetic crystals". In: *J. Magn. Magn. Mater.* 138.3 (1994), pp. 255–269. DOI: 10.1016/0304-8853(94)90046-9 (cit. on pp. 5, 11).

[25] A. Bogdanov and A. Hubert. "The stability of vortex-like structures in uniaxial ferromagnets". In: *J. Magn. Magn. Mater.* 195.1 (1999), pp. 182–192. DOI: 10.1016/S0304-8853(98)01038-5 (cit. on p. 5).

[26] S. Mühlbauer, B. Binz, F. Jonietz, C. Pfleiderer, A. Rosch, A. Neubauer, R. Georgii, and P. Böni. "Skyrmion lattice in a chiral magnet." In: *Science* 323.5916 (2009), pp. 915–919. DOI: 10.1126/science.1166767. arXiv: 1006.3973 (cit. on pp. 5, 11–13, 16).

[27] H.-B. Braun. "Topology of static and dynamic spin textures: Skyrmions, vortices and hedgehogs". In: *Topol. Matter - Topol. Insul. Skyrmions Majoranas*. Forschungszentrum Jülich GmbH, 2017. Chap. C 3 (cit. on p. 7).

[28] C. Melcher. "Topological solitons in chiral magnetism". In: *Topol. Matter - Topol. Insul. Skyrmions Majoranas*. Forschungszentrum Jülich GmbH, 2017. Chap. A9 (cit. on pp. 7, 10).

[29] M. Hoffmann, B. Zimmermann, G. P. Müller, D. Schürhoff, N. S. Kiselev, C. Melcher, and S. Blügel. "Antiskyrmions stabilized at interfaces by anisotropic Dzyaloshinskii-Moriya interactions". In: *Nat. Commun.* 8.1 (2017), p. 308. DOI: 10.1038/s41467-017-00313-0. arXiv: 1702.07573 (cit. on pp. 9, 14, 121).

[30] A. O. Leonov, T. L. Monchesky, J. C. Loudon, and A. N. Bogdanov. "Three-dimensional chiral skyrmions with attractive interparticle interactions". In: *J. Phys. Condens. Matter* 28.35 (2016), 35LT01. DOI: 10.1088/0953-8984/28/35/35LT01 (cit. on p. 10).

[31] F. N. Rybakov, A. B. Borisov, S. Blügel, and N. S. Kiselev. "New spiral state and skyrmion lattice in 3D model of chiral magnets". In: *New J. Phys.* 18.4 (2016), p. 045002. DOI: 10.1088/1367-2630/18/4/045002. arXiv: 1601.05752 (cit. on p. 10).

[32] N. S. Kiselev, B. Zimmermann, and J. Chico. "Atomistic and micromagnetic models of magnetism". In: *Topol. Matter - Topol. Insul. Skyrmions Majoranas*. Forschungszentrum Jülich GmbH, 2017. Chap. C1 (cit. on p. 10).

[33] I. Dzyaloshinsky. "A thermodynamic theory of "weak" ferromagnetism of antiferromagnetics". In: *J. Phys. Chem. Solids* 4.4 (1958), pp. 241–255. DOI: 10.1016/0022-3697(58)90076-3 (cit. on p. 10).

[34] T. Moriya. "Anisotropic Superexchange Interaction and Weak Ferromagnetism". In: *Phys. Rev.* 120.1 (1960), pp. 91–98. DOI: 10.1103/PhysRev.120.91 (cit. on p. 10).

[35] T. Gilbert. "Classics in Magnetics A Phenomenological Theory of Damping in Ferromagnetic Materials". In: *IEEE Trans. Magn.* 40.6 (2004), pp. 3443–3449. DOI: 10.1109/TMAG.2004.836740 (cit. on p. 11).

[36] P. F. Bessarab, V. M. Uzdin, and H. Jónsson. "Method for finding mechanism and activation energy of magnetic transitions, applied to skyrmion and antivortex annihilation". In: *Comput. Phys. Commun.* 196 (2015), pp. 335–347. DOI: 10.1016/J.CPC.2015.07.001 (cit. on p. 11).

[37] K. Zeissler, M. Mruczkiewicz, S. Finizio, J. Raabe, P. M. Shepley, A. V. Sadovnikov, S. A. Nikitov, K. Fallon, S. McFadzean, S. McVitie, T. A. Moore, G. Burnell, and C. H. Marrows. "Pinning and hysteresis in the field dependent diameter evolution of skyrmions in Pt/Co/Ir superlattice stacks". In: *Sci. Rep.* 7.1 (2017), p. 15125. DOI: 10.1038/s41598-017-15262-3 (cit. on p. 11).

[38] C. Melcher. "Chiral skyrmions in the plane". In: *Proc. Roy. Soc. A* 470.2172 (2014), pp. 20140394–20140394. DOI: 10.1098/rspa.2014.0394 (cit. on p. 11).

[39] B. Dupé, M. Hoffmann, C. Paillard, and S. Heinze. "Tailoring magnetic skyrmions in ultra-thin transition metal films". In: *Nat. Commun.* 5.May (2014), p. 4030. DOI: 10.1038/ncomms5030 (cit. on p. 11).

[40] A. A. Thiele. "Steady-State Motion of Magnetic Domains". In: *Phys. Rev. Lett.* 30.6 (1973), pp. 230–233. DOI: 10.1103/PhysRevLett.30.230 (cit. on p. 11).

[41] C. Franz, F. Freimuth, A. Bauer, R. Ritz, C. Schnarr, C. Duvinage, T. Adams, S. Blügel, A. Rosch, Y. Mokrousov, and C. Pfleiderer. "Real-space and reciprocal-space Berry phases in the Hall effect of Mn(1-x)Fe(x)Si." In: *Phys. Rev. Lett.* 112.18 (2014), p. 186601. DOI: 10.1103/PhysRevLett.112.186601. arXiv: arXiv:1404.4363v1 (cit. on pp. 12–14, 44, 45, 49, 56, 88, 108).

[42] A. Feoktystov and K. Nemkovski. "Observation of chiral bulk skyrmion". In: *Topol. Matter - Topol. Insul. Skyrmions Majoranas*. Forschungszentrum Jülich GmbH, 2017. Chap. C4 (cit. on p. 12).

[43] A. Kovacs and R. Dunin-Borkowski. "Magnetic imaging of skyrmions". In: *Topol. Matter - Topol. Insul. Skyrmions Majoranas*. Forschungszentrum Jülich GmbH, 2017. Chap. C7 (cit. on p. 12).

[44] X. Z. Yu, Y. Onose, N. Kanazawa, J. H. Park, J. H. Han, Y. Matsui, N. Nagaosa, and Y. Tokura. "Real-space observation of a two-dimensional skyrmion crystal". In: *Nature* 465.7300 (2010), pp. 901–904. DOI: 10.1038/nature09124 (cit. on pp. 12, 13).

[45] C. Hanneken, F. Otte, A. Kubetzka, B. Dupé, N. Romming, K. von Bergmann, R. Wiesendanger, and S. Heinze. "Electrical detection of magnetic skyrmions by tunnelling non-collinear magnetoresistance". In: *Nat. Nanotech.* 10.12 (2015), pp. 1039–1042. DOI: 10.1038/nnano.2015.218 (cit. on p. 13).

[46] K. von Bergmann. "Skyrmions in STM". In: *Topol. Matter - Topol. Insul. Skyrmions Majoranas*. Forschungszentrum Jülich GmbH, 2017. Chap. C6 (cit. on pp. 13, 27).

[47] W. Münzer, A. Neubauer, T. Adams, S. Mühlbauer, C. Franz, F. Jonietz, R. Georgii, P. Böni, B. Pedersen, M. Schmidt, A. Rosch, and C. Pfleiderer. "Skyrmion lattice in the doped semiconductor Fe(1-x)Co(x)Si". In: *Phys. Rev. B* 81.4 (2010), p. 041203. DOI: 10.1103/PhysRevB.81.041203 (cit. on p. 13).

[48] N. Romming, A. Kubetzka, C. Hanneken, K. von Bergmann, and R. Wiesendanger. "Field-Dependent Size and Shape of Single Magnetic Skyrmions". In: *Phys. Rev. Lett.* 114.17 (2015), p. 177203. DOI: 10.1103/PhysRevLett.114.177203 (cit. on pp. 13, 16).

[49] K. G. Rana, O. Meshcheriakova, J. Kübler, B. Ernst, J. Karel, R. Hillebrand, E. Pippel, P. Werner, A. K. Nayak, C. Felser, and S. S. P. Parkin. "Observation of topological Hall effect in Mn_2RhSn films". In: *New J. Phys.* 18.8 (2016), p. 085007. DOI: 10.1088/1367-2630/18/8/085007 (cit. on p. 13).

[50] C. Moreau-Luchaire, C. Moutafis, N. Reyren, J. Sampaio, C. A. F. Vaz, N. Van Horne, K. Bouzehouane, K. Garcia, C. Deranlot, P. Warnicke, P. Wohlhüter, J.-M. George, M. Weigand, J. Raabe, V. Cros, and A. Fert. "Additive interfacial chiral interaction in multilayers for stabilization of small individual skyrmions at room temperature". In: *Nat. Nanotech.* 11.5 (2016), pp. 444–448. DOI: 10.1038/nnano.2015.313. arXiv: 1502.07853 (cit. on p. 13).

[51] S. Woo, K. Litzius, B. Krüger, M.-Y. Im, L. Caretta, K. Richter, M. Mann, A. Krone, R. M. Reeve, M. Weigand, P. Agrawal, I. Lemesh, M.-A. Mawass, P. Fischer, M. Kläui, and G. S. D. Beach. "Observation of room-temperature magnetic skyrmions and their current-driven dynamics in ultrathin metallic ferromagnets". In: *Nat. Mater.* 15.5 (2016), pp. 501–506. DOI: 10.1038/nmat4593 (cit. on p. 13).

[52] A. Soumyanarayanan, M. Raju, A. L. Gonzalez Oyarce, A. K. C. Tan, M.-Y. Im, A. P. Petrović, P. Ho, K. H. Khoo, M. Tran, C. K. Gan, F. Ernult, and C. Panagopoulos. "Tunable room-temperature magnetic skyrmions in Ir/Fe/Co/Pt multilayers". In: *Nat. Mater.* 16.9 (2017), pp. 898–904. DOI: 10.1038/nmat4934. arXiv: 1606.06034 (cit. on pp. 13, 46).

[53] J. Matsuno, N. Ogawa, K. Yasuda, F. Kagawa, W. Koshibae, N. Nagaosa, Y. Tokura, and M. Kawasaki. "Interface-driven topological Hall effect in $SrRuO_3$-$SrIrO_3$ bilayer". In: *Sci. Adv.* 2.7 (2016) (cit. on p. 13).

[54] S. Seki, J.-H. Kim, D. S. Inosov, R. Georgii, B. Keimer, S. Ishiwata, and Y. Tokura. "Formation and rotation of skyrmion crystal in the chiral-lattice insulator Cu_2OSeO_3". In: *Phys. Rev. B* 85.22 (2012), p. 220406. DOI: 10.1103/PhysRevB.85.220406 (cit. on p. 13).

[55] K. Shibata, J. Iwasaki, N. Kanazawa, S. Aizawa, T. Tanigaki, M. Shirai, T. Nakajima, M. Kubota, M. Kawasaki, H. S. Park, D. Shindo, N. Nagaosa, and Y. Tokura. "Large anisotropic deformation of skyrmions in strained crystal". In: *Nat. Nanotech.* 10.7 (2015), pp. 589–592. DOI: 10.1038/nnano.2015.113 (cit. on p. 13).

[56] P. J. Hsu, A. Kubetzka, A. Finco, N. Romming, K. Von Bergmann, and R. Wiesendanger. "Electric-field-driven switching of individual magnetic skyrmions". In: *Nat. Nanotech.* 12.2 (2017), pp. 123–126. DOI: 10.1038/nnano.2016.234. arXiv: 1601.02935 (cit. on p. 13).

[57] C. Jin, Z.-A. Li, A. Kovács, J. Caron, F. Zheng, F. N. Rybakov, N. S. Kiselev, H. Du, S. Blügel, M. Tian, Y. Zhang, M. Farle, and R. E. Dunin-Borkowski. "Control of morphology and formation of highly geometrically confined magnetic skyrmions". In: *Nat. Commun.* 8 (2017), p. 15569. DOI: 10.1038/ncomms15569 (cit. on p. 13).

[58] A. K. Nayak, V. Kumar, T. Ma, P. Werner, E. Pippel, R. Sahoo, F. Damay, U. K. Rößler, C. Felser, and S. S. P. Parkin. "Magnetic antiskyrmions above room temperature in tetragonal Heusler materials". In: *Nature* 548.7669 (2017), pp. 561–566. DOI: 10.1038/nature23466 (cit. on p. 13).

[59] F. Büttner, C. Moutafis, M. Schneider, B. Krüger, C. M. Günther, J. Geilhufe, C. v. K. Schmising, J. Mohanty, B. Pfau, S. Schaffert, A. Bisig, M. Foerster, T. Schulz, C. A. F. Vaz, J. H. Franken, H. J. M. Swagten, M. Kläui, and S. Eisebitt. "Dynamics and inertia of skyrmionic spin structures". In: *Nat. Phys.* 11.3 (2015), pp. 225–228. DOI: 10.1038/nphys3234 (cit. on p. 13).

[60] C. Niu, P. M. Buhl, G. Bihlmayer, D. Wortmann, S. Blügel, and Y. Mokrousov. "Topological crystalline insulator and quantum anomalous Hall states in IV-VI-based monolayers and their quantum wells". In: *Phys. Rev. B* 91.20 (2015), p. 201401. DOI: 10.1103/PhysRevB.91.201401 (cit. on p. 13).

[61] C. Niu, P. M. Buhl, G. Bihlmayer, D. Wortmann, S. Blügel, and Y. Mokrousov. "Two-dimensional topological crystalline insulator phase in quantum wells of trivial insulators". In: *2D Mater.* 3.2 (2016), p. 025037. DOI: 10.1088/2053-1583/3/2/025037 (cit. on p. 13).

[62] C. Niu, P. M. Buhl, G. Bihlmayer, D. Wortmann, Y. Dai, S. Blügel, and Y. Mokrousov. "Robust dual topological character with spin-valley polarization in a monolayer of the Dirac semimetal Na_3Bi". In: *Phys. Rev. B* 95.7 (2017), p. 075404. DOI: 10.1103/PhysRevB.95.075404 (cit. on p. 13).

[63] J. Tominaga, A. V. Kolobov, P. Fons, T. Nakano, and S. Murakami. "Ferroelectric Order Control of the Dirac-Semimetal Phase in GeTe-Sb_2Te_3 Superlattices". In: *Adv. Mater. Interfaces* 1.1 (2014), p. 1300027. DOI: 10.1002/admi.201300027 (cit. on p. 13).

[64] S. Parkin and S.-H. Yang. "Memory on the racetrack". In: *Nat. Nanotech.* 10.3 (2015), pp. 195–198. DOI: 10.1038/nnano.2015.41 (cit. on p. 13).

[65] J. Müller. "Magnetic skyrmions on a two-lane racetrack". In: *New J. Phys.* 19.2 (2017), p. 025002. DOI: 10.1088/1367-2630/aa5b55 (cit. on p. 13).

[66] D. Pinna, F. Abreu Araujo, J.-V. Kim, V. Cros, D. Querlioz, P. Bessiere, J. Droulez, and J. Grollier. "Skyrmion Gas Manipulation for Probabilistic Computing". In: *Phys. Rev. Appl.* 9.6 (2018), p. 064018. DOI: 10.1103/PhysRevApplied.9.064018. arXiv: 1701.07750 (cit. on p. 14).

[67] X. Zhang, Y. Zhou, M. Ezawa, G. P. Zhao, and W. Zhao. "Magnetic skyrmion transistor: skyrmion motion in a voltage-gated nanotrack". In: *Sci. Rep.* 5.1 (2015), p. 11369. DOI: 10.1038/srep11369 (cit. on p. 14).

[68] S. Meyer, B. Dupé, P. Ferriani, and S. Heinze. "Dzyaloshinskii-Moriya interaction at an antiferromagnetic interface: First-principles study of Fe/Ir bilayers on Rh(001)". In: *Phys. Rev. B* 96.9 (2017), p. 094408. DOI: 10.1103/PhysRevB.96.094408 (cit. on p. 14).

[69] J. C. Gallagher, K. Y. Meng, J. T. Brangham, H. L. Wang, B. D. Esser, D. W. McComb, and F. Y. Yang. "Robust Zero-Field Skyrmion Formation in FeGe Epitaxial Thin Films". In: *Phys. Rev. Lett.* 118.2 (2017), p. 027201. DOI: 10.1103/PhysRevLett.118.027201 (cit. on p. 14).

[70] Z. Liu and H. Ian. "Numerical studies on antiferromagnetic skyrmions in nanodisks by means of a new quantum simulation approach". In: *Chem. Phys. Lett.* 649 (2016), pp. 135–140. DOI: 10.1016/J.CPLETT.2016.02.054 (cit. on p. 15).

[71] H. Velkov, O. Gomonay, M. Beens, G. Schwiete, A. Brataas, J. Sinova, and R. A. Duine. "Phenomenology of current-induced skyrmion motion in antiferromagnets". In: *New J. Phys.* 18.7 (2016), p. 075016. DOI: 10.1088/1367-2630/18/7/075016. arXiv: 1604.05712 (cit. on p. 15).

[72] C. A. Akosa, O. A. Tretiakov, G. Tatara, and A. Manchon. "Theory of the Topological Spin Hall Effect in Antiferromagnetic Skyrmions: Impact on Current-Induced Motion". In: *Phys. Rev. Lett.* 121.9 (2018), p. 097204. DOI: 10.1103/PhysRevLett.121.097204. arXiv: 1709.02931 (cit. on pp. 15, 50, 92).

[73] F. Freimuth, R. Bamler, Y. Mokrousov, and A. Rosch. "Phase-space Berry phases in chiral magnets: Dzyaloshinskii-Moriya interaction and the charge of skyrmions". In: *Phys. Rev. B* 88.21 (2013), p. 214409. DOI: 10.1103/PhysRevB.88.214409. arXiv: 1307.8085 (cit. on p. 16).

[74] G. P. Müller, M. Hoffmann, C. Disselkamp, D. Schürhoff, S. Mavros, M. Sallermann, N. S. Kiselev, H. Jónsson, and S. Blügel. "Spirit: Multifunctional Framework for Atomistic Spin Simulations". In: (2019). arXiv: 1901.11350 (cit. on p. 18).

[75] G. Sundaram and Q. Niu. "Wave-packet dynamics in slowly perturbed crystals: Gradient corrections and Berry-phase effects". In: *Phys. Rev. B* 59.23 (1999), pp. 14915–14925. DOI: 10.1103/PhysRevB.59.14915. arXiv: 9908003 [cond-mat] (cit. on pp. 21–24).

[76] R. Cheng and Q. Niu. "Electron dynamics in slowly varying antiferromagnetic texture". In: *Phys. Rev. B* 86.24 (2012), p. 245118. DOI: 10.1103/PhysRevB.86.245118. arXiv: arXiv:1201.3523v4 (cit. on pp. 21, 25, 27–29, 31, 33, 34, 57, 81, 85, 119).

[77] O. Gomonay. "Berry-phase effects and electronic dynamics in a noncollinear antiferromagnetic texture". In: *Phys. Rev. B* 91.14 (2015), p. 144421. DOI: 10.1103/PhysRevB.91.144421. arXiv: 1501.1189 (cit. on pp. 21, 28, 35–37, 39).

[78] D. Xiao, M. C. Chang, and Q. Niu. "Berry phase effects on electronic properties". In: *Rev. Mod. Phys.* 82.3 (2010), pp. 1959–2007. DOI: 10.1103/RevModPhys.82.1959. arXiv: 0907.2021 (cit. on pp. 21, 23, 24, 27, 53, 54).

[79] G. A. Hagedorn. "Semiclassical quantum mechanics". In: *Commun. Math. Phys.* 71.1 (1980), pp. 77–93 (cit. on p. 22).

[80] D. Culcer, J. Sinova, N. A. Sinitsyn, T. Jungwirth, A. H. MacDonald, and Q. Niu. "Semiclassical Spin Transport in Spin-Orbit-Coupled Bands". In: *Phys. Rev. Lett.* 93.4 (2004), p. 046602. DOI: 10.1103/PhysRevLett.93.046602 (cit. on p. 23).

[81] Y. Gao, S. A. Yang, and Q. Niu. "Geometrical effects in orbital magnetic susceptibility". In: *Phys. Rev. B* 91.21 (2015), p. 214405. DOI: 10.1103/PhysRevB.91.214405 (cit. on pp. 23, 27).

[82] M.-C. Chang and Q. Niu. "Berry phase, hyperorbits, and the Hofstadter spectrum: Semiclassical dynamics in magnetic Bloch bands". In: 53.11 (1996), pp. 7010–7023. DOI: 10.1103/PhysRevB.53.7010. arXiv: 9511014 [cond-mat] (cit. on p. 24).

[83] J. Ye, Y. B. Kim, A. J. Millis, B. I. Shraiman, P. Majumdar, and Z. Tešanović. "Berry Phase Theory of the Anomalous Hall Effect: Application to Colossal Magnetoresistance Manganites". In: *Phys. Rev. Lett.* 83.18 (1999), pp. 3737–3740. DOI: 10.1103/PhysRevLett.83.3737 (cit. on p. 25).

[84] C. Pfleiderer and A. Rosch. "Condensed-matter physics: Single skyrmions spotted." In: *Nature* 465.7300 (2010), pp. 880–1. DOI: 10.1038/465880a (cit. on p. 26).

[85] D. Culcer, Y. Yao, and Q. Niu. "Coherent wave-packet evolution in coupled bands". In: *Phys. Rev. B* 72.8 (2005), p. 085110. DOI: 10.1103/PhysRevB.72.085110. arXiv: 0411285 [cond-mat] (cit. on pp. 28, 30, 31).

[86] R. Shindou and K.-I. Imura. "Noncommutative geometry and nonabelian Berry phase in the wave-packet dynamics of Bloch electrons". In: *Nucl. Phys. B* 720.3 (2004), pp. 399–435. DOI: 10.1016/j.nuclphysb.2005.05.019. arXiv: 0411105 [cond-mat] (cit. on pp. 28, 30).

[87] T. Hayata and Y. Hidaka. "Kinetic theory and anomalous transports in the presence of nonabelian phase-space Berry curvatures". In: *Prog. Theor. Exp. Phys.* 2017.7 (2017). DOI: 10.1093/ptep/ptx097. arXiv: 1701.04012 (cit. on pp. 28, 30).

[88] O. A. Bauchau and L. Trainelli. "The Vectorial Parameterization of Rotation". In: *Nonlinear Dyn.* 32.1 (2003), pp. 71–92. DOI: 10.1023/A:1024265401576 (cit. on p. 35).

[89] Y. Zhang, J. Železný, Y. Sun, J. van den Brink, and B. Yan. "Spin Hall effect emerging from a noncollinear magnetic lattice without spin–orbit coupling". In: *New J. Phys.* 20.7 (2018), p. 073028. DOI: 10.1088/1367-2630/aad1eb. arXiv: 1704.03917 (cit. on p. 38).

[90] E. H. Hall. "On a New Action of the Magnet on Electric Currents". In: *Am. J. Math.* 2.3 (1879), p. 287. DOI: 10.2307/2369245. arXiv: arXiv:1212.4783 (cit. on p. 41).

[91] E. H. Hall. "On the "Rotational Coeficient" in Niokel and Cobalt". In: *Phil. Mag.* 12 (1881), p. 157 (cit. on p. 41).

[92] D. Xiao, Y. Yao, Z. Fang, and Q. Niu. "Berry-Phase Effect in Anomalous Thermoelectric Transport". In: *Phys. Rev. Lett.* 97.2 (2006), p. 026603. DOI: 10.1103/PhysRevLett.97.026603 (cit. on p. 42).

[93] R. Karplus and J. M. Luttinger. "Hall Effect in Ferromagnetics". In: *Phys. Rev.* 95.5 (1954), pp. 1154–1160. DOI: 10.1103/PhysRev.95.1154 (cit. on p. 42).

[94] T. Jungwirth, Q. Niu, and A. H. MacDonald. "Anomalous Hall Effect in Ferromagnetic Semiconductors". In: *Phys. Rev. Lett.* 88.20 (2002), p. 207208. DOI: 10.1103/PhysRevLett.88.207208 (cit. on p. 43).

[95] J. Smit. "The spontaneous hall effect in ferromagnetics I". In: *Physica* 21.6-10 (1955), pp. 877–887. DOI: 10.1016/S0031-8914(55)92596-9 (cit. on p. 43).

[96] J. Smit. "The spontaneous hall effect in ferromagnetics II". In: *Physica* 24.1-5 (1958), pp. 39–51. DOI: 10.1016/S0031-8914(58)93541-9 (cit. on p. 43).

[97] L. Berger. "Influence of spin-orbit interaction on the transport processes in ferromagnetic nickel alloys, in the presence of a degeneracy of the 3d band". In: *Physica* 30.6 (1964), pp. 1141–1159. DOI: 10.1016/0031-8914(64)90105-3 (cit. on p. 43).

[98] N. A. Sinitsyn. "Semiclassical theories of the anomalous Hall effect". In: *J. Phys. Condens. Matter* 20.2 (2008), p. 023201. DOI: 10.1088/0953-8984/20/02/023201 (cit. on pp. 43, 49, 50, 52).

[99] K. v. Klitzing, G. Dorda, and M. Pepper. "New Method for High-Accuracy Determination of the Fine-Structure Constant Based on Quantized Hall Resistance". In: *Phys. Rev. Lett.* 45.6 (1980), pp. 494–497. DOI: 10.1103/PhysRevLett.45.494 (cit. on p. 43).

[100] C.-Z. Chang, J. Zhang, X. Feng, J. Shen, Z. Zhang, M. Guo, K. Li, Y. Ou, P. Wei, L.-L. Wang, Z.-Q. Ji, Y. Feng, S. Ji, X. Chen, J. Jia, X. Dai, Z. Fang, S.-C. Zhang, K. He, Y. Wang, L. Lu, X.-C. Ma, and Q.-K. Xue. "Experimental observation of the quantum anomalous Hall effect in a magnetic topological insulator." In: *Science* 340.6129 (2013), pp. 167–70. DOI: 10.1126/science.1234414 (cit. on p. 43).

[101] T. Schulz, R. Ritz, A. Bauer, M. Halder, M. Wagner, C. Franz, C. Pfleiderer, K. Everschor, M. Garst, and A. Rosch. "Emergent electrodynamics of skyrmions in a chiral magnet". In: *Nat. Phys.* 8.4 (2012), pp. 301–304. DOI: 10.1038/nphys2231 (cit. on p. 44).

[102] K. Zeissler, S. Finizio, K. Shahbazi, J. Massey, F. A. Ma'Mari, D. M. Bracher, A. Kleibert, M. C. Rosamond, E. H. Linfield, T. A. Moore, J. Raabe, G. Burnell, and C. H. Marrows. "Discrete Hall resistivity contribution from Néel skyrmions in multilayer nanodiscs". In: *Nat. Nanotech.* 13.12 (2018), pp. 1161–1166. DOI: 10.1038/s41565-018-0268-y. arXiv: 1706.06024 (cit. on pp. 44, 46).

[103] R. Ritz, M. Halder, C. Franz, A. Bauer, M. Wagner, R. Bamler, A. Rosch, and C. Pfleiderer. "Giant generic topological Hall resistivity of MnSi under pressure". In: *Phys. Rev. B* 87.13 (2013), p. 134424. DOI: 10.1103/PhysRevB.87.134424 (cit. on p. 45).

[104] J. Gayles, F. Freimuth, T. Schena, G. Lani, P. Mavropoulos, R. A. Duine, S. Blügel, J. Sinova, and Y. Mokrousov. "Dzyaloshinskii-Moriya Interaction and Hall Effects in the Skyrmion Phase of $Mn_{1-x}Fe_xGe$". In: *Phys. Rev. Lett.* 115.3 (2015), p. 036602. DOI: 10.1103/PhysRevLett.115.036602. arXiv: 1503.04842v1 (cit. on p. 46).

[105] C. S. Spencer, J. Gayles, N. A. Porter, S. Sugimoto, Z. Aslam, C. J. Kinane, T. R. Charlton, F. Freimuth, S. Chadov, S. Langridge, J. Sinova, C. Felser, S. Blügel, Y. Mokrousov, and C. H. Marrows. "Helical magnetic structure and the anomalous and topological Hall effects in epitaxial B20 $Fe_{1-y}Co_yGe$ films". In: *Phys. Rev. B* 97.21 (2018), p. 214406. DOI: 10.1103/PhysRevB.97.214406. arXiv: 1803.03281 (cit. on p. 46).

[106] K. Hamamoto, M. Ezawa, and N. Nagaosa. "Quantized topological Hall effect in skyrmion crystal". In: *Phys. Rev. B* 92.11 (2015), p. 115417. DOI: 10.1103/PhysRevB.92.115417. arXiv: 1504.06024 (cit. on pp. 46, 50).

[107] D. Maccariello, W. Legrand, N. Reyren, K. Garcia, K. Bouzehouane, S. Collin, V. Cros, and A. Fert. "Electrical detection of single magnetic skyrmions in metallic multilayers at room temperature". In: *Nat. Nanotech.* 13.3 (2018), pp. 233–237. DOI: 10.1038/s41565-017-0044-4. arXiv: 1706.05809 (cit. on p. 46).

[108] M. Raju, A. Yagil, A. Soumyanarayanan, A. K. C. Tan, A. Almoalem, O. M. Auslaender, and C. Panagopoulos. "Chiral magnetic textures in Ir/Fe/Co/Pt multilayers: Evolution and topological Hall signature". In: (2017). arXiv: 1708.04084 (cit. on p. 46).

[109] J. E. Hirsch. "Spin Hall Effect". In: *Phys. Rev. Lett.* 83.9 (1999), pp. 1834–1837. DOI: 10.1103/PhysRevLett.83.1834 (cit. on p. 47).

[110] M. Althammer. "Anomalous Hall effect, spin Hall effect and magnetoresistance". In: *Topol. Matter - Topol. Insul. Skyrmions Majoranas*. Forschungszentrum Jülich GmbH, 2017. Chap. A5 (cit. on pp. 47, 48).

[111] C. L. Kane and E. J. Mele. "Quantum Spin Hall Effect in Graphene". In: *Phys. Rev. Lett.* 95.22 (2005), p. 226801. DOI: 10.1103/PhysRevLett.95.226801 (cit. on p. 47).

[112] L. Fu and C. L. Kane. "Topological insulators with inversion symmetry". In: *Phys. Rev. B* (2007). DOI: 10.1103/PhysRevB.76.045302. arXiv: 0611341 [cond-mat] (cit. on p. 48).

[113] L. Fu. "Topological crystalline insulators". In: *Phys. Rev. Lett.* (2011). DOI: 10.1103/PhysRevLett.106.106802. arXiv: 1010.1802 (cit. on p. 48).

[114] G. Yin, Y. Liu, Y. Barlas, J. Zang, and R. K. Lake. "Topological spin Hall effect resulting from magnetic skyrmions". In: *Phys. Rev. B* 92.2 (2015), p. 024411. DOI: 10.1103/PhysRevB.92.024411. arXiv: 1503.00242 (cit. on pp. 48, 50).

[115] B. Göbel, A. Mook, J. Henk, and I. Mertig. "Antiferromagnetic skyrmion crystals: Generation, topological Hall, and topological spin Hall effect". In: *Phys. Rev. B* 96.6 (2017), p. 060406. DOI: 10.1103/PhysRevB.96.060406 (cit. on pp. 48, 50).

[116] N. Nagaosa, J. Sinova, S. Onoda, A. H. MacDonald, and N. P. Ong. "Anomalous Hall effect". In: *Rev. Mod. Phys.* 82.2 (2010), pp. 1539–1592. DOI: 10.1103/RevModPhys.82.1539. arXiv: 0904.4154 (cit. on p. 49).

[117] R. Kubo. "Statistical-Mechanical Theory of Irreversible Processes. I. General Theory and Simple Applications to Magnetic and Conduction Problems". In: *J. Phys. Soc. Japan* 12.6 (1957), pp. 570–586. DOI: 10.1143/JPSJ.12.570 (cit. on p. 49).

[118] S. G. Jakobs. "Keldysh formalism for nonequilibrium transport through quantum systems". In: *Topol. Matter - Topol. Insul. Skyrmions Majoranas*. Forschungszentrum Jülich GmbH, 2017. Chap. B2 (cit. on pp. 49, 50).

[119] N. A. Sinitsyn, A. H. MacDonald, T. Jungwirth, V. K. Dugaev, and J. Sinova. "Anomalous Hall effect in a two-dimensional Dirac band: The link between the Kubo-Streda formula and the semiclassical Boltzmann equation approach". In: *Phys. Rev. B* 75.4 (2007), p. 045315. DOI: 10.1103/PhysRevB.75.045315 (cit. on p. 50).

[120] C. W. Groth, M. Wimmer, A. R. Akhmerov, and X. Waintal. "Kwant: a software package for quantum transport". In: *New J. Phys.* 16.6 (2014), p. 063065. DOI: 10.1088/1367-2630/16/6/063065 (cit. on p. 50).

[121] P. B. Ndiaye, C. A. Akosa, and A. Manchon. "Topological Hall and spin Hall effects in disordered skyrmionic textures". In: *Phys. Rev. B* 95.6 (2017), p. 064426. DOI: 10.1103/PhysRevB.95.064426 (cit. on p. 50).

[122] B. Göbel, A. Mook, J. Henk, and I. Mertig. "Signatures of lattice geometry in quantum and topological Hall effect". In: *New J. Phys.* 19.6 (2017), p. 063042. DOI: 10.1088/1367-2630/aa709b (cit. on p. 50).

[123] N. W. Ashcroft and N. D. Mermin. *Solid State Physics*. 1976 (cit. on p. 50).

[124] G. Czycholl. *Theoretische Festkörperphysik*. Springer-Lehrbuch. Berlin, Heidelberg: Springer Berlin Heidelberg, 2008. DOI: 10.1007/978-3-540-74790-1 (cit. on p. 50).

[125] R. Gross and A. Marx. *Festkörperphysik*. De Gruyter Oldenbourg, 2014, p. 404 (cit. on p. 51).

[126] K. S. Denisov, I. V. Rozhansky, N. S. Averkiev, and E. Lähderanta. "Electron Scattering on a Magnetic Skyrmion in the Nonadiabatic Approximation". In: *Phys. Rev. Lett.* 117.2 (2016), p. 027202. DOI: 10.1103/PhysRevLett.117.027202. arXiv: 1602.03660 (cit. on p. 53).

[127] K. S. Denisov, I. V. Rozhansky, N. S. Averkiev, and E. Lähderanta. "A nontrivial crossover in topological Hall effect regimes". In: *Sci. Rep.* 7.1 (2017), p. 17204. DOI: 10.1038/s41598-017-16538-4 (cit. on p. 53).

[128] D. Xiao, J. Shi, and Q. Niu. "Berry Phase Correction to Electron Density of States in Solids". In: *Phys. Rev. Lett.* 95.13 (2005), p. 137204. DOI: 10.1103/PhysRevLett.95.137204. arXiv: 0502340 [cond-mat] (cit. on p. 54).

[129] B. Zimmermann. "Ab initio description of transverse transport due to impurity scattering in transition metals". PhD thesis. RWTH Aachen University, 2014, p. 164 (cit. on p. 65).

[130] D. Go, J.-P. Hanke, P. M. Buhl, F. Freimuth, G. Bihlmayer, H.-W. Lee, Y. Mokrousov, and S. Blügel. "Toward surface orbitronics: giant orbital magnetism from the orbital Rashba effect at the surface of sp-metals". In: *Sci. Rep.* 7 (2017), p. 46742. DOI: 10.1038/srep46742. arXiv: 1611.04674 (cit. on p. 65).

[131] J. R. Shewchuk. "Triangle: Engineering a 2D quality mesh generator and Delaunay triangulator". In: *Appl. Comput. Geom. Towar. Geom. Eng.* Springer Berlin Heidelberg, 1996, pp. 203–222. DOI: 10.1007/BFb0014497 (cit. on p. 69).

[132] J. R. Shewchuk. "Delaunay refinement algorithms for triangular mesh generation". In: *Comput. Geom.* 22.1-3 (2002), pp. 21–74. DOI: 10.1016/S0925-7721(01)00047-5 (cit. on p. 69).

[133] H.-J. Kull. *Computational Physics -Lecture notes-*. 2013 (cit. on p. 69).

[134] J. P. Perdew and Y. Wang. "Accurate and simple analytic representation of the electron-gas correlation energy". In: *Phys. Rev. B* 45.23 (1992), pp. 13244–13249. DOI: 10.1103/PhysRevB.45.13244 (cit. on p. 95).

[135] J. P. Perdew, K. Burke, and M. Ernzerhof. "Generalized Gradient Approximation Made Simple". In: *Phys. Rev. Lett.* 77.18 (1996), pp. 3865–3868. DOI: 10.1103/PhysRevLett.77.3865 (cit. on pp. 95, 99).

[136] V. I. Anisimov, F. Aryasetiawan, and A. I. Lichtenstein. "First-principles calculations of the electronic structure and spectra of strongly correlated systems: the LDA + U method". In: *J. Phys. Condens. Matter* 9.4 (1997), pp. 767–808. DOI: 10.1088/0953-8984/9/4/002 (cit. on p. 95).

[137] J. Tao, J. P. Perdew, V. N. Staroverov, and G. E. Scuseria. "Climbing the Density Functional Ladder: Nonempirical Meta–Generalized Gradient Approximation Designed for Molecules and Solids". In: *Phys. Rev. Lett.* 91.14 (2003), p. 146401. DOI: 10.1103/PhysRevLett.91.146401 (cit. on p. 95).

[138] J. P. Perdew, M. Ernzerhof, and K. Burke. "Rationale for mixing exact exchange with density functional approximations". In: *J. Chem. Phys.* 105.22 (1998), p. 9982. DOI: 10.1063/1.472933 (cit. on p. 95).

[139] A. A. Mostofi, J. R. Yates, G. Pizzi, Y.-S. Lee, I. Souza, D. Vanderbilt, and N. Marzari. "An updated version of wannier90: A tool for obtaining maximally-localised Wannier functions". In: *Comput. Phys. Commun.* 185.8 (2014), pp. 2309–2310. DOI: 10.1016/j.cpc.2014.05.003 (cit. on pp. 97, 98).

[140] I. Souza, N. Marzari, and D. Vanderbilt. "Maximally localized Wannier functions for entangled energy bands". In: *Phys. Rev. B* 65.3 (2001), p. 035109. DOI: 10.1103/PhysRevB.65.035109 (cit. on p. 98).

[141] *http://www.flapw.de* (cit. on p. 98).

[142] J.-P. Hanke, F. Freimuth, S. Blügel, and Y. Mokrousov. "Higher-dimensional Wannier functions of multiparameter Hamiltonians". In: *Phys. Rev. B* 91.18 (2015), p. 184413. DOI: 10.1103/PhysRevB.91.184413 (cit. on p. 100).

[143] M. N. Baibich, J. M. Broto, A. Fert, F. N. Van Dau, F. Petroff, P. Etienne, G. Creuzet, A. Friederich, and J. Chazelas. "Giant Magnetoresistance of (001)Fe/(001)Cr Magnetic Superlattices". In: *Phys. Rev. Lett.* 61.21 (1988), pp. 2472–2475. DOI: 10.1103/PhysRevLett.61.2472 (cit. on p. 103).

[144] P. Bruno. "Theory of interlayer exchange coupling". In: *Magn. Schichtsysteme*. Forschungszentrum Jülich GmbH, 1999. Chap. B8 (cit. on p. 103).

[145] S. Mirbt, A. M. N. Niklasson, B. Johansson, and H. L. Skriver. "Calculated oscillation periods of the interlayer coupling in Fe/Cr/Fe and Fe/Mo/Fe sandwiches". In: *Phys. Rev. B* 54.9 (1996), pp. 6382–6392. DOI: 10.1103/PhysRevB.54.6382 (cit. on p. 103).

[146] S. S. P. Parkin, N. More, and K. P. Roche. "Oscillations in exchange coupling and magnetoresistance in metallic superlattice structures: Co/Ru, Co/Cr, and Fe/Cr". In: *Phys. Rev. Lett.* 64.19 (1990), pp. 2304–2307. DOI: 10.1103/PhysRevLett.64.2304 (cit. on p. 103).

[147] S. S. P. Parkin, Z. G. Li, and D. J. Smith. "Giant magnetoresistance in antiferromagnetic Co/Cu multilayers". In: *Appl. Phys. Lett.* 58.23 (1991), p. 2710. DOI: 10.1063/1.104765 (cit. on p. 103).

[148] A. Fuß, S. Demokritov, P. Grünberg, and W. Zinn. "Short- and long period oscillations in the exchange coupling of Fe across epitaxially grown Al- and Au-interlayers". In: *J. Magn. Magn. Mater.* 103.3 (1992), pp. L221–L227. DOI: 10.1016/0304-8853(92)90192-Q (cit. on p. 103).

[149] J. Unguris, R. Celotta, and D. Pierce. "Oscillatory magnetic coupling in Fe/Ag/Fe(100) sandwich structures". In: *J. Magn. Magn. Mater.* 127.1-2 (1993), pp. 205–213. DOI: 10.1016/0304-8853(93)90216-O (cit. on p. 103).

[150] W. R. Bennett, W. Schwarzacher, and W. F. Egelhoff. "Concurrent enhancement of Kerr rotation and antiferromagnetic coupling in epitaxial Fe/Cu/Fe structures". In: *J. Appl. Phys.* 70.10 (1990), p. 5881. DOI: 10.1063/1.350093 (cit. on p. 104).

[151] A. Niklasson, S. Mirbt, M. Aldén, H. Skriver, and B. Johansson. "Exchange coupling in a Fe/Cu_n/Fe bcc (001) trilayer". In: *J. Magn. Magn. Mater.* 148.1-2 (1995), pp. 209–210. DOI: 10.1016/0304-8853(95)00211-1 (cit. on p. 104).

[152] A. Kubetzka, P. Ferriani, M. Bode, S. Heinze, G. Bihlmayer, K. von Bergmann, O. Pietzsch, S. Blügel, and R. Wiesendanger. "Revealing Antiferromagnetic Order of the Fe Monolayer on W(001): Spin-Polarized Scanning Tunneling Microscopy and First-Principles Calculations". In: *Phys. Rev. Lett.* 94.8 (2005), p. 087204. DOI: 10.1103/PhysRevLett.94.087204 (cit. on p. 121).

[153] M. Bode, E. Y. Vedmedenko, K. von Bergmann, A. Kubetzka, P. Ferriani, S. Heinze, and R. Wiesendanger. "Atomic spin structure of antiferromagnetic domain walls". In: *Nat. Mater.* 5.6 (2006), pp. 477–481. DOI: 10.1038/nmat1646 (cit. on p. 121).

[154] M. Bode, S. Heinze, A. Kubetzka, O. Pietzsch, X. Nie, G. Bihlmayer, S. Blügel, and R. Wiesendanger. "Magnetization-Direction-Dependent Local Electronic Structure Probed by Scanning Tunneling Spectroscopy". In: *Phys. Rev. Lett.* 89.23 (2002), p. 237205. DOI: 10.1103/PhysRevLett.89.237205 (cit. on p. 121).

[155] S. Blügel, M. Weinert, and P. H. Dederichs. "Ferromagnetism and antiferromagnetism of 3*d*-metal overlayers on metals". In: *Phys. Rev. Lett.* 60.11 (1988), pp. 1077–1080. DOI: 10.1103/PhysRevLett.60.1077 (cit. on p. 122).

[156] S. Blügel and P. H. Dederichs. "Ferromagnetism and Antiferromagnetism of 3*d* Metal Overlayers on Noble-Metal Substrates". In: *Europhys. Lett.* 9.6 (1989), pp. 597–602. DOI: 10.1209/0295-5075/9/6/018 (cit. on p. 122).

[157] P. Kurz, G. Bihlmayer, and S. Blügel. "Noncollinear magnetism of Cr and Mn monolayers on Cu(111)". In: *J. Appl. Phys.* 87.9 (2000), p. 6101. DOI: 10.1063/1.372622 (cit. on p. 122).

Publications

Magnetic skyrmions: structure, stability, and transport phenomena.
G. Bihlmayer, P. M. Buhl, B. Dupé, I. L. Fernandes, F. Freimuth, J. Gayles, S. Heinze, N. Kiselev, S. Lounis, Y. Mokrousov, and S. Blügel
Ψ_k *Scientific Highlight of the Month*, February (2018)
— I wrote Section 5.2 of that paper which summarizes major results of this thesis.

Topological spin Hall effect in antiferromagnetic skyrmions.
P. M. Buhl, F. Freimuth, S. Blügel, and Y. Mokrousov
Physica status solidi RRL **11**, 1700007 (2017)
— This paper summarizes the computational method and investigates the FeCuFe-trilayer as covered in Sec. 8. All calculations were performed by me and I contributed to the entire text.

Toward surface orbitronics: giant orbital magnetism from the orbital Rashba effect at the surface of *sp*-metals.
D. Go, J.-P. Hanke, P. M. Buhl, F. Freimuth, G. Bihlmayer, H.-W. Lee, Y. Mokrousov, and S. Blügel
Scientific Reports **7**, 46742 (2017)
— I calculated the Fermi-surfaces of Fig. 4 using the computational procedure as discussed in Sec. 5.2.1 of this thesis.

Topological crystalline insulator and quantum anomalous Hall states in IV-VI-based monolayers and their quantum wells.
C. Niu, P. M. Buhl, G. Bihlmayer, D. Wortmann, S. Blügel, and Y. Mokrousov
Physical Review B **91**, 201401 (2015)
— Results obtained in this paper are not discussed in this thesis.

Two-Dimensional Topological Crystalline Insulator and Topological Phase Transition in TlSe and TlS Monolayers.
C. Niu, P. M. Buhl, G. Bihlmayer, D. Wortmann, S. Blügel, and Y. Mokrousov
Nano Letters **15**, 6071-6075 (2015)
— Results obtained in this paper are not discussed in this thesis.

Two-dimensional topological crystalline insulator phase in quantum wells of trivial insulators.
C. Niu, P. M. Buhl, G. Bihlmayer, D. Wortmann, S. Blügel, and Y. Mokrousov
2D Materials **3**, 025037 (2016)
— Results obtained in this paper are not discussed in this thesis.

Robust dual topological character with spin-valley polarization in a monolayer of the Dirac semimetal Na_3Bi.
C. Niu, P. M. Buhl, G. Bihlmayer, D. Wortmann, Y. Dai, S. Blügel, and Y. Mokrousov
Physical Review B **95**, 075404 (2017)
— Results obtained in this paper are not discussed in this thesis.

Two-dimensional topological nodal line semimetal in layered X_2Y (X = Ca, Sr, and Ba; Y = As, Sb, and Bi).
C. Niu, P. M. Buhl, G. Bihlmayer, D. Wortmann, Y. Dai, S. Blügel, and Y. Mokrousov
Phys. Rev. B **95**, 235138 (2017)
— Results obtained in this paper are not discussed in this thesis.

Quantum spin Hall effect and topological phase transitions in honeycomb antiferromagnets.
C. Niu, J. P. Hanke, P. M. Buhl, G. Bihlmayer, D. Wortmann, S. Blügel, and Y. Mokrousov
submitted, preprint arXiv:1705.07035
— Results obtained in this paper are not discussed in this thesis.

Distinct magnetotransport and orbital fingerprints of chiral bobbers.
M. Redies, F. R. Lux, J. P. Hanke, P. M. Buhl, G. P. Müller, N. S. Kiselev, S. Blügel, and Y. Mokrousov
Phys. Rev. B **99**, 140407 (2019)
— Results obtained in this paper are not discussed in this thesis.

Magnonic Weyl states in Cu_2OSeO_3.
L. Zhang, Y. A. Onykiienko, P. M. Buhl, Y. V. Tymoshenko, P. Čermák, A. Schneidewind, A. Henschel, M. Schmidt, S. Blügel, D. S. Inosov, Y. Mokrousov
submitted, preprint arXiv:1901.06192
— Results obtained in this paper are not discussed in this thesis.

Acknowledgment

Throughout preparing this thesis many people contributed directly and indirectly to its creation. As is custom, I would like to acknowledge their help and thank for their support here at its end.

Foremost, I thank Prof. Dr. Stefan Blügel for giving me the opportunity of doing this PhD thesis in his excellent institute. He took the important task of being my first referee while also providing great guidance in strategic decisions, supplying scientific advise, and securing my financial well-being.

This thesis would have been impossible without Prof. Dr. Yuriy Mokrousov who introduced me to this topic and acted as direct supervisor. Hence, he taught me the majority of the applied concepts, devised the initial idea, provided helpful literature references, and secured sufficient computational resources. Moreover, his superior writing constantly mended my gothic phrasing while his lenient character created a pleasant working atmosphere which made my stay both enjoyable and successful.

I thank Prof. Dr. Stefan Wessel for readily agreeing to be my second referee.

Further invaluable support was granted by Dr. Frank Freimuth who was always able to provide extensive and well-founded answers to my more or less naive questions regarding various topics such as transport frameworks and FLEUR-characteristics.

Additionally, I thank Prof. Dr. Helen Gomonay who explained her extensions of the semi-classical wave-packet dynamics to degenerate non-collinear materials, which opened an exciting new application possibility of the developed mechanism, and who carefully examined my attempts at applying that theory.

Exchange of information between PhD-students is a further important aid when tackling every-day scientific problems. In that regard, I would like to particularly acknowledge Jan-Philipp Hanke, Gideon Müller, and Markus Hoffmann for sharing their knowledge about Wannier-functions, spin-dynamic simulations, and skyrmion properties, respectively.

Since constant focus on one narrow subject is dull, I am happy that I was able to participate in other people's scientific endeavors more or less closely related to my topic. In that regard, I am primarily indebted to Dr. Chengwang Niu whose thorough work with fruitful results granted me insight into exciting physical phenomena. Moreover, I experienced engaging research with Dongwook Go, Peter Schmitz, Matthias Redies, and Lichuan Zhang which broadened my horizon and served as productive distraction.

In general, I thank all members of the PGI-1/IAS-1 institute, and particular of the topological nanoelectronics group, for creating a most pleasant environment at the workplace, during conferences, and at the social events. Amongst the multiple people deserving praise I want to particularly highlight my office mates, Matthias Redies, Lichuan Zhang, Kerstin Dörr, and Dongwook Go, who filled the office with life, and the administrative assistance of the institute, Ute Winkler, who solved countless bureaucratic issues thus significantly smoothing my stay.

Furthermore, I thank my parents for their financial and psychological support which allowed me to be where I am now.

Lastly, I thank my girlfriend Anaïs Harneit whose mere existence already strengthened my scientific perseverance enabling this study.

Band / Volume 184
Translation Initiation with 70S Ribosomes: A Single Molecule Study
C. Remes (2018), iv, 113 pp
ISBN: 978-3-95806-358-7

Band / Volume 185
Scanning tunneling potentiometry at nanoscale defects in thin films
F. Lüpke (2018), iv, 144 pp (untersch. Pag.)
ISBN: 978-3-95806-361-7

Band / Volume 186
Inelastic neutron scattering on magnetocaloric compounds
N. Biniskos (2018), iii, 92 pp
ISBN: 978-3-95806-362-4

Band / Volume 187
Magnetic Order and Excitation in Frustrated Pyrochlore 5d - Transition Metal Oxides
E. Feng (2018), iv, 182 pp
ISBN: 978-3-95806-365-5

Band / Volume 188
Finite-Difference Time-Domain Simulations Assisting to Reconstruct the Brain's Nerve Fiber Architecture by 3D Polarized Light Imaging
M. Menzel (2018), ix, 296 pp
ISBN: 978-3-95806-368-6

Band / Volume 189
Characterization of the cell-substrate interface using surface plasmon resonance microscopy
E. M. Kreysing (2018), xiii, 260 pp
ISBN: 978-3-95806-369-3

Band / Volume 190
Scattering! Soft, Functional and Quantum Materials
Lecture Notes of the 50th IFF Spring School 2019
11 – 22 March 2019, Jülich, Germany
ed. by M. Angst, T. Brückel, S. Förster, K. Friese, R. Zorn (2019),
ca 1000 pp
ISBN: 978-3-95806-380-8

Band / Volume 191
Absolute scale off-axis electron holography of thin dichalcogenide crystals at atomic resolution
F. Winkler (2019), xxiii, 187 pp
ISBN: 978-3-95806-383-9

Band / Volume 192
High-resolution genome and transcriptome analysis of *Gluconobacter oxydans* 621H and growth-improved strains by next-generation sequencing
A. Kranz (2019), III, 182 pp
ISBN: 978-3-95806-385-3

Band / Volume 193
Group IV (Si)GeSn Light Emission and Lasing Studies
D. Stange (2019), vi, 151 pp
ISBN: 978-3-95806-389-1

Band / Volume 194
Construction and analysis of a spatially organized cortical network model
J. Senk (2019), 245 pp
ISBN: 978-3-95806-390-7

Band / Volume 195
Large-scale Investigations of Non-trivial Magnetic Textures in Chiral Magnets with Density Functional Theory
M. Bornemann (2019), 143 pp
ISBN: 978-3-95806-394-5

Band / Volume 196
Neutron scattering
Experimental Manuals of the JCNS Laboratory Course held at Forschungszentrum Jülich and at the Heinz-Maier-Leibnitz Zentrum Garching
edited by T. Brückel, S. Förster, G. Roth, and R. Zorn (2019),
ca 150 pp
ISBN: 978-3-95806-406-5

Band / Volume 197
Topological transport in non-Abelian spin textures from first principles
P. M. Buhl (2019), vii, 158 pp
ISBN: 978-3-95806-408-9

Weitere ***Schriften des Verlags im Forschungszentrum Jülich*** unter
http://wwwzb1.fz-juelich.de/verlagextern1/index.asp

Schlüsseltechnologien / Key Technologies
Band / Volume 197
ISBN 978-3-95806-408-9

Mitglied der Helmholtz-Gemeinschaft

JÜLICH
Forschungszentrum